Jordan Journal of
PHYSICS
An International Peer-Reviewed Research Journal

Volume 17, No. 3, August 2024, Safar 1446 H

Jordan Journal of Physics (*JJP*): An International Peer-Reviewed Research Journal funded by the Scientific Research and Innovation Support Fund, Jordan, and published quarterly by the Deanship of Research and Graduate Studies, Yarmouk University, Irbid, Jordan.

Manuscripts should be submitted to:

Prof. Mahdi Salem Lataifeh
Editor-in-Chief, Jordan Journal of Physics
Deanship of Research and Graduate Studies
Yarmouk University-Irbid-Jordan
Tel. 00 962 2 7211111 Ext. 2075
E-mail: *jjp@yu.edu.jo*
Website: *http://Journals.yu.edu.jo/jjp*

Jordan Journal of
PHYSICS
An International Peer-Reviewed Research Journal

Volume 17, No. 3, August 2024, Safar 1446 H

The Hashemite Kingdom of Jordan

Yarmouk University

Jordan Journal of PHYSICS

An International Peer-Reviewed Research Journal

Funded by the Scientific Research and Innovation Support Fund

Volume 17, No. 3, August 2024, Safar 1446 H

Instructions to Authors

Instructions to authors concerning manuscript organization and format apply to hardcopy submission by mail, and also to electronic online submission via the Journal homepage website (http://jjp.yu.edu.jo).

Manuscript Submission

Manuscripts are submitted electronically through the journal's website:

https://jjp.yu.edu.jo/index.php/jjp

Original *Research Articles*, *Communications* and *Technical Notes* are subject to critical review by minimum of two competent referees. Authors are encouraged to suggest names of competent reviewers. *Feature Articles* in active Physics research fields, in which the author's own contribution and its relationship to other work in the field constitute the main body of the article, appear as a result of an invitation from the Editorial Board, and will be so designated. The author of a *Feature Article* will be asked to provide a clear, concise and critical status report of the field as an introduction to the article. *Review Articles* on active and rapidly changing Physics research fields will also be published. Authors of *Review Articles* are encouraged to submit two-page proposals to the Editor-in-Chief for approval. Manuscripts submitted in *Arabic* should be accompanied by an Abstract and Keywords in English.

Organization of the Manuscript

Manuscripts should be typed double spaced on one side of A4 sheets (21.6 x 27.9 cm) with 3.71 cm margins, using Microsoft Word 2000 or a later version thereof. The author should adhere to the following order of presentation: Article Title, Author(s), Full Address and E-mail, Abstract, PACS and Keywords, Main Text, Acknowledgment. Only the first letters of words in the Title, Headings and Subheadings are capitalized. Headings should be in **bold** while subheadings in *italic* fonts.

Title Page: Includes the title of the article, authors' first names, middle initials and surnames and affiliations. The affiliation should comprise the department, institution (university or company), city, zip code and state and should be typed as a footnote to the author's name. The name and complete mailing address, telephone and fax numbers, and e-mail address of the author responsible for correspondence (designated with an asterisk) should also be included for official use. The title should be carefully, concisely and clearly constructed to highlight the emphasis and content of the manuscript, which is very important for information retrieval.

Abstract: A one paragraph abstract not exceeding 200 words is required, which should be arranged to highlight the purpose, methods used, results and major findings**.**

Keywords: A list of 4-6 keywords, which expresses the precise content of the manuscript for indexing purposes, should follow the abstract.

PACS: Authors should supply one or more relevant PACS-2006 classification codes, (available at http://www.aip.org/pacs/pacs06/pacs06-toc.html)

Introduction: Should present the purpose of the submitted work and its relationship to earlier work in the field, but it should not be an extensive review of the literature (e.g., should not exceed 1 ½ typed pages).

Experimental Methods: Should be sufficiently informative to allow competent reproduction of the experimental procedures presented; yet concise enough not to be repetitive of earlier published procedures.

Results: should present the results clearly and concisely.

Discussion: Should be concise and focus on the interpretation of the results.

Conclusion: Should be a brief account of the major findings of the study not exceeding one typed page.

Acknowledgments: Including those for grant and financial support if any, should be typed in one paragraph directly preceding the References.

References: References should be typed double spaced and numbered sequentially in the order in which they are cited in the text. References should be cited in the text by the appropriate Arabic numerals, enclosed in square brackets. Titles of journals are abbreviated according to list of scientific periodicals. The style and punctuation should conform to the following examples:

1. Journal Article:

a) Heisenberg, W., Z. Phys. 49 (1928) 619.
b) Bednorz, J. G. and Müller, K. A., Z. Phys. B64 (1986) 189
c) Bardeen, J., Cooper, L.N. and Schrieffer, J. R., Phys. Rev. 106 (1957) 162.
d) Asad, J. H., Hijjawi, R. S., Sakaji, A. and Khalifeh, J. M., Int. J. Theor. Phys. 44(4) (2005), 3977.

2. Books with Authors, but no Editors:

a) Kittel, C., "Introduction to Solid State Physics", 8th Ed. (John Wiley and Sons, New York, 2005), chapter 16.
b) Chikazumi, S., C. D. Graham, JR, "Physics of Ferromagnetism", 2nd Ed. (Oxford University Press, Oxford, 1997).

3. Books with Authors and Editors:

a) Allen, P. B. "Dynamical Properties of Solids", Ed. (1), G. K. Horton and A. A. Maradudin (North-Holland, Amsterdam, 1980), p137.
b) Chantrell, R. W. and O'Grady, K., "Magnetic Properities of Fine Particles" Eds. J. L. Dormann and D. Fiorani (North-Holland, Amsterdam, 1992), p103.

4. Technical Report:

Purcell, J. "The Superconducting Magnet System for the 12-Foot Bubble Chamber", report ANL/HEP6813, Argonne Natt. Lab., Argonne, III, (1968).

5. Patent:

Bigham, C. B., Schneider, H. R., US patent 3 925 676 (1975).

6. Thesis:

Mahmood, S. H., Ph.D. Thesis, Michigan State University, (1986), USA (Unpublished).

7. Conference or Symposium Proceedings:

Blandin, A. and Lederer, P. Proc. Intern. Conf. on Magnetism, Nottingham (1964), P.71.

8. Internet Source:

Should include authors' names (if any), title, internet website, URL, and date of access.

9. Prepublication online articles (already accepted for publication):

Should include authors' names (if any), title of digital database, database website, URL, and date of access.

For other types of referenced works, provide sufficient information to enable readers to access them.

Tables: Tables should be numbered with Arabic numerals and referred to by number in the Text (e.g., Table 1). Each table should be typed on a separate page with the legend above the table, while explanatory footnotes, which are indicated by superscript lowercase letters, should be typed below the table.

Illustrations: Figures, drawings, diagrams, charts and photographs are to be numbered in a consecutive series of Arabic numerals in the order in which they are cited in the text. Computer-generated illustrations and good-quality digital photographic prints are accepted. They should be black and white originals (not photocopies) provided on separate pages and identified with their corresponding numbers. Actual size graphics should be provided, which need no further manipulation, with lettering (Arial or Helvetica) not smaller than 8 points, lines no thinner than 0.5 point, and each of uniform density. All colors should be removed from graphics except for those graphics to be considered for publication in color. If graphics are to be submitted digitally, they should conform to the following minimum resolution requirements: 1200 dpi for black and white line art, 600 dpi for grayscale art, and 300 dpi for color art. All graphic files must be saved as TIFF images, and all illustrations must be submitted in the actual size at which they should appear in the journal. Note that good quality hardcopy original illustrations are required for both online and mail submissions of manuscripts.

Text Footnotes: The use of text footnotes is to be avoided. When their use is absolutely necessary, they should be typed at the bottom of the page to which they refer, and should be cited in the text by a superscript asterisk or multiples thereof. Place a line above the footnote, so that it is set off from the text.

Supplementary Material: Authors are encouraged to provide all supplementary materials that may facilitate the review process, including any detailed mathematical derivations that may not appear in whole in the manuscript.

Revised Manuscript and Computer Disks

Following the acceptance of a manuscript for publication and the incorporation of all required revisions, authors should submit an original and one more copy of the final disk containing the complete manuscript typed double spaced in Microsoft Word for Windows 2000 or a later version thereof. All graphic files must be saved as PDF, JPG, or TIFF images.

Allen, P.B., "…….", in: Horton, G.K., and Muradudin, A. A., (eds.), "Dynamical…….", (North……..), pp….

Reprints

Twenty (20) reprints free of charge are provided to the corresponding author. For orders of more reprints, a reprint order form and prices will be sent with the article proofs, which should be returned directly to the Editor for processing.

Copyright

Disclaimer

Indexing

JJP is currently indexing in:

<table>
<tr><td> 
</td><td>Emerging Sources Citation Index (ESCI)

Journal Impact Factor 2022

0.7</td></tr>
<tr><td colspan="2"> 
</td></tr>
</table>

Jordan Journal of
PHYSICS
An International Peer-Reviewed Research Journal

Volume 17, No. 3, August 2024, Safar 1446 H

Table of Contents:

Volume 17, Number 3, 2024. pp. 261-271

Jordan Journal of Physics

ARTICLE

Time Dependent Spectral Ratio Technique for Micro-seismic Exploration in the Niger Delta Region of Nigeria

Emetere Moses Eterigho[a,b]

[a] *Department of Physics, Bowen University Iwo, Nigeria.*

[b] *Department of Mechanical Engineering Science, University of Johannesburg, South Africa.*

Doi: **https://doi.org/10.47011/17.3.1**

Received on: 05/01/2022; *Accepted on: 12/12/2022*

Abstract: Since the discovery of the hydrocarbon micro-tremors, there have been numerous efforts to understand the causes of these microseisms related to oil and gas. A spectral ratio (SR) time-dependent equation was derived based on geological principles. The equation showed tremendous success in analyzing multi-layered geological terrain and estimating the spectral ratio in the Niger Delta region of Nigeria. This study seeks to develop a reliable model using standard seismic reflection data to analyze microseismic datasets from hydrocarbon reservoirs. Type A-SR acts over a longer duration and can be used to determine hydrocarbon reservoirs. Type B-SR acts in a short time with maximum impact. It can be used to determine gas condensate flow in the hydrocarbon reservoir. It is recommended that this technique be applied in real time to ascertain its accuracy.

Keywords: Niger Delta, Microseismic, Amplitude, Special ratio, Geology.

Introduction

The outcomes of seismic investigations have increasingly become complex due to puzzling geological features within the subsurface and depositional trends [1]. Advances in new technologies and numerically efficient computing systems have provided an in-depth understanding of subsurface complexity [2]. However, a few anomalies in understanding the subsurface may stem from the foundational theories of the equipment or technique used. So far, numerical solutions of mathematically derived seismic attributes are salient in pre-modeling complex situations. Thus, this concept is a critical part of the model-building technique for the determination of seismic imaging and attribute anomalies.

The horizontal-to-vertical (H/V) spectral ratio of the seismic noise technique has gained wide usage since it was proposed by Nogoshi and Igarashi [3, 4]. This technique has proven to be very useful in a deltaic environment for characterizing the sediments on top of the bedrock [5-7]. The technique basically computes the ratio between the Fourier amplitude spectra of the horizontal and vertical components of seismic noise measurements, as depicted in the formula below:

$$\frac{H}{V} = \frac{S_{NS}+S_{EW}}{2*S_V} \quad (1)$$

where S_{NS}, S_{EW}, and S_V are the magnitudes of the smoothed Fourier spectra of the north-south, east-west, and vertical components, respectively. The experimental factors often affect the H/V spectral ratio (HVSR) results. These factors include complex geological terrains, subsalts, formations beneath volcanic rocks, formations with low acoustic impedance contrast, and seismic damage distributions [8, 9]. Also, the general trends of the H/V technique indicate that horizontal motion is larger than vertical motion on soft ground, while horizontal and vertical motions are similar on hard ground. This can

Corresponding Author: Emetere Moses E. **Email**: emeteremoses@gmail.com

pose a major challenge when the geology terrain includes integrated profiles of hard and soft ground or rock formations.

Basically, the HVSR is mainly obtained from microtremor surveys. Beyond its above-listed application, the HVSR technique is now adopted in oil and gas exploration for estimating drilling risk and monitoring reservoirs [10, 11]. Haris *et al.* compared the results of microtremor surveys and time-reverse modeling (TRM) over a hydrocarbon reservoir [12]. It was observed that HVSR showed a potential hydrocarbon zone, while TRM predicted the depth range of this zone. HVSR is used for modeling sedimentary basins using a simple two-layer model, consisting of node side (hard rock basement) and open-end (surface of the basin).

Hydrocarbon reservoirs within the sedimentary basin act as frequency converters, producing a unique spectral signature that is used as a direct hydrocarbon indicator. Many companies have affirmed that low-frequency passive seismic anomalies are common features of hydrocarbon reservoirs [13, 14].

However, the quality of signal resolution is quite important as it helps clarify the effects of some geological features. Q estimation is widely used, as it is a proven tool to obtain better signal resolution via inverse Q filtering principles. Q refers to the attenuation factor of the transmitted seismic wavelet. Various scientists who have worked on the building technique of seismic technologies have made discoveries that show the dynamism of the subsurface. For example, the cyclic succession of sand and shale properties was used to create a 1D seismic model for lithological elements [15]. The Q estimation factor for quantifying attenuation has been used to characterize rock properties, reservoir heterogeneity, and subtle geological structures [14, 16, 17]. Q can also be used in reservoir characterization [17].

It has been established that the zero-offset ray-tracing technique for primary P waves is efficient for creating a 2D seismic model to predict the seismic responses of geological features [18]. Therefore, Q-factor can be derived from transmission data, such as vertical seismic profiling (VSP) data [19], crosswell dataset [20], and sonic logging datasets [21]. Q estimation depends on frequency shifts in the geological or geotechnical setting. Li *et al.* [17] used this concept (frequency shifting) to prevent the exponential decay of seismic amplitude with respect to time and depth. In other words, Q estimation is largely dependent on theoretical configurations. These configurations include time-domain modification of the spectral ratio method [22], statistical analysis of spectral ratio [23], frequency shift method [17], and spectral ratio time-dependent method [24], all of which are essential for fieldwork to obtain Q-factor.

Since the discovery of hydrocarbon microtremors, there have been numerous efforts to understand the causes of this phenomenon related to oil and gas [25]. In this paper, the time-dependent spectral ratio (TDSR) is modified to enable the use of standard seismic reflection data to analyze the microseismic emissions from hydrocarbon reservoirs. The second section of the paper introduces the theoretical formulations. The mathematical implications of the technicalities of the theory are explained in the third section. The application of the new theory to an oil field is illustrated in the fourth section. The oil field is located in the Niger Delta region of Nigeria. The surface geology of the region is illustrated in the red box in Fig. 1.

Background Theories and Formulation

Seismic waves lose energy and magnitude of frequency when traveling through the subsurface of the Earth. The time-frequency decomposition $S(\tau,\omega)$ of a seismic trace $s(t)$ in the presence of inelastic attenuation Q and time-varying amplitude is given as:

$$S(\tau,\omega) = W(\omega) \times A(\tau) \times A_o exp\left(\frac{-\omega\tau}{2Q(\tau)}\right) \quad (2)$$

where ω is the frequency, τ is the time, $W(\omega)$ represents the frequency/amplitude spectrum of the underlying wavelet, $A(\tau)$ is the time-varying amplitude effect, and $A_o exp\left(\frac{-\omega\tau}{2Q(\tau)}\right)$ defines the time-varying Q contribution. Most researchers have tried to modify the amplitude using a constant Q model:

$$A_n(f) = A_o(f)\exp(-\frac{\pi f t}{Q}) \quad (3)$$

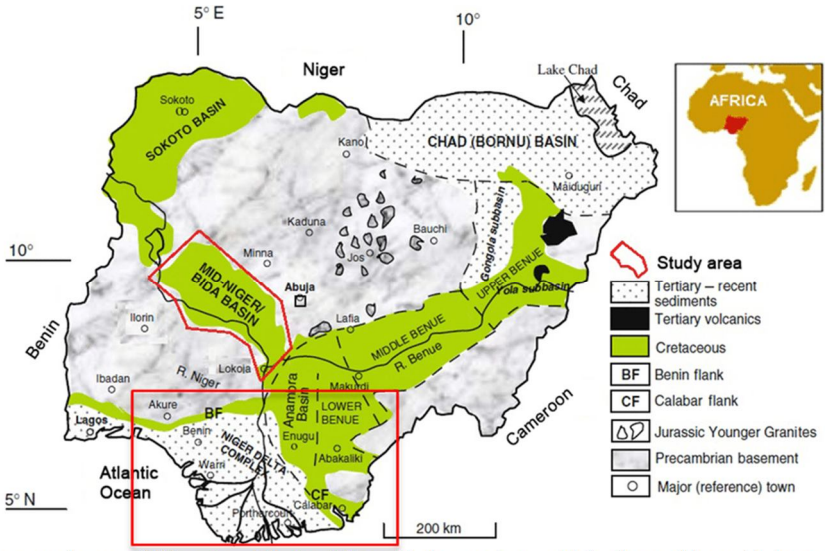

FIG. 1. Surface geology of Nigeria with the Niger Delta region within the red box (Adapted from [36]).

Emetere *et al*. modified the ratio of the amplitude in Eq. (3) and used Maclaurin's series to simulate the multilayer implementation of seismic signals through the subsurface [24]. From the amplitude misfit function and its corresponding gradient, the volume of hydrocarbons can be estimated using a multi-layer probe.

$$V_n = A\varphi.\frac{sQ}{\pi ft}\sum_{n=1}^{\infty}\sqrt[n]{\frac{A_n(f,t)}{A_o(f,t)}} \tag{4}$$

where A is the area of the areal extent of the deposition, s is the speed of the seismic probe, and φ is the porosity.

In this research, the time-frequency decomposition of two geographical points within the same location was adopted to modify Eq. (2). The mathematical implication is illustrated in Eq. (5). Technically, the reason for adopting two seismic signals is to capture the conversion processes as microseismic events come from passive seismology, while seismic reflection-wave surveys are related to active methods of seismic exploration [26].

$$S(\tau,\omega) = W(\omega_n-\omega_1)\times A(\tau_n-\tau_1)\times A_o exp\left(\frac{-(\omega_n-\omega_1)(\tau_n-\tau_1)}{2Q((\tau_n-\tau_1))}\right) \tag{5}$$

where $W(\omega) = \sin(2n\pi\omega\tau) + \cos(2n\pi\omega\tau)$

Hence, adopting the assumption that $\omega_n\tau_1 = 0\ and\ \omega_1\tau_n = 0$, the expanded Eq. (5) becomes:

$$S(\tau,\omega) = \{\sin(2n\pi\omega_1\tau_1(\cos(2n\pi\omega_n\tau_n) - \sin(2n\pi\omega_n\tau_n)) + \cos(2n\pi\omega_1\tau_1(\sin(2n\pi\omega_n\tau_n) + \cos(2n\pi\omega_n\tau_n))\}\times A(\Delta\tau)\times A_o exp\left(\frac{\omega_1\tau_1-\omega_n\tau_n}{2Q(\Delta\tau)}\right) \tag{6}$$

Dividing Eq. (6) by Eq. (5) under the assumption that $Q(\tau)\approx Q(\Delta\tau)$, we get:

$$\frac{A(\Delta\tau)}{A(\tau)} = \frac{\sin(2n\pi\omega\tau)+\cos(2n\pi\omega\tau)}{\sin(2n\pi\omega_1\tau_1(\cos(2n\pi\omega_n\tau_n)-\sin(2n\pi\omega_n\tau_n))+\cos(2n\pi\omega_1\tau_1(\sin(2n\pi\omega_n\tau_n)+\cos(2n\pi\omega_n\tau_n))}\times exp\left(\frac{\omega_1\tau_1}{2Q(\tau)}\right) \tag{7}$$

or

$$\frac{A(\Delta\tau)}{A(\tau)} = \frac{\sin(2n\pi\omega\tau)+\cos(2n\pi\omega\tau)}{\sin(2n\pi\omega_1\tau_1(\cos(2n\pi\omega_n\tau_n)-\sin(2n\pi\omega_n\tau_n))+\cos(2n\pi\omega_1\tau_1(\sin(2n\pi\omega_n\tau_n)+\cos(2n\pi\omega_n\tau_n))}\times exp\left(\frac{-2\omega_1\tau_1+\omega_n\tau_n}{2Q(\tau)}\right) \tag{8}$$

However, based on the estimation of individual seismic signals at each geographical point, Eqs. (7) and (8) can be simplified into :

$$\frac{A(\Delta\tau)}{A(\tau)} = \frac{\sin(2n\pi\omega_n\tau_n)+\cos(2n\pi\omega_n\tau_n)}{\sin(2n\pi\omega_1\tau_1(\cos(2n\pi\omega_n\tau_n)-\sin(2n\pi\omega_n\tau_n))+\cos(2n\pi\omega_1\tau_1(\sin(2n\pi\omega_n\tau_n)+\cos(2n\pi\omega_n\tau_n))}\times exp\left(\frac{\omega_1\tau_1}{2Q(\tau)}\right) \tag{9}$$

or

$$\frac{A(\Delta\tau)}{A(\tau)} = \frac{\sin(2n\pi\omega_n\tau_n)+\cos(2n\pi\omega_n\tau_n)}{\sin(2n\pi\omega_1\tau_1(\cos(2n\pi\omega_n\tau_n)-\sin(2n\pi\omega_n\tau_n))} \times \\ +\cos(2n\pi\omega_1\tau_1(\sin(2n\pi\omega_n\tau_n)+\cos(2n\pi\omega_n\tau_n)) \\ exp\left(\frac{-2\omega_1\tau_1+\omega_n\tau_n}{2Q(\tau)}\right) \quad (10)$$

$$\frac{A(\Delta\tau)}{A(\tau)} = \frac{\sin(2n\pi\omega_1\tau_1)+\cos(2n\pi\omega_1\tau_1)}{\sin(2n\pi\omega_1\tau_1(\cos(2n\pi\omega_n\tau_n)-\sin(2n\pi\omega_n\tau_n))} \times \\ +\cos(2n\pi\omega_1\tau_1(\sin(2n\pi\omega_n\tau_n)+\cos(2n\pi\omega_n\tau_n)) \\ exp\left(\frac{\omega_1\tau_1}{2Q(\tau)}\right) \quad (11)$$

or

$$\frac{A(\Delta\tau)}{A(\tau)} = \frac{\sin(2n\pi\omega_1\tau_1)+\cos(2n\pi\omega_1\tau_1)}{\sin(2n\pi\omega_1\tau_1(\cos(2n\pi\omega_n\tau_n)-\sin(2n\pi\omega_n\tau_n))} \times \\ +\cos(2n\pi\omega_1\tau_1(\sin(2n\pi\omega_n\tau_n)+\cos(2n\pi\omega_n\tau_n)) \\ exp\left(\frac{-2\omega_1\tau_1+\omega_n\tau_n}{2Q(\tau)}\right) \quad (12)$$

Numerical Analysis of the Spectral Amplitude on the Niger Delta Field

The parameters adopted in this section were obtained from Barton, where the Q factor ranged between 26 and 200 and the frequency between 450 and 725 Hz [27]. Though the travel time of S waves through the sedimentary rock was estimated by Campbell to be 1.10 s [28], a maximum time of 4 s was considered to accommodate the physics of the site attenuation (Q) parameter, which may dependend on either the maximum frequency [29, 30] or corner frequency. The spectral amplitude was observed to gradually decrease with depth in the inhomogeneous subsurface. The decrease trend of the SR method with respect to time was monitored as shown in Figs. 2-4.

Figure 2(a) presents a scenario where $A_n(f,t)$ and $A_o(f,t)$ are in their original forms. The amplitude misfit is highest at the maximum spectral and modified amplitudes. The projections of the spectral and modified amplitudes are shown in Figs. 2(b) and 2(c). These features suggest that the trends of the spectral and modified amplitudes are critical for understanding deposits incomplex geological settings like the Niger Delta. This is because the distribution of sub-weathering velocities in the subsurface is affected by high-velocity Palaeozoic carbonates and lower-velocity Cretaceous clastic [31]. When a multi-layered petroleum system is considered in the complex geometry, as described by Eq. (4), the distribution of sub-weathering velocities changes, as shown in Figs. 3-4. Figures 3(a) and 4(a) depict the sine and cosine forms of the amplitude misfit under the influence of the individual spectral and modified amplitudes.

Application of Spectral Amplitude: Case Study of the Niger Delta Field

The cross-sectional profile of the Akata Formation in the Niger Delta region of Nigeria is presented in Fig. 5.

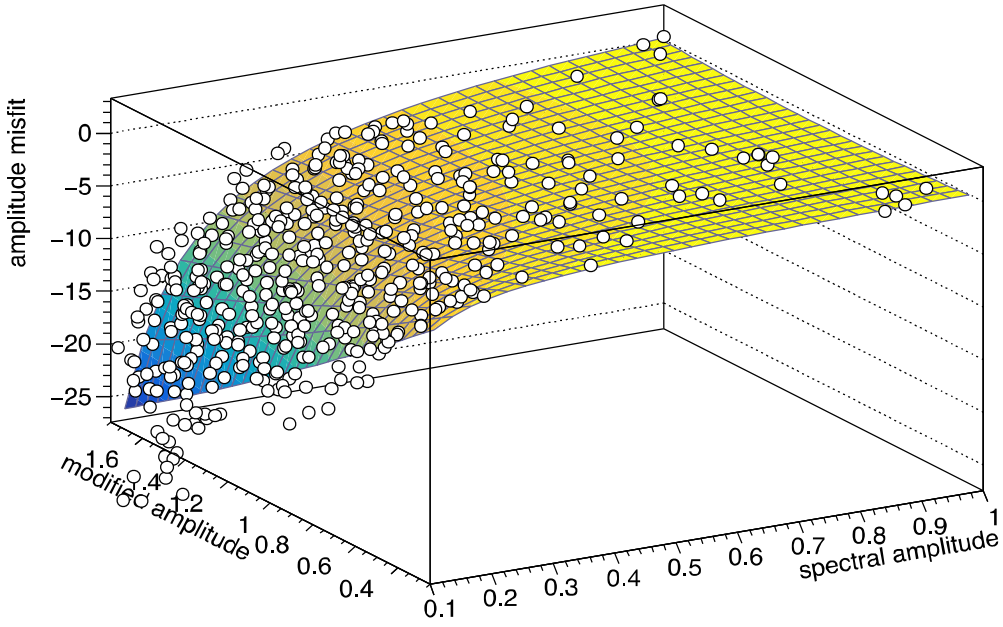

FIG. 2(a). $A_n(f,t)$ and $A_o(f,t)$ in their original form.

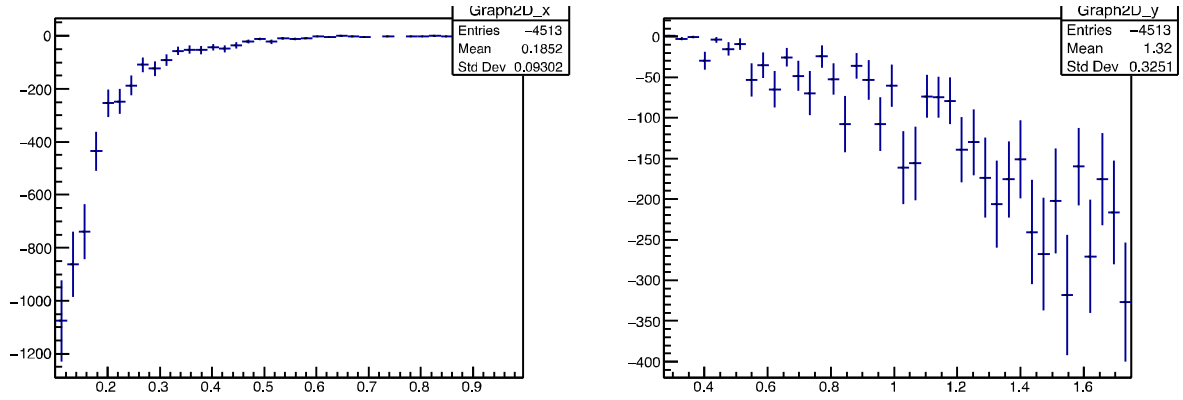

FIG. 2. (b) The misfit amplitude projection under the influence of $A_o(f,t)$. (c) The misfit amplitude projection under the influence of $A_n(f,t)$.

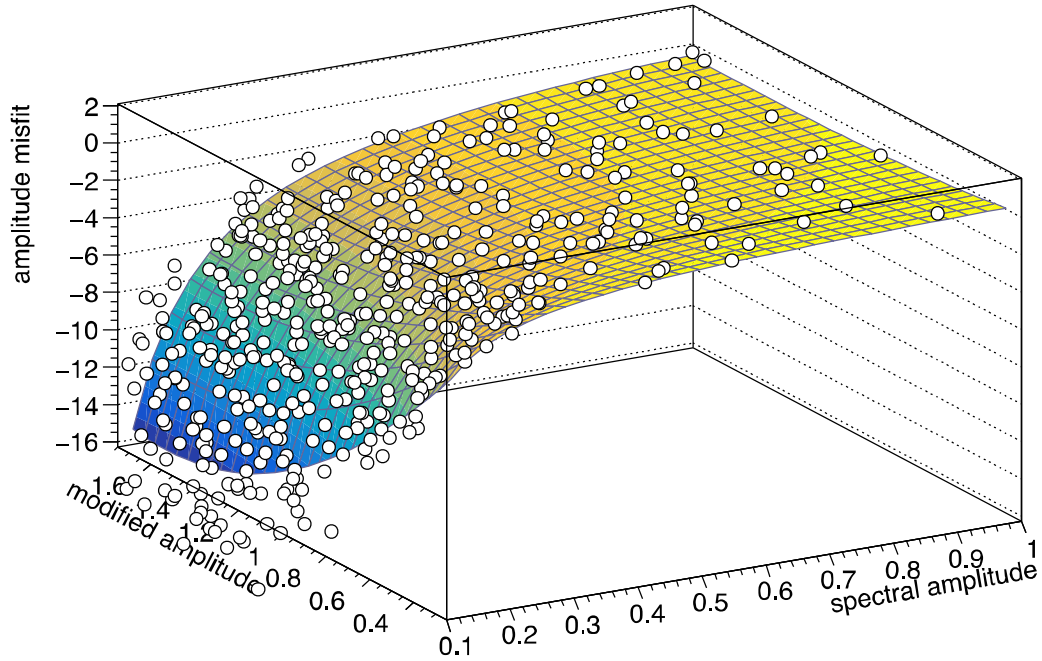

FIG. 3(a). $A_n(f,t)$ and $A_o(f,t)$ in their sine form.

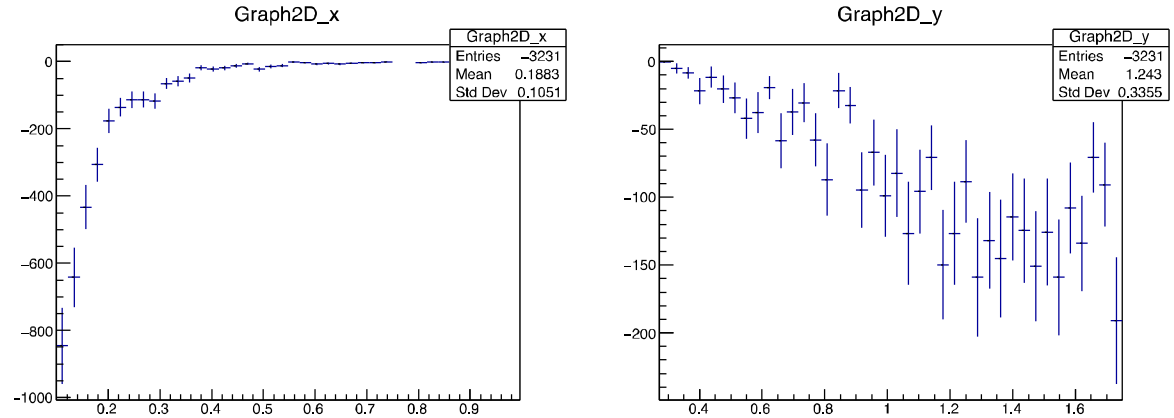

FIG. 3. (b) The misfit amplitude projection under the influence of the sine form of $A_o(f,t)$. (c) The misfit amplitude projection under the influence of the sine form of $A_n(f,t)$.

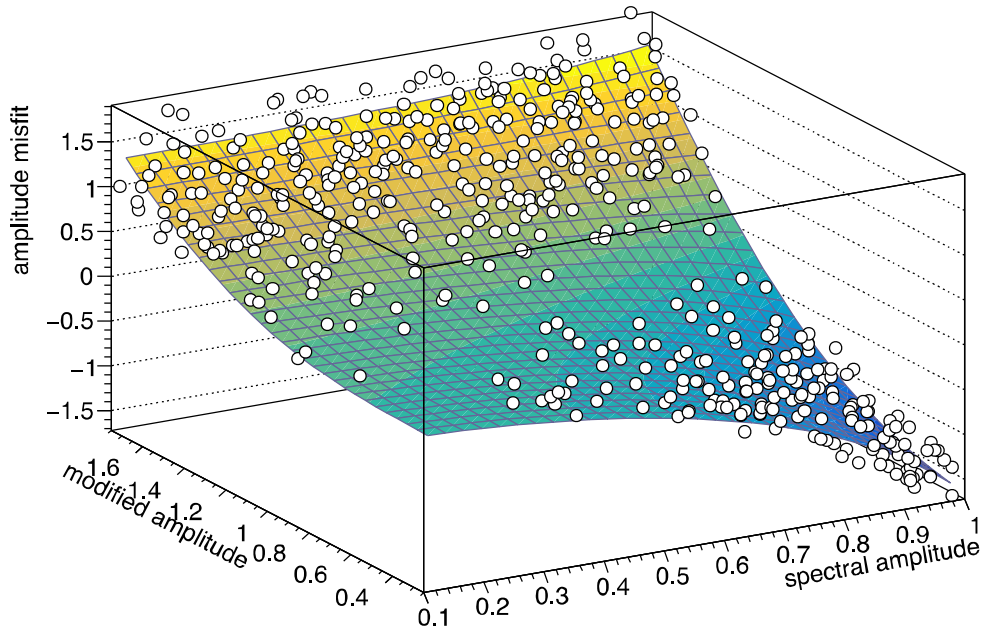

FIG. 4(a). $A_n(f,t)$ and $A_o(f,t)$ in their cosine form.

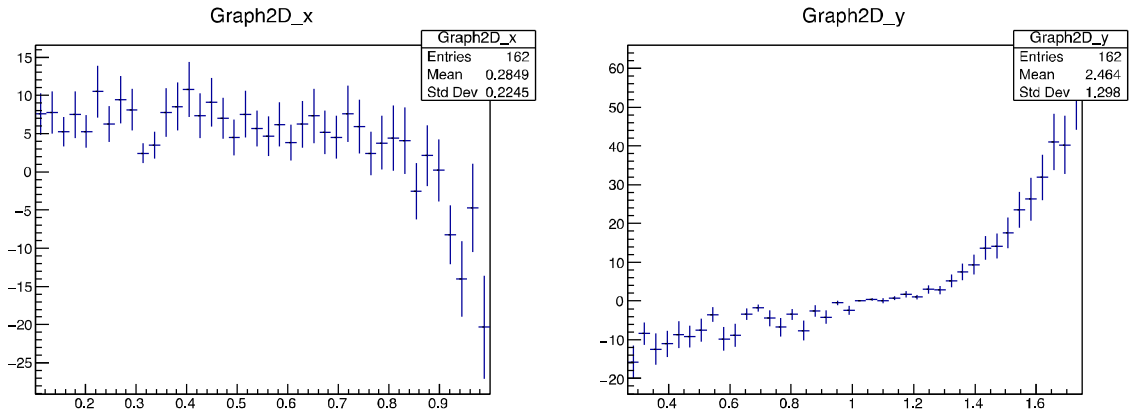

FIG. 4. (b) The misfit amplitude projection under the influence of the cosine form of $A_o(f,t)$. (c) The misfit amplitude projection under the influence of the cosine form of $A_n(f,t)$.

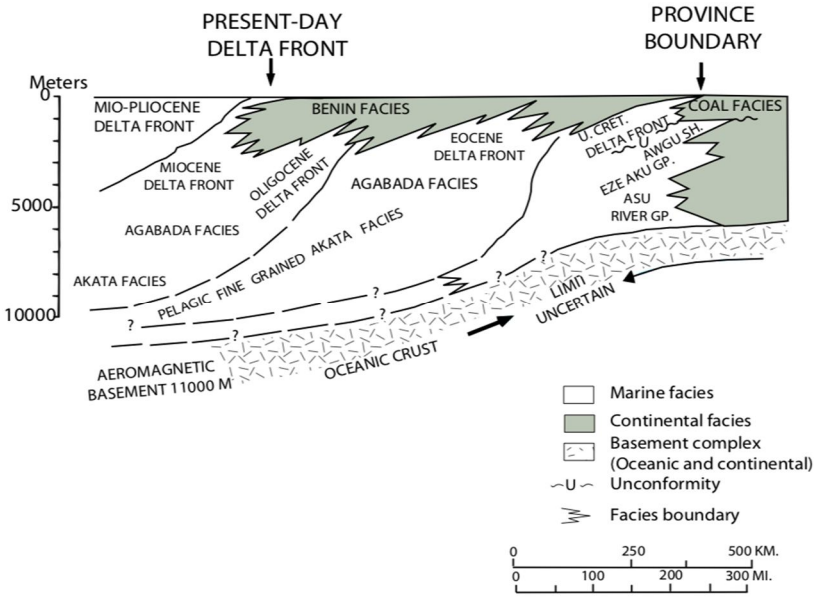

FIG. 5. The depth profile of the Niger Delta region [32].

The Akata Formation is known to have the highest number of hydrocarbon reservoirs in the Niger Delta [33-35]. The primary source rocks in the Niger Delta petroleum system include the upper Akata Formation, the marine-shale facies of the delta, and the interbedded marine shale of the lowermost Agbada Formation. The higher-density delta-front sands in the Agbada Formation and the under-compacted delta-slope clays in the Akata Formation influence seismic transmission in the Niger Delta as presented in Fig. 5 [32].

In this study, the depth profile analysis of the Akata Formation is illustrated in Fig. 6. Two seismic signals are presented in Fig. 6. The source of the dataset is documented in Tuttle *et al*. [32]. The iso-reflectance (Ro) values and their corresponding depths are 0.6 at 2.5 km, 0.8 at 3.2 km, 1.2 at 4.2 km, and 2.0 at 5.4 km.

The theory presented in Eqs. (2)-(12) propounds that two seismic signals within the same geographical site can generate microseismic events, which are used to determine salient geological features, such as hydrocarbon reservoirs. The two seismic signals presented in Fig. 6 are analyzed at two different depths: 6 km and 7 km. The combined effect of the two seismic signals depends on the reference frame chosen. If the higher seismic signal is used as the reference, Eq. (7) applies. Similarly, if the lower seismic signal is the reference, Eq. (8) is applied. Furthermore, Eqs. (7) and (8) can be classified into individual seismic signals, as presented in Eqs. (9)-(12). Equation (12) is referred to as case 1, Eq. (10) as case 2, Eq. (11) as case 3, and Eq. (9) as case 4.

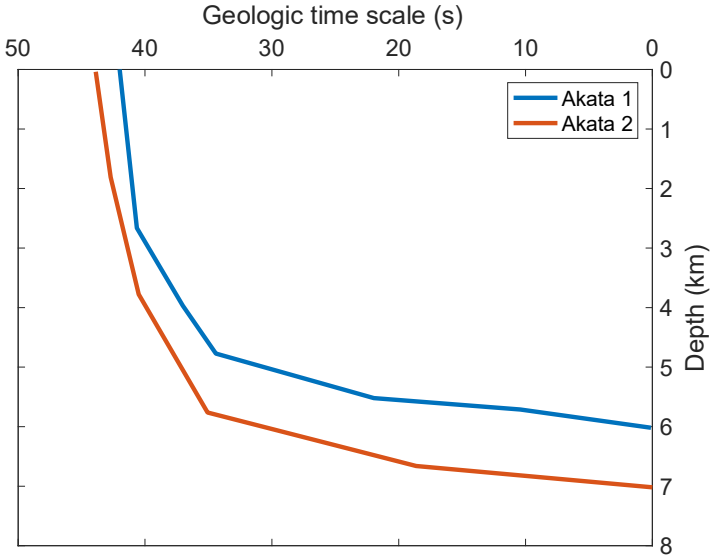

FIG. 6. Depth profile of two close seismic signals in Akata Formation.

The spectral ratio against the depth for $exp\left(\frac{-2\omega_1\tau_1+\omega_n\tau_n}{2Q(\tau)}\right)$ is presented in Fig. 7. This scenario reflects a situation where the lower seismic signal dominates the microseismic events. Usually, the microtremors of hydrocarbons have energy in the low-frequency spectrum. Hence, there is a possibility of wave superposition if an experiment is carried out in real time. In this case, it was observed that the hydrocarbon microtremor (HDM) could be found within 6-7 km depth in the Niger Delta region. This spectral ratio, termed Type A-SR, is generally lower compared to scenarios where higher seismic signals dominate, as presented in Fig. 8.

The advantage of the latter scenario, where a larger seismic signal dominates the micro-seismic event, is its potential to locate the gas condensate flows, found at the depth of 1850 m in this study. It is salient to note that the above condition leads to spectral ratio attenuation to zero at lower depths (Fig. 8). This type of spectral ratio is named Type B-SR. The hypothesis in this regard is that there will be spectral ratio quenching at higher depths when the seismic signal is $exp\left(\frac{\omega_1\tau_1}{2Q(\tau)}\right)$.

The analysis of the spectral ratio versus the geological time scale is presented in Figs. 9 and 10. Type A-SR has a broad operational duration with its maximum at 18 s (Fig. 9). Hence, the HDM can also be estimated at a maximum (type A) spectral ratio when the exponential conversion from the seismic reflection wave

survey to the micro-seismic event is $\left(\frac{-2\omega_1\tau_1+\omega_n\tau_n}{2Q(\tau)}\right)$. Also, it was observed that the Type B-SR acts within a short time at high magnitude (Fig. 10) when the exponential conversion from the seismic reflection wave survey to the micro-seismic event is $\left(\frac{\omega_1\tau_1}{2Q(\tau)}\right)$.

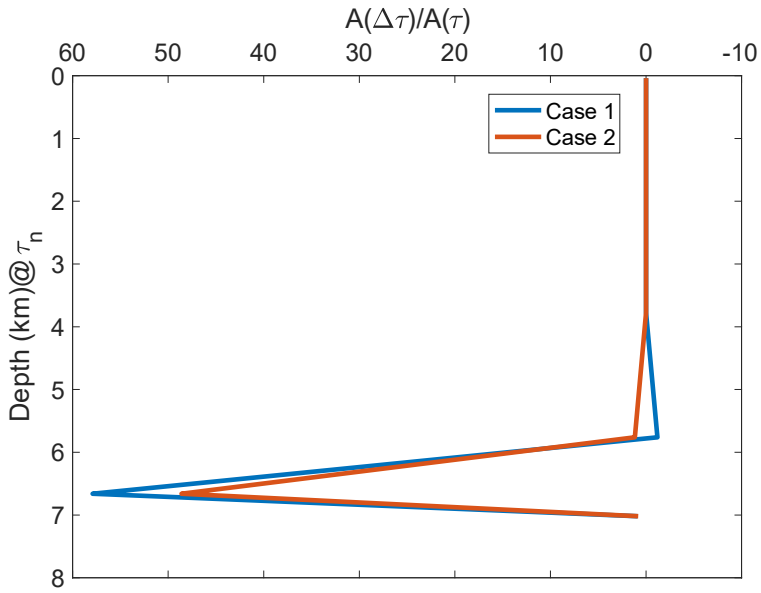

FIG. 7. Spectral ratio variation within $exp\left(\frac{-2\omega_1\tau_1+\omega_n\tau_n}{2Q(\tau)}\right)$ depth profile.

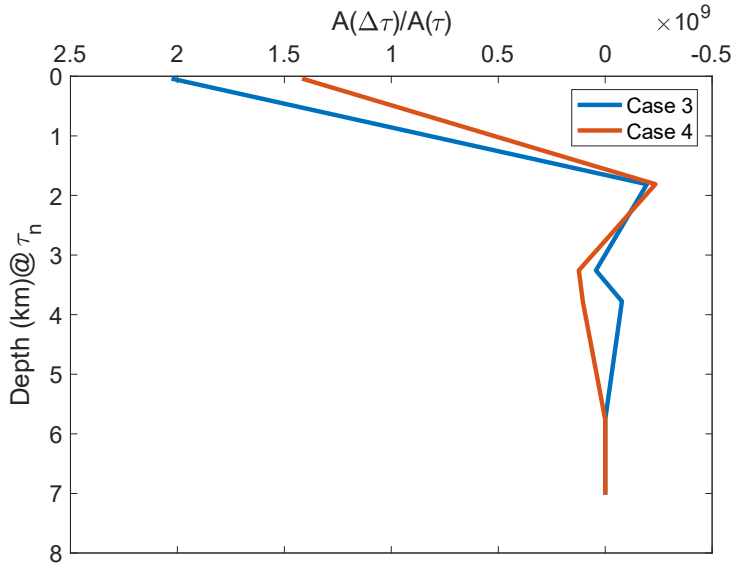

FIG. 8. Spectral ratio variation within $exp\left(\frac{\omega_1\tau_1}{2Q(\tau)}\right)$ depth profile.

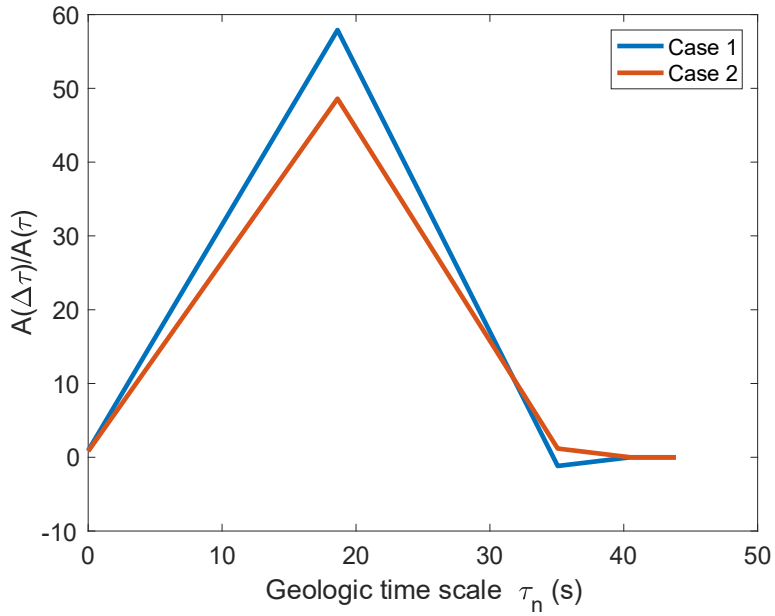

FIG. 9. Spectral ratio variation within $exp\left(\frac{-2\omega_1\tau_1+\omega_n\tau_n}{2Q(\tau)}\right)$ geologic time scale.

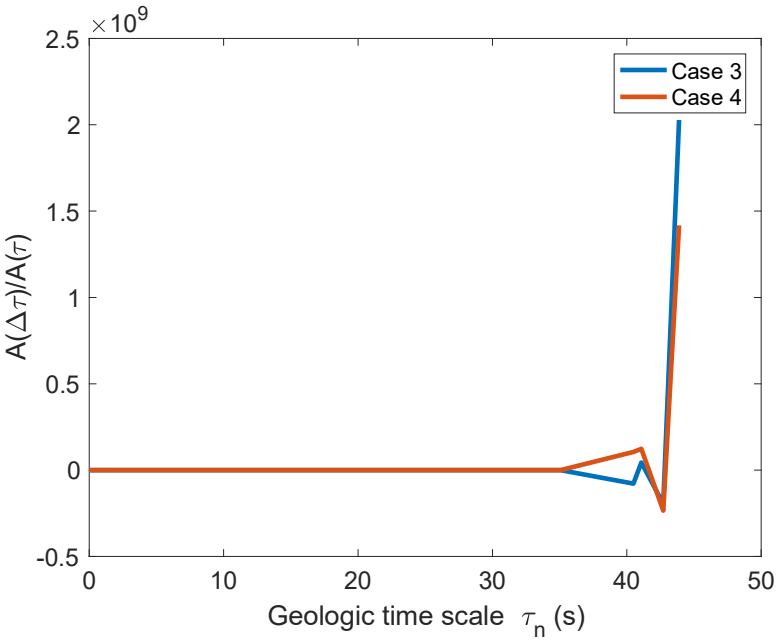

FIG. 10. Spectral ratio variation within $exp\left(\frac{\omega_1\tau_1}{2Q(\tau)}\right)$ geologic time scale.

In other words, the actual determination of the HDM depends on the seismic signal and the geological profiles of a geographical location.

Conclusion

These features of the SR time-dependent method suggest that the trend of the spectral and modified amplitudes is a vital parameter for understanding deposits within the complex geology of a petroleum system. The distribution of sub-weathering velocities in the subsurface is determined by the magnitude of the spectral and modified amplitudes. The adoption of the SR time-dependent method in a complex geological setting, such as the Niger Delta, depends on the active to passive seismic conversion process between two seismic signals within the same geographical location. Two types of spectral ratios were proposed. Type A spectral ratio acts over a longer time and can be used to determine hydrocarbon reservoirs. Type B spectral ratio acts over a shorter time with maximum impact and can be used to detect gas condensate flow in the hydrocarbon reservoir. It is recommended that this technique be applied in real time to ascertain its accuracy.

Conflict of interest

The author declares no competitive interest.

Data Availability Statement

Some or all data, models, or codes that support the findings of this study are available from the corresponding author upon reasonable request.

References

[1] Piazza, J.L., Donati, M., Martin, F.D., Castro, J., Gordillo, C., and Belhouchet, T., 76th EAGE Conference and Exhibition, Amsterdam, (2014).

[2] Alaei, B. and Petersen, S.A., Pet. Geosci., 13 (2007) 241.

[3] Nogoshi, M. and Igarashi, T., J. Seism. Soc. Japan, 23 (1970) 264.

[4] Nogoshi, M. and Igarashi, T., J. Seism. Soc. Japan, 24 (1971) 26.

[5] Xu, R. and Wang, L., EURASIP J. Adv. Signal Process, 2021 (2021) 75.

[6] Bonnefoy-Claudet, S., Baize, S., Bonilla, L.F., Berge-Thierry, C., Pasten, C., Campos, J., Volant, P., and Verdugo, R., Geophys. J. Int., 176 (2009) 925.

[7] Fah, D., Kinf, F., and Giardini, D., Geophys. J. Int., 145 (2001) 535.

[8] Farfour, M. and Yoon, W.J., J. Adv. Res., 7 (3) (2016) 515.

[9] Panou, A.A., Theodulidis, N.P., Hatzidimitriou, P.M., Stylianidis, K., and Papazachos, C.B., Soil Dyn. Earthq. Eng., 25 (2005) 261.

[10] Schmalholz, S.M., Podladchikov, Y.Y., Holzner, R., and Saenger, E.H., First EAGE Passive Seismic Workshop-Exploration and Monitoring Applications. European Association of Geoscientists and Engineers, Houten, Netherlands, (2006) p. A06.

[11] Saenger, E.H., Schmalholz, S.M., Podladchikov, Y.Y., Holzner, R., Lambert, M., Steiner, B., and Frehner, M., 69th EAGE Conference and Exhibition Incorporating SPE EUROPEC 2007. European Association of Geoscientists and Engineers, Houten, Netherlands, (2007) p. A033.

[12] Haris, A., Riyanto, A., Syahputra, R., Gunawan, A., Panguriseng, M.J., Nuratmaja, S., and Adriansyah, J. Geophys. Eng., 16 (2019) 16.

[13] Roy, B.N., Agarwal, S., Roy, K., and Rastogi, B.K., Biennial International Conference and Exposition on Petroleum Geophysics, (2012) p. 279.

[14] Korneev, V.A., Goloshubin, G.M., Daley, T.M., and Silin, D.B., Geophysics, 69 (2004) 522.

[15] Khattri, K. and Gir, R., Geophys. Prospect., 24 (1976) 454.

[16] Parra, J.O. and Hackert, C.L., The Leading Edge, 21 (2002) 564.

[17] Li, F., Zhou, H., Jiang, N., Bi, J., and Marfurt, K.J., J. Geophys. Eng., 12 (2015) 577.

[18] May, B., and Hron, F., Geophysics, 43(6) (1978) 1119

[19] Tonn, R., Geophys. Prosp., 39 (1991) 1.

[20] Quan, Y. and Harris, J.M., Geophysics, 62 (1997) 895.

[21] Sun, X., Tang, X., Cheng, C.H., and Frazer, L.N., Geophysics, 65 (2000) 755.

[22] Cheng, P. and Margrave, G.F., 82nd Annual International Meeting, SEG, Expanded Abstracts, (2012) 1.

[23] Sun, S.Z., Wang, Y., Sun, X., Yue, H., Yang, W., and Li, C., 84th Annual International Meeting, SEG, Expanded Abstracts, (2014) 3709.

[24] Emetere, M.E., Oritseneyemi, C.T., and Ojo, O.O., Pet. Coal, 59 (3) (2015) 319.

[25] Holzner, R., Eschle, P., Dangel, S., Frehner, M., Narayanan, C., and Lakehal, D., Commun. Nonlinear Sci. Numer. Simul., 14 (2009) 160.

[26] Chichinina, T.I., Hogoev, E.A., and Reyes-Pimentel, A., 76th EAGE Conference and Exhibition, Amsterdam, Netherlands, (2014), 1.

[27] Barton, N., "Rock Quality, Seismic Velocity, Attenuation and Anisotropy", (Taylor and Francis, London, 2006).

[28] Campbell, K.W., Bull. Seismol. Soc. Am., 99 (4) (2009) 2365.

[29] Hanks, T.C., Bull. Seismol. Soc. Am., 72 (1982) 1867.

[30] Papageorgiou, A.S. and Aki, K., Bull. Seismol. Soc. Am., 73 (1983) 953.

[31] Helen, I. and Don, L., AAPG Annual Convention, Denver, Colorado, June 7-10, (2009).

[32] Tuttle, L.W., Mlchele, R.R.C., and Michael, E.B., USGS Open-File Report 99-50-H, (1999).

[33] Aigbedion, I. and Aigbedion, H.O., Int. J. Geosci., 2 (2011) 179.

[34] Ihianle, O.E., Alile, O.M., Azi, S.O., Airen, J.O., and Osuji, O.U., Sci. Technol., 3 (2) (2013) 47.

[35] Ameloko, A.A. and Owoseni, A.M., Int. J Innov. Sci. Res., 15 (2015) 193.

[36] Obaje, N.G. et al., "Geology and mineral resources of Nigeria". Lecture Notes in Earth Sciences, (2009).

Volume 17, Number 3, 2024. pp. 273-282

Jordan Journal of Physics

ARTICLE

A Study of the Abundance of Aluminium in Massive Stars

Alaa I. Abdallah and **N. M. Ershaidat**

Physics Department, The University of Jordan, Amman, 11942, Jordan.

Doi: **https://doi.org/10.47011/17.3.2**

Received on: 15/03/2022; *Accepted on: 02/03/2023*

Abstract: This study presents the results of the calculation of the mass fractions of isotopes from hydrogen to nickel during the entire core burning phases of a 25 $M_{\odot}$ star. A simple stellar model was used, considering four main parameters: temperature, density, initial composition, and time, without accounting for mass loss or mixing. The mass fractions of the isotopes were calculated using the open-source package NucNet Tools and the updated reaction rates from the JINA Reaclib database. A comparison of our results with existing similar data is performed and acceptable agreement is conspicuous. Hydrodynamic conditions in massive stars favor the production of ^{26}Al, therefore particular attention was given to the isotopes ^{26}Al and ^{27}Al and the ratio of their mass fractions R_{Al} for comparison with the literature. The averaged value of the controversial R_{Al} during the star's lifetime is found to be 1.68×10^{-4}.

Keywords: Elemental abundances in stars, Evolution, Stellar, Nuclear astrophysics, Hydrostatic stellar nucleosynthesis, Nucleosynthesis: stellar, Stars formation.

PACS: 97.10.Tk, 87.23.-n, 97.10.Cv, 26.20.-f, 7.10.Cv, 97.10.Bt.

Introduction

The study of massive stars plays a significant role in the advancement of theories dealing with the evolution of the universe. Stars with main-sequence masses of 20-25 $M_{\odot}$ are crucial sites of nucleosynthesis because they produce elements up to the iron peak in reasonable agreement with solar abundance ratios [1]. Rates of nucleosynthesis are high in these massive luminous stars. The synthesis of low Z elements, especially those with atomic numbers 8 to 20 is generally attributed to stars having masses greater than 10 $M_{\odot}$ [2]. Aluminium-26 is significantly produced with an initial mass above ~2 $M_{\odot}$ by proton capture on ^{25}Mg during core and shell hydrogen burning in all stars. In massive stars, additional phases of carbon and neon convective shell burning contribute to ^{26}Al production [3, 4]. Such stars end their lives as supernovae with the explosive ejection and explosive processing of their ashes from previous helium, carbon, neon, oxygen, and silicon burning phases [2]. Studying the elemental composition of stars and galaxies is crucial for understanding the origin and evolution of the universe. The abundance of an element is defined as the relative elemental content in a given system (e.g., the sun, a planet, a meteorite, or a comet). It can be determined by the mass fraction of that element relative to the total mass of the star. The sun, being the nearest star to us, is the best-known reference for abundance analyses of other stars. Solar system abundances are derived from the outer layers of the sun and meteorites [5, 6].

Aluminium is the 12th most abundant element in the universe. Amongst its 21 known isotopes, ^{27}Al is the only stable one, while ^{26}Al is non-stable with a half-life of 0.7 Myr. ^{26}Al and ^{27}Al

Corresponding Author: N. M. Ershaidat **Email**: n.ershaidat@ju.edu.jo

are synthesized from magnesium isotopes through the MgAl cycle reactions. The main production reaction is $^{25}Mg(p,\gamma)^{26}Al$ with ^{25}Mg produced by the neutron capture reaction: $^{24}Mg(n,\gamma)^{25}Mg$. It transforms almost all available ^{25}Mg into ^{26}Al. About 80% of the created ^{26}Al is in the ground state $^{26}Al^{g}$, while the remaining 20% exists in the isomeric state $^{26}Al^{i}$ which disintegrates in 6.3 s into ^{26}Mg [7].

Aluminium-26 is an important isotope because it plays a key role in γ-ray astronomy and cosmochemistry [8]. Since the lifetime of this nucleus is very short compared to the time scale of galactic evolution, it offers an opportunity to confront nucleosynthesis theories with observational data [9]. Interest in ^{26}Al increased following the discovery that this nuclide decays into various meteoritic inclusions, leading to an observed ^{26}Mg excess, known as the Mg anomaly[1]. This anomaly indicates that the measured isotopic ratio of magnesium cannot be related to the solar composition of the given element [10]. This is compatible with an average abundance ratio of $^{26}Al/^{27}Al \simeq 5\times10^{-5}$ at the time of formation of the solar system.

Interest in ^{26}Al was further amplified by the discovery of the 1.8 MeV γ-ray line, which is produced in beta decay of ^{26}Al. The disciplines of gamma-ray astronomy and nuclear astrophysics are brought closer together because of this particular line. Based on the intensity of this line, it is estimated that about 3-4 $M_{\odot}$ of ^{26}Al nuclides are present in the interstellar medium of our galaxy. This discovery has provided insight into the possible astrophysical sources of ^{26}Al and their distribution throughout the galaxy [11, 12].

The synthesis of aluminum can occur in various astrophysical sites: 1) during the burning phases of stellar evolution, e.g., massive main sequence stars, 2) in asymptotic giant branch stars, and 3) in explosive and non-explosive burning events, e.g., supernovae and novae [11].

[1] This anomaly can be explained as the result of the bombardment of a gas of solar composition by high fluxes of energetic protons. It follows that ^{26}Mg is mainly created and stored in the form of ^{26}Al by the reaction ^{26}Mg (p, n)^{26}Al. The beta decay of ^{26}Al restores ^{26}Mg. Aluminum-rich materials condensing in meteorites have positive ^{26}Mg anomalies, whereas magnesium-rich materials have negative anomalies [10].

The production and destruction reaction rates of ^{26}Al depend on the different temperature and density regimes of these corresponding astrophysical sites. Theoretical calculations have determined uncertainties for some of these reactions, but others couldn't be calculated because of a lack of information. This is mainly due to experimental uncertainties in measuring expected low-energy resonances in proton decay [13].

Earlier work on computing the abundance of $^{26}Al/^{27}Al$ in massive stars has been done by several authors. Wallerstein *et al*. calculated the time evolution of the mass fractions of the MgAl chain reactions at temperatures ~ 0.05 GK, assuming a constant density of 100 g cm^{-3} and solar initial abundances [14]. They found that the mass fraction of ^{26}Al is on the order of 10^{-6}, while the mass fraction of ^{27}Al is around 6×10^{-4} during 10^{10} s. They concluded that the main effect of the MgAl cycle at low temperatures is the production of ^{26}Al at the expense of ^{25}Mg, which also leads to the production of ^{26}Mg via the β^{+} decay of ^{26}Al. High $^{26}Al/^{27}Al$ ratios (0.38-0.95) were achieved, with uncertainty in this ratio attributed to the uncertainty in the $^{26}Mg(p,\gamma)^{27}Al$ and $^{26}Al(p,\gamma)^{27}Si$ reaction rates. For higher temperatures, Wallerstein *et al*. performed the calculations at a constant temperature of 0.3 GK and density of 6×10^{3}g cm^{-3}. These conditions might be found at the peak of a nova explosion on an O-Ne white dwarf. The mass fractions of ^{26}Al and ^{27}Al were found to be in the range of 10^{-6}-10^{-5} and 10^{-5}-10^{-4} during 10^{3} s, respectively. They concluded that ^{26}Al evolves in parallel with ^{25}Mg, and the drop in ^{24}Mg diminishes the production of ^{25}Mg, resulting in a decrease in both ^{25}Mg and ^{26}Al. The ^{27}Al mass fraction shows the effects of competition between the $^{26}Mg(p,\gamma)^{27}Al$ reaction and the $^{27}Al(p,\gamma)^{28}Si$ and $^{27}Al(p,\alpha)^{24}Mg$ reactions [14].

Nucleosynthesis occurring in the carbon shell of a massive star ($M_{\star}$= 12 $M_{\odot}$), with emphasis on the production of ^{26}Al, is studied by Arnett and Wefel [15]. They used an over-simplified model for their chosen star, with a temperature greater than 2 GK and a density of 10^{5}g cm^{-3}. They found that the $^{26}Al/^{27}Al$ ratio is approximately (1-2) × 10^{-3} [15].

Iliadis studied the nucleosynthesis of isotopes produced during the burning phases of a 25 $M_{\odot}$ with solar initial composition as per Lodders [6].

The calculations were performed using a post-processing reaction network that requires constant temperature, density, time, and initial composition. The used network is not available publicly. Using their reaction rates, Iliadis *et al*. obtained the mass fractions of the isotopes during the advanced burning phases [16, 17].

In this work, the mass fractions (abundances) of isotopes (H to Ni) were calculated using a similar simple model but with updated reaction rates from the JINA Reaclib database for a 25 $M_{\odot}$ star. This was done for comparison purposes with the results of Iliadis [17]. The $^{26}Al/^{27}Al$ ratio was also calculated and compared to findings from previous studies.

Methodology

A nuclear reaction network is a set of reactions between nuclear species that leads to the production and destruction of elements. Abundances can be calculated by solving a system of coupled equations, the so-called Bateman equations, using specific temperature and density as initial conditions. The open-source package "NucNet Tools", developed by the Webnucleo project headed by Bradley Meyer from the Astronomy and Astrophysics group at Clemson University, South Carolina, USA, is used to compute the abundances of a selection of isotopes ranging from H to Ni [18, 19]. NucNet Tools uses the Newton-Raphson method to iteratively solve these equations until a defined convergence is reached. The procedure is detailed and well explained by Meyer [20].

In this work, the nucleosynthesis of elements from H to Ni, in a $25M_{\odot}$ star is studied. Such a star undergoes six burning phases: hydrogen burning, helium burning, carbon burning, neon burning, oxygen burning, and silicon burning.

A simple model was used to obtain the abundance of the mentioned isotopes, utilizing parameters such as temperature, density, initial composition, and the lifetime needed for each stage to burn its content. This simple model is aligned with the parameters used by Iliadis [17] for comparison purposes.

The main parameters used for initializing the calculations - temperature and density - depend on the expansion timescale τ, which can be defined as $\frac{1}{\tau} = -\frac{1}{\rho}\frac{\partial \rho}{\partial t}$. By choosing τ to be infinity, the core temperature and density, expressed as $T(t) = T(0)\ e^{-t/\tau}$ and $\rho(t) = \rho(0)\ e^{-t/\tau}$, are kept constant all along the calculations. These static calculations for such a star with solar initial composition have been performed using NucNet Tools [6].

This assumption is representative of the hydrostatic status of the core during the burning phases. Although this does not represent a real star, it is useful for obtaining physical insights into nucleosynthesis and energy production.

The initial abundances of the isotopes for core hydrogen burning were taken from Lodders' solar composition data [6]. The final values of abundances of each phase (ashes), resulting from the solution of coupled equations, served as the initial abundances for the next phase.

Appropriate nuclides and reaction data from the JINA (Joint Institute for Nuclear Astrophysics) database were used to obtain the reaction rates of the isotopes [21].

Calculations for each of the six burning phases, mentioned earlier, were performed using the initial conditions of temperature, density, and lifetime, as shown in Table 1. These conditions are similar to those used by Iliadis [17] and Woosley *et al*., 2002 [22].

TABLE 1. Initial conditions for the core burning phases.

Burning Phase	Temperature (GK)	Density (g cm^{-3})	Phase Duration
Hydrogen	0.0381	3.81	6.7 Myr
Helium	0.196	7.6×10^{2}	0.839 Myr
Carbon	0.9	1×10^{5}	3.2 kyr
Neon	1.5	5×10^{6}	0.891 yr
Oxygen	2.2	3×10^{6}	0.412 yr
Silicon	3.6	3×10^{7}	0.733 yr

Results and Discussion

For clarity, calculations are arranged by burning phase containing the discussion of the properties and the results of each single phase. The special case of aluminum isotopes is treated in detail at the end of this section.

Hydrogen Burning

In this first phase, hydrogen burns to produce helium via the proton-proton (pp) chains and the carbon-nitrogen-oxygen (CNO) cycles. The star now is in its main sequence phase and will continue burning hydrogen for approximately 6.7 Myr. Initially, the star is predicted to contain 0.7491 hydrogen, 0.2377 helium, and 0.0133 metals (elements heavier than helium). Calculations for the first phase were performed at T = 0.0381 GK (denoted as t_9 = T in GK in the following sections) and $\rho = 3.81$ g cm^{-3}.

The mass fraction of the produced helium reaches the value of 0.985, and the calculation is terminated when the mass fraction of hydrogen decreases to 2.73×10^{-5}. The main product of this phase is ^{4}He, and most of the initial ^{12}C and ^{16}O are converted to ^{14}N during the CNO burning. The time evolution of the mass fractions of ^{1}H, ^{4}He, ^{12}C, ^{13}C, ^{14}N, ^{16}O, ^{17}O, and ^{18}O during core hydrogen burning is shown in Fig. 1.

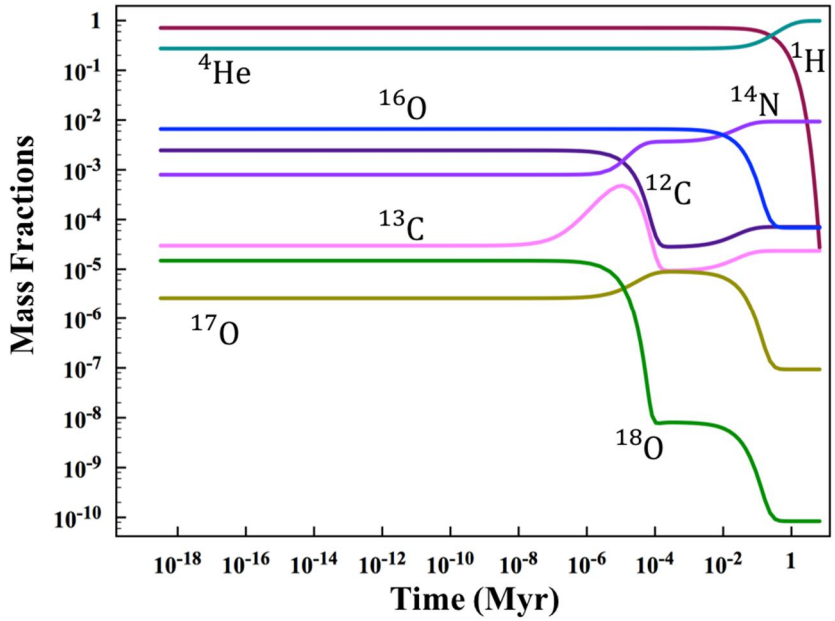

FIG. 1. Time evolution of the mass fractions during core hydrogen burning. Hydrogen isotopes are sufficiently transformed into ^{4}He isotopes, which accumulate in the core to initiate the next burning phase. The calculations are terminated when hydrogen mass fractions fall below 2.73×10^{-5}.

Helium Burning

Once hydrogen is exhausted inside the core, leaving helium as the product of the previous burning phase, the core's temperature rises to around 0.1 GK, initiating helium burning. Meanwhile, hydrogen burning continues in a shell around the core. The star now moves to the next phase, the so-called red supergiant phase, where helium is transformed into heavier elements over approximately 0.839 Myr. The calculations were conducted at 0.196 GK and 0.76×10^{3} g cm^{-3}. The final mass fractions from the end of the hydrogen-burning phase were used as initial values for helium burning. The mass fraction of helium after the burning decreases to 0.006, while the mass fractions of carbon and oxygen increase to 0.308, and 0.667, respectively. The core becomes composed of carbon and oxygen, which are the main products of this phase. Figure 2 shows the time evolution of the mass fractions of ^{4}He, ^{12}C, ^{16}O, ^{20}Ne, ^{24}Mg, ^{25}Mg, and ^{26}Mg during core helium burning. The most abundant nuclides at the end of the calculation are ^{12}C (0.3075), ^{16}O (0.6671), and ^{20}Ne (0.0141). The mass fractions of the other isotopes are less than 10^{-3}.

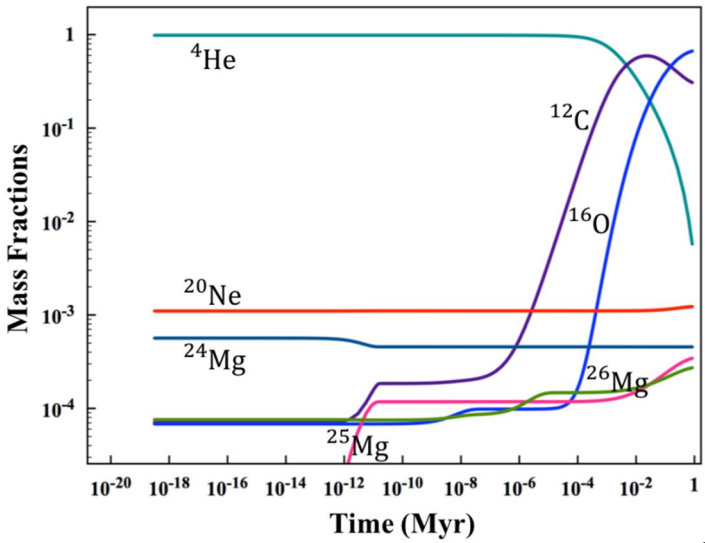

FIG. 2. Time evolution of the mass fractions during core helium burning. In this phase, ^{4}He is transformed into ^{12}C and ^{16}O, which become the main fuel for the carbon-burning phase. The calculations are terminated when the mass fraction of helium reaches 0.006. The mass fractions of carbon and oxygen increase to 0.308, and 0.667, respectively.

Carbon Burning

At the end of the helium-burning phase, the mass fraction of helium decreases by a factor of nearly 100, and the core becomes composed of carbon and oxygen. The temperature rises to around 0.9 GK where carbon burning begins, and helium burning continues in a shell around the core. During the burning, the existing free α particles, protons, and neutrons interact with the nuclei present, including CNO nuclei from the hydrogen- and helium-burning phases, leading to the production of heavier elements.

At the end of the calculation, the mass fraction of carbon decreases to 0.004, while the mass fractions of oxygen and neon increase to 0.497, and 0.409, respectively. Figure 3 shows the time evolution of the mass fractions of ^{12}C, ^{16}O, ^{20}Ne, ^{21}Ne, ^{22}Ne, ^{23}Na, ^{24}Mg, ^{25}Mg, ^{26}Mg, and ^{27}Al during core carbon burning. The most abundant nuclides at the end of the calculation are ^{16}O (0.497), ^{20}Ne (0.409), ^{23}Na (0.023), ^{24}Mg (0.040), and ^{25}Mg (0.011). The other isotopes have mass fractions less than 10^{-3}. Results for the main isotopes, ^{16}O and ^{20}Ne, agree rather well with previous studies, showing values of 0.600 and 0.350, respectively [17].

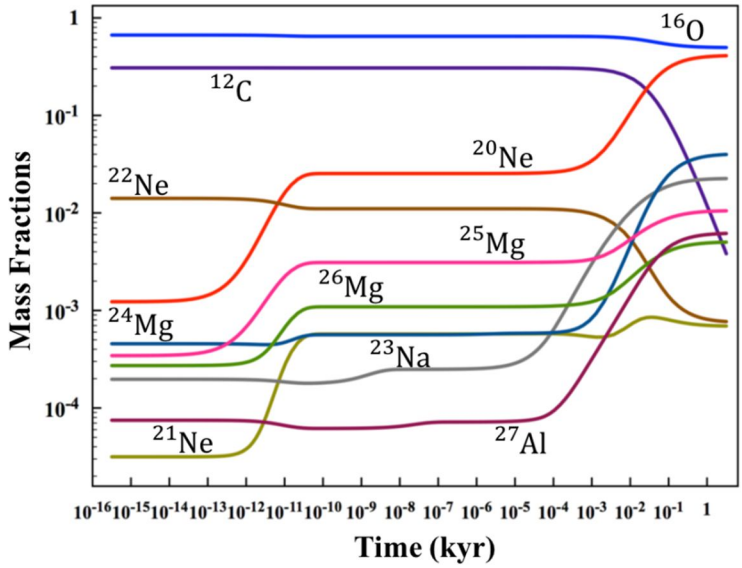

FIG. 3. Time evolution of the mass fractions during core carbon burning. The main fuel in this phase is ^{12}C and it burns to produce ^{16}O and ^{20}Ne, which are needed for the next burning phase. The mass fraction of carbon decreased to 0.004, while the mass fractions of oxygen and neon increased to 0.497, and 0.409, respectively.

Neon Burning

Neon burning starts with the reaction ^{20}Ne (γ, α) ^{16}O when the central temperature t_9 = 1.5 and the density ρ = 5×10^6 g cm^{-3}. This temperature is enough to photodisintegrate ^{20}Ne, and the freed α particles can combine readily with ^{20}Ne to form ^{24}Mg. The main products of this phase are ^{16}O, ^{24}Mg, and ^{28}Si. Figure 4 shows the time evolution of the mass fractions of ^{16}O, ^{20}Ne, ^{24}Mg, ^{25}Mg, ^{26}Mg, ^{27}Al, ^{28}Si, ^{29}Si, and ^{30}Si during core neon burning. The most abundant nuclides at the end of the calculation are ^{16}O (0.708), ^{24}Mg (0.115), ^{27}Al (0.015), ^{28}Si (0.112), ^{29}Si (0.015), and ^{30}Si (0.013). The mass fractions of ^{16}O and ^{24}Mg agree with the values reported in [17]: 0.770 and 0.110, respectively.

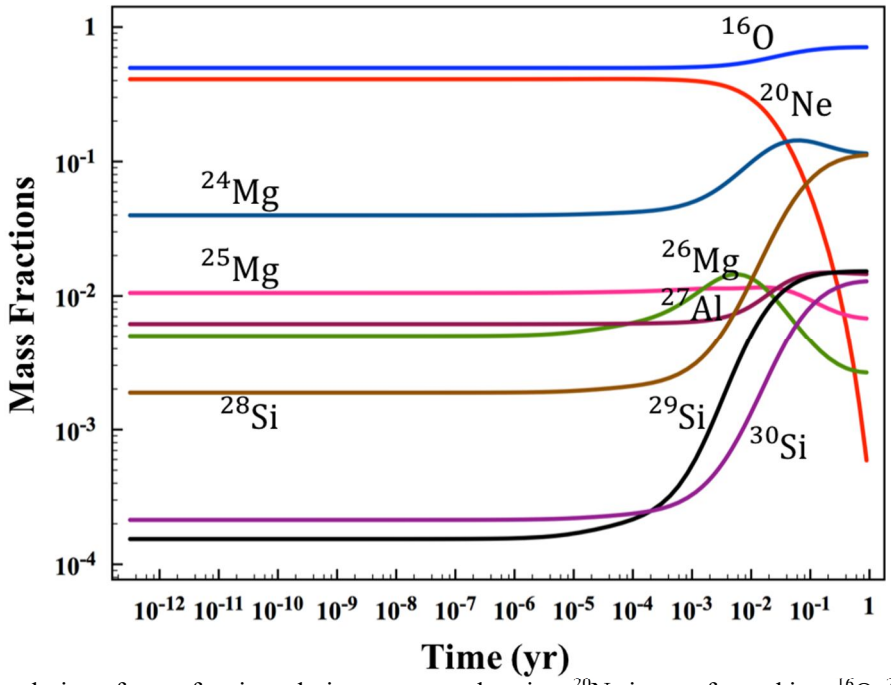

FIG. 4. Time evolution of mass fractions during core neon burning. ^{20}Ne is transformed into ^{16}O, ^{24}Mg, and ^{28}Si, preparing the with fuel for the subsequent oxygen burning.

Oxygen Burning

Oxygen burning begins when the core temperature rises to around 2.2 GK, while neon continues burning in a shell around the core. The oxygen nuclei begin to fuse together, producing ^{28}Si and α particles. Several reactions occur, freeing α particles, protons, and neutrons that interact with the present nuclei and produce heavier elements. The main isotopes resulting from this phase are ^{28}Si and ^{32}S. Figure 5 shows the time evolution of the mass fractions of ^{16}O, ^{27}Al, ^{28}Si, ^{29}Si, ^{30}Si, ^{31}P, ^{32}S, ^{33}S ^{34}S, ^{35}Cl, and ^{36}Ar during core oxygen burning at a constant temperature t_9 = 2.2 and density ρ = 3×10^{6}g cm^{-3}. The most abundant nuclides at the end of the calculation are ^{28}Si (0.565), ^{32}S (0.299), ^{34}S (0.031), and ^{36}Ar (0.028). These abundances agree rather well with the corresponding values in [17]: ^{28}Si (0.54), ^{32}S (0.280), ^{34}S (0.044), and ^{36}Ar (0.027). For all other isotopes, calculations give mass fractions less than 10^{-3}.

Silicon Burning

At the end of the oxygen-burning phase, the mass fraction of oxygen decreases, and the core becomes composed of silicon and sulfur. The temperature rises to around 3.6 GK, where silicon burning begins, while oxygen-burning continues in a shell around the core. This phase involves a series of nuclear reactions that start with the products of the oxygen burning and synthesize nuclei up to the iron peak. Photodisintegration of the nuclei produces α particles, protons, and neutrons, which are essential for this synthesis. Figure 6 shows the time evolution of the mass fractions of ^{24}Mg, ^{27}Al, ^{28}Si, ^{29}Si, ^{30}Si, ^{32}S, ^{34}S, ^{36}Ar, ^{52}Cr, ^{53}Mn, ^{54}Fe, ^{55}Fe, ^{56}Fe, ^{57}Co, and ^{58}Ni during core silicon burning. The calculation assumes a constant temperature t_9 = 3.6 and density ρ = 3×10^7 g cm^{-3}. The most abundant nuclides at the end of the calculation are ^{52}Cr (0.008), ^{53}Mn (0.018), ^{54}Fe (0.683), ^{55}Fe (0.047), ^{56}Fe (0.081),

^{57}Co (0.020), and ^{58}Ni (0.103). These values do not agree with those reported in [17]. The mass fractions of the other isotopes are found to be less than 10^{-4}.

At the end of this phase, the core will be composed of iron. Since iron nuclei are the most stable nuclei, the core will collapse into a neutron star and release an enormous amount of energy. A tiny fraction of this energy is sufficient to explode the star as a supernova [21].

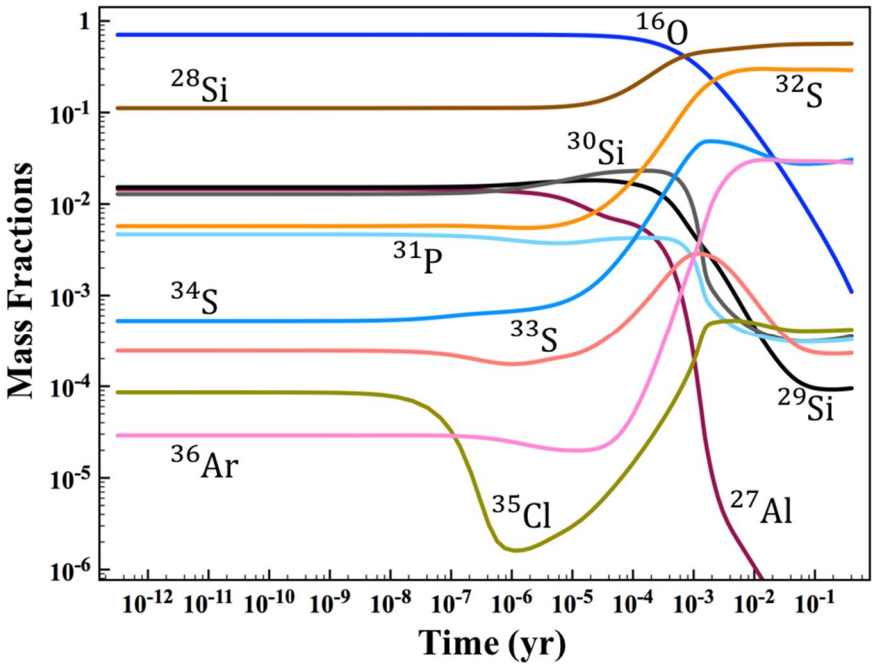

FIG. 5. Time evolution of the mass fractions during core oxygen burning. The mass fraction of oxygen decreases to 0.001, while the mass fractions of ^{28}Si and ^{32}S increase to 0.565 and 0.290, respectively, preparing them for the silicon burning phase.

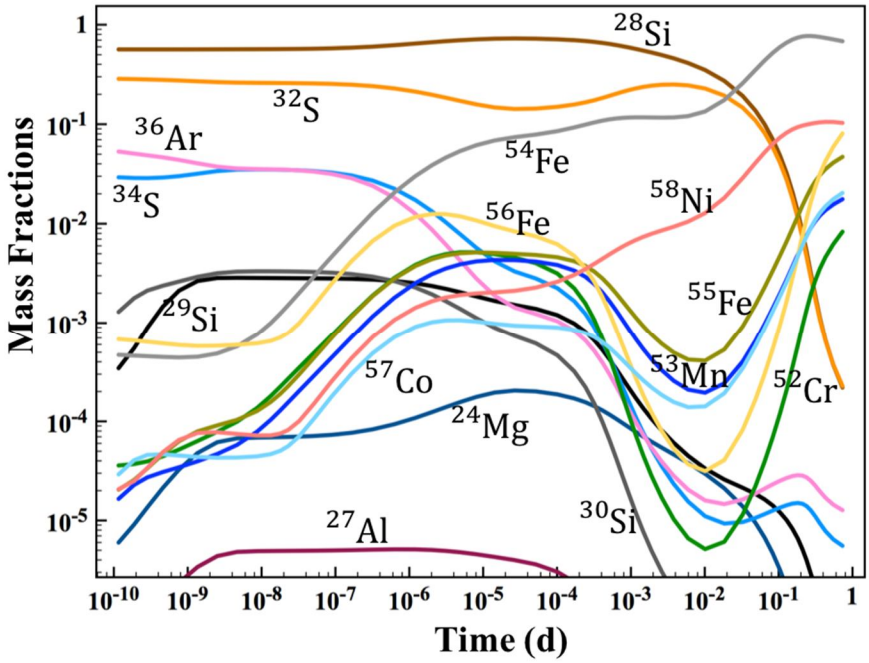

FIG. 6. Time evolution of the mass fractions during core silicon burning. Si nuclei burn to produce heavier elements (up to the iron peak). Iron isotopes cannot undergo further fusion, they rather let the core collapse to a neutron star and release an enormous amount of energy. The star now starts to explode as a supernova.

^{26}Al and ^{27}Al

Detailed calculations were performed for the mass fractions of ^{26}Al and ^{27}Al and the ratio R_{Al} was defined as:

$$R_{Al} = \frac{mass\ fraction\ of\ ^{26}Al}{mass\ fraction\ of\ ^{27}Al} \quad (1)$$

The production and destruction of aluminum isotopes come from several reactions, including proton-induced, neutron-induced, α-induced, and photodisintegration reactions. Figures 7 and 8 show the time evolution of the mass fractions of ^{26}Al and ^{27}Al and the variation with of their mass fractions ratio during the advanced burning phases, respectively.

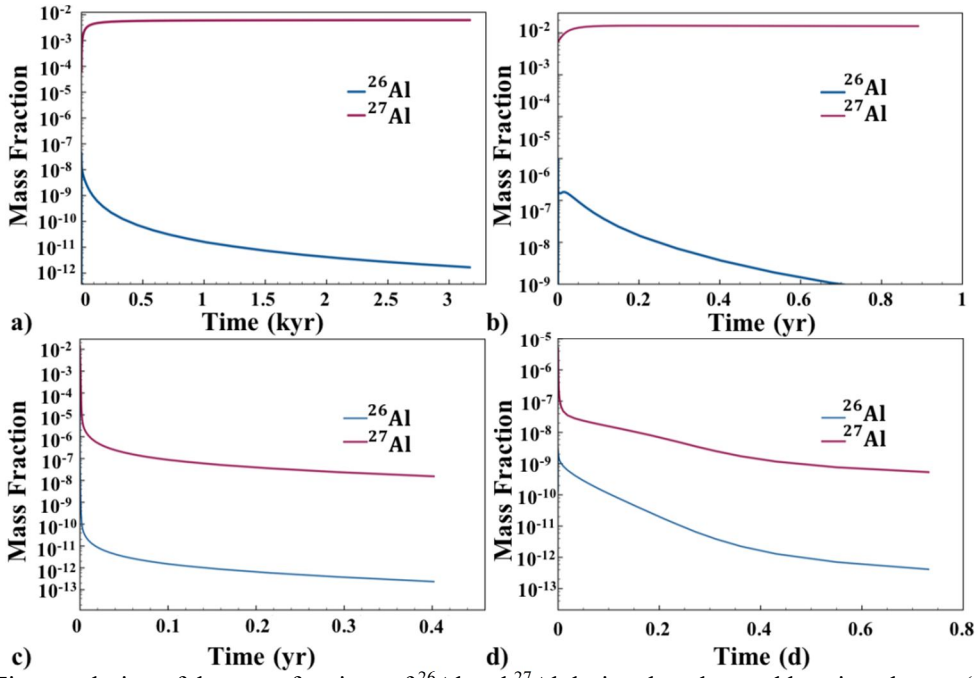

FIG. 7. Time evolution of the mass fractions of ^{26}Al and ^{27}Al during the advanced burning phases: (a) carbon burning (b) neon burning, (c) oxygen burning, and (d) silicon burning. It is concluded that ^{26}Al has high destruction reaction rates, and the reaction rate of ^{26}Mg(p, γ)^{27}Al is higher than the reaction ^{25}Mg(p, γ)^{26}Al in these phases.

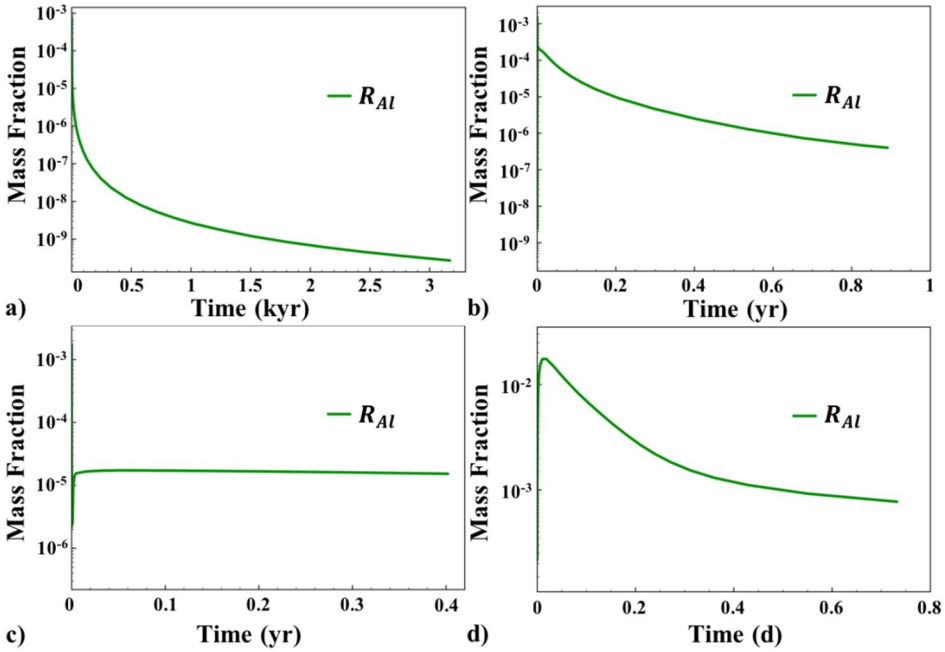

FIG. 8. The time variation of the mass fraction ratio ^{26}Al/^{27}Al during the burning phases: (a) carbon burning, (b) neon burning, (c) oxygen burning, and (d) silicon burning.

During the evolution of the star, the core evolves to a higher temperature where the production and destruction reaction rates increase [23]. We notice that at 0.9 GK, the required temperature for the core carbon burning phase, most of ^{26}Al is destroyed during the final two thousand years. This would also mean that the ratio R_{Al} should normally decrease, as shown in Fig. 8(a). When the temperature is around 1.5 GK, which is the required temperature for neon burning, the production and destruction reaction rates of both ^{26}Al and ^{27}Al indicate that the ratio R_{Al} should decrease during the major part of the phase, and this is what we observe in Fig. 8(b).

During oxygen burning, both isotopes are destructed, thus, R_{Al} decreases from its initial value, as shown in Fig. 8(c). In the final phase, an increase of the ratio R_{Al} is observed for the period of [0.001-0.05] d, followed by a decrease for the remainder of the phase, as seen in Fig. 8(d). A thorough study should consider the possible systematic and statistical errors.

Conclusions

The open-source package NucNet-tools from the Webnucleo group was used to calculate the mass fractions of isotopes from H to Ni in a 25 $M_{\odot}$ star across six burning phases: hydrogen, helium, carbon, neon, oxygen, and silicon (Figs.1-6). Special attention was given to the isotopes ^{26}Al and ^{27}Al. Comparisons were made with the results of Iliadis [17] for the advanced burning phases. The comparison shows a satisfactory agreement for the carbon, neon, and oxygen-burning phases. This is due to the fact that calculations for these phases have been performed with the same input physics using simple nuclear networks. However, differences were noted in the silicon burning phase. Iliadis [17] used different initial mass fractions for ^{28}Si and ^{30}Si, set at 0.70 and 0.30, respectively, while our calculations yielded 0.56 and 0.001, ashes of the oxygen-burning phase, respectively. These discrepancies can be attributed to differences in initial abundances, nuclear reaction networks involved, and reaction rates used in the calculations.

The average value of the calculated aluminum ratio, R_{Al}^{avg}, was found to be 2.85×10^{-4}, 2.23×10^{-4}, 1.29×10^{-4}, and 3.46×10^{-3} in carbon, neon, oxygen, and silicon burning phases, respectively. For the first three advanced phases, it was observed that as the temperature increases inside the core, the aluminum ratio R_{Al}^{avg} decreases. For the silicon burning phase, reactions favoring the production of both isotopes have higher reaction rates than the destruction ones, which explains the different behavior of the variation of R_{Al}, as seen in Fig. 8(d), hence the peculiar value of $R_{Al}^{avg} = 3.46\times10^{-3}$.

One way of testing the calculation procedure is to observe the time evolution of the mass fractions of the main fuels during the various core burning phases. As expected, the latter initially varies smoothly, followed by a more pronounced decrease during the later stages of each phase.

The results of this study are, hopefully, expected to provide new insights into nucleosynthesis and the evolution of massive stars.

Acknowledgment

The authors would like to thank Professor Bradley Meyer, Physics Department, Clemson University, SC, USA, and his students for sharing the open-source package NucNet Tools/Webnucleo project for solving some astrophysical problems.

References

[1] Nomoto, K. and Hashimoto, M., Phys. Rep., 1 (1988) 163.

[2] Woosley, S. and Weaver, T., ApJ, 238 (1980) 1017.

[3] Brinkman, H.E., Doherty, C.L., Pols, O.R., et al., ApJ, 884 (2019) 38

[4] Lemongi, M. and Chieffi, A., ApJ, 647 (2006) 483.

[5] Grevesse, N. and Sauval, A., IOP, 3 (2005).

[6] Lodders, K., ApJ, 591 (2003) 1220.

[7] Mowlavi, N. and Meynet, G., ApJ, 361 (2000) 959.

[8] Siess, L. and Arnould, M., A&A, 489 (2008) 395.

[9] Prantzos, N., AIP Conf. Proc., 232 (1991) 129.

[10] Kuroda, P.K. and Bakhtiar, S.N., GJ, 20 (1986) 311.

[11] Forestini, M., Arnould, M., and Paulus, G., A&A, 252 (1991) 597.

[12] Iliadis, C., Schange, T., Rolfs, C., et al., Nucl. Phys. A, 512 (1990) 509.

[13] Iliadis, C., D'auria, J.M., Starrfield, S., et al., ApJS, 134 (2001).

[14] Wallerstein, G., Icko Iben, Jr., Parker, P., et al., Rev. Mod. Phys., 69 (1997) 4.

[15] Arnett, W.D. and Wefel, J.P., ApJ, 224 (1978) L139.

[16] Iliadis, C., Longland, R., Champagne, A.E., et al., Nucl. Phys. A, 841 (2010) 31.

[17] Iliadis, C., "Nuclear Physics of Stars", 2nd Ed.., (John Wiley & Sons, Weinheim, 2015).

[18] Meyer, B.S., PoS. (NIC XII), 146 (2013) 096.

[19] Talafha, M., Al-Wardat, M., and Ershaidat, N., Astrophys. Bull., 73 (2018) 2.

[20] Meyer, B., "Webnucleo Technical Report: Network Calculations with lib-nucnet", (2011), http://libnucnet.sourceforge.net/pubs/technical_reports/2011-04-17-1.pdf.

[21] Cyburt, R., Amthor, A., Ferguson, R., et al., ApJS, 189 (2010) 240. (see also https://reaclib.jinaweb.org/index.php).

[22] Woosley, S., Heger, A., and Weaver, T., Rev. Mod. Phys., 74 (2002) 1015.

[23] LeBlanc, F., "An Introduction to Stellar Astrophysics", 1st Ed., (John Wiley & Sons, West Sussex, U.K, 2010).

Volume 17, Number 3, 2024. pp. 283-289

Jordan Journal of Physics

ARTICLE

The Bound Band Structure in a Strong Attractive Dirac Comb

Sid A. Sfiat

Faculté de physique, BP 1505 El Mnaouar, USTO-MB, 31000 Oran, Algeria.

Doi: **https://doi.org/10.47011/17.3.3**

Received on: 09/04/2022; *Accepted on: 12/01/2023*

Abstract: The Dirac comb problem in quantum mechanics is revisited by estimating its energy band structure, including the band gap, bandwidth, and the effective mass at band edges. The case of an attractive strong Dirac comb potential is considered. Our findings show the existence of a single bound energy band state, which is flat with a small width and a large effective mass at both of its edges; positive at its lower edge and negative at its upper edge.

Keywords: Dirac comb, Bound energy, Band structure, Dispersion relation, Band gap, Bandwidth, Effective mass.

1. Introduction

In quantum mechanics, only a handful of problems can be solved analytically. One of these problems is the Kronig-Penney potential, introduced in the early 1930s to model the short-range nature of the atomic potentials and the periodic lattice structure [1]. A year later, Kronig and Penney simplified the original model and introduced the Dirac comb potential, which consists of one-dimensional evenly spaced delta-function peaks. This model is suitable for obtaining many general properties of realistic quantum systems. It is a solvable model frequently used to describe systems with very short-range interactions which are located around evenly spaced given points [2, 3].

The impressive progress in experimental physics in the early 1980s, coupled with the advances in semiconductor technology and nanophysical systems twenty years later, made possible the fabrication of heterostructures, quantum wells, and new synthetic materials. This renewed the interest of scientists and engineers in this elementary type of simple model [4, 5]. It has contributed immensely to explaining the electronic band structure in a crystalline solid such as band gap formation [4, 5]. This has led to a huge advancement in solid-state and condensed-matter physics. Many macroscopic properties of materials are closely related to their microscopic band structures. They are of extreme practical importance because they play a major role in understanding the transport phenomena theory of insulation and conduction in solids [6-11].

Because material properties are strongly influenced by energy band patterns, many physical properties of solids are determined from the location of band edges, band gaps, and their widths [6-11]. The goal of this work is to estimate the energy band structure (band gap, bandwidth, and effective mass) of an electron under the influence of a strong attractive Dirac comb potential. Similar attempts have been made for bound and unbound band structures under the influence of a weak attractive Dirac comb potential [12, 13].

2. Band Gap and Band Width Calculation

One of the few problems in quantum mechanics that can be solved analytically is the Dirac comb [14-17]. This work considers only

Corresponding Author: Sid A. Sfiat **Email**: sidahmed.sfiat@univ-usto.dz

the attractive case of this model, where the associated potential is expressed as:

$$V(x) = -\boldsymbol{\lambda}\sum_{n}^{\infty}\delta(\mathrm{x}-\mathrm{n}\mathbf{a}) \quad (1)$$

with strength $\boldsymbol{\lambda}$ and lattice spacing **a**.

Only the bound states are considered and therefore the electron energy is negative and expressed as:

$$\boldsymbol{E} = -\frac{\hbar^2\mathbf{K}^2}{2\mathrm{m}} \quad (2)$$

K is related to the Bloch wave number **k** through the following transcendental equation [14-17]:

$$-\boldsymbol{P}\frac{\sinh(\mathbf{K}\mathrm{a})}{\mathbf{K}\mathrm{a}} + \cosh(\mathbf{K}\mathrm{a}) = \cos(\mathbf{k}\mathrm{a}) \quad (3)$$

where $\boldsymbol{P} = \frac{ma\lambda}{\hbar^2}$ is a dimensionless parameter representing the scattering power of the Dirac comb potential.

Equation (3) determines the permitted energies $\boldsymbol{E}$ through the values of the parameter **K**. This transcendental equation cannot be solved analytically; it can only be solved numerically or graphically.

These permitted energies are determined because the right-hand side of Eq. (3) is bounded:

$$-1 \le \cos(\mathbf{k}\mathrm{a}) \le 1 \quad (4)$$

Analyzing Eq. (3) numerically (see Table 1) and graphically (Figs. 1-5), we note the following facts:

- A single bound energy band is formed, regardless of the value of the scattering power $\boldsymbol{P}$.
- The band is partial and not complete when $0 < \boldsymbol{P} < 2$. It does not span the entire half-interval of the first Brillouin zone from 0 to π, but rather the interval from 0 to arccos (1-$\boldsymbol{P}$).
- The band is complete and spans the whole half-interval of the first Brillouin zone from 0 to π when $\boldsymbol{P} \ge 2$.
- The band width increases very fast when $0 < \boldsymbol{P} < 2$.
- The band width reaches its maximum value when $\boldsymbol{P} = 2$.
- The band width decreases at a slower rate than the initial increase when $\boldsymbol{P} > 2$.
- The band width almost vanishes and cannot be detected when $\boldsymbol{P} \ge 15$.

TABLE 1. The energies at both ends of the band and its width

$\boldsymbol{P}$	$(Ka)_0$	$(Ka)_\pi$	$E_0(\frac{\hbar^2}{2ma^2})$	$E_\pi(\frac{\hbar^2}{2ma^2})$	$W(\frac{\hbar^2}{2ma^2})$
0	0	x	0		0
0.5	1.04363	x	-1.08916	0	1.08916
1.0	1.54340	x	-2.38208	0	2.38208
1.5	1.98036	x	-3.92183	0	3.92183
2.0	2.39936	0	-5.75693	0	5.75693
2.5	2.81770	1.77603	-7.93943	-3.15428	4.78515
3.0	3.24364	2.57568	-10.52100	-6.63413	3.88687
3.5	3.68095	3.23488	-13.54939	-10.46445	3.08494
4.0	4.13068	3.83007	-17.06252	-14.66944	2.39308
4.5	4.59212	4.38973	-21.08757	-19.26973	1.81784
5.0	5.06363	4.92812	-25.64035	-24.28637	1.35398
10.0	10.0090	9.99909	-100.18008	-99.98009	0.19999
15.0	15.0000	15.0000	-225.0000	-225.0000	0

* Numerical values in Table 1 are provided by dCode equation solver tool.

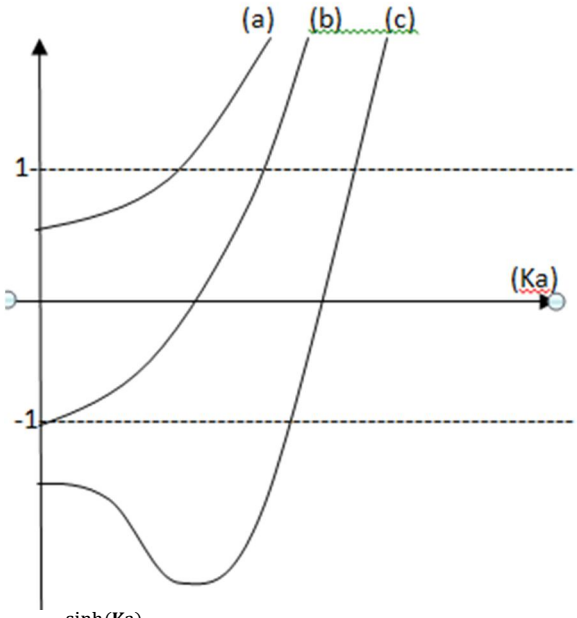

FIG. 1. The function "$-\boldsymbol{P}\frac{\sinh(\mathbf{K}a)}{\mathbf{K}a}+\cosh(\mathbf{K}a)$" versus $\mathbf{K}a$ for (a) $0<\boldsymbol{P}<2$, (b) $\boldsymbol{P}=2$, (c) $\boldsymbol{P}>2$.

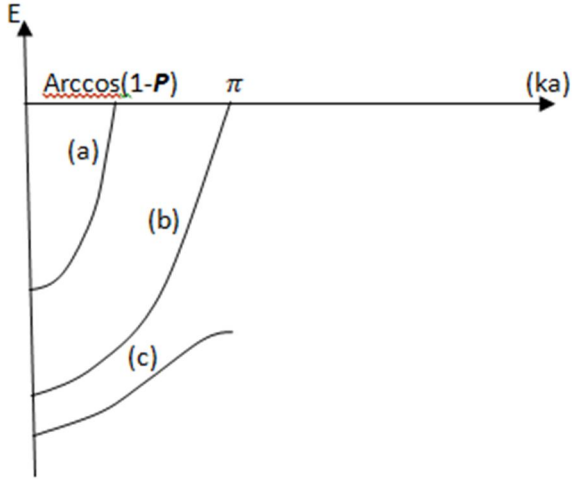

FIG. 2. Dispersion relation versus $\mathbf{k}a$ for (a) $0<\boldsymbol{P}<2$, (b) $\boldsymbol{P}=2$, (c) $\boldsymbol{P}>2$.

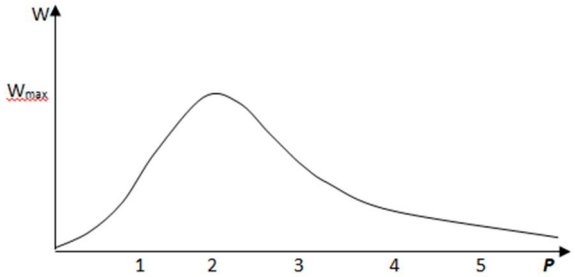

FIG. 3. The band width as a function of the scattering power $\boldsymbol{P}$.

The case of the strong Dirac comb potential is considered in this work and therefore the scattering power $\boldsymbol{P}>>1$.

Analyzing Fig. 4 below, we notice that the left-hand side of Eq. (3) intersects the axis $\mathbf{K}a$ at a value very close to $\boldsymbol{P}$. It also intersects the horizontal lines representing the points $\mathbf{k}a=0$ and $\mathbf{k}a=\pi$ at:

$$\mathbf{K}_0 a=\boldsymbol{P}+\delta_0 \tag{5}$$

and

$$\mathbf{K}_\pi a=\boldsymbol{P}-\delta_\pi \tag{6}$$

respectively, where $0\le\delta_0<<1$ and $0\le\delta_\pi<<1$.

Inserting Eq. (5) into Eq. (3) when $\mathbf{k}a=0$, we get:

$$-\boldsymbol{P}\frac{\sinh(\mathrm{P}+\delta_0)}{(\mathrm{P}+\delta_0)}+\cosh(\mathrm{P}+\delta_0)=1 \quad (7)$$

Solving for δ_0 to the first-order approximation, yields [18, 19]:

$$\delta_0 \approx 2\boldsymbol{P}\mathrm{e}^{-\boldsymbol{P}} \quad (8)$$

Therefore,

$$\mathbf{K}_0\mathrm{a} \approx \boldsymbol{P}(1+2\mathrm{e}^{-\boldsymbol{P}}) \quad (9)$$

The lowest energy of the band is at:

$$\boldsymbol{E}_0 = -\frac{\hbar^2\mathbf{K}_0^2}{2\mathrm{m}} \approx -\frac{\hbar^2\boldsymbol{P}^2(1+4\mathrm{e}^{-\boldsymbol{P}})}{2\mathrm{ma}^2} \quad (10)$$

Similarly, for $\mathbf{k}\mathrm{a}=\pi$, the same approach yields:

$$\delta_\pi \approx 2\boldsymbol{P}\mathrm{e}^{-\boldsymbol{P}} \quad (11)$$

and

$$\mathbf{K}_\pi\mathrm{a} \approx \boldsymbol{P}(1-2\mathrm{e}^{-\boldsymbol{P}}) \quad (12)$$

The highest energy of the band is at:

$$\boldsymbol{E}_\pi = -\frac{\hbar^2\mathbf{K}_\pi^2}{2\mathrm{m}} \approx -\frac{\hbar^2\boldsymbol{P}^2(1-4\mathrm{e}^{-\boldsymbol{P}})}{2\mathrm{ma}^2} \quad (13)$$

Therefore, the width of the band is:

$$\boldsymbol{W} = \boldsymbol{E}_\pi - \boldsymbol{E}_0 = \frac{4\hbar^2\boldsymbol{P}^2\mathrm{e}^{-\boldsymbol{P}}}{\mathrm{ma}^2} \quad (14)$$

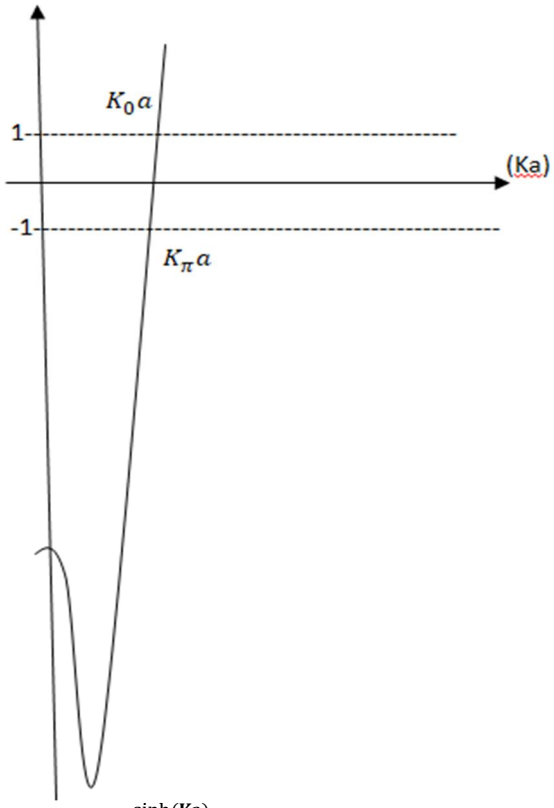

FIG. 4. The function "$-\boldsymbol{P}\frac{\sinh(\mathbf{Ka})}{\mathbf{Ka}}+\cosh(\mathbf{Ka})$" versus **Ka** for large values of ***P***.

Fig. 5 below shows the dispersion relation. It consists of a single bound energy band lying very far below the zero line. It is almost flat, with its width decreasing with increasing values of the scattering power ***P***.

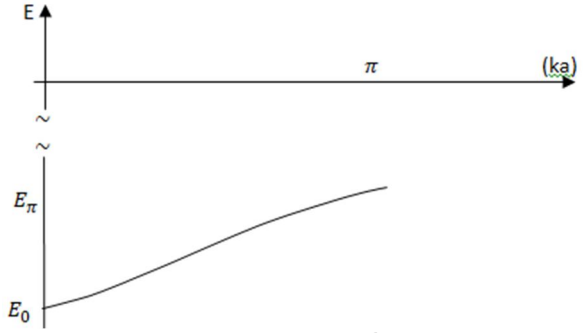

FIG. 5. The dispersion relation versus **ka** for large values of ***P***.

Let us now find an analytical approximation for the dispersion relation $\boldsymbol{E(k)}$. For that, we make use of the observation made from the graph in Fig. 4. The left-hand side of Eq. (3), between the two horizontal lines representing the points $\mathbf{k}a = 0$ and $\mathbf{k}a = \pi$, can be approximated by a straight line passing through points $(\mathbf{K}_\pi a, -1)$, $(\boldsymbol{P},0)$, and $(\mathbf{K}_0 a, 1)$. Hence, this side of Eq. (3) can be expressed as:

$$\text{L.H.S} = \frac{1}{\delta_0}(\mathbf{K}a - \boldsymbol{P}) \tag{15}$$

and this leads to:

$$\mathbf{K}a = \delta_0 \cos(\boldsymbol{ka}) + \boldsymbol{P} \tag{16}$$

Therefore, the energy $\boldsymbol{E(k)}$ can be expressed as a function of the Bloch wave number $\mathbf{k}$ as:

$$\boldsymbol{E(ka)} = -\frac{\hbar^2 \boldsymbol{p^2}}{2ma^2}[2e^{-\boldsymbol{P}}\cos(\boldsymbol{ka}) + 1]^2 \tag{17}$$

The width of the band can also be expressed as:

$$\boldsymbol{W} = \boldsymbol{E(\pi)} - \boldsymbol{E(0)} = \frac{4\hbar^2 \boldsymbol{P}^2 e^{-\boldsymbol{P}}}{ma^2} \tag{18}$$

The above dispersion relation $\boldsymbol{E(ka)}$ will be used in the next section to confirm and verify the final findings regarding the effective mass estimations. It is worth noting that Eqs. (17) and (18) are compatible with the results obtained in Eqs. (10) and (13) when the scattering power $\boldsymbol{P}$ >>1.

With increasing scattering power $\boldsymbol{P}$, the dependence of the above dispersion relation $\boldsymbol{E(ka)}$ on the Bloch wave number $\mathbf{k}$ weakens and becomes practically undetectable beyond $\boldsymbol{P}$ = 15, where the energy band collapses to a single energy level $\boldsymbol{E} = -\frac{\hbar^2 \boldsymbol{p^2}}{2ma^2}$. This energy is similar to that of a particle under the influence of a single delta function potential. Consequently, this form of energy confinement leads to a spatial localization phenomenon near the delta spike.

3. Effective Mass Calculation

The effective mass is an important tool in the theory of solids. It is used to describe the features of band structure in semiconductors and insulators, where most experimental features arise from electron and hole occupation near the endpoints of valence and conduction bands [20-23]. In this section, we evaluate the effective mass at both edges of the single bound energy band found in the previous section.

- The lowest edge of the band: $\mathbf{k}a = 0$.

This edge corresponds to:

$$\mathbf{K}a = \mathbf{K}_0 a - \in(\mathbf{k}a) \tag{19}$$

with $\in(\mathbf{k}a) << 1$ and $\in(0) = 0$

The corresponding energy is expressed as:

$$\boldsymbol{E}_0 = -\frac{\hbar^2 \mathbf{K}^2}{2m} = -\frac{\hbar^2}{2ma^2}[\mathbf{K}_0 a - \in]^2 \tag{20}$$

Combining Eqs. (19) and (3) yields:

$$-\boldsymbol{P}\frac{\sinh(\mathbf{K}_0 a - \in)}{(\mathbf{K}_0 a - \in)} + \cosh(\mathbf{K}_0 a - \in) - 1 = \delta(\mathbf{k}a) \tag{21}$$

where

$$\delta(\mathbf{k}a) = -1 + \cos(\mathbf{k}a) \tag{22}$$

Expanding the above expression for $\delta(\mathbf{k}a)$ in Eq. (21) as a Taylor power series in $\in \ll 1$ yields:

$$\delta(\mathbf{k}a) = \frac{[(\mathbf{K}_0 a)\cosh(\mathbf{K}_0 a) - \sinh(\mathbf{K}_0 a)]\boldsymbol{P} - (\mathbf{K}_0 a)^2 \sinh(\mathbf{K}_0 a)}{(\mathbf{K}_0 a)^2} \in + O(\in^2) \tag{23}$$

Using the Taylor reversion process for Eq. (23) yields [18, 19]:

$$\in = \frac{(\mathbf{K}_0 a)^2}{[(\mathbf{K}_0 a)\cosh(\mathbf{K}_0 a) - \sinh(\mathbf{K}_0 a)]\mathrm{P} - (\mathbf{K}_0 a)^2 \sinh(\mathbf{K}_0 a)}\delta + O(\delta^2) \tag{24}$$

By using Eqs. (20), (22), and (24), the effective mass expression at the lowest edge of the band becomes:

$$\left[\frac{d^2 E}{dk^2}\right]_0 = \frac{\hbar^2}{m^*} = -\frac{\hbar^2}{m}\frac{(\mathbf{K}_0 a)^3}{[(\mathbf{K}_0 a)\cosh(\mathbf{K}_0 a) - \sinh(\mathbf{K}_0 a)]\boldsymbol{P} - (\mathbf{K}_0 a)^2 \sinh(\mathbf{K}_0 a)} \tag{25}$$

Hence, at the bottom of the band, the ratio (m*/m) of the effective mass to the mass of the electron is expressed as:

$$\left[\frac{m^*}{m}\right]_0 = -\frac{[(\mathbf{K}_0 a)\cosh(\mathbf{K}_0 a) - \sinh(\mathbf{K}_0 a)]\boldsymbol{P} - (\mathbf{K}_0 a)^2 \sinh(\mathbf{K}_0 a)}{(\mathbf{K}_0 a)^3} \tag{26}$$

Using Eq. (9) and the fact that $\boldsymbol{P}$ >> 1, the effective mass ratio can be simplified to:

$$\left[\frac{m^*}{m}\right]_0 \approx \frac{e^{\boldsymbol{P}}}{\boldsymbol{2P^2}} \tag{27}$$

The dispersion relation (17) is now used to verify and confirm the result of Eq. (27):

$$[\frac{d^2E}{dk^2}]_0 = \frac{\hbar^2}{m^*} = 2\frac{\hbar^2}{m}\boldsymbol{P^2}e^{-\boldsymbol{P}}(1+e^{-\boldsymbol{P}}) \quad (28)$$

Therefore, the effective mass ratio (m*/m) is estimated as:

$$[\frac{m^*}{m}]_0 \approx \frac{e^{\boldsymbol{P}}}{\boldsymbol{2P^2}}(1-e^{-\boldsymbol{P}}) \approx \frac{e^{\boldsymbol{P}}}{\boldsymbol{2P^2}} \quad (29)$$

which is exactly what was found in Eq. (27).

In conclusion, the effective mass at the lowest edge of the band is positive and large in value.

- The highest edge of the band: $\mathbf{k}a = \pi$.

This edge corresponds to:

$$\mathbf{K}a = \mathbf{K}_\pi a + \in(\mathbf{k}a) \quad (30)$$

with $\in(\mathbf{k}a) \ll 1$ and $\in(\pi) = 0$

The corresponding energy is expressed as:

$$\boldsymbol{E}_\pi = -\frac{\hbar^2\mathbf{K}^2}{2m} = -\frac{\hbar^2}{2ma^2}[\mathbf{K}_\pi a+\in]^2 \quad (31)$$

Combining Eqs. (28) and (3) yields:

$$-\boldsymbol{P}\frac{\sinh(\mathbf{K}_\pi a+\in)}{(\mathbf{K}_\pi a+\in)} + \cosh(\mathbf{K}_\pi a+\in) + 1 = \Delta(\mathbf{k}a) \quad (32)$$

where:

$$\Delta(\mathbf{k}a) = 1+\cos(\mathbf{k}a) \quad (33)$$

Expanding the above expression $\Delta(\mathbf{k}a)$ in Eq. (32) as a Taylor power series in $\in \ll 1$ yields:

$$\Delta(\mathbf{k}a) = -\frac{[(\mathbf{K}_\pi a)\cosh(\mathbf{K}_\pi a)-\sinh(\mathbf{K}_\pi a)]\boldsymbol{P}-(\mathbf{K}_\pi a)^2\sinh(\mathbf{K}_\pi a)}{(\mathbf{K}_\pi a)^2}\in +O(\in^2) \quad (34)$$

Using the Taylor reversion process for Eq. (34) yields [18, 19]:

$$\in = -\frac{(\mathbf{K}_\pi a)^2}{[(\mathbf{K}_\pi a)\cosh(\mathbf{K}_\pi a)-\sinh(\mathbf{K}_\pi a)]\boldsymbol{P}-(\mathbf{K}_\pi a)^2\sinh(\mathbf{K}_\pi a)}\Delta + O(\Delta^2) \quad (35)$$

By using Eqs. (31), (33), and (35), the effective mass expression at the highest edge of the band becomes:

$$[\frac{d^2E}{dk^2}]_\pi = \frac{\hbar^2}{m^*} = \frac{\hbar^2}{m}\frac{(\mathbf{K}_\pi a)^3}{[(\mathbf{K}_\pi a)\cosh(\mathbf{K}_\pi a)-\sinh(\mathbf{K}_\pi a)]\boldsymbol{P}-(\mathbf{K}_\pi a)^2\sinh(\mathbf{K}_\pi a)} \quad (36)$$

Hence, at the top of the band, the ratio (m*/m) of the effective mass to the mass of the electron is expressed as:

$$[\frac{m^*}{m}]_\pi = \frac{[(\mathbf{K}_\pi a)\cosh(\mathbf{K}_\pi a)-\sinh(\mathbf{K}_\pi a)]\boldsymbol{P}-((\mathbf{K}_\pi a)^2\sinh(\mathbf{K}_\pi a)}{(\mathbf{K}_\pi a)^3} \quad (37)$$

Using Eq. (12) and the fact that $\boldsymbol{P} \gg 1$, the effective mass ratio simplifies to:

$$[\frac{m^*}{m}]_\pi \approx -\frac{e^{\boldsymbol{P}}}{\boldsymbol{2P^2}} \quad (38)$$

Let us now use the dispersion relation (17) to verify and confirm the result of Eq. (38):

$$[\frac{d^2E}{dk^2}]_\pi = \frac{\hbar^2}{m^*} = -2\frac{\hbar^2}{m}\boldsymbol{P^2}e^{-\boldsymbol{P}}(1-e^{-\boldsymbol{P}}) \quad (39)$$

Therefore, the effective mass ratio (m*/m) is estimated as:

$$[\frac{m^*}{m}]_\pi \approx -\frac{e^{\boldsymbol{P}}}{\boldsymbol{2P^2}}\left(1+e^{-\boldsymbol{P}}\right) \approx -\frac{e^{\boldsymbol{P}}}{\boldsymbol{2P^2}} \quad (40)$$

which is exactly what we have found in Eq. (38)

In conclusion, the effective mass at the highest edge of the band is negative and large in value.

4. Discussion and Conclusion

Under the influence of an attractive Dirac comb potential, an electron exhibits a single-bound band structure.

With increasing values of the scattering power $\boldsymbol{P}$, the bandwidth initially increases rapidly for $0 < \boldsymbol{P} < 2$ and then decreases at a slower rate when $\boldsymbol{P} > 2$. The band is at its maximum width at $\boldsymbol{P} = 2$.

When the scattering power $\boldsymbol{P}$ is very large, the band is found to be lying below the zero line of the reference energy. The band becomes nearly flat, with a weak dependence on the Bloch wave number. As a result, it collapses into an energy level of a particle under the influence of a single delta function potential, with its energy confinement and spatial localization phenomenon.

The dispersion relation is estimated and used to verify and confirm the findings regarding the effective mass at both ends of this single band. The effective mass is found to be very large, positive at the band's lowest edge, and negative at its highest edge.

Future investigations will aim to answer the following important questions: Can we expect similar results in the original case of the Kronig-Penney potential? If so, what conditions on the

size and depth of the well must be met for the single band to exhibit a similar pattern as in the Dirac comb potential?

References

[1] Kronig, R.de L. and Penney, W.G., Proc. Roy. Soc. London, A130 (1930), 499.

[2] Flugge, S., "Practical Quantum Mechanics", (Berlin: Springer-Verlag, 1971).

[3] Ashcroft, N.W. and Mermin, N.D., "Solid State Physics", (Brooks/Cole, 1976).

[4] Kolbas, R.M. and Holonyak, N., Amer. J. Phys., 52 (1984) 431.

[5] Mitin, V.V., Sementsov, D.I., and Vagidov, N.Z., "Quantum Mechanics for Nanostructures", (Cambridge University Press, 2010).

[6] Harrison, W.A., "Electronic Structure and the Properties of Solids", (ISBN 0-486-66021-4), (Dover, 1980).

[7] Pastori Parravicini, G., "Electronic States and Optical Transitions in Solids". (Pergamon Press, 1975).

[8] Dharani, M. and Shastry, C.S., Physica B, 500 (2016) 66.

[9] Dharani, M. and Shastry, C.S., Mater. Today: Proc., Part 3, 5 (8) (2018) 16214.

[10] Erman, F., Gadella, M. and Uncu, H., Eur. J. Phys., 39 (2018) 01.

[11] Nussbaum, A., IEEE Trans. Educ., 33 (4) (1990) 359.

[12] Sfiat, S., Adv. Stud. Theor. Phys., 7 (13) (2013) 605.

[13] Sfiat, S., Adv. Studies Theory. Phys., 7 (13) (2013) 611.

[14] Dekker, A.J., "Solid State Physics", (Prentice-Hall, Englewood Cliffs, NJ, 1962).

[15] Kittel, C., "Quantum Theory of Solids", (John Wiley and Sons, New York, 1976).

[16] Kittel, C. "Introduction to Solid State Physics", 7th Ed., (New York, Wiley, 1996).

[17] Griffiths, D., "Introduction to Quantum Mechanics", (Cambridge University Press, UK, 2016).

[18] Dwight, H.B., "Table of Integrals and Other Mathematical Data", 4th Ed., (New York: Macmillan, 1961).

[19] Bronstein, I.N., Semendyayev, K.A., Musiol, G., and Muehlig, H., "Handbook of Mathematics". (Berlin, Heidelberg, New York, Springer, 2004).

[20] Pekar, S., Zh. Eksp. Teor. Fiz., 16 (1946) 933.

[21] Burt, M.G., J. Phys.: Condens. Matter, 4 (32) (1992) 6651.

[22] Wasserman et al., Adv. Phys., 45 (1996) 471.

[23] Sputai, S.V., XIV International Scientific-Technical Conference on Actual Problems of Electronics Instrument Engineering (APEIE), (2018), p. 178.

Volume 17, Number 3, 2024. pp. 291-298

Jordan Journal of Physics

ARTICLE

Some Phenomenological Aspects of Higgs Production in Two Leptons and $b\bar{b}$ Final State Processes

Aissa Belhouari

Department of Physics, Faculty of Exact Science and Computing, Chemin des Cretes ex INEX 27000 University Abd el Hamid Ibn Badis-Mostaganem, Algeria.

Doi: **https://doi.org/10.47011/17.3.4**

Received on: 22/06/2022; *Accepted on: 30/10/2022*

Abstract: We present a partonic-level analysis of the two leptons and $b\bar{b}$ final states processes at the ILC $e^+e^- \to e^+e^-b\bar{b}$. This process contains Higgs production with an electron-positron pair, where the Higgs decays into a $b\bar{b}$ quark pair as a sub-process, $e^+e^- \to e^+e^-H \to e^+e^-b\bar{b}$. We tried to isolate this sub-process with a minimum set of cuts. Particularly, cross-sections are estimated at different energies, and the main distributions of kinematic variables characterizing the process are derived using the software Calchep [16]. The results provide information on signal and background characteristics for different ILC operating stages.

Keywords: Higgs physics at ILC, Higgsstrahlung process, ZZ fusion process, Calchep.

1. Introduction

The discovery of the Higgs particle at the LHC by the Atlas and CMS collaborations [1, 2] has constituted a starting point of an extensive Higgs physics program aimed at determining its principal properties. LHC data have allowed the determination of the spin, charge, and parity which are not enough to confirm it as the SM Higgs because other models predict scalars with the same properties [3]. The couplings and width are poorly constrained and require high precision measurements since BSM physics predicts a few percent deviation from their SM values.

One of the main fields of focus for the next generation of colliders is to perform high-precision Higgs physics experiments. With a precise initial state energy and a clean environment with respect to the LHC, because of the low QCD background, the ILC is without doubt the ideal machine to achieve this goal [4-6]. The three principal Higgs production channels are: Higgsstrahlung $e^+e^- \to ZH$, WW fusion $e^+e^- \to W^+W^-\nu\bar{\nu} \to H\nu\bar{\nu}$, and ZZ fusion $e^+e^- \to ZZe^+e^- \to e^+e^-H$, whose lowest order diagrams are illustrated in Fig.1.

To measure such Higgs properties as the Higgs mass and width or the HZZ coupling at ILC, several studies have focused mainly on the Higgsstrahlung process using the mass recoil variable to extract these properties in a model-independent way (an inclusive Higgs production) [7-14]. The recoil mass technique is based on measuring the decay products of the Z boson, which recoils against the Higgs boson independently of the Higgs decay mode. One gets a better signal selection efficiency, especially when only leptonic Z decays are considered [10].

$$e^+e^- \to (Z \to l^+l^-)(H \to X) \to l^+l^-X \qquad (1)$$

The recoil mass is given by the expression:

$$M^2_{rec} = S + \sqrt{S}\,E_{l^+l^-} + M^2_{l^+l^-} \qquad (2)$$

Corresponding Author: Aissa Belhouari **Email**: aissa.belhouari@univ-mosta.dz

where S is the center of mass energy squared, E_l+l- and M_l+l- are the energy and the invariant mass of the lepton pair, respectively. The M_{rec} distribution peaks at the Higgs mass (Fig. 2), from which the signal yield can be extracted. The $e^+e^- \rightarrow ZH$ cross section is maximal at 250 GeV, [8, 10, 13] but at higher energies, other channels become important, like Higgs production via ZZ fusion $e^+e^- \rightarrow ZZe^+e^- \rightarrow e^+e^-H$ [14, 15], as can be seen in Fig. 4 and Table 1.

Figure 4 shows a comparison between the Higgsstrahlung cross-section $\sigma(e^+e^- \rightarrow ZH \rightarrow e^+e^-H)$ and the total $\sigma(e^+e^- \rightarrow e^+e^-H)$ computed with unpolarized beams.

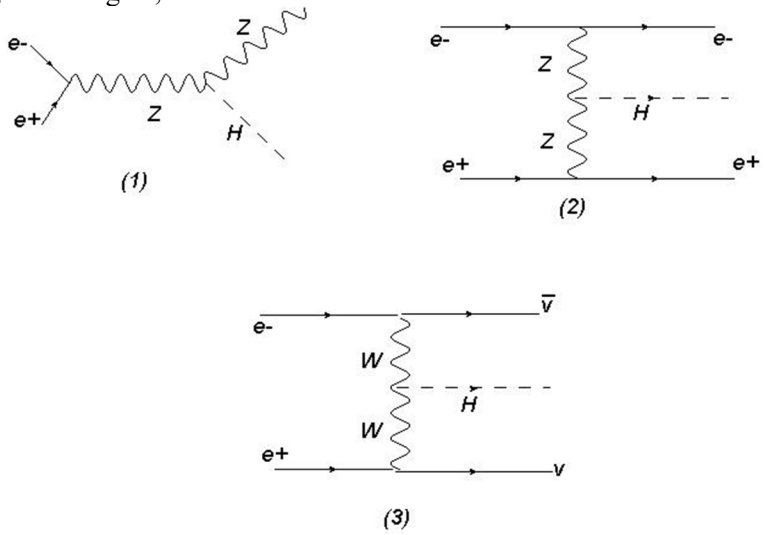

FIG. 1. Feynman diagrams for the three principal Higgs production channels at ILC: (1) Higgsstrahlung, (2) ZZ fusion, and (3) WW fusion.

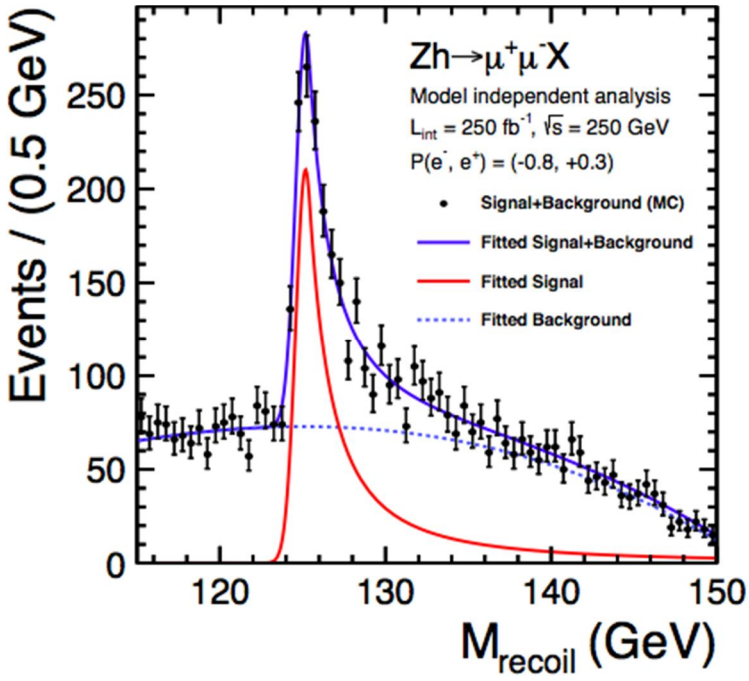

FIG. 2. Recoil mass distribution of $e^+e^- \rightarrow ZH$ followed by $Z \rightarrow \mu^+\mu^-$ at 250 GeV with a Higgs mass of 125 GeV taken from Ref. [5].

Their values and ratios at 250, 500, and 1000 GeV are also reported in Table 1. This confirms the results obtained in previous work [14]. For the Higgs mass of 125 GeV, the highest branching ratio is Br($H \rightarrow b\bar{b}$).

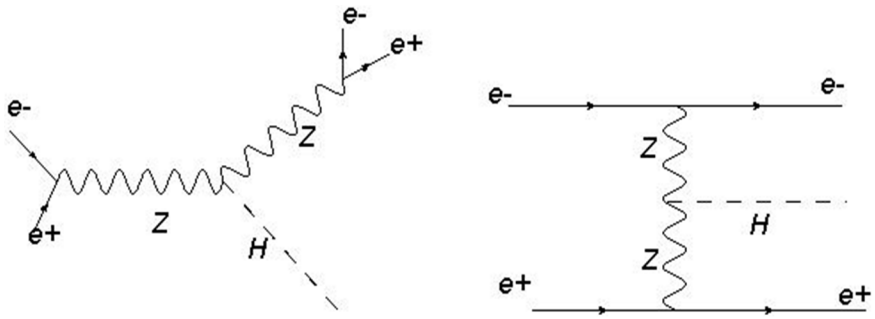

FIG. 3. Feynman diagrams of the process e+e− → e+e−H.

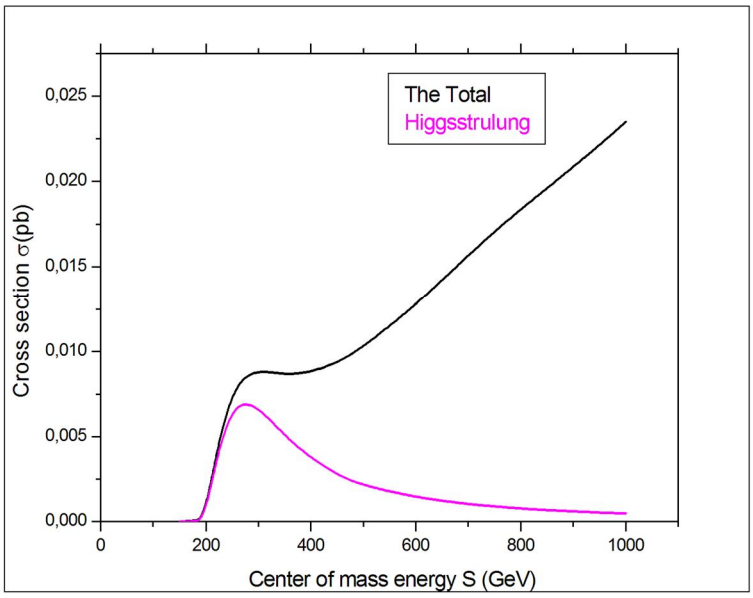

FIG. 4. Cross sections of the Higgsstrahlung and the total processes as a function of the CM energy.

TABLE 1. Cross sections of the Higgsstrahlung and the total processes as a function of the CM energy.

CM energy (GeV)	Total cross sec (pb)	Higgsstrahlung cross sec (pb)	Ratio
250	9.60×10^{-3}	8.75×10^{-3}	1.1
500	1.03×10^{-2}	2.13×10^{-3}	4.8
1000	2.35×10^{-2}	4.78×10^{-4}	49

Because of their high statistics and the b tagging and lepton identification capabilities of ILC, processes where the Higgs is produced with a pair of leptons, followed by a Higgs decay to a b quarks pair, $e^+e^- \rightarrow l^+l^-H \rightarrow l^+l^-b\bar{b}$, are particularly interesting.

2. Results and Analysis

In most analyses, the production times decay approximation ($\sigma \cdot Br$) is commonly used since it makes calculations simpler. However, this approach sacrifices valuable information and ignores the irreducible background, which may be significant. In this analysis, we used the Calchep software [16] (see appendix) to make a complete and exact computation of cross-sections and distributions for different kinematical variables of the process $e^+e^- \rightarrow e^+e^-b\bar{b}$, as illustrated in Figs. 5 and 6.

We are interested especially in the subprocess $e^+e^- \rightarrow e^+e^-H \rightarrow e^+e^-b\bar{b}$, which constitutes the signal, as depicted in Fig. 5. The irreducible background is represented by the diagrams in Fig. 6. One has to permute the e^+e^- and $b\bar{b}$ pairs in the diagrams (1) and (2) and attach the Z and photon propagator to the different legs in (3).

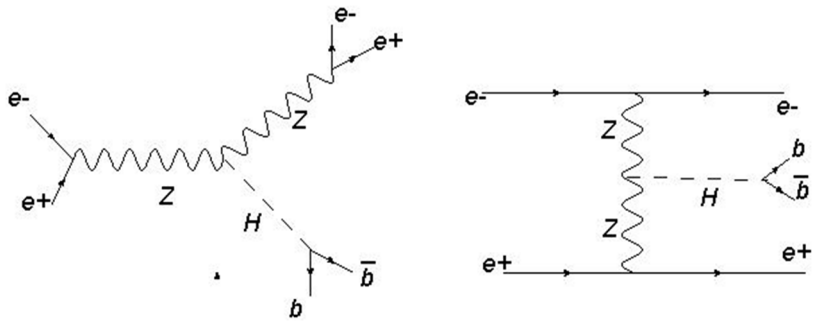

FIG. 5. Feynman diagrams of the signal.

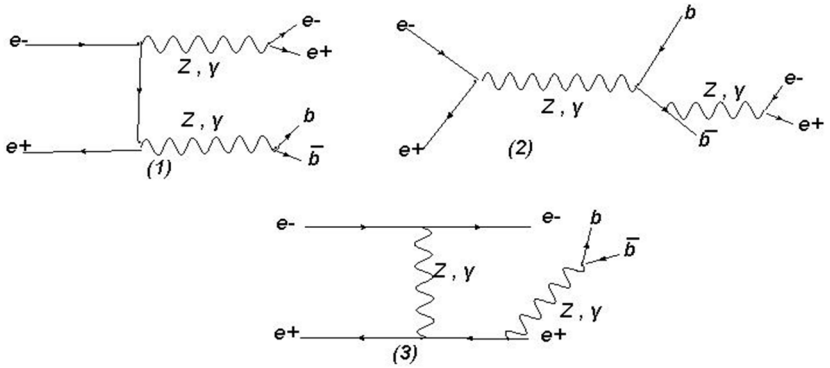

FIG. 6. Feynman diagrams of the background.

To extract the signal, we applied a cut on the $b\bar{b}$ invariant mass. It must be within the window $Mh - 10 < M(b\bar{b}) < Mh + 10$ where $Mh = 125$ GeV is the Higgs mass. Additionally, we applied cuts on the electron and positron transverse momentum $P_t > 10$ GeV and their invariant mass $M(e^+e^-) > 20$ GeV. These cuts serve to avoid the pole $q^2 = 0$ of the photon propagator because we are considering the electron and the positron as massless. We computed the cross-sections and obtained distributions of different kinematical variables, especially electron and b-quark rapidity and energy, both with the $M(b\bar{b})$ cut applied (signal) and without this cut (total = signal + background) at different energies (250 GeV, 500 GeV, and 1 TeV).

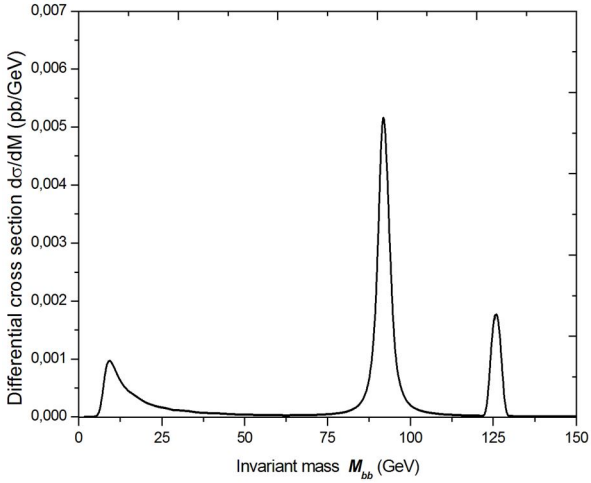

FIG. 7. The invariant mass distribution of the $b\bar{b}$ quarks pair shows the signal peak at 125 and the two background peaks: the Z peak and the low M peak.

TABLE 2. The computed cross sections with the M($b\bar{b}$) cut (signal) and without it (total).

CM Energy (GeV)	Signal (pb) (S)	Signal + Background (pb) (S+B)	Ratio S/(S+B)
250	6.36×10^{-3}	4.66×10^{-2}	0.136
500	7.15×10^{-3}	6.32×10^{-2}	0.113
1000	1.63×10^{-2}	9.05×10^{-2}	0.180

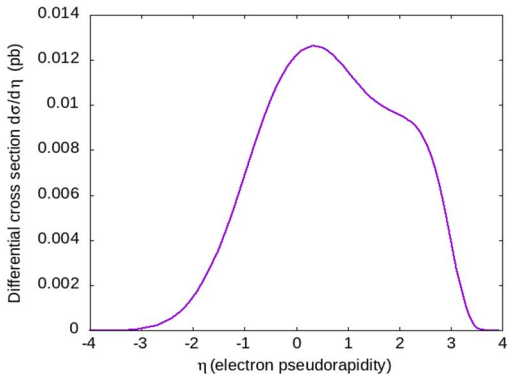

FIG. 8. Pseudorapidity distribution of the electron at 250 GeV without the $M(b\bar{b})$ cut.

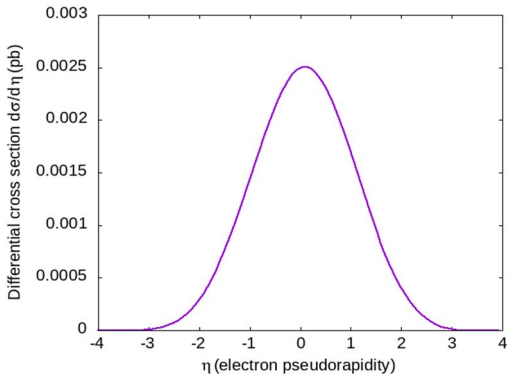

FIG. 9. Pseudorapidity distribution of the electron at 250 GeV with the $M(b\bar{b})$ cut.

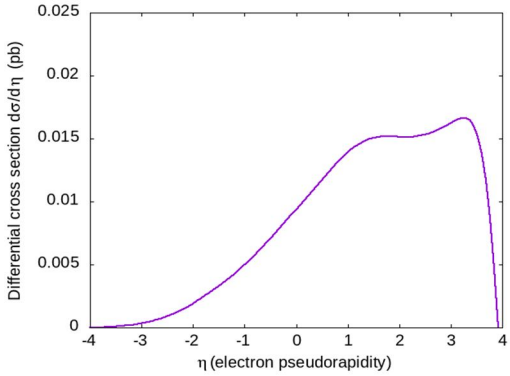

FIG. 10. Pseudorapidity distribution of the electron at 500 GeV without the $M(b\bar{b})$ cut.

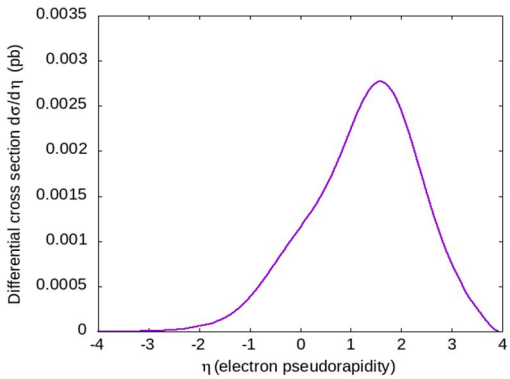

FIG. 11. Pseudorapidity distribution of the electron at 500 GeV with the $M(b\bar{b})$ cut.

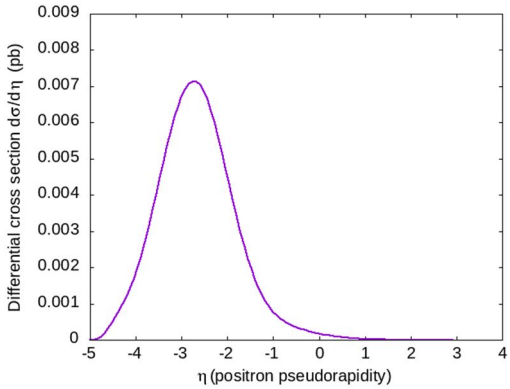

FIG. 12. Pseudorapidity distribution of the positron at 1 TeV with the $M(b\bar{b})$ cut.

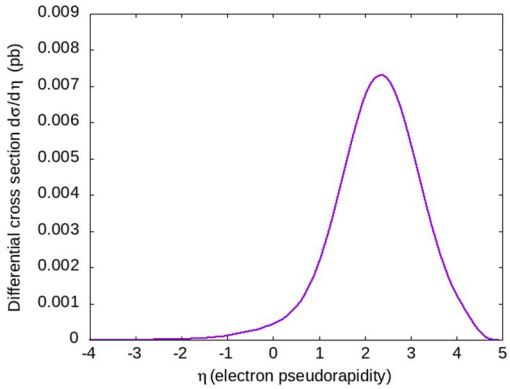

FIG. 13. Pseudorapidity distribution of the electron at 1 TeV with the $M(b\bar{b})$ cut.

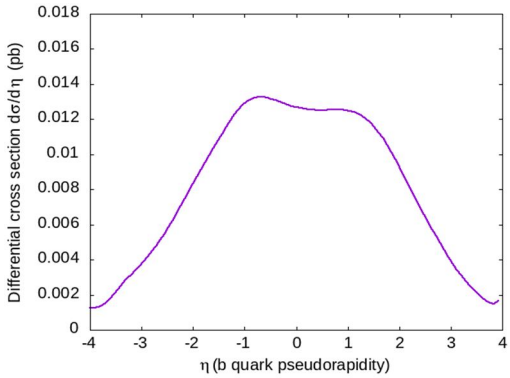

FIG. 14. Pseudorapidity distribution of the b jets at 500 GeV without the $M(b\bar{b})$ cut.

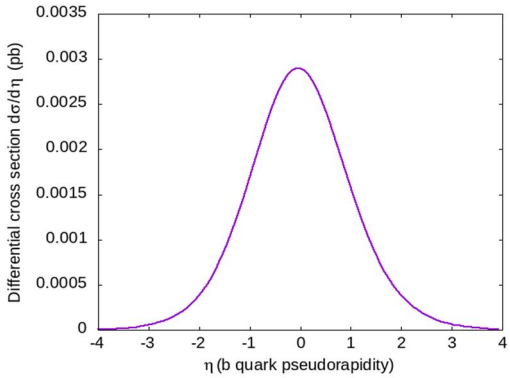

FIG. 15. Pseudorapidity distribution of the b jets at 500 GeV with the $M(b\bar{b})$ cut.

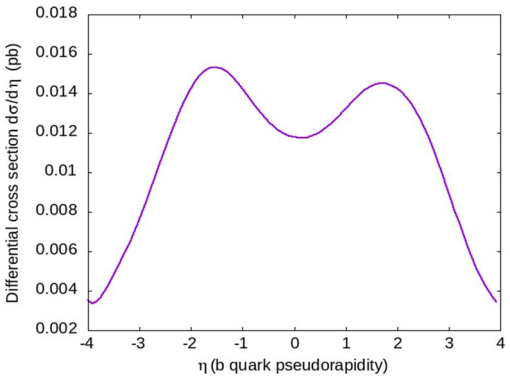

FIG. 16. Pseudorapidity distribution of the b jets at 1 TeV without the $M(b\bar{b})$ cut.

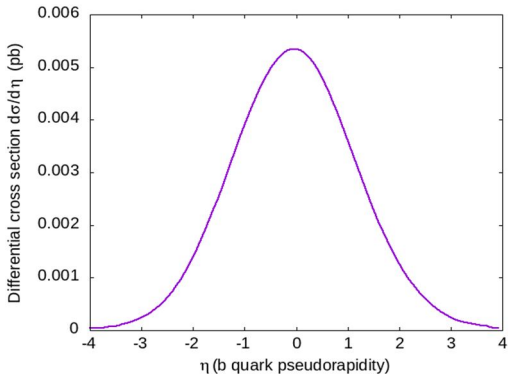

FIG. 17. Pseudorapidity distribution of the b jets at 1 TeV with the $M(b\bar{b})$ cut.

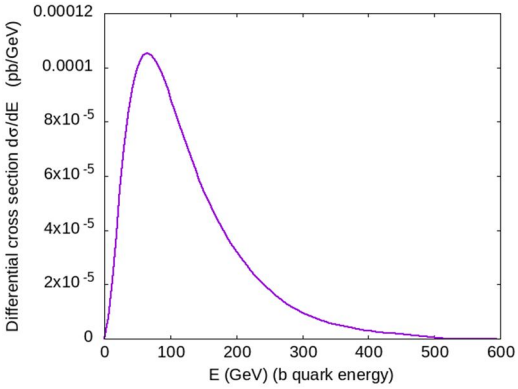

FIG. 18. Energy distribution of the b jets at 1 TeV with the $M(b\bar{b})$ cut.

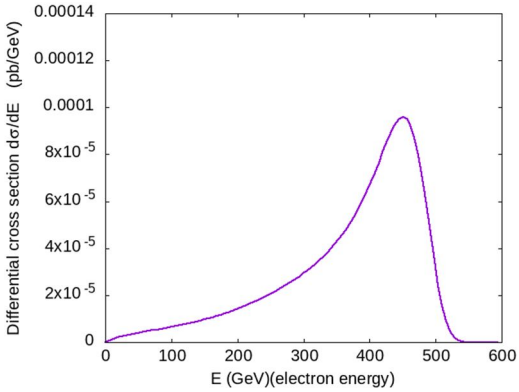

FIG. 19. Energy distribution of the electron at 1 TeV with the $M(b\bar{b})$ cut.

3. Conclusion

The signal $e^+e^- \to e^+e^-H \to e^+e^-b\bar{b}$ receives contributions from Higgsstrahlung $e^+e^- \to ZH \to e^+e^-b\bar{b}$ and ZZ fusion processes $e^+e^- \to e^+e^-ZZ \to e^+e^-H \to e^+e^-b\bar{b}$. Higgsstrahlung is an s-channel process, whereas Z vector boson fusion is a t-channel process. As the center of mass energy s increases, the Higgsstrahlung cross-section decreases as 1/s, but the Z-boson fusion production cross-section grows logarithmically.

The ILC operation starts with the collision energy of 250 GeV (just above the threshold for HZ production), where the Higgsstrahlung process is dominant and the contributions of the fusion processes are small. At higher energies, the Z-boson fusion cross-section becomes larger than the Higgsstrahlung cross-section for s > 450 GeV, and at s = 1 TeV the Z-boson fusion is dominant, as shown in Fig. 4 and Table 1. Figure 7 displays the $b\bar{b}$ invariant mass distributions, illustrating that the background is not negligible, This is evident from a comparison of the M_h peak (signal) with the Z and the low-value $M(b\bar{b})$ peaks (background). The largest background is $e^+e^- \to ZZ \to e^+e^-b\bar{b}$. As a consequence, the $M(b\bar{b})$ is efficient in eliminating the irreducible background by reducing events from non-Higgs processes. At the starting energy of 250 GeV, the Higgs is predominantly produced by the process $e^+e^- \to ZH \to e^+e^-b\bar{b}$. The signal is characterized by a central electron (positron) as shown in Fig. 9, and two central b jets from Higgs decays to $b\bar{b}$, with their invariant mass consistent with the Higgs because of the Higgsstrulung dominance. The background contains events with larger electron and positron pseudorapidity values $|\eta| > 2$ (forward electrons, backward positrons), as depicted in Fig. 8.

At higher energies, 500 GeV and 1 TeV, the ZZ fusion process becomes dominant. In this regime, the Higgs is primarily produced by the process $e^+e^- \to ZZe^+e^- \to e^+e^-b\bar{b}$. The signal characteristics change as a consequence: it is characterized by two forward (backward) energetic electrons (positrons), respectively, as shown in Figs. 11, 12, 13, and 19, and central,

less energetic, b jets, as depicted in Figs. 17 and 18.

The b jets of the background are mainly produced in the forward and backward directions (see Fig. 16). So at high energy, the signal characteristics confirm the dominance of the ZZ fusion Higgs production at high energies. This should be exploited to make maximal use of the high energy reach of ILC. This provides essential motivation to increase the energy after running at 250 GeV.

As a perspective, we can consider studying other processes with different final states [17, 18] and in other machines [19].

4. Appendix

CalcHEP is a package for the automatic calculation of elementary particle collisions and decays at the lowest order of perturbation theory (the tree approximation). It can be run in interactive or batch (non-interactive) modes. The interactive session of CalcHEP is graphical and menu-driven, guiding the user through the calculation by breaking it up into a series of steps. The batch session of CalcHEP is controlled by a set of scripts that perform common tasks non-interactively. Besides the standard model, CalcHEP has implemented many other models of particle interactions, such as the minimal supersymmetric extension of the standard model, the next-to-minimal supersymmetric extension of the standard model the Technicolor model, and the little Higgs model.

Example of a setup file (batch mode)

```
########################################
#  batch_file for CalcHEP              #
#  It has to be launched via           #
#          ./calchep_batch batch_file  #
# Lines beginning with # are ignored.  #
########################################
########################################
#              Model Info              #
#  Model is the exact model name.      #
#  Gauge specifies gauge. Choices are  #
#          Feynman or unitary.         #
########################################
Model: SM
Model changed: False
Gauge: Unitary
########################################
# Process Info                         #
# Process specifies the process.       #
########################################
Process: e,E->e,E,b,B
########################################
#              PDF Info                #
# ISR and Beamstrahlung are only available #
#          for electrons and positrons,  #
#          Default pdf: OFF            #
########################################
pdf1: OFF
pdf2: OFF
########################################
#  Momentum Info(center of mass energy) #
#              in GeV                  #
########################################
p1: 500
p2: 500
########################################
#        Physical_Parameters Info      #
########################################
Parameter: EE = 3.1343E-01
Parameter: Mb = 4.2500E+00
Parameter: MZ = 9.1188E+01
Parameter: MW = 8.0385E+01
Parameter: Mh = 1.2500E+02
Parameter: wZ = 2.49444E+00
Parameter: wW = 2.08895E+00
########################################
#              Cut Info                #
########################################
Cut parameter: M(b,B)
Cut invert: False
Cut min: 115
Cut max: 135
Cut parameter: T(e)
Cut invert: False
Cut min: 10
Cut max:
Cut parameter: T(E)
Cut invert: False
Cut min: 10
Cut max:
Cut parameter: M(e,E)
Cut invert:      False
Cut min:         20
Cut max:
########################################
#              Kinematics Info         #
########################################
Kinematics: 12 -> 34, 56
Kinematics: 34 -> 3, 4
Kinematics: 56 -> 5, 6
########################################
#           Regularization Info        #
```

```
########################################
Regularization momentum: 34
Regularization mass: MZ
Regularization width: wZ
Regularization power: 2
Regularization momentum: 56
Regularization mass: MZ
Regularization width: wZ
Regularization power: 2
Regularization momentum: 56
Regularization mass: Mh
Regularization width: wh
Regularization power: 2
########################################
#              Distribution Info       #
#   Only 1 dimensional distributions are #
#           currently supported.       #
########################################
Dist parameter: M(b,B)
Dist min:       0
Dist max:       500
Dist n bins:    300
Dist x-title:   M(b,B) (GeV)
Dist parameter: N(e)
Dist min:       -4
Dist max:       5
Dist n bins:    300
Dist x-title:   N(e) (GeV)
Dist parameter: N(E)
Dist min:       -4
Dist max:       5
Dist n bins:    300
Dist x-title:   N(E)
########################################
#              Vegas integration       #
#    nSess_1: number of the 1st sessions #
#  nCalls_1: number of calls per 1st sessions #
#   nSess_2: number of the 2nd sessions  #
# nCalls_2: number of calls per 2nd sessions #
########################################
nSess_1: 5
nCalls_1: 10000000
nSess_2: 5
nCalls_2: 10000000
```

References

[1] Aad, G. et al., Phys. Lett. B, 716 (2012) 1.

[2] Chatrchyan, S. et al., Phys. Lett. B, 716 (2012) 30.

[3] Azevedo, D., Ferreira, P., M¨uhlleitner, M.M., Santos, R., and Wittbrodt, J., Phys. Rev. D, 99 (2019) 055013.

[4] Asner, D.M. et al., arXiv:1310.0763 [hep-ph].

[5] van der Kolk, N., PoS DIS, 2016 (2016) 245.

[6] Kawada, S., PoS PANIC, 2021 (2022) 396.

[7] Tian, J. et al., PoS EPS-HEP, 2013 (2013) 316.

[8] Li, H. et al., arXiv:1202.1439 [hep-ex].

[9] Craig, N., Farina, M., McCullough, M., and Perelstein, M., J. High Energ. Phys. 146 (2015).

[10] Yan, J., Watanuki, S., Fujii, K., Ishikawa, A., Jeans, D., Strube, J., Tian, J., and Yamamoto, H., Phys. Rev. D, 94 (2016)113002.

[11] Ogawa, T., PoS ICHEP, 2018 (2019) 681.

[12] Drechsel, P., Moortgat-Pick, G., and Weiglein, G., Eur. Phys. J. C, 80 (10) (2020) 922.

[13] Jeans, D., PoS ICHEP, 2020 (2021) 057.

[14] Han, T., Liu, Z., Qian, Z., and Sayre, J., Phys. Rev. D, 91 (2015) 113007.

[15] Banerjee, S., Gupta, R.S., Ochoa-Valeriano, O. et al., J. High Energ. Phys., (2022) 176

[16] Belyaev, A., Christensen, N.D., and Pukhov, A., Comput. Phys. Commun., 184 (7) (2013) 1729.

[17] Antonov1, E. and Drutskoy1, A., Phys. Rev. D, 104 (2021) 093007.

[18] Yu, D., Ruan, M., Boudry, V. et al., Phys. J. C, 80 (2020) 7.

[19] de Blas, J., Cepeda, M., D'Hondt, J. et al., J. High Energ. Phys., (2020) 139.

Volume 17, Number 3, 2024. pp. 299-311

Jordan Journal of Physics

ARTICLE

Surface Texturing of Silicon Wafers by Two-step Ag-assisted Etching Process with New NSR Solution

Mayyadah Habeeb Hussein and **Samir Mahmmod Ahmad**

Department of Physics, College of Science, Mosul University, Mosul 41002, Iraq.

Doi: **https://doi.org/10.47011/17.3.5**

Received on: 04/08/2022; *Accepted on: 10/01/2023*

Abstract: Solar cells made of monocrystalline silicon can convert more solar energy into electrical energy if the cells can absorb greater amounts of light. Recently, it has been observed that metal-assisted catalyzed etching (MACE) is a good technology for manufacturing micro and nanostructures on silicon substrates. In this work, we use silver as a catalyst in a two-step metal-assisted etching process followed by a rebuilding nanostructure (NSR). We study the effect of changing the parameters of the second step in the MACE process (concentrations of etching solution materials, temperature, and reaction time), where black silicon was obtained with a reduced reflection of 3% without the NSR process. We tested the effect of two types of alkaline solutions in the NSR process on the surface structure of silicon. After performing an NSR operation with sodium hydroxide solution, the field emission scanning electron microscopy (FESEM) image shows a surface with upright pyramidal structures intertwined with deep cavities, and with a reflectance of 10.74%. However, after performing the NSR process with a solution of sodium silicate, the FESEM image shows a rough surface with non-overlapping pores of small cross-sections, achieving a reflectance of 8.65% within the wavelength range of 550-850nm.

Keywords: Texturing, Monocrystalline silicon, Ag-assistance chemical etching, Black silicon, Reflectance.

Introduction

Solar cells are considered one of the promising technologies in the field of renewable energy due to their potential for low-carbon energy production and cost reduction [1]. Despite expectations that their production costs had reached a minimum, they have decreased by another 20% [2]. The field of photovoltaics has witnessed significant advancements in recent years, with ongoing studies aimed at increasing the capacity of cells and reducing production costs [3]. Crystalline silicon cells dominate the solar cell market, accounting for 90% of the global photovoltaic market [4].

The dominance of silicon photovoltaic cells can be attributed to several factors: silicon is abundant, making it inexpensive and non-toxic, with its energy gap is almost suitable for the solar spectrum [4, 5]. However, one of its main disadvantages is its low photon absorption which results in lower cell efficiency [4]. Therefore, absorbance must be increased, either by using an anti-reflection coating [6, 7] or by the texturing process [8]. Texturizing the silicon surface leads to the formation of micro- or nanostructures, which alter the mechanical and electrical properties of the surface [9].

The indirect bandgap of silicon makes it difficult to transfer electrons from the valence band to the conduction band [4]. However, nanoscale silicon structures such as porous silicon [10], quantum dots [11], and nanowires [12], have a direct bandgap, facilitating easier electron movement between the valence and conduction bands.

Corresponding Author: Mayyadah Habeeb Hussein **Email**: gardenrose81522@gmail.com

The texturing process on crystalline silicon wafers can be carried out in several ways, including lithography [13], mechanical grooving [13, 14], reactive ion texturing [16], laser texturing [17], acidic texturing [18], alkaline texturing [19], and metal assistant chemical etching [20]. The efficiency of a solar cell can be increased by performing a wet chemical etching process with the help of metals, either in a single-step [21] or two-step [22] procedure. MACE, one of many fabrication techniques, has become popular as a low-cost, adaptable method for creating Si nanostructures with simple control over position, diameter, and length [22-24]. In MACE, a Si substrate is etched in an oxidant-containing HF solution using noble metal particles or membranes with pores. Si substrates covered in noble metal particles or films etch substantially more quickly than those without metal coverage. Thus, the morphology of the resultant Si nanostructures can be modified by varying the morphology of the precipitated noble metal.

The nanostructure rebuilding (NSR) process is used to change the shape of the nanostructure formed by chemical etching with the help of minerals on the silicon surface and to enhance the light absorption process [26]. Pu *et al*. reported that a one-step metal-assisted chemical etching process using Ag/Cu, followed by the NSR process, leads to the formation of uniform inverted pyramids with a reflection rate of 19.77% [27]. Chen *et al*. applied the two-step metal-assisted chemical etching process to single and multicrystalline silicon wafers, achieving reflectivity rates of 19.4% and 18.7%, respectively [28].

In this work, we textured monocrystalline silicon wafers using a two-step metal-assisted chemical etching process followed by the NSR process. We varied the main parameters of the second step in the metal-assisted etching process (concentration, temperature, and reaction time) and compared the use of sodium hydroxide with a new solution of sodium silicate in the NSR process.

Materials and Methods

This study used P-type (Nexolon) monocrystalline silicon wafers, 200 ± 20 µm thick, with an area of 6 cm^2 and resistivity of 0.5-3.0Ω.cm as substrates. To remove saw damage, the wafers were dipped in a 10% sodium hydroxide solution (KOH) for 15 min at 75°C, followed by immersion in a 10% hydrofluoric acid (HF) solution at room temperature for 2 min to remove the native oxide.

The two-step MACE process involved a first step with a solution of $AgNO_3$:HF:DIW = 0.004:8:50 at room temperature for 10 s. The second step used varying concentrations, temperatures, and reaction times of $AgNO_3$:HF:H_2O_2: DIW, as detailed in Table 1. Ag nanoparticles were removed by immersing the wafers in H_2O_2:NH_3.H_2O (1:3) for 90 s at room temperature. The NSR process was applied using a sodium hydroxide and isopropyl alcohol solution (NaOH:IPA:DIW) for 10 min at 75°C.

TABLE 1. Experimental groups of silicon wafers for studying the effects of parameters in the silver-assisted chemical etching process and subsequent NSR process using a NaOH:IPA:DIW solution. (DIW volume: 25 ml)

Groups	HF:H_2O_2 (ml)	Time (s)	Temperature (°C)
TA1	4:6 6:8 8:10	70	55
TA2	8:10	60 70 80	55
TA3	8:10	60	45 50 55
TA4	6:8 8:10 10:12	60	50

We selected wafers etched with the MACE process under conditions of $HF:H_2O_2$ = 4:6, 70 s, and 55°C to test the sodium silicate solution for the NSR process, as outlined in Table 2.

TABLE 2. Group division of silicon wafers for studying the effects of Na_2SiO_3 concentration and etching time in the NSR process (DIW volume: 25 ml).

Groups	Na_2SiO_3 (g)	IPA (ml)	Temperature (°C)	Time (min)
TA5	1.5	0.5	80	1 2 3
TA6	1.5 2 5	0.5	80	1

After measuring the reflectance and obtaining the NSR conditions that yielded the lowest reflectance (Na_2SiO_3:IPA:DIW = 5:0.5:25, 1 min, 80°C), the NSR process was performed on the etched wafers, as shown in Table 3.

TABLE 3. Group division of silicon wafers for studying the effects of parameters in the two-step silver-assisted chemical etching process, followed by the NSR process using a Na_2SiO_3:IPA:DIW solution.

Groups	$HF:H_2O_2$ (ml)	Time (s)	Temperature (°C)
TA7	6:8 8:10 10:12	60	50
TA8	8:10	60 70 80	50

The reflectance of the wafers was measured using a Shimadzu UV-2550, and the wafers were imaged by field emission scanning electron microscopy (FESEM) (ZEISS SIGMA FE-SEM).

Results and Discussion

In the first step, silver nanoparticles were deposited on silicon wafers using an $AgNO_3$:HF precipitation solution through a galvanic displacement reaction, where two simultaneous processes occur on the silicon surface [12]:

Cathode reaction:

$$2H^+ + 2e^- \longrightarrow H_2 \quad (1)$$

$$Ag^+ + e^- \longrightarrow Ag \quad (2)$$

Anode reaction:

$$Si + 2F^- \longrightarrow SiF_2 + 2e^- \quad (3)$$

$$Si + 2F^- + 2H^+ \longrightarrow SiF_2 \quad (4)$$

After the silver particle deposition process, the silicon wafers were placed in the etching solution ($HF:H_2O_2$). The presence of silver particles on the wafer surfaces stimulates the etching of silicon. Holes are generated through redox reactions at the interface between the metal particles and etching solution. According to Eq. (5), the metal catalyzes the process of reduction of the oxidizing agent (H_2O_2), which subsequently injects holes into the silicon surface directly under the metal particles [29]:

$$H_2O_2 + 2H^+ \longrightarrow 2H_2O + 2h^+ \quad (5)$$

The open space around the metal particles allows the etching solution to penetrate, oxidize the silicon, and dissolve it using HF. Thus, the metal particle penetrates the silicon surface. Immediately below the metallic particle, the hole density is high, as silicon is removed extensively there. The silicon is first oxidized by the process described in Eq. (6), and then the oxide is dissolved by HF, as shown in Eq. (7) [30]:

$$Si + H_2O_2 + 4h^+ \longrightarrow SiO_2 + 4H^+ \quad (6)$$

$$SiO_2 + 6HF \longrightarrow H_2SiF_6 + 2H_2O \quad (7)$$

After etching in the $HF:H_2O_2$ solution, FESEM images showed that the rough surface of black silicon possesses sponge-like nanostructures, with random formation of

nonporous, as seen in Fig. 1(a). This structure resulted in a reflectance of 3%, as seen in Fig. 1(b), when the etching solution concentration was 4:6, the temperature was 55°C, and the etching time was 70 seconds.

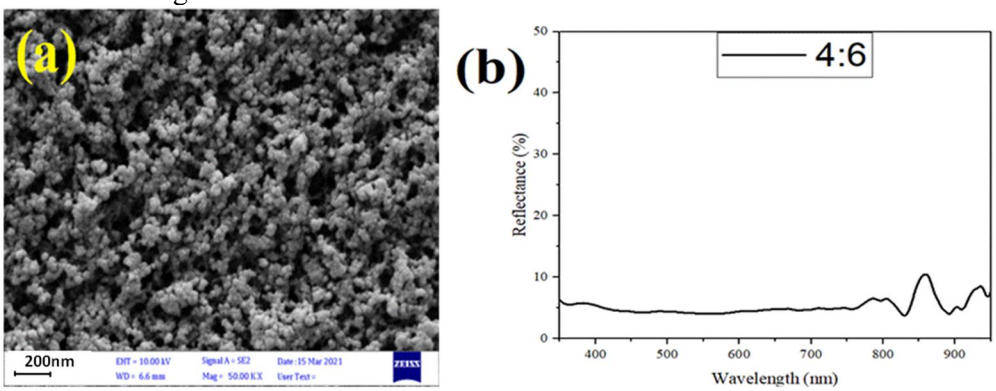

FIG. 1. (a) FESEM image showing the porous structure of the silicon surface. (b) Reflection spectrum as a function of wavelength (350-950 nm) for etched silicon with a concentration of HF:H_2O_2=4:6 at 55°C and an etching time of 70 s.

NSR Process by NaOH Solution.

After the etching process, nanostructure rebuilding (NSR) was carried out by immersing the wafers in an alkaline etching solution (NaOH:IPA:DIW). Three groups were prepared to study the effects of the etching solution's material concentration, temperature, and etching time.

Effect of Changing the Concentration of Etching Solution Materials at 55°C for 70 seconds.

In group TA1 (Table 1), we studied the effect of changing HF:H_2O_2 ratios while maintaining a fixed DIW volume of 25 ml, with the etching temperature at 55°C and time at 70 s.

The lowest reflection of 12.78% was recorded at a concentration ratio of 8:10 (Fig. 2). The H_2O_2 concentration is crucial for adjusting the silicon nanostructures during the texturization process. Increasing the H_2O_2 concentration raises the silicon etching rate, leading to the formation of nanostructures with porous walls due to the presence of metallic nanoparticles [31]. These porous walls can be etched later by the NSR process, forming new structures on the silicon surface, with their shape depending on the depth of the pore structures formed by the metal-assisted etching process [9]. Depending on the concentration of H_2O_2, the precipitated Ag NPs can decompose into Ag^+ ions and re-deposit elsewhere on the silicon, causing the MACE process to restart at those sites [32].

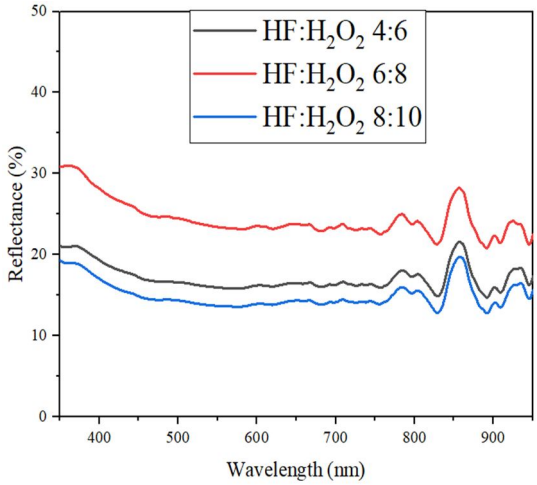

FIG. 2. Reflectance spectra as a function of wavelength (350-950 nm) for silicon wafers of the TA1 group etched with different concentrations of HF:H_2O_2.

Fig. 3 shows FESEM images of the silicon after etching with different solution ratios. At a low ratio (4:6), inverted pyramidal structures mixed with deep cavities resulted in a relatively high reflectance of 14.73%, as seen in Fig. 3(a). As the etching solution ratio increased to 6:8, the surface reflectance rose to 20.78%. Figure 3(b) illustrates that the formed cavities had defined walls, with the presence of some inverted pyramid structures separating these deep cavities with flat, empty spaces from any geometric shapes, contributing to the high reflection.

The reflectance decreased to 12.8% with the increase of the ratio of the etching solution to 8:10. The FESEM images in Fig. 3(c) reveal a combination of inverted pyramidal structures and the appearance of moderate pyramidal structures, with deep cavities covering most of the surface.

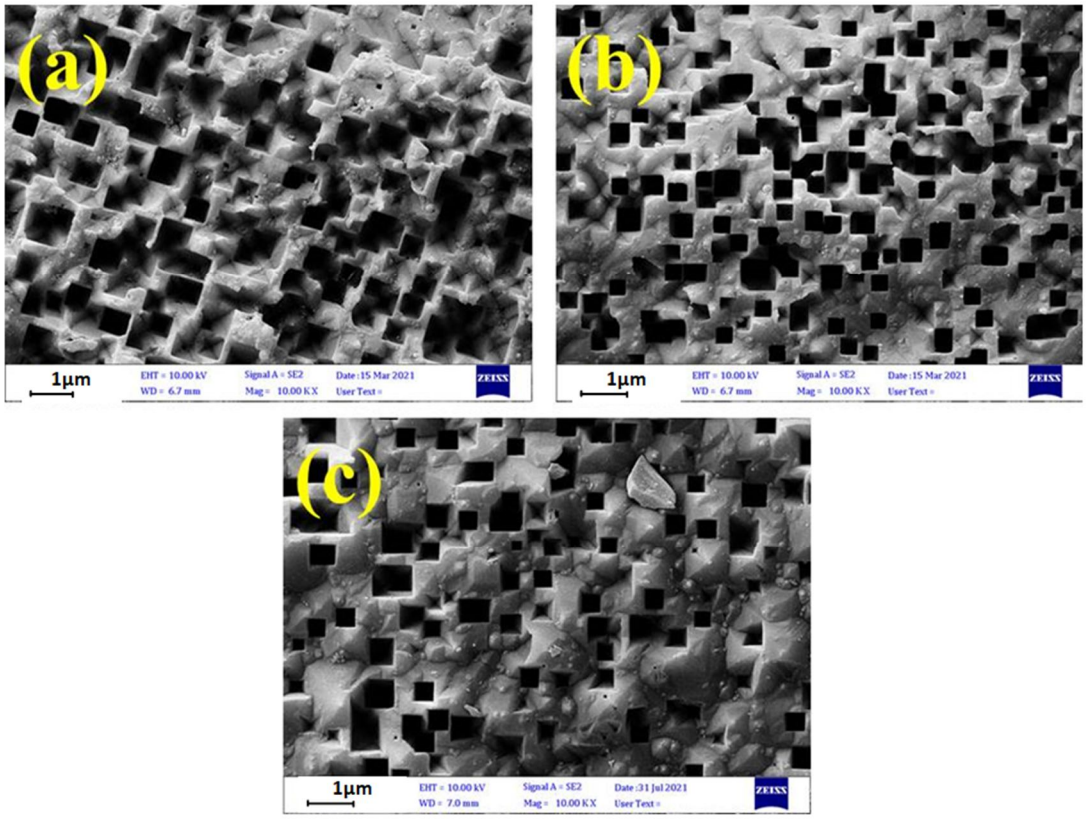

FIG. 3. FESEM images of Si wafers in the TA1 group etched at 55°C for 70 s with different concentrations of HF: H_2O_2: (a) 4:6 ml, (b) 6:8 ml, (c) 8:10 ml.

Effect of Changing the Etching Process Time on the Optical and Morphological Properties of the Wafers.

To study the effect of etching time on silicon reflectance and surface composition, TA2 group samples were prepared with etching times of 60, 70, and 80 s using an 8:10:25 etching solution ratio at 55°C. The lowest reflectance of 11.39% was obtained at 60 s (Fig. 4).

FESEM images in Fig. 5(a) display a defective pyramidal structure overlapping with some deep cavities appearing at an etching time of 60 s. At 70 s, the surface reflectance increased to 12.78%, as the upright pyramid structures disappeared and inverted pyramids appeared alongside deep cavities, as depicted in Fig. 5(b). Further increasing the etching time to 80 s resulted in a higher reflectance of 19.8%, as shown in Fig. 5(c), where deep cavities overlap with flat areas devoid of geometrical structures.

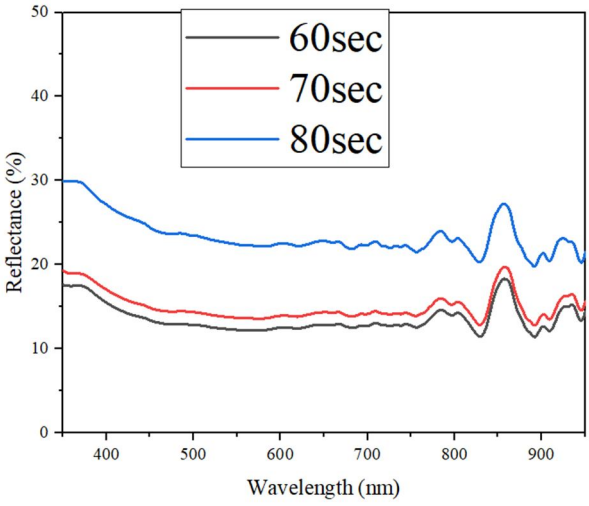

FIG. 4. Reflectance spectra as a function of wavelength (350-950 nm) for TA2 group silicon wafers etched for different durations (60, 70, and 80 s).

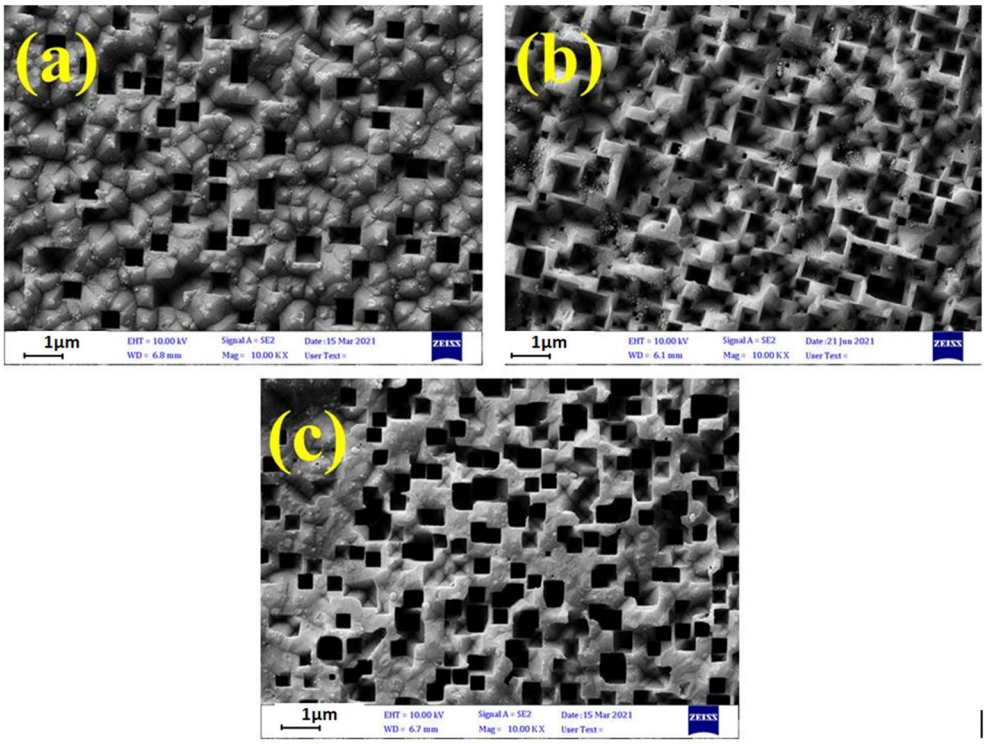

FIG. 5. FESEM images of Si wafers in the TA2 group etched for different durations: (a) 60, (b) 70, and (c) 80 s.

Effect of Changing the Temperature of the Etching Solutions on the Optical and Morphological Properties of the Wafers.

In the TA3 group, we studied the effect of varying the temperature of the etching solution, specifically at 45°C, 50°C, and 55°C. The porous layer formed before the etching process affects the shape and depth of the porous nanostructures formed by the metal-assisted etching process at different temperatures, with the thickness of the black silicon layer increasing at higher temperatures [33].

Fig. 6 shows the reflectance of the wafers. A reflectance of 20.38% was obtained when the temperature of the etching solution was 45°C. This high reflectance can be attributed to the surface morphology, characterized by upright pyramid structures, with some areas still containing silver particles due to the incomplete etching process at a relatively low temperature, as shown in Fig. 7(a).

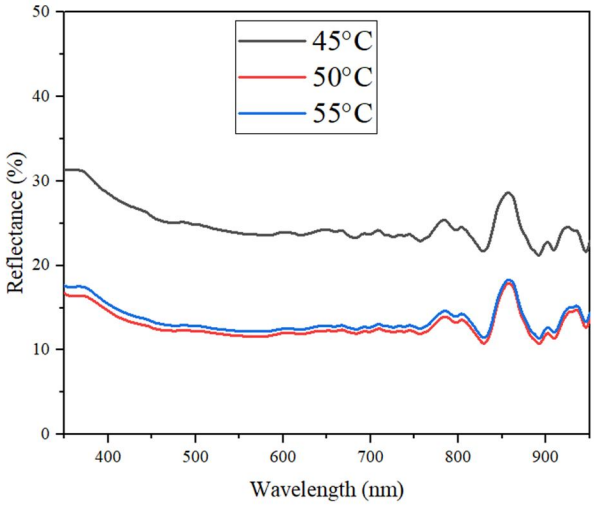

FIG. 6. Reflectance spectra as a function of wavelength (350-950 nm) for TA3 group silicon wafers etched at different temperatures (45°C, 50°C, and 55°C).

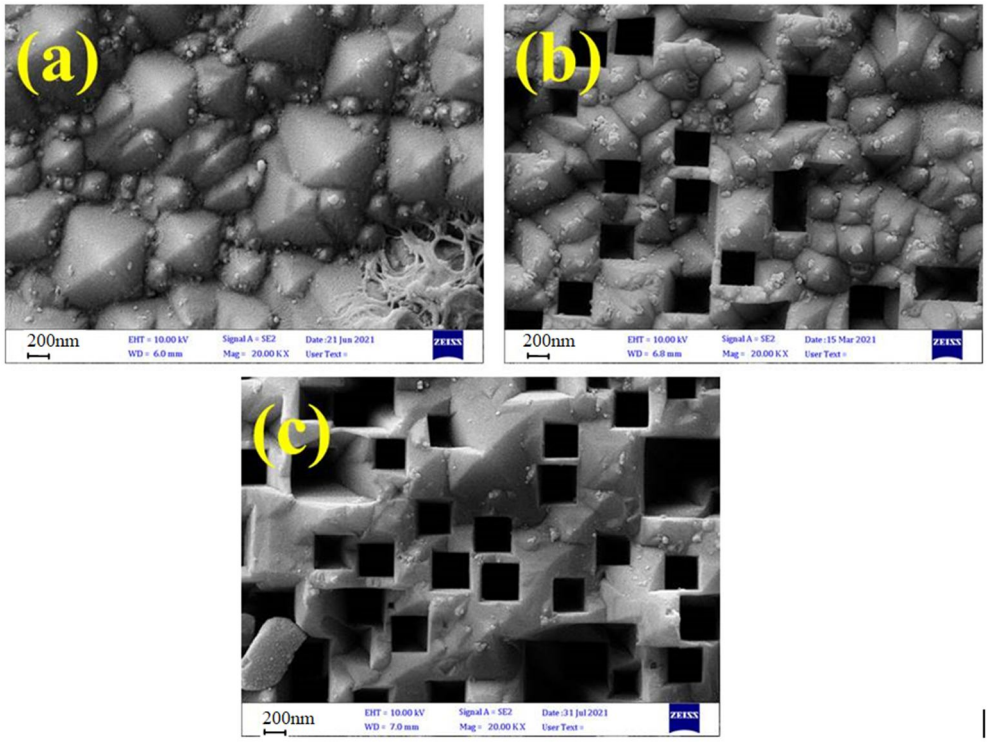

FIG. 7. FESEM image of Si wafers of the TA3 group etched at different temperatures: (a) 45°C, (b) 50°C, and (c) 55°C.

When the temperature was raised to 50°C, the surface reflectance decreased to 10.74% as the silicon surface became covered with moderate hierarchical structures intertwined with deep cavities, as shown in Fig. 7(b). The surface reflectance increased to 11.39% after raising the temperature to 55°C, as the number of deep cavities increased. As for the upright pyramid structures, their number decreased significantly, with flat areas separating the deep cavities, leading to an increase in reflectivity, as seen in Fig. 7(c).

Effect of Changing the Concentration of Etching Solution Materials at a Temperature of 50°C and Etching Time of 60 seconds.

In group TA4, we studied the effect of etching solution material ratios, as outlined in Table 1, with a constant DIW ratio of 25 ml for all solutions, at 50°C and 60 s etching time.

Fig. 8 shows the reflectance spectra of the wafers. A high reflectance of 22.27% was obtained at a low etching solution concentration of 6:8, where the surface structure of the silicon exhibited deep, overlapping cavities, as shown in Fig. 9(a). As the concentration of the etching solution increased to 8:10, the reflectance decreased to 10.74%, and the surface structure transformed into upright pyramidal structures intertwined with deep cavities, as seen in Fig. 9(b). The reflectance rose to 22.51% when the concentration increased to 10:12, and the surface structure changed into irregular pyramids in height, with the inverted pyramidal structures disappearing, as depicted in Fig. 9(c).

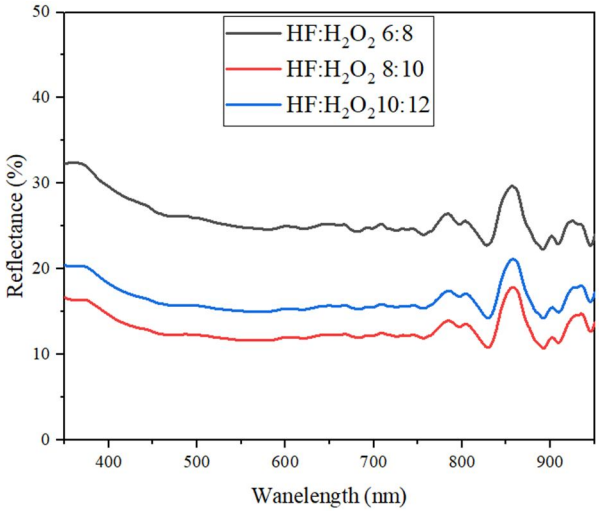

FIG. 8. Reflectance spectra as a function of wavelength (350-950 nm) for silicon wafers in the TA4 group, etched with different concentrations of HF:H_2O_2.

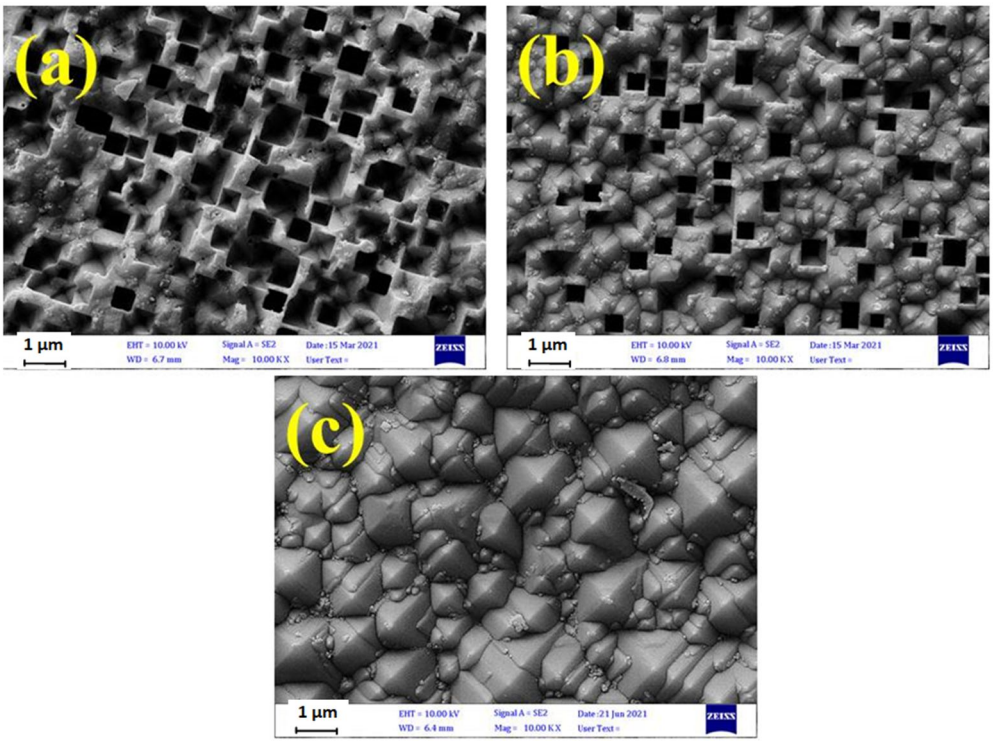

FIG. 9. FESEM images of Si wafers from the TA4 group etched at 50°C for 60 s using different concentrations of HF:H_2O_2: (a) 6:8 ml, (b) 8:10 ml, (c) 10:12 ml.

Texturing Process Using Two-step Ag-assisted Chemical Etching Followed by the NSR Process with Sodium Silicate (Na_2SiO_3) Solution.

The NSR process was performed on wafers that had been etched using a two-step silver-assisted etching method. For the second step of the etching, the conditions were as follows: the etching solution consisted of 4 ml of HF and 6 ml of H_2O_2 added to 25 ml of DIW. The process was conducted at a temperature of 55°C with an etching time of 70 s.

Studying the Effect of Changing the NSR Process Time on the Optical and Morphological Properties of the Wafers.

In group TA5 (Table 2) we studied the effect of NSR etching time while maintaining a constant Na_2SiO_3 concentration (1.5 g) and IPA concentration (0.5 ml) in 25 ml of DIW at a temperature of 80°C. At an etching time of 1 min, a reflectance of 16.68% was obtained, as shown in Fig. 10. FESEM images in Fig. 11(a) revealed a rough surface with deep cavities, free of pyramid structures, resembling a porous surface where the layer was not fully removed.

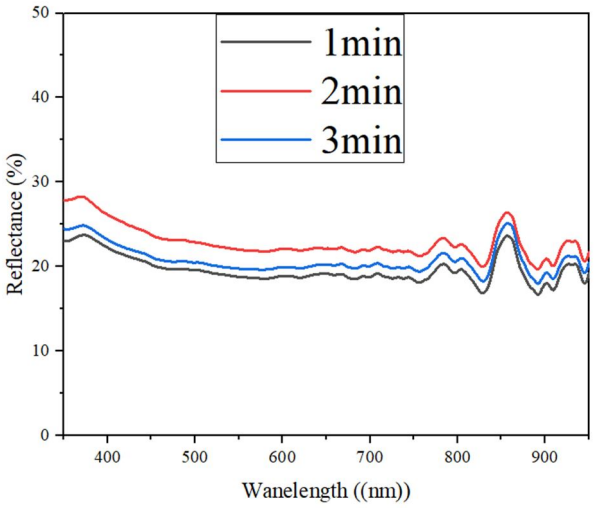

FIG. 10. Reflectance spectra as a function of wavelength (350-950 nm) for silicon wafers group TA5, processed with the NSR method at different etching times (1, 2, and 3 min).

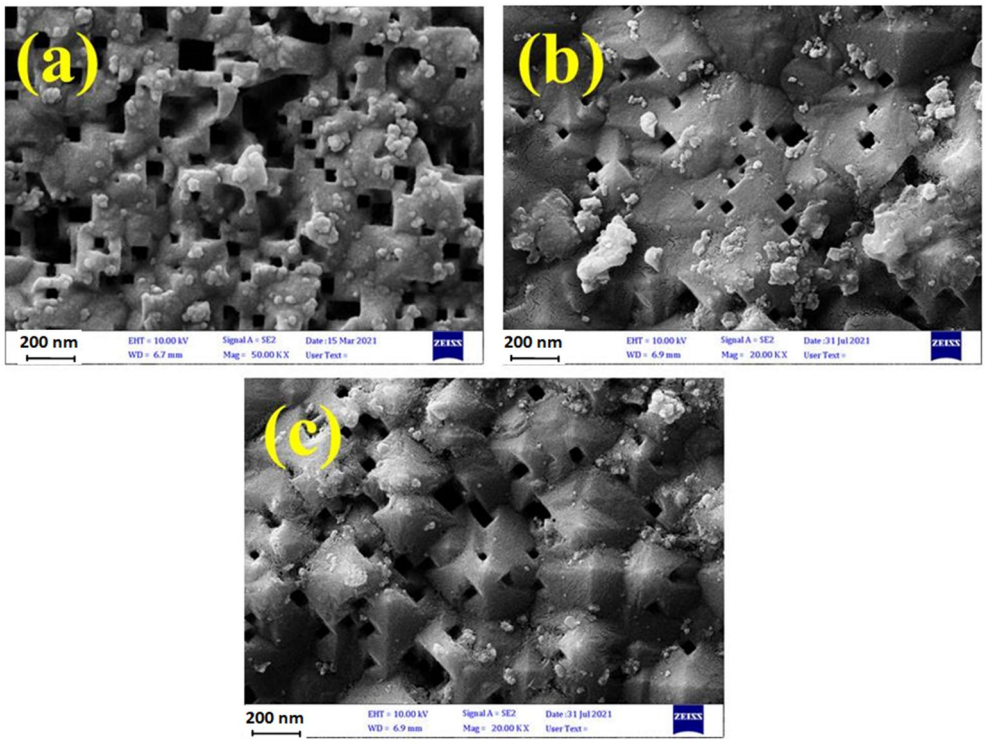

FIG. 11. FESEM image of Si wafers in group TA5 etched using the NSR process at different etching times: (a) 1 min, (b) 2 min, and (c) 3 min.

As the etching time increased to 2 min, surface reflection rose to 19.68%. The FESEM images in Fig. 11(b) show that the surface became irregular and free of pyramid structures, with small pores present. At an etching time of 3 min, the reflection decreased to 17.89% as the etching depth increased, causing the porous layer to disappear and pyramid structures to appear, interspersed with deep cavities, as seen in Fig. 11(c).

Study of the Effect of Changing the Na_2SiO_3 Concentration in the NSR Process on the Optical and Morphological Properties of Wafers.

In group TA6 (Table 2), we investigated the effect of changing the concentration of Na_2SiO_3 in the etching solution (1.5, 2 and 5 g), while keeping the IPA concentration fixed at 0.5 ml, the etching time at 1 min, and the temperature at 80°C. At a low Na_2SiO_3 concentration of 1.5 g, a reflectance of 16.68% was obtained (Fig. 12). The silicon surface exhibited a rough texture

with deep intervening cavities, similar to a porous surface and free of pyramid structures, as seen in Fig. 13(a).

With the increase of the concentration to 2 g, the surface reflectance decreased to 14.23%, and a rough surface was formed as seen in Fig. 13(b), with the disappearance of overlapping deep pores. At a concentration of 5 g, the reflectance decreased to 8.65%, with the formation of a rough surface characterized by non-overlapping pores with a smaller cross-section, as shown in Fig. 13(c).

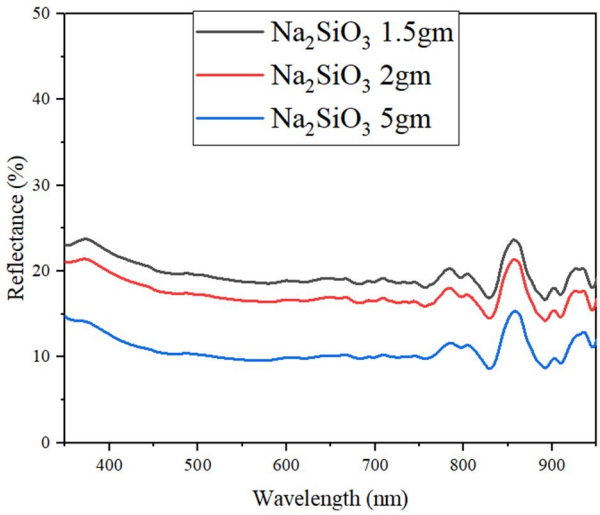

FIG. 12. Reflectance spectra as a function of wavelength (350-950 nm) for silicon wafers in group TA6, processed with the NSR method at different Na_2SiO_3 concentrations (1.5, 2, and 5 g).

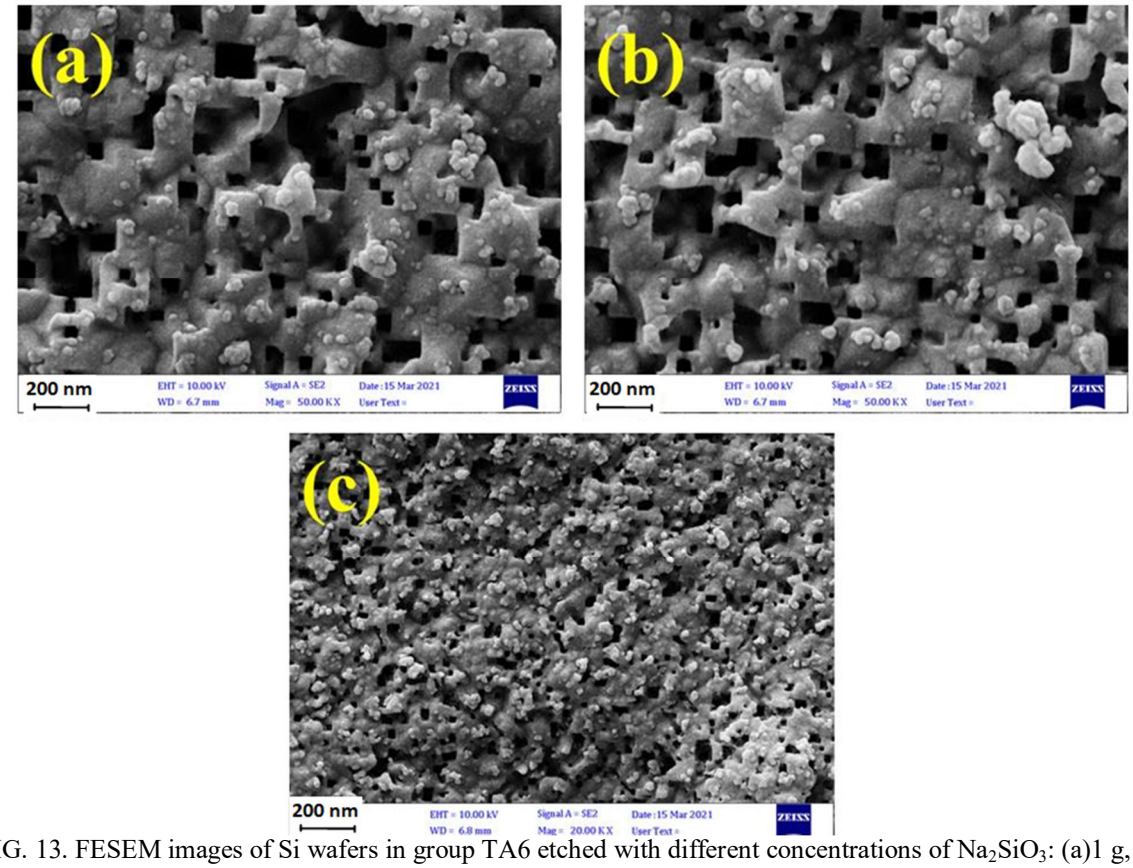

FIG. 13. FESEM images of Si wafers in group TA6 etched with different concentrations of Na_2SiO_3: (a)1 g, (b) 2 g, and (c) 5 g.

Testing the Effect of the NSR Process on the Optical Properties of Etched Wafers Using Different Etching Solution Concentrations and Etching Times.

We also tested the NSR process on wafers textured by a two-step silver-assisted etching process at different etching times and concentrations while maintaining a constant temperature of 50°C. For the NSR process, the etching solution concentration was Na_2SiO_3:IPA:DIW = 5:0.5:25, with an etching time of 1 min at a temperature of 80°C.

Effect of Changing the Etching Solution Concentration on the Optical Properties of the Wafers.

In group TA7, we studied the effect of the concentration of etching solution materials ($HF:H_2O_2$:DIW) in different ratios (6:8, 8:10, and 10:12) at a temperature of 50°C and an etching time of 60 s. The reflectance measurements for the TA7 wafers are shown in Fig. 14. The results were very similar across the different concentrations, with the lowest reflectance of 24.88% obtained at a concentration of (6:8).

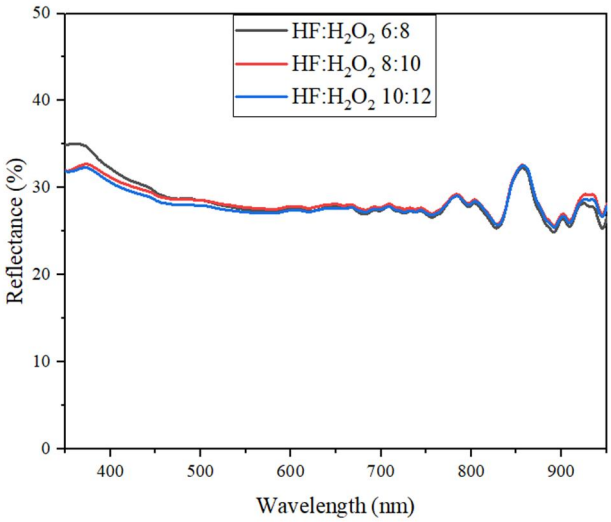

FIG. 14. Reflectance spectra as a function of wavelength (350-950 nm) for silicon wafers of the TA7 group etched at different etching solution concentrations (6:8, 8:10, and 10:12).

The Effect of Changing the Etching Process Time on the Optical Properties of the Wafers

In the TA8 group, the effect of the etching process time (60, 70, and 80 s) was tested at a temperature of 50°C with an etching solution concentration of 8:10. The wafer reflection is shown in Fig. 15. The reflectance measurements were similar across the samples, with the lowest reflectance of 18.34% observed an etching time of 80 s.

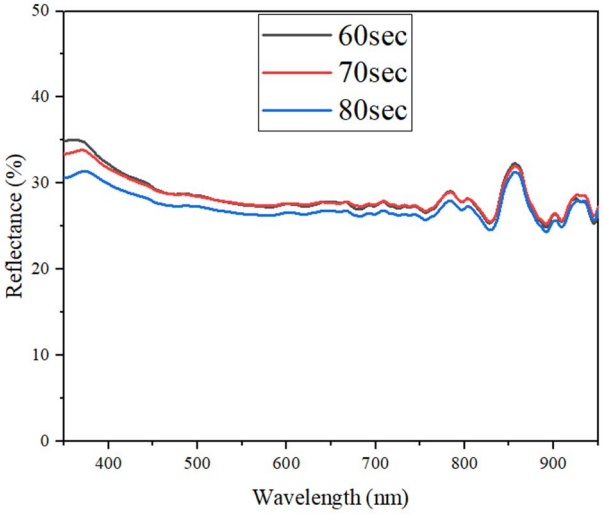

FIG. 15. Reflection spectra as a function of wavelength (350-950 nm) for silicon wafers in the TA8 group at different etching times (60, 70, and 80 s).

Conclusion

In our work, we investigated the effect of the NSR process on the wafers that were textured using a two-step silver-assisted chemical etching process. The NSR process was performed on the wafers after the metal-assistance etching process to change the shape of the surface structure from black porous silicon to pyramid structures, deep pores, and a rough surface with small pores.

For the NSR process, two solutions were tested. The first solution consisted of sodium hydroxide and isopropyl alcohol. We examined the effects of the etching process parameters, including materials concentration, etching time, and temperature. When studying the concentration of the etching solution, the lowest reflection of 12.78% was obtained with an NSR process ratio of HF:H_2O_2 = 8:10. In terms of etching time, the minimum reflection of 11.39% was obtained with an etching duration of 60 seconds. Regarding temperature, the lowest reflection of 10.74% occurred at 50°C, resulting in surface structures that featured pyramids overlapping with deep cavities.

When using sodium silicate (Na_2SiO_3) solution and isopropyl alcohol (IPA) in the NSR process, the effect of the etching process parameters (materials concentration, etching time) was studied. The lowest reflection of 17.89% was observed when the NSR process was performed for 1 minute. Additionally, when the etching solution concentration was Na_2SiO_3:IPA = 5:0.5, the lowest reflection of 8.65% was achieved, and the wafer surfaces exhibited a rough texture.

References

[1] Lai, J,-H., “Development of Low-Cost High-Efficiency Commerical-Ready Advanced Silicon Solar Cells”, (2014).

[2] van Sark, W.G.J.H.M., Alsema, E.A., Junginger, H.M., de Moor, H.H.C., and Schaeffer, G.J., Prog. Photovolt.: Res. Appl., 16 (2008) 441.

[3] IEA-PVPS, Survey Report of Selected IEA Countries between 1992 and 2013, (2014).

[4] Solanki, C.S. and Singh, H.K., “Anti-reflection and Light Trapping in c-Si Solar Cells”, (Singapore: Springer Nature, 2017).

[5] Liu, Y., Zi, W., Liu, S., and Yan, B., Sol. Energy Mater. Sol. Cells, 140 (2015) 180.

[6] Goetzberger, A., Knobloch, J., and Vob, B., “Crystalline Silicon Solar Cells”, (Freiburg, Germany: John Wiley Sons, 1994).

[7] Abushaara, K., Shabat, M., El-Amassi, D., and Schaadt, D., Jordan J. Phys., 13 (1) (2020) 87.

[8] Raval, M.C. and Reddy, S.M., “Industrial Silicon Solar Cells”, In: “Solar Cells”, (Intech Open, 2019).

[9] Lin, Y.K., Chen, Y.S., and Hsueh, C.H., Results Phys., 12 (2019) 244.

[10] Li, S., Ma, W., Zhou, Y., Chen, X., Xiao, Y., Ma, M., Zhu, W., and Wei, F, Nanoscale Res. Lett., 9 (2014) 1.

[11] Rokhinson, L.P., Guo, L.J., Chou, S.Y., and Tsui, D.C., Appl. Phys. Lett., 76(2000) 1591.

[12] Peng, K., Hu, J., Yan, Y., Wu, Y., Fang, H., Xu, Y., Lee, S., and Zhu, J., Adv. Funct. Mater., 16 (2006) 387.

[13] Zhao, J., Wang, A., and Campbell, P., IEEE Trans. Electron. Devices, 46 (1999) 1978.

[14] Willeke, G., Nussbaumer, H.H.B., and Bucher, E., Sol. Energy Mater. Sol. Cells, 26 (1992) 345.

[15] Yuwen, Z., Zhongming, L., Chundong, M, and Shaoqi, H., Sol. Energy Mater. Sol. Cells, 48 (1997) 167.

[16] Inomata, Y., Fukui, K., and Shirasawa, K., Sol. Energy Mater. Sol. Cells, 48 (1997) 237.

[17] Dobrzański, L.A., J. Achiev. Mater. Manuf. Eng., 31 (2008) 77.

[18] Watanabe, R., Abe, S., Haruyama, S., Suzuki, T., Onuma, M., and Saito, Y., Int. J. Photoenergy, 2013 (2013) 1.

[19] Zubel, I., Rola, K., and Kramkowska, M., Sensors Actuators, A Phys., 171 (2011) 436.

[20] Wang, Y., Yang, L., Liu, Y., Mei, Z., Chen, W., Li, J., Liang, H., Kuznetsov, A., and Xiaolong, D., Sci. Rep., 5 (2015) 1.

[21] Yang, W., Shen, H., Jiang, Y., Tang, Q., Raza, A., and Gao, K., Phys. Status Solidi Appl. Mater. Sci., 216 (2019) 1.

[22] Zhong, S., Wang, W., Zhuang, Y., Huang, Z., and Shen, W., Adv. Funct. Mater., 26 (2016) 4768.

[23] Fang, H., Wu, Y., Zhao, J., and Zhu, J., Nanotechnology, 17 (2006) 3768.

[24] Li, X. and Bohn, P.W., Appl. Phys. Lett., 77 (2000) 2572.

[25] Tsujino, K. and Matsumura, M., Adv. Mater., 17 (2005) 1045.

[26] Tang, Q., Shen, H., Yao, H., Jiang, Y., Li, Y., Zhang, L., Ni, Z., and Wei, Q., Appl. Surf. Sci., 455 (2018) 283.

[27] Pu, T., Shen, H., Zheng, C., Xu, Y., Jiang, Y., Tang, Q., Yang, W., Rui, C., and Li, Y., Energies, 13 (2020) 4890.

[28] Chen, K., Zha, J., Hu, F., Ye, X., Zou, S., Vähänissi, V., Pearce, J.M., Savin, H., Su, X., and Pearce, J.M., Sol. Energy Mater. Sol. Cells, 191 (2019) 1.

[29] Chartier, C. and Bastide, S., Electrochim. Acta, 53 (2008) 5509.

[30] Xia, X.H., Ashruf, C.M.A., French, P.J., and Kelly, J.J., Chem. Mater, 12 (2000) 1671.

[31] Qu, Y., Liao, L., Li, Y., Zhang, H., Huang, Y., and Duan, X., Nano Lett., 9 (2009) 4539.

[32] Zhong, X., Qu, Y., Lin, Y.-C., Liao, L., and Duan, X., Acs. Appl. Mater. Interfaces, 3 (2011) 261.

[33] Tang, Q., Shen, H., Yao, H., Gao, K., Jiang, Y., Yang, W., and Liu, Y., Sol. Energy, 170 (2018) 263.

Volume 17, Number 3, 2024. pp. 313-321

Jordan Journal of Physics

ARTICLE

Structural and Luminescent Characteristics of Divalent Europium Activated Barium Aluminate with the Tridymite Structure Synthesized by the Sol-Gel Technique

Ruba I. Alzubi[a,b], **Yazan A. Mousa**[b] and **Hassan K. Juwhari**[a]

[a] *Department of Physics, School of Science, University of Jordan, Amman 11942, Jordan.*
[b] *Jordan Atomic Energy Commission, Amman 11934, Jordan.*

Doi: **https://doi.org/10.47011/17.3.6**
Received on: 07/08/2022; *Accepted on: 27/11/2022*

Abstract: In this study, alkaline earth aluminates were investigated as potential hosts for new blue luminescent materials with nanoparticles. $Ba_{1-x}Eu_xAl_2O_4$ with the stuffed tridymite hexagonal structure was successfully synthesized at 900 °C under controlled sol-gel conditions. Divalent europium was effectively used to activate this host material, producing a brilliant blue-emitting phosphor. Its spectral photoluminescence at 408 nm appears to be in a region close to the laser blue region, with chromaticity coordinate values suitable for the standard blue of the PAL TV system.

Keywords: Blue phosphors, $BaAl_2O_4$, Divalent Europium (Eu^{2+}), Sol-Gel synthesis, Critical energy transfer.

Introduction

New phosphors are in constant demand, mostly for flat panel display applications where specific color rendition and adequate chemical and physical stability are required under the harsh environment of display operations [1-3]. Potential new blue phosphors are of great interest, especially if their optimal emission peaks are close to 405 nm.

The most common alkaline earth aluminate MAl_2O_4 (M = Ba, Ca, and Sr) is the $BaAl_2O_4$ hexagonal structure (space group $P6_322$, 182). Various synthesis methods have been used to prepare $BaAl_2O_4$. These include solid-state reactions [4, 5], combustion [6, 7], and sol-gel synthesis [8]. When these techniques are compared to each other, the sol-gel technique offers several advantages, including relatively low preparation temperatures, ease of stoichiometry control, and the no need for expensive setups or equipment.

Divalent europium Eu^{2+} is one of the most common rare-earth elements used for doping $BaAl_2O_4$ among alkali metal-based aluminate phosphors [8-10]. Consequently, considerable efforts have been dedicated to studying the reduction processes of Eu^{3+} to Eu^{2+} during phosphor preparation [11-13]. These techniques usually require complicated systems of furnaces coupled to quartz tubes through which inert gases are forced to flow to produce reducing atmospheres. These reducing atmospheres may include only H_2 or a mixture of gases such as N_2 + H_2 [14]. Alternatively, a carbon atmosphere can be employed as a simplified method, sometimes favored for its ease of application across various systems [2]. Moreover, based on the model of the charge compensation mechanism, some complexes tend to allow spontaneous self-reduction of their constituents in air [15].

Corresponding Author: Hassan K. Juwhari **Email**: h.juwhari@ju.edu.jo

The current work presents findings on the barium aluminate $BaAl_2O_4$ which can be activated with divalent europium to yield blue photoluminescence. Previous work on $BaAl_2O_4$ produced luminescence around 500 nm due to the effect of the preparation methods and conditions [9].

Experimental Methods

In a modified sol-gel technique, powder samples of $Ba_{1-x}Eu_xAlO_4$ with varying concentrations of 0-8 mole % were prepared. The starting materials were powders of $Al(NO_3)_3.9H_2O$ (98% extra pure, Alpha Chemika), $Ba(NO_3)_2$ (ACS: > 99.0% KT, Puriss. P.A.), and citric acid anhydrous ($C_6H_8O_7{\cdot}H_2O$, extra pure). $Eu(NO_3)_3.5H_2O$ (99.9% trace metals basis, ALORICH) was added as the activator. Barium nitrate and aluminum nitrate were used as the source for metals, while citric acid acted as a polymerizing and chelating agent. The stoichiometric amount of citric acid was added to the solution in a 1:1 molar ratio with respect to the total cations (Ba^{2+} and Al^{3+}) to complex the cations. All the starting materials were made part of a homogeneous solution in deionized water, D.I. [10]. The resultant clear solution was then heated for 30 minutes on a magnetic stirrer. Meanwhile, an ethylene diamine was added to this clear solution drop by drop to adjust the pH to 6. The mixture was then dried overnight using an infrared lamp.

The collected mixture was then placed in a muffle furnace at 700 °C for 6 hours to remove all organic components. The recovered powder was later divided into two equal batches, each transferred to a separate crucible. These crucibles were placed individually in a regular muffle furnace and heated at 900 °C for 3 hours with a heating rate of 5 °C/min. One crucible was annealed in the presence of air, while the other was treated in a carbon atmosphere using a double crucible technique. In this technique, the sample is placed in the inner crucible, while activated charcoal powder fills the space between the inner and outer crucibles.

Results and Discussion

$BaAl_2O_4$ was prepared in both pure and doped phases, as shown in Figs. 1 and 2, and was found to be stable up to at least 1100 °C. The X-ray diffraction patterns agreed well with the reference pattern from the International Collection of Diffraction Data for Powders (ICDD Card No. 96-100-8090). These figures show several doping concentrations of Eu^{2+} synthesized in air (1-8 mole %) and in a carbon atmosphere (1-3 mole %) compared to the ICDD standard card for $BaAl_2O_4$.

The calculated unit cell parameters for the non-doped pure phase were a = b = 5.152 Å and c = 8.744 Å. These results can be compared compared to the values of Ref. [18], where a = b = 5.209 Å and c = 8.761 Å. These results were based on the collected diffraction pattern. Moreover, utilizing the Debye-Scherer's equation for the calculation of the average crystallite sizes at the maximum peak (h k l) = (0 1 2) for the hexagonal configuration, yielded values ranging from ~32 to 40, nm depending on the calcination time and duration. XRD measurements were performed using a Shimadzu XRD-7000 diffractometer with Cu K_α radiation (λ = 1.5404 Å).

The particle size of freshly prepared powder samples was studied utilizing scanning electron microscopy (SEM, JEOL JSM6300 model). The images in Fig. 3 show a moderately well-controlled distribution of particle sizes, with the nanocrystalline nature of the samples apparent. Moreover, the samples prepared in the presence of activated charcoal, as shown in Fig. 3(b), exhibited a larger density of relatively tiny particles residing on top of larger grains compared to samples prepared in air, as depicted in Fig. 3(a).

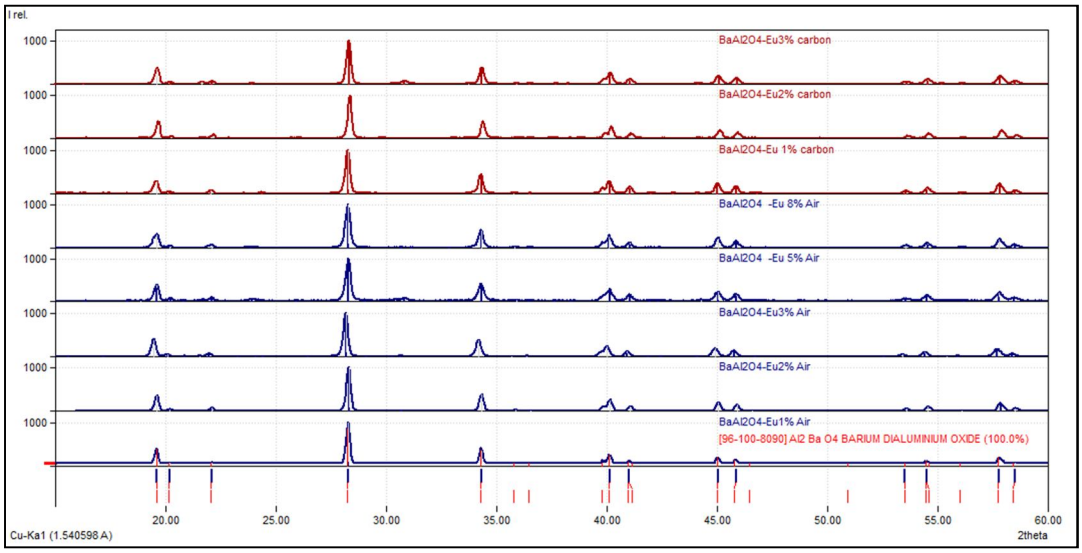

FIG. 1. Powder XRD of sol-gel synthesized $BaAl_2O_4$ annealed at 900°C for 3 h, with various concentrations of Eu^{2+}, both in air and in the presence of activated charcoal.

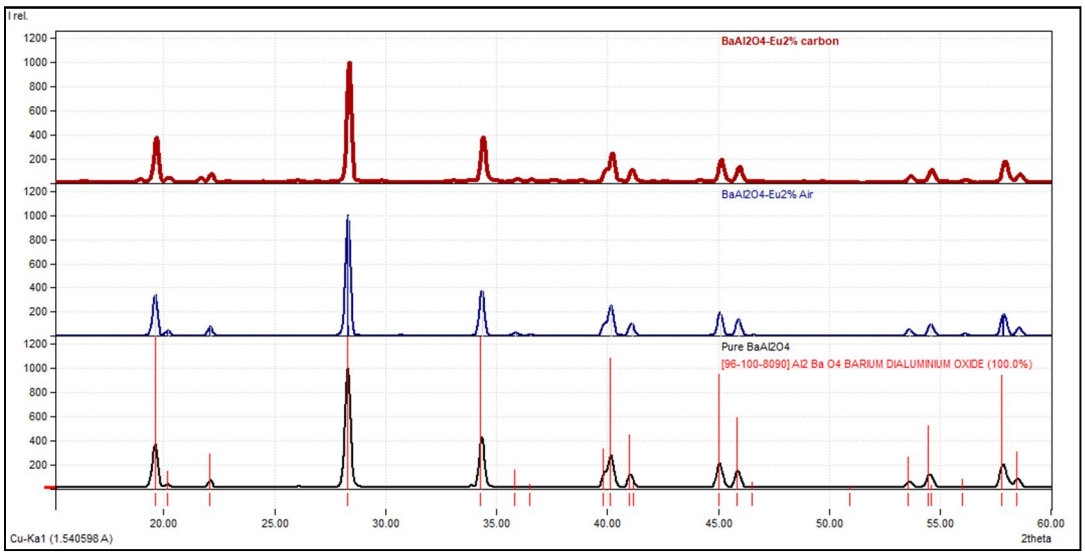

FIG. 2. Enlarged view of powder XRD for sol-gel synthesized $BaAl_2O_4$ annealed at 900 °*C* for 3 h (pure phase vs. 2 mole % Eu^{2+}, annealed in air and in the presence of activated charcoal), compared to ICDD standard card No. 96-100-8090.

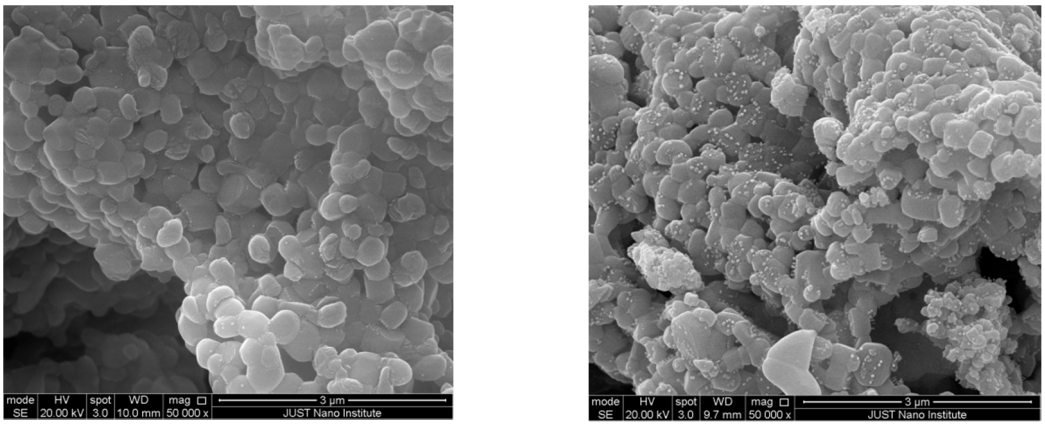

(a) (b)

FIG. 3. SEM images of the freshly prepared $Ba_{0.99}Eu_{0.01}AlO_4$ in (a) air and (b) the presence of activated charcoal. Note the higher density of smaller particles atop the larger ones in the sample prepared in the presence of carbon atmosphere compared to the sample prepared in air.

The room temperature photoluminescent spectra (PL) of the freshly prepared powders were recorded using a Cary Eclipse (Varian) spectrofluorometer. The instrument settings included adjusting the voltage to 600 V to maximize the output of the Xenon lamp, which served as the light source. The excitation spectra were scanned and collected at a photoemission wavelength of 495 nm for both samples prepared in air and under a carbon atmosphere. The emission spectra were scanned at excitation wavelengths of 334 and 325 nm for samples prepared in air and under a carbon atmosphere, respectively. The emission spectra of $Ba_{1-x}Eu_xAlO_4$ prepared in air, shown in Fig. 4(a), reveal two spectral broa-band emissions peaking at ~ 405 and 495 nm. Similar dual emission peaks have been reported recently [16], attributed to two distinct sites available for rare earth cations in the $BaAl_2O_4$ tridymite structure at the Ba Sites [19, 20]. These different sites likely favor different environmental preparation conditions. This was obvious from the distinct luminescent behaviors of the two samples shown in Figs. 4(a) and 4(b), prepared in air and under a carbon atmosphere, respectively.

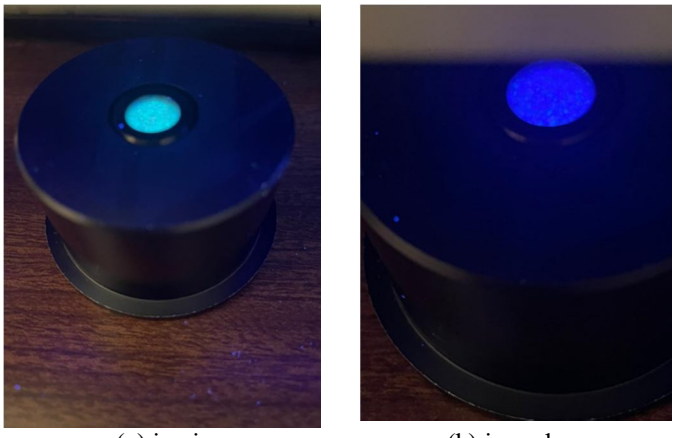

(a) in air (b) in carbon

FIG. 4. Emission behavior of the two samples of $Ba_{0.98}Eu_{0.02}AlO_4$ prepared in (a) air and (b) under the influence of carbon. Both samples were excited with a UV xenon handheld lamp at 365 nm.

Usually, photoluminescence and absorption spectra of divalent europium exhibit broad bands due to electronic transitions from the ground state $^8S_{7/2}$ ($4f^7$) to the crystal field components of the $4f^65d$ excited state configuration [21]. This emission of the Eu^{2+} can occur at any wavelength, extending from the blue region to the red region of the visible light, depending on the host material structure and the preparation conditions. The reduction of Eu^{3+} to Eu^{2+} in solid-state compounds prepared at high temperatures in air is generally governed by four conditions (model of charge compensation mechanism): (1) the host compounds must not contain any oxidizing ions; (2) the cation (europium in this investigation) must substitute a divalent cation in the host matrix; (3) the substituted cation must have a radius of the order comparable to that of the substituent (Eu^{2+}) ion; and (4) the host compound should possess an appropriate structure, typically involving tetrahedral anion groups BO_4, SO_4, PO_4, SiO_4 or AlO_4. Even though all these conditions may apply to the studied host structure, the varying luminescence intensities with different dopant concentrations suggest that spontaneous reduction of Eu^{3+} to Eu^{2+} can't be a complete process without a reducing atmosphere. Citric acid used in the preparation may indeed act as a reducing agent, but this reduction was limited. Applying a reducing atmosphere results in further reduction and apparently to higher concentrations of Eu^{2+} cations. Considering this is the case, then the more reduced the dopants, the more help in producing the luminescence is recorded and shown in the figures.

As shown in Fig. 5(a), the photoluminescence spectra of $Ba_{1-x}Eu_xAlO_4$ (x = 0.01, 0.02, 0.03, 0.05, and 0.08) powders synthesized in air, in the wavelength range of 400 to 600 nm, reveal two broad peaks centered around 415 and 495 nm. The 495 nm band is more pronounced than the other band at the lower wavelength when samples are heated in air. We were successful in forcing luminescence to be concentrated near the wavelength of 408 nm at the expense of the other emission band by adjusting the sintering atmosphere to include carbon during this process and controlling the heating rate at a relatively slow 5°C/min up to soaking temperature. This

treatment resulted in the photoluminescence shown in Fig. 5(b) for $BaAl_2O_4$ doped with xEu^{2+} (x = 0.01, 0.02, 0.03, 0.05, and 0.08), where the rare-earth europium divalent cations favor residing on one of the barium sites. Moreover, the presence of carbon during the heating of the samples enhanced the relative luminescence intensity, as shown in Fig. 5(c).

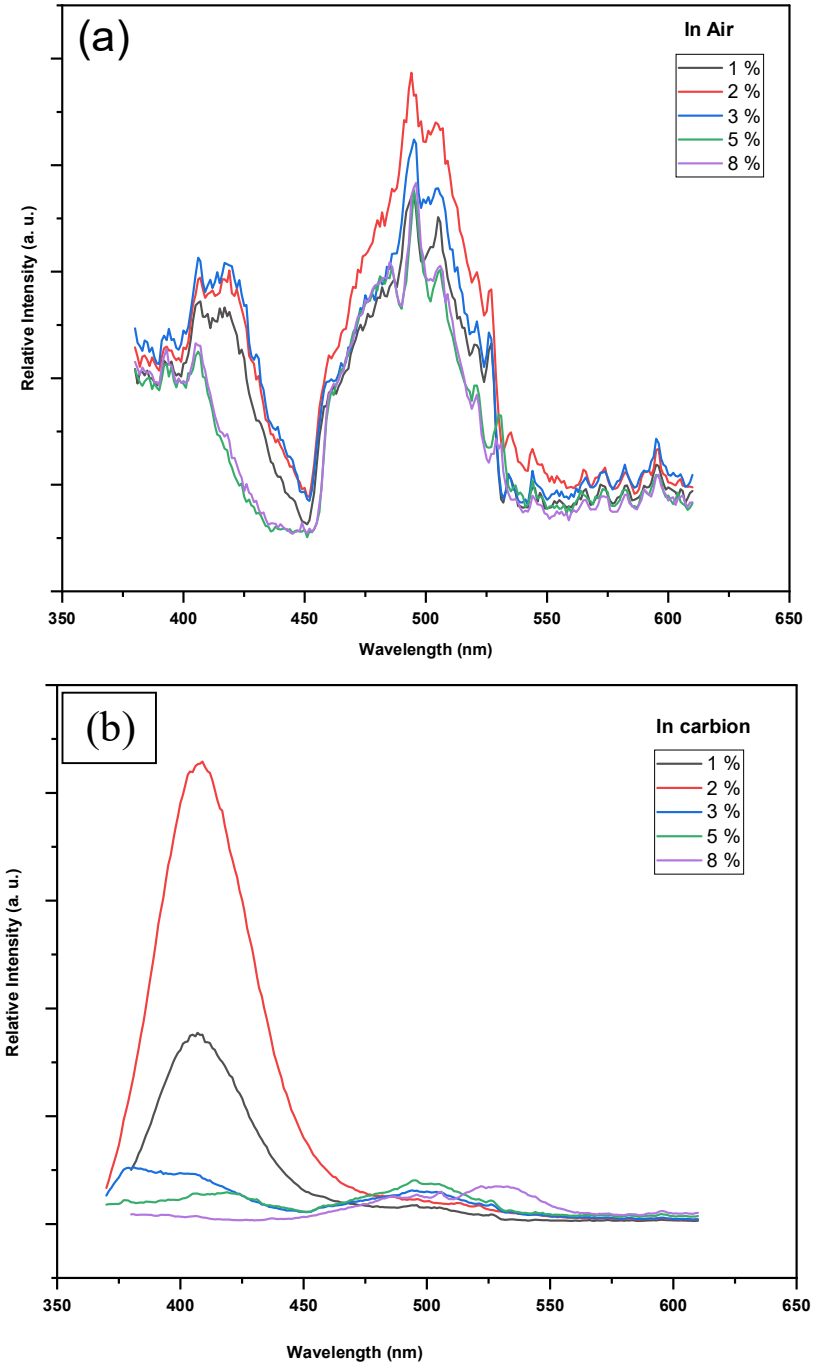

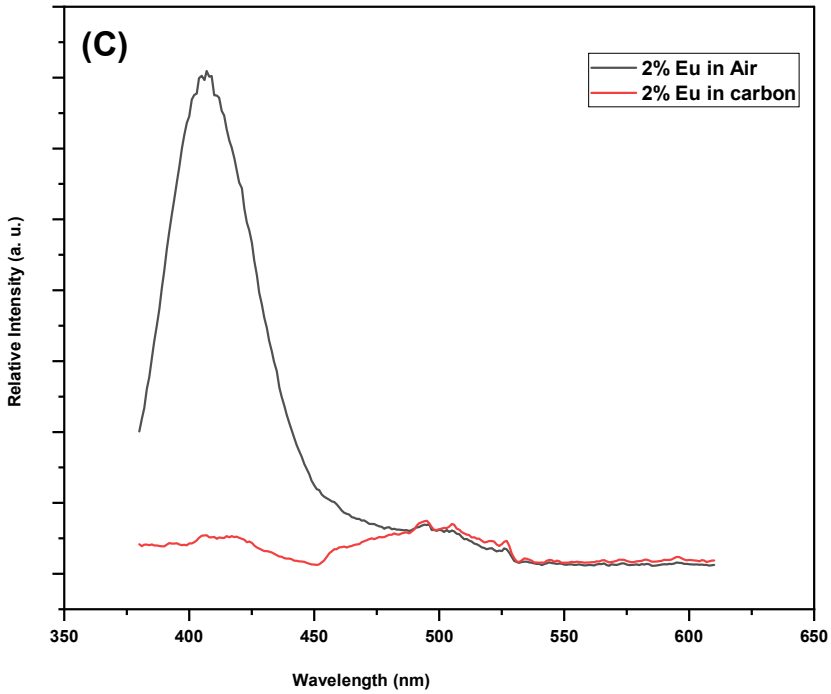

FIG. 5. Emission spectra of $Ba_{1-x}Eu_xAlO_4$. The spectral bandpasses were kept at 2.5 nm for both the excitation and emission monochromators for all samples for comparison reasons. Samples were prepared (a) in air and (b) in the presence of carbon. (c) Comparison of spectra.

In an attempt to estimate the critical energy-transfer distance (r_c) for divalent europium activators in the host matrix material, we utilized the subsequent equation [15]: $R_c = 2[3V/4\pi X_c Z]^{1/3}$. Here, $Z = 2$ represents the available cation sites within the unit cell acknowledging two accessible distinct crystallographic sites for divalent europium in the $BaAl_2O_4$ crystal structure. X_c represents the Eu^{2+} critical concentration in the $BaAl_2O_4$ host material (~ 0.02) and $V = 198.69$ Å^3 represents the unit cell volume. As such, the Eu^{2+} critical energy-transfer distance was approximated to be 21.2 Å.

Three competing mechanisms could describe the non-radiative processes between Eu^{2+} activators: excitation–emission spectral overlap, exchange-intercalation, and electric-multipolar intercalation. Out of these, the transfer-intercalation necessitates shorter critical distances of a few Å or less, separating the donor-acceptor pairs, as it is typically responsible for the forbidden energy-transfer transitions. However, since the electric dipole ($^8S_{7/2} \rightarrow 5d$) transition of the divalent europium is parity-allowed [22], the exchange-intercalation mechanism can be neglected in $BaAl_2O_4:Eu^{2+}$ phosphors. Moreover, the registered insignificant spectral overlap in the $BaAl_2O_4:Eu^{2+}$ phosphors (Fig. 5) suggests that the radiation-reabsorption mechanism is to be disregarded also for this particular luminescent behavior since this mechanism can only be considered when substantial overlap is shown between the excitation and emission spectra. Hence, we are only left with the possibility that the electric-multipolar intercalation processes of divalent europium activators in $BaAl_2O_4$ are possibly accountable for the photoluminescence quenching and the energy transfer.

The blue emission near 408 nm of the $BaAl_2O_4:0.02Eu^{2+}$, along with its excitation spectrum shown in Fig. 6, indicates that this material could be a promising candidate for blue phosphors. This potential makes it worthwhile to check its chromaticity coordinates for comparison with other emerging blue phosphors.

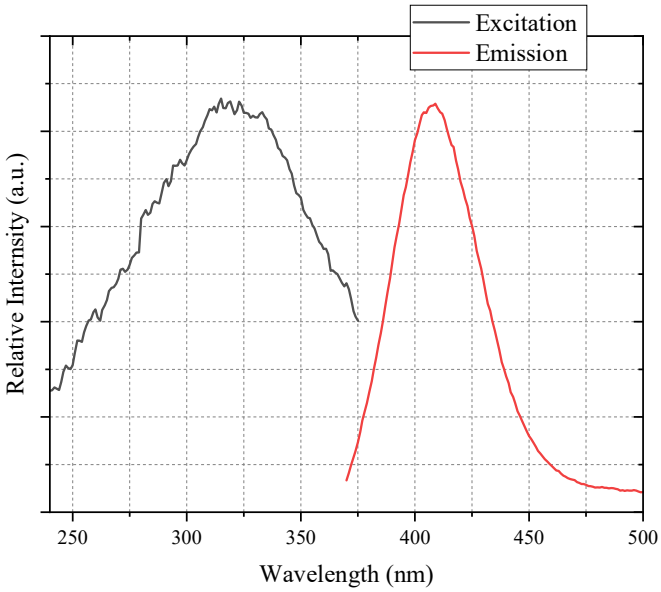

FIG. 6. Excitation and emission spectra for $Ba_{0.98}Eu_{0.02}Al_2O_4$. The spectral monochromator slits were set to 2.5 nm, with medium voltage setting adjusted to 600 V.

The chromaticity coordinates of the sol-gel prepared $BaAl_2O_8:Eu^{2+}$ powder samples based on the CIE 1931 were calculated depending on the emission spectra and plotted on the chromaticity diagram (Fig. 7). It is worth mentioning here that the white-point chromaticity coordinates are (0.333, 0.333). In order to display the degree of the color purity of the luminescent emission, one typically determines how far the color is shifted from the saturated color locus at the spectralboundary. Hence, color purity is calculated as the length of the line representing how far the calculated chromaticity coordinates with respect to the chromaticity coordinates of the white point divided by the length of the line representing how far the chromaticity coordinates of the saturated color locus compared to the chromaticity coordinates of the white point multiplied by 100%. Based on this procedure, it is found that the $BaAl_2O_8:Eu^{2+}$ color purity amounts to 88.4%, compared to 94.9% reported for $CaB_2Si_2O_8:Eu^{2+}$ which was found suitable for the NTSC values for the blue standard [22], and 83.9% for the Osram-Sylvania BAM (used as a reference for blue phosphor) [23].

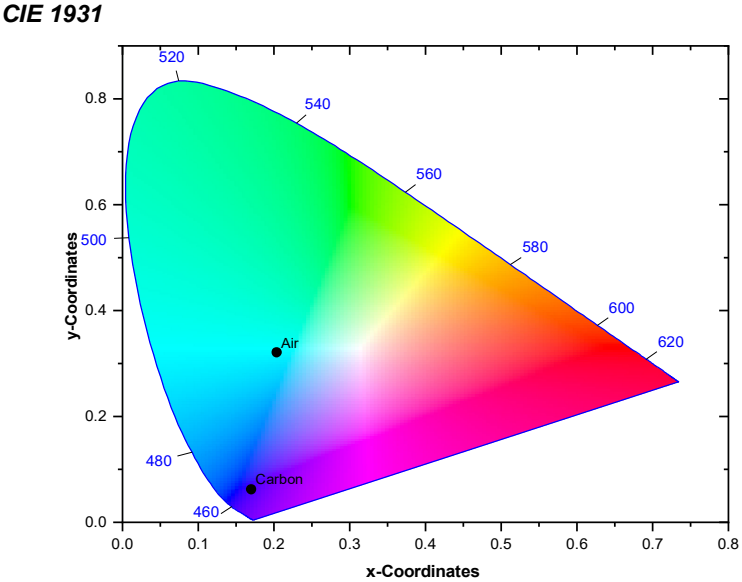

FIG. 7. CIE 1931 chromaticity diagram with chromaticity coordinate points labeled “Carbon” and “Air”, indicating the calculated color coordinates obtained from the luminescence emission spectra of sol-gel prepared $Ba_{1-x}Al_2O_4:xEu^{2+}$ phosphor samples either in air or in the presence of carbon.

The two points for the 2% doped samples prepared in air and under a reducing atmosphere are placed on the chromaticity diagram adjacent to the saturated color locus and specified on the color space diagram by their locations. The color purity coordinates of the $Ba_{0.98}Eu_{0.02}Al_2O_4$ powder sample prepared with activated charcoal are listed in Table 1, alongside those of $Ca_{0.96}Eu_{0.04}B_2Si_2O_8$ and the Osram Sylvania Blue reference phosphor. Moreover, the color purity of the prepared $Ba_{0.98}Eu_{0.02}Al_2O_4$ powder sample, shown in Fig. 7, is found to be close to the standard CIE PAL TV primary values for blue [23].

TABLE 1. CIE chromaticity coordinates of sol-gel synthesized barium aluminate activated with divalent europium in the presence of carbon, compared to divalent europium-activated danburite and the BAM Osram Sylvania blue reference phosphor type 2461.

Concentration (mol %)	X Coordinate	Y Coordinate	
$Ba_{0.98}Eu_{0.02}AlO_4$	0.1697	0.0630	This Work
$Ca_{0.96}Eu_{0.04}B_2Si_2O_8$	0.1427	0.0576	Synthetic Danburite [22]
BAM Reference	0.1417	0.1072	[Osram-Sylvania type 2461 Reference phosphor]

Conclusion

Phase-pure nanocrystalline barium aluminate with the stuffed tridymite structure was successfully prepared via a modified sol-gel reaction of barium nitrate and aluminum nitrate. When activated by Eu^{2+}, it exhibited initial emission from cations residing on both Ba^{2+} competing sites. Annealing under a reducing atmosphere resulted in an enhanced probability of reducing Eu^{3+} and hence improving their likelihood of occupying favorable sites. This process resulted in a brilliant, single blue broad-band phosphor with a maximum centered at ~ 408 nm. This wavelength, suitable for the laser blue color rendition, is produced at the optimal doping concentration of about 2 mol.% of Eu^{2+} in the $BaAl_2O_4$ host. In addition, the critical energy transfer distance was calculated to be ~ 21.2 Å. The calculated chromaticity coordinates of these successfully sol-gel synthesized phosphors were found to be (0.169, 0.063). Finally, based on the 1931 CIE chromaticity diagram and the tables of the PAL TV systems for blue phosphors, these prepared materials appear to be promising candidates.

Acknowledgment

This work was partially accomplished during the sabbatical year of one of the authors (H. K. Juwhari) spent at the University of Jordan during the academic year 2019/2020. This research is also partially funded by the School of Graduate Studies at the University of Jordan (R. I. Al-Zubi and H. K. Juwhari).

References

[1] Singh, D., Tanwar, V., Simantilleke, A.P., Mari, B., Kadyan, P.S., and Singh, I., J. Mater. Sci.: Mat. Elect., 27 (3) (2016) 2260.

[2] Guzmán-Rocha, M., Oliva, J., Diaz-Torres, L.A., and Montes, J., Solgel. Sci. Technol., 95 (2) (2020) 423.

[3] Mothudi, B.M., Ntwaeaborwa, O.M., Botha, J.R., and Swart, H.C., Physica B Condens Matter., 404(22) (2009) 4440.

[4] Sathaporn, T. and Niyomwas, S., Energy Procedia., 9 (2011) 410.

[5] Peng, M. ad Hong, G., J. Lumin., 127 (2) (2007) 735.

[6] Satapathy, K.K., Mishra, G.C., and Khan, F., Chem. Sci. Trans., 2 (2013) 1262.

[7] den Engelsen, D., Fern, G.R., Ireland, T.G., Yang, F., and Silver, J., J. Opt. Mater. Express, 10 (8) (2020) 1962.

[8] Maphiri, V.M., Mhlongo, M.R., Hlatshwayo, T.T., Motaung, T.E., Koao, L.F., and Motloung, S.V., Opt. Mater., 109 (2020) 110244.

[9] Araujo, R.M., dos Santos Mattos, E.F., dos Santos Júnior, B.F., Rezende, M.V.D.S., Valerio, M.E., and Jackson, R.A., J. Lumin., 236 (2021) 118011.

[10] Lephoto, M.A., Ntwaeaborwa, O.M., Pitale, S.S., Swart, H.C., Botha, J.R., and Mothudi, B.M., Physica B Condens Matter, 407 (10) (2012) 1603.

[11] Bierwagen, J., Delgado, T., Jiranek, G., Yoon, S., Gartmann, N., Walfort, B., and Hagemann, H., J. Lumin., 222, (2020) 117113.

[12] Xu, Y., Sun, Z., Wei, Y., Jia, M., Hou, B., Li, X., and Fu, Z., J. Am. Ceram. Soc., 103 (10) (2020) 5721.

[13] Xie, H., Lu, J., Guan, Y., Huang, Y., Wei, D., and Seo, H.J., Inorg. Chem., 53 (2) (2014) 827.

[14] Aitasalo, T., Hölsä, J., Jungner, H., Lastusaari, M., and Niittykoski, J., J. Phys. Chem. B, 110 (10) (2006) 4589.

[15] Wang, Z., Liu, Y., Chen, J., Fang, M., Huang, Z., and Mei, L., J. Adv. Ceram., 6 (2) (2017) 81.

[16] Rodrigues, L.C.V., Stefani, R., Brito, H.F., Felinto, M.C.F.C., Hölsä, J., Lastusaari, M., Laamanen, T., and Malkamäki, M., J. Solid State Chem., 183 (10) (2010) 2365.

[17] Mishenina, L.N., Selyunina, L.A., and Botvina, T. M., Key Eng. Mater., 670 (2016) 95.

[18] Hörkner, W. and Müller-Buschbaum, H.Z., Anorg. Allg. Chem., 451 (1) (1979) 40.

[19] Volhard, M., Yu, L., den Engelsen, D., Fern, G.R., Ireland, T.G., and Silver, J., Opt. Mater. Express, 10 (8) (2020) 1951.

[20] Stefani, R., Rodrigues, L.C.V., Carvalho, C.A.A.D., Felinto, M.C.F.D.C., Brito, H.F.D., Lastusaari, M., and Hölsä, Opt. Mater. Amst., 31 (12) (2009) 1815.

[21] Marí, B., Singh, K.C., Verma, N., Mollar, M., and Jindal, Trans. Indian Ceram. Soc., 74 (3) (2015) 157.

[22] Juwhari, H.K. and White, W.B., Mater. Lett., 88 (2012) 16.

[23] Broadbent, A.D., Color Res. Appl., 29 (4) (2004) 267.

Volume 17, Number 3, 2024. pp. 323-330

Jordan Journal of Physics

ARTICLE

Influence of Applied Discharge Voltage and Gas Flow Rate on Nickel Plasma Jet Parameters Diagnosed by Optical Emission Spectroscopic Technique

Ibrahim K. Abbas

Department of Physics, College of Science, University of Baghdad, 10017, Baghdad, Iraq.

Doi: **https://doi.org/10.47011/17.3.7**

Received on: 07/09/2022; *Accepted on: 28/12/2022*

Abstract: In this work, we measure the plasma parameters by using an AC high-voltage power supply that generates a non-thermal plasma jet system at atmospheric pressure. A nickel (Ni) metal strip, with dimensions of 1.5 × 10 cm^2, was connected to the anode electrode of the AC power supply. This nickel strip was immersed in a flask with a small amount of distilled water positioned below the plasma plume nozzle. Optical emission spectroscopy (OES) was used to diagnose the plasma system at different argon gas flow rates (1-5 L/min) and varying applied voltage values (11-15 kV). It is significant to know the processes accompanying plasma generation to measure their parameters which include the electron temperature (T_e), electron number density (n_e) of the plasma, Debye length (λ_D), and plasma frequency (f_p). Our results showed an increase in the intensity of spectral lines with the increase in applied discharge voltage (11-15 kV). The maximum peak for ArI was observed at a wavelength of 811.531 nm, and the maximum peaks for nickel (Ni) were observed at wavelengths of 285.21 and 519.70 nm. Also, the results indicated a gradual increase in electron temperature (T_e) and electron density (n_e) values at the applied voltage of 0.403-0.468 eV. Likewise, the electron density (n_e) was in the range of (11.486-13.851) × 10^{17} cm^{-3}.

Keywords: Atmospheric plasma jet, Nickel (Ni) plasma parameters, Electron temperature, Spectroscopic optical emission (OES).

1. Introduction

Plasma has free-charged particles at the macroscopic level, with both negative and positive charges storing roughly the same amount of energy [1]. The energy needed to generate plasma can be supplied in several ways: through heat from a combustion process, through the interaction between laser radiation and a solid, a liquid, or gas, or through electrical discharges in gases, in which free electrons take energy field and lose it through excitation and ionization processes of the atoms and molecules in the gas. On a macroscopic scale, plasmas are electrically neutral since the number of positive and negative charges is similar [2]. The goal of plasma diagnostics is to obtain information about plasma parameters through various experimental techniques [3]. In order to determine plasma attributes, it is necessary to understand the effects of the numerous physical processes that occur and to determine the effects of these processes. Electrical sampling and optical spectroscopy of emissions are examples of such diagnostics [4]. Spectroscopic procedures, such as laser dispersion, emission, absorption, and fluorescence spectrometry, are unique methods for collecting distinct sections of plasma without altering its status or structure [5]. One of these techniques is optical emission spectroscopy (OES), which relies on calculating the plasma's optical radiation to describe plasma parameters in the chemical, molecular, and ionic radiator's near environments [6, 8]. So, in order to obtain

Corresponding Author: Ibrahim K. Abbas **Email**: Ibrahim.kareem1104a@sc.uobaghdad.edu.iq

information about plasma, such as electron density, excited species state densities, collisional electron–atom, atom-atom, and ion–atom effects, energetic distribution of species, temperature of species, charge transfer between plasma components, rotating structure of molecules, and even electric charge, spectroscopy serves as a non-intrusive method for analyzing electromagnetic radiation from a plasma source [7, 9] Atomic spectra are primarily concerned with the exchange of energy between the atom and electromagnetic radiation, which can be associated with a valence electron changing its orbit in the simplest model [7, 10].

Recent developments have sparked renewed interest in using atmospheric pressure plasmas in a myriad of applications biology, nanotechnology, and agriculture [11]. This is especially true in biomedicine, where uses include inhibiting microorganisms, regenerating tissue, and whitening teeth, among others [12]. For such low-density plasmas, the population densities of the new rates are computed using a balance between radiative decay to ground state and collisional excitations. Due to its ability to recognize and forecast particular properties of plasma, such as populations with particle velocity distribution and relative energy levels, the temperature of the plasma is a crucial thermodynamic attribute. The electron temperature (T_e in eV) is calculated using the equation below [3]:

$$ln\left[\frac{\lambda_{ji}I_{ji}}{hcA_{ji}g_j}\right] = -\frac{1}{K_BT_e}(E_j) + \ln\left|\frac{N}{U(T)}\right| \quad (1)$$

where g_j denotes the statistical weight of the second spectrum line, λ_{ji} denotes the wavelength of the second level (j) and the first level (i), and E_j is the excited state energy of the upper level. E_i is the first level in the spectrum of plasma in eV, I_{ji} denotes the spectrum intensity of the second level (j) and the first level (i), A_{ji} denotes the transition probability of the second (j) and the first level (i), N denotes the density of the state's population, and K_B denotes the Boltzmann constant. Another main parameter for plasma, the electron density, can be calculated from the equation [3]:

$$n_e = \left[\frac{\Delta\lambda}{2\omega_s}\right] N_r \ (cm^{-3}) \quad (2)$$

where $\Delta\lambda$ is the full width at half maximum (FWHM) in nm of the line, ω_s is the Stark broadening parameter found in standard tables, N_r is the reference electron density. In the analysis of plasma spectra, Stark broadening is an essential factor in spectral line widening because it provides the necessary electron density at the desired plasma electron temperature [13]. Doppler broadening, instrumental broadening, and natural broadening all contribute to the Gaussian profile [14]. If electron impact widening is considered while the ion dynamics are neglected during the radiative process, a Lorentzian profile can be obtained. The frequency of plasma is determined from the following equation [15]:

$$f_p = \sqrt{\frac{e^2n_e}{\varepsilon_\circ m_e}} = 8.98\sqrt{n_e}\ (\text{Hz}) \quad (3)$$

where e^2 represents electron charge, n_e electron number density, m_e electron mass, and $\varepsilon_\circ$ permittivity. Debye shielding is the response of charged particles to lower local electric fields, giving plasma its quasi-neutrality feature. To calculate the Debye length λ_D, we can use this equation [16]:

$$\lambda_D = \sqrt{\frac{\varepsilon_O K_B T_e}{n_e e^2}} = 743 \times \sqrt{\frac{T_e}{n_e}}\ (cm) \quad (4)$$

The main objective of this paper is to describe the use of OES to analyze a nickel plasma jet, calculate plasma parameters by the Boltzmann plot method, which is used to estimate the electron temperature, calculate other plasma parameters, and understand the effects of increasing applied voltage and gas flow on the behavior of electron temperature and electron density.

2. Material and Methods

2.1. Preparation of Nickel Metal and Main Tools

A small flask containing distilled water was used to partially submerge a nickel-metal (Ni) plate. The detection instrument of the spectrometer was installed close to the plasma jet head to measure the intensity of the emission spectra. An S3000-UV-NIR spectrometer was used to measure the spectral wavelengths emitted during plasma jet generation, with the spectral emission recorded in the range of 270-1000 nm. The dimensions of the nickel plate were 1.5 × 10 cm, with 6 cm of nickel (Ni) submerged in the distilled water. The optical fiber of the spectrometer device sensed the spectral emissions during the generation of the plasma and its interaction with the distilled water

in the flask. The length of the plasma was controlled by the gas flow device (flowmeter) at an applied voltage of 11-15 kV.

2.2. Setup of Plasma Jet System

To generate plasma in this system, argon gas was used. A high alternating voltage power supply of up to 20 kV was used with a cut-off frequency of 50 kHz. The high-voltage power supply represented the main unit in the plasma jet system for ionizing the argon gas and obtaining plasma at room pressure. The cathode electrode of the voltage supply was connected to the tip of the plasma jet, while the anode electrode high-voltage power supply was connected through a connecting wire with nickel metal, which connected with the protruding part of the nickel metal immersed in the flask below the plasma jet as shown in Fig. 1. The voltage used to generate plasma was changed from 11 to 15 kV with the gas flow value fixed at 5 L/min. Similarly, the gas flow rate was varied between 1 and 5 L/min while keeping the applied voltage fixed at 15 kV. Diagnostics were performed in the laboratory at the atmospheric pressure of the room. A spectrometer linked to a control unit (PC) was used to record the resulting spectra and obtain spectral data at the above variables. The plasma spectrum of argon gas was collected at 690-975 nm, while the nickel spectrum data (NiI) was recorded at 280-915 nm. These recorded data were examined and matched with data from the National Institute of Standards and Technology (NIST). Finally, the nickel metal plasma parameters were calculated, and their properties were explained.

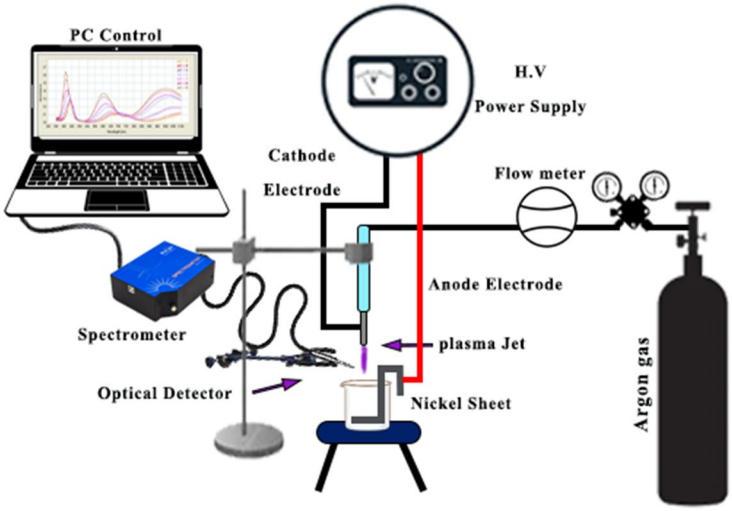

FIG. 1. Schematic setup of atmospheric nickel plasma jet and spectroscopic device with the rest of the tools, including the high voltage power supply to generate plasma, argon gas bottle, and gas flow device controlled by a flowmeter.

3. Results and Discussion

After preparing the plasma system for optical diagnostics, the S3000-UV-NIR optical diagnostic device was prepared, and its optical fiber detector was positioned close to the generated plasma plume. An optical spectrum of the system was obtained using the spectrometer diagnostic device. Figure 2 presents the optical emission spectrum for the plasma jet system at different voltages with a fixed value of argon gas flow. Figure 3 presents the measured optical spectrum for the plasma system at a different flow of argon gas, with the applied voltage fixed at 15 kV.

In both figures, the influence of applied voltage and gas flow on the optical diagnosis is evident, as the peak intensities increase progressively with both factors. The peaks of nitrogen gas (N_2I) appear in the wavelength range of 280 to 422 nm, while the peaks of argon gas (ArI) are observed from 690 to 975 nm. In both figures, the highest peak of nitrogen gas (N_2I) is at a wavelength of 336.93 nm, and the highest peak of argon gas is at 811.53 nm. It is also clear from the figures that multiple peaks of nickel metal NiI are visible from 285 to 915 nm, including peaks at 285.21, 317.39, 335.62, and 409.55 nm, and so on, up to 915.34 nm. These peaks become more pronounced with the

increasing values of influencing factors, indicating a rise in the number of interactions between plasma particles and an increase in the emission of ArI gas. All the peaks illustrated in the two figures correspond to the data from the National Institute of Standards and Technology (NIST) and are consistent with the results of previous studies by other researchers [17-19].

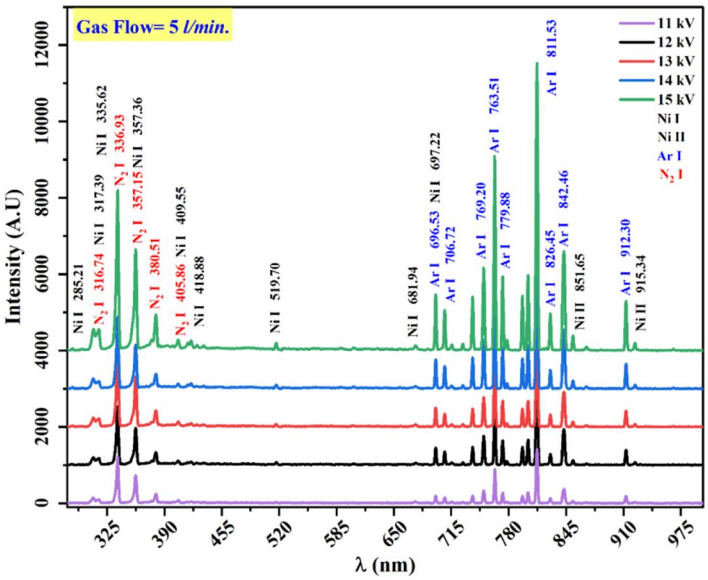

FIG. 2. Diagnosed optical spectrum of a nickel plasma jet system using OES at different discharge voltages (11-15 kV) with a fixed gas flow rate of 5 L/min. The spectrum lines include nickel (Ni), (Ar), and (N_2), ranging from 285.21 to 915.34 nm.

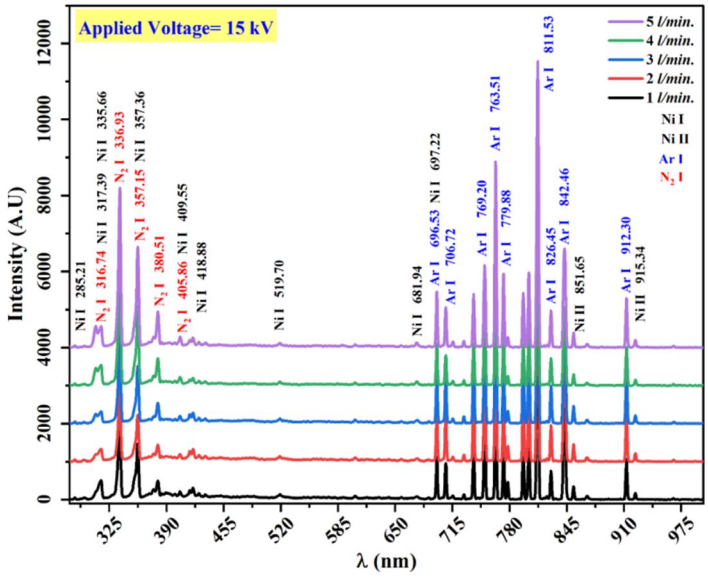

FIG. 3. Diagnosed optical spectrum of a nickel plasma jet system using OES at different gas flow rates (1-5 L/min) with a constant discharge voltage of 15 kV. The spectrum lines include nickel (Ni), (Ar), and (N_2), ranging from 285.21 to 915.34 nm.

At a low flow level of argon gas, a small part of the gas atoms emerging from the plasma nozzle ionizes through interactions and thermal collisions between the atoms. With the gradual increase in the level of gas flow (1-5 L/min) or applied voltage (11-15 kV), and as a result of the applied voltage difference between the electrodes, electrons are released from the negative electrode and are then accelerated. This process, coupled with an increase in the level of gas flow or an increase in the voltage applied, leads to an increase in the collisions of gas atoms. These collisions generate pairs of electrons and ions by interacting with neutral atoms, causing further ionization for these neutral atoms. Nickel metal, which contains secondary electrons on its surface, contributes to the chain of reactions inside the flask, with the increasing flow of argon gas and applied voltage used to generate plasma during diagnostics.

One of the most important parameters of plasma is the electron temperature. Using Eq. (1), one can calculate the temperature by determining the slope of the linear fit of the curve obtained from plotting $ln[\lambda_{ji}I_{ji}/hcA_{ji}g_j]$ versus E_j, as shown in Fig. 4. Another important plasma parameter is the electron number density (ne), which can be determined through the data obtained by using Eq. (2). This calculation involves the full width at half maximum (FWHM) values at each applied voltage (11-15 kV), as shown in Fig. 5.

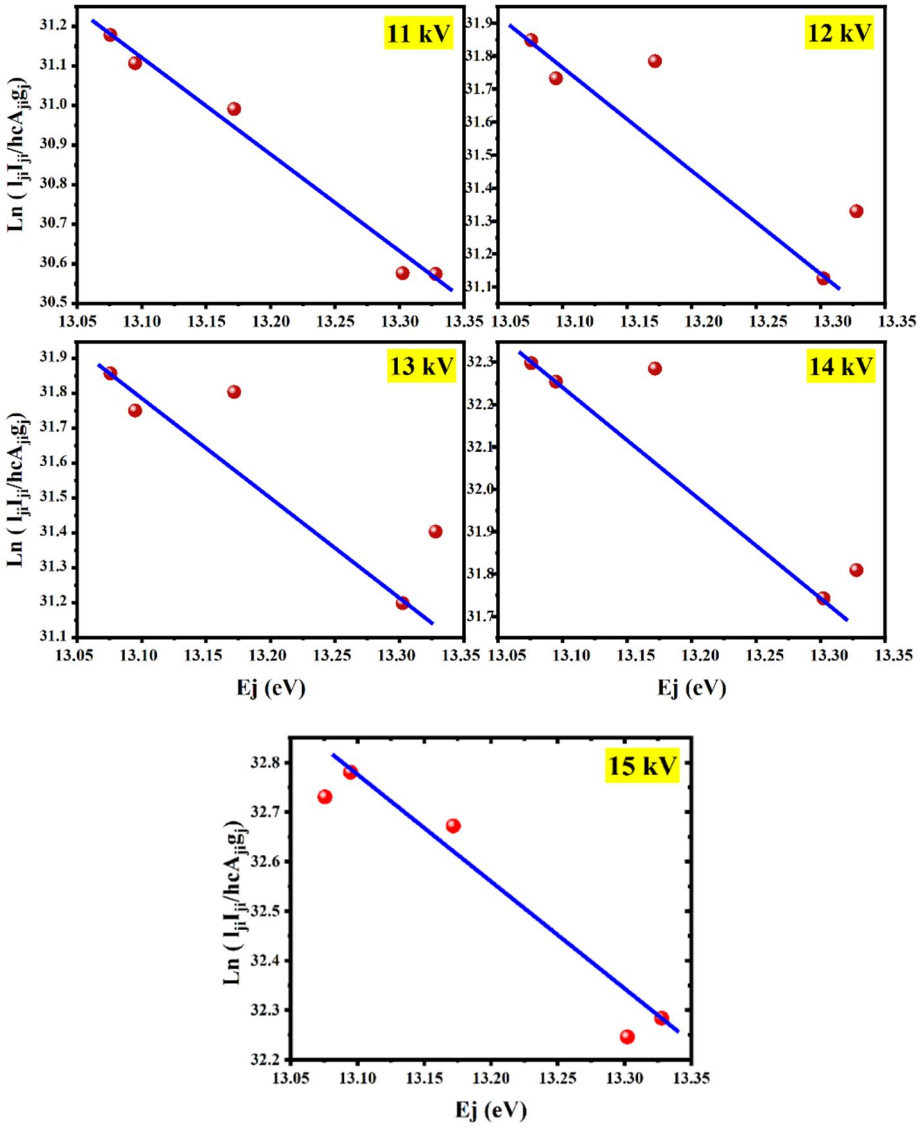

FIG. 4. Boltzmann plot of $ln[\lambda_{ji}I_{ji}/hcA_{ji}g_j]$ vs. the upper energy level (E_j) of nickel metal spectrum generated by an atmospheric plasma jet system for different values of applied voltage (11-15 kV) and constant gas flow rate of 5 L/min.

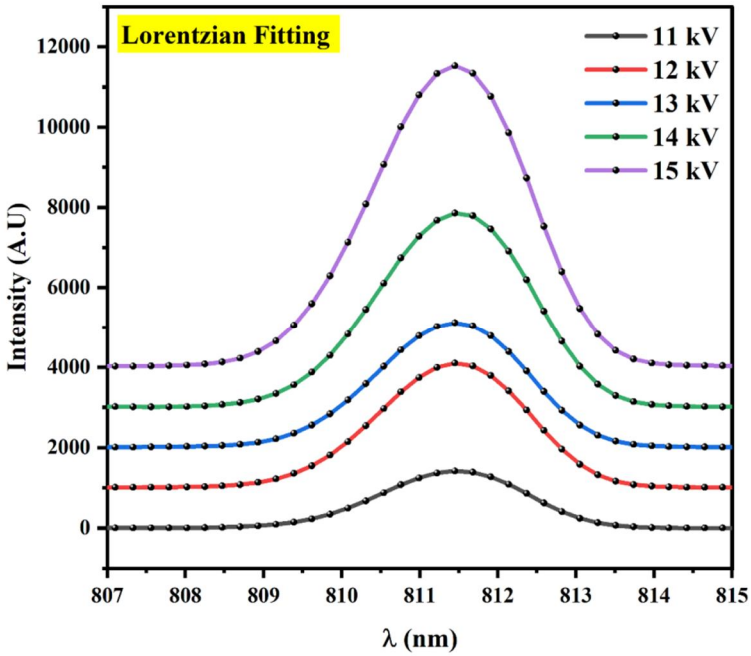

FİG. 5. Full width at half maximum (FWHM) of the nickel metal spectrum in an atmospheric plasma jet system at different values of applied voltage (11-15 kV) and a constant gas flow rate of 5 L/min (Lorentzian Fitting) at 807-815 nm.

Table 1 shows the measured plasma parameters diagnosed at a variable applied voltage of 11-15 kV, with the gas flow value being fixed at 5 L/min. These plasma jet parameters were determined using Eqs. (1) - (4). It is clear from the table that the measured plasma frequency f_p increases with the increase in the applied voltage values, while the Debye length λ_D decreases with the increase in the applied voltage under the same argon gas flow conditions.

TABLE 1. Atmospheric plasma jet parameters for nickel metal (Ni) at different applied voltages (11-15 kV) with a fixed gas flow rate of 5 L/min.

V (kV)	Te (ev)	FWHM (nm)	ne x 10^{17} (cm^{-3})	f_p x 10^{12} (Hz)	λ_D (x 10^{-6} cm)
11	0.403	1.700	11.486	9.624	0.440
12	0.427	1.800	12.162	9.903	0.428
13	0.451	1.900	12.838	10.175	0.441
14	0.448	2.000	13.514	10.439	0.430
15	0.468	2.050	13.851	10.569	0.432

Figure 6 depicts the correlation between electron temperature and electron number density as a function of the applied voltage used to generate plasma in this system. The results show a clear increase in electron temperature from 0.403 to 0.468 eV with increasing applied voltage at a constant argon gas flow rate of 5 L/min. Similarly, the electron density increases from 11.486 x 10^{17} to 13.851 x 10^{17} cm^{-3} at an applied voltage of 11-15 kV. At the first value of the applied voltage, 11 kV, the electron temperature was 0.403 eV and the electron density was 11.486 x 10^{17} cm^{-3}. With the increased value of the applied voltage, electron temperature and density began to rise. The reason for this is the increase in the neutral electronic collisions that occur on the walls of the plasma jet. The value of the electron temperature at 15 kV is 0.468 eV, and the electron density is 13.851x10^{17} cm^{-3}.

There are more collisions between electrons and argon atoms before getting out of the plasma nozzle when the applied voltage is gradually increased, which results in an increase in the amount of energy transferred from electrons to gas molecules, which increases the temperature of the gas, so the electron density will gradually increase, especially since gas flow is 5 L/min.

This behavior indicates that the amount of argon gas passing through the plasma is substantial, leading to a slight increase in both

electron temperature and density. It is clear that the applied voltage is directly related to the measured plasma parameters, as electrons are accelerated from the cathode to the anode, gaining kinetic energy and colliding with gas molecules between the electrodes. This acceleration continues until the electron collides with an argon gas molecule. At lower collision energies, only elastic scattering occurs. However, as the applied voltage increases gradually from 11 kV to 15 kV, electrons can lose significant amounts of energy by exciting gas molecules to higher internal energy states, and at even higher energies, ionization can occur within the plasma jet.

The ionization process is, of course, essential to achieve an increase in electron temperature and number density. Consequently, some of electrons are absorbed by the neutral particles, while others are lost in collisions (electron-neutral particles). The loss of charged particles (electrons and ions) takes place through diffusion to the walls of the plasma jet tube, where they recombine. In the case of the plasma jet, the shape of the plasma tube resembles a cylinder, with ionization and collision events occurring along and inside this cylindrical column. Under these conditions, the tube radius of the plasma jet influences electron distribution through collisions and diffusion to the walls by an increase in applied discharge voltage and argon gas flow [20-22]. As the applied field accelerates the newly liberated and colliding electrons, a secondary ionization process occurs, leading to the collapse process, which increases electron temperature and electron number density in the plasma jet system, as shown in Fig. 6, consistent with previous studies [3,14].

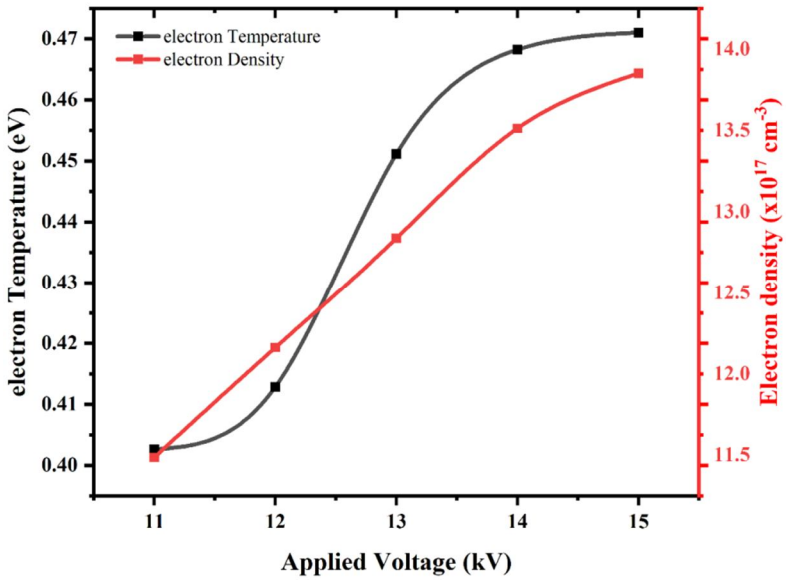

FIG. 6. Electron temperature (T_e) and electron number density (n_e) plot for the nickel metal plasma jet at different applied voltages (11-15 kV) and a constant flow rate of 5 *l/min*. The highest electron temperature (Te = 0.468 eV) and electron number density (n_e=13.851x10^{17} cm^{-3}) were both observed at an appplied voltage of 15 kV.

4. Conclusions

In this research, the results obtained by measuring and studying the plasma parameters of nickel showed a clear discrepancy between electron temperature (T_e) in the plasma and electron number density (n_e) with the gradual increase of applied voltage from 11 to 15 kV during plasma generation. The electron temperature ranged from 0.403 to 0.468 eV, while the electron number density values ranged from 11.486 x 10^{17} to 13.851 x 10^{17} cm^{-3} for the different applied voltages. Many spectral peaks of these emissions were observed as well, including spectral lines for Argon (ArI), (NiI), and (N_2I). The highest intensity for argon gas (ArI) was obtained at a wavelength of 811.53 nm, while the maximum peak for nitrogen gas (N_2I) was found at 336.93 nm. Multiple nickel emission line peaks appeared, ranging from 285.21 to 915.34 nm. According to the results, the rise in spectral emission intensity caused by the passage of argon gas indicates that the number of gas molecules is increasing. This implies that the electrolyte field's energy is

sufficient to induce secondary ionization of molecules, hence ionizing the vast majority of gas particles traveling through the plasma tube. Consequently, this points to a close correlation between the increase in energy and the increase in the values of the measured plasma parameters.

Acknowledgments

I would like to express my gratitude and thanks to the plasma laboratory in the Physics Department, College of Science, University of Baghdad. I would also like to express gratitude to everyone who inspired me to continue on the path of knowledge.

References

[1] Aadim, K.A. and Jassim, R.H., AIP Conference Proceedings, 2372 (2021) 80014.

[2] Khlyustova, A., Labay, C.P., Machala, Z., Ginebra, M.P. and Barnils, C., Front. Chem. Sci. Eng., 13 (2019) 238.

[3] Baniya, H.B., Shrestha, R., Guragain, R.P., Pandey, B.P. and Subedi, D.P., Int. J. Polym. Sci., 2020 (2020) 9247642.

[4] Lu, X., Xiong, Z., Zhao, F., Xian, Y., Xiong, Q., Gong, W., Zou, C., Jiang, Z. and Pan, Y., Appl. Phys. Lett., 95 (2009) 181501.

[5] Adamovich, I., Baalrud, S.D., Bogaerts, A., Bruggeman, P.J. and Cappelli, M., J. Phys. D. Appl. Phys., 50 (2017) 323001.

[6] Suhail, M.H., Adim, K.A. and Wanas, A.H., Br. J. Appl. Sci. Technol., **7** (2015) 263.

[7] Hyde, A. and Batishchev, O., Rev. Sci. Instrum., 91 (2020) 63502.

[8] Akatsuka, H., Adv. Phys. X, 4 (2019) 1592707.

[9] Asenjo-Castillo, J. and Vargas-Blanco, I., Rev. Tecnol. en Marcha., 29 (2016) 47.

[10] Donati, G.L., Amais, R.S. and Williams, C.B., J. Anal. At. Spectrom., 32 (2017) 1283.

[11] Yong, W., Cong, L.I., Jielin, S.H.I., Xingwei, W.U. and Hongbin, D., Plasma Sci. Technol., 19 (2017) 115403.

[12] Chen, Z., Chen, G., Obenchain, R., Zhang, R. and Bai, F., Mater. Today, 54 (2022) 153.

[13] Safeen, A., Shah, W.H., Khan, R., Shakeel, A. and Iqbal, Y., Dig. J. Nanomater. Biostructures, 14 (2019) 29.

[14] Garcia, M.C., Yubero, C. and Rodero, A., Plasma Sources Sci. Technol., 29 (2020) 55006.

[15] Benedikt, J., Kersten, H. and Piel, A., Plasma Sources Sci. Technol., 30 (2021) 33001.

[16] Wu, F., Li, J., Xian, Y., Tan, X. and Lu, X., Plasma Process. Polym., 18 (2021) 2100033.

[17] Aadim, K.A., Iraqi J. Phys., 15 (2018) 117.

[18] Mohammed, R.S., Aadim, K.A. and Ahmed, K.A., AIP Conference Proceedings, 2386 (2022) 80050.

[19] Zaplotnik, R., Primc, G. and Vesel, A., Appl. Sci., 11 (2021) 22.

[20] Michel, A., Jacques, D., Anne, L. and Cédric, D.V., (Springer, 2006) ISBN 978-94-007.

[21] Rodero, A. and Garcia, M.C., J. Qua. Spectroscopy & Rad. Tr., 198 (2017) 93.

[22] Sanghoo, P., Wonho, C., Se, Y.M. and Suk, J.Y., Adv. Phys. X, 4 (2019) 1526114.

Volume 17, Number 3, 2024. pp. 331-340

Jordan Journal of Physics

ARTICLE

First-principles Study on Structural and Electronic Properties: The Li Based of Full-Hesulter Alloys $LiGa_2Ir$

A. Ouahdani, R. Takassa, F. Elfatouaki, O. Farkad, S. Hassine, A. El Mouncharih, O.Choukri, E.A. Ibnouelghazi and **D. Abouelaoualim**

LaMEE, Department of Physics, Faculty of Sciences Semlalia, Cadi Ayyad University, P.O. Box 2390, 40000 Marrakech, Morocco.

Doi: **https://doi.org/10.47011/17.3.8**

Received on: 24/09/2022; *Accepted on: 17/01/2023*

Abstract: Due to their excellent electronic properties, full-Heusler compounds have become one of the most interesting families of alloys in superconductivity. More recently, computational methods have been actively employed to support the rapid discovery of new complete Heusler alloys by identifying stable compositions with desired properties. Therefore, we investigated the stability, structure, and electronic properties of the lithium-based Heusler compound $LiGa_2Ir$ using first-principles calculations. We explored the effects of exchange-correlation, namely Perdew-Burke-Ernzerhof (PBE), PBE+U, and Tran-Blaha modified Becke-Johnson potentials, as well as the effect of heavy metal spin-orbit coupling on these Heusler compounds. The results show that $LiGa_2Ir$ is energetically stable, and the obtained lattice parameter value (a = 6.0927 Å) agrees with the experimental results. $LiGa_2Ir$ exhibits metallic behavior under all three exchange-correlation estimates. A much stronger spin-orbit coupling effect is observed for electronic states with energies below the Fermi level E_F, especially in the Tran-Blaha modified Becke-Johnson approximation. Significant spin-orbit coupling effects are evident from the total and partial density of states figures, especially in the energy range from -4.5 eV to -2 eV. The contributions from Ir-d and Ga-p orbitals are the largest, while the contribution from the Li atom is small. Our findings will benefit future theoretical and practical work on lithium-based full-Heusler alloys.

Keywords: Full-Heusler, DFT, Spin-orbit coupling, Electronic properties, Density of states.

1. Introduction

Heusler alloys have received significant attention due to their attractive physical properties [1] such as interesting magnetic properties [2, 3], high spin polarization [4], spin-gapless semiconducting nature [5], superconductivity [6], diverse optoelectronic [7] and thermoelectric properties [8]. They are considered among the most promising nanomaterials for applications that include thermoelectric materials [9], new spintronic devices [10-13], optoelectronic [14], ferromagnets [15], magnetocaloric materials [16], topological insulators [17], superconductors [6], shape memory alloys [18], and more recently, catalysts [19].

Heusler compounds are among the best intermetallic compounds. They are represented by the general formula X2YZ, XYZ, or XX′YZ, where X, X′, and Y are transition metal atoms and Z is a main group element. Depending on the configuration and number of elements involved, the compounds can be full, half, inverse, semi, or quaternary Heusler alloys. All Heusler compounds crystallize in the L21 cubic

Corresponding Author: D. Abouelaoualim **Email**: dr.abouelaoualim@uca.ac.ma

structure (space group Fm-3m), with four interpenetrating face-centered cubic (fcc) structures [20].

Identifying Heusler materials with interesting physical properties has proven to be a difficult task in scientific research. Among these Heusler compounds, Li-based Heusler materials are gaining increasing attention due to their extraordinary properties and potential applications, particularly in optical and photonic devices, semiconductors for high-efficiency power electronics, and superconductors [14].

Damewood *et al*. investigated the role of Li in half-Heusler LiMnZ (where Z = N, P, Si) in stabilizing and increasing the magnetic moments of half-metals [21]. LiMgBi, LiZnP, LiCdP, and LiAlSi were studied using first-principles density functional calculations by Kandpal *et al*. [22]. This report focused on the examination of band gaps and the nature (covalent or ionic) of bonding in semiconducting half-Heusler compounds [22].

Amudhavalli *et al*. also employed first-principles calculations based on density functional theory to study semiconducting Li-based half-Heusler compounds (LiBeAs, LiBeSb, LiBeBi, and LiScGe) [14]. Their computed electronic structure profile reveals the semiconducting behavior of these materials [14].

Manoj *et al*. studied the thermoelectric properties of Li-based half-Heusler alloys LiYZ (Y = Be, MgZn, Cd and Z = N, P, As, Sb, Bi), showing that all the compounds have larger values of power factors [23].

Weibo Yao *et al*. reported using first-principle predictions of the half-metallic ferrimagnetism in Li-based full-Heusler alloys Mn_2LiZ (Z = Sb, As) with highly ordered structure [24].

The structural, electronic, magnetic, and thermoelectric properties of the new full-Heusler compounds Mn_2LiZ (Z = Si, Ge, and Sn) were investigated by Hadji *et al*., who showed that these compounds exhibit half-metallic ferrimagnetism with a fairly large gap and a low net spin magnetic moment [25].

The superconductivity in $LiGa_2Rh$ was studied experimentally by Carnicom *et al*., and it was demonstrated that the full-Heusler compound $LiGa_2Rh$ is a superconductor with a Tc of 2.4K [26].

Using first-principles calculations, Hadji *et al*. reported the structural, electronic, magnetic, and electronic transport properties of new Heusler compounds Mn_2LiZ with Z = Al and Ga [27]. Their findings from the band structure calculations indicated that the Mn_2LiAl compound is a spin-gapless semiconductor and Mn_2LiGa is a nearly spin-semimetal [27].

More recently, Karolina *et al*. studied experimentally and theoretically the superconductivity in the $LiGa_2Ir$ Heusler-type compound. Their measurements indicated a bulk superconductivity with a Tc of 2.94K. Through first-principles calculations, they examined the electron-phonon interaction and the SOC effect on the electronic structure. The phonon dispersion curve showed the dynamical stability of the compound, while the electronic bands and DOS curves indicated a small effect of SOC near the Fermi energy (E_F).

The efficiency and accuracy of DFT are given by the best choice of exchange-correlation (XC) functionals. In the present work, we applied DFT calculations to study the Heusler-type compound $LiGa_2Ir$ with different XC functionals, namely Perdew-Burke-Ernzerhof (GGA-PBE), the Tran-Blaha modified Becke-Johnson (TBmBJ) exchange potential, and the generalized gradient approximation developed by PBE with Coulomb Potential (PBE + U). These functionals have been found to perform better in calculating the structural and electronic properties of several Heusler-type compounds, although they have not been applied previously to $LiGa_2Ir$ examined in the present paper.

We carried out systematic calculations using these XC functionals, combined with SOC effects, to analyze the thermodynamic stability, as well as structural and electronic properties of the $LiGa_2Ir$ Heusler-type compound. This work is structured as follows. Section 2 describes how to calculate. Section 3 presents the results and the discussion on stability, structural properties, and the effects of XC and SOC on the electronic band structure, along with total and partial density of states (DOS and PDOS) profiles. Finally, Section 4 presents the conclusion.

2. Computational Method

We performed calculations in the context of density functional theory (DFT) using the full-potential linearized enhanced plane wave method

(FP-LAPW) implemented in the Wien2k code [28] to characterize the structural and electrical features of the $LiGa_2Ir$ Heusler compound. To approximate the XC energy function, we added the PBE form to the GGA, the exchange potential TB-mBJ, and the Coulomb potential to be used (PBE + U). The Hubbard effective potential U_{eff} = U - J (where U represents the Coulomb interaction and J expresses the exchange interaction for both Ir and Ga atoms) was used for strongly d- or f-correlated electrons [29]. In this work, we used an effective U_{eff} = 1.6 eV on the Ir atom site (strongly 5d correlated electrons), computed using the constrained random-phase approximation (cRPA) [30], which yields a very good account of the ground-state electronic and magnetic properties [31-33]. For different approximations of the XC, we performed the calculations in the presence and absence of SOC.

The $LiGa_2Ir$ compound consists of three atoms with electronic valence configurations as follows: Ir ($4f^{14}$, $5d^7$, $6s^2$), Ga ($4s^2$, $3d^{10}$, $4p^1$), and Li ($2s^1$). The cutoff energy separating the core and valence states was set at -6 Ry. The muffin-tin (MT) radii used for Li, Ga, and Ir were 2, 2.24, and 2.47 a.u, respectively. The crystal structure was relaxed until the force on each atom converged to less than 0.01 Ry/u.a. We expanded the basis function to $R_{MT}xK_{max} = 7$, where R_{MT} is the minimum radius of the atomic sphere and K_{max} is the largest k-vector in the plane wave expansion. The charge density of the Fourier expansion was truncated at $G_{max}= 12R_y^{1/2}$. The maximum angular momentum of the atomic orbital basis functions was set to l_{max} = 10. The total number of k-points in the first Brillouin zone (BZ) was determined to equal 1000. The iteration process was stopped when the total energy convergence threshold of 0,0001 R_Y was reached.

3. Numerical Results and Discussion

3.1. Structural Properties and Stability

The compound $LiGa_2Ir$ crystallizes in a face-centered cubic structure with space group Fm-3m (No. 225). It has the formula unit in the primitive Bravais cell, with atoms occupying the following Wyckoff positions: Li at (4b) (1/2, 1/2, 1/2), Ga (8c) (1/4, 1/4, 1/4), and Ir (4a) (0,0,0). The crystal structure of $LiGa_2Ir$ is shown in Fig. 1. The unit cell volume of $LiGa_2Ir$ has been optimized.

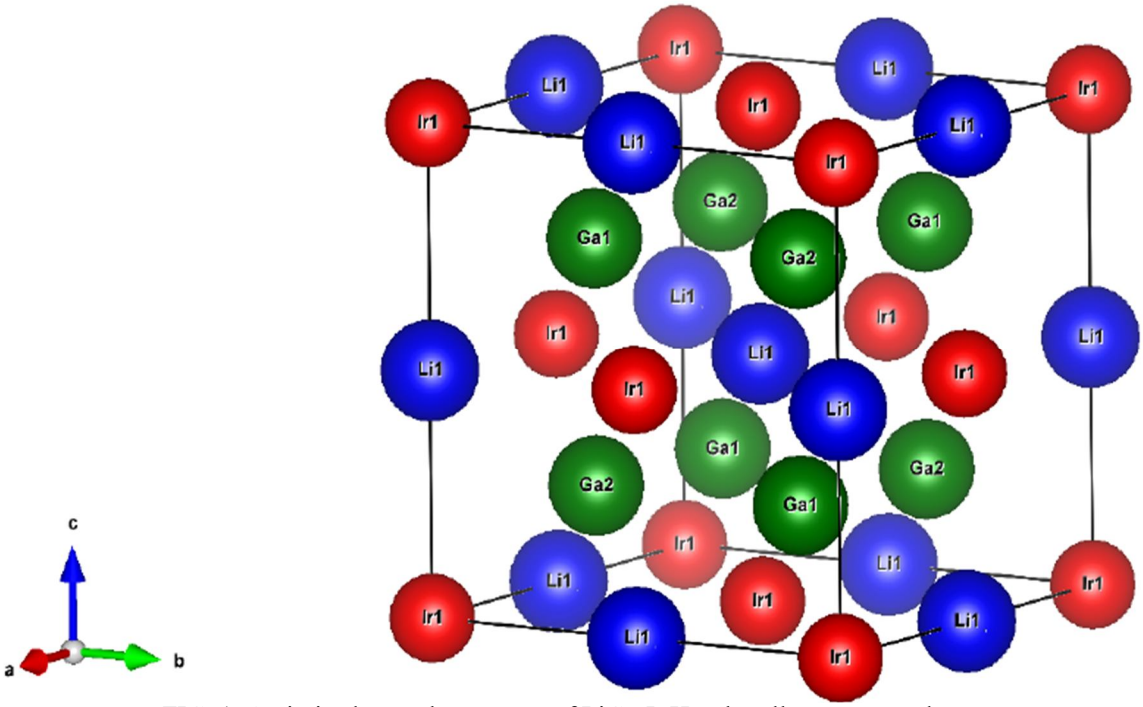

FIG. 1. Optimized crystal structures of $LiGa_2Ir$ Heusler alloy compounds.

To assess the stability and ground-state properties of the $LiGa_2Ir$ structure, we plotted the variation in unit cell volume as a function of total energy using the Murnaghan equation of state [35], given by:

1. Ref. [34] Experimental value.
2. Ref. [34] GGA-PBEsol without SOC.
3. Ref. [34] GGA-PBEsol with SOC.
4. Ref. [26] Other theoretical methods.

$$E(V) = E_0 + \left[\frac{B_0 V}{B_0'}\left(\frac{(V_0/V)^{B_0'}}{B_0'-1}+1\right) - \frac{B_0 V}{B_0'-1}\right]\frac{1}{14703.6} \quad (1)\ (1)$$

where E_0 is the minimum energy at 0 K, V is the unit cell volume, V_0 is the unit cell volume at P = 0 GPa, B_0 is the bulk modulus, and B_0' is the pressure derivative of the bulk modulus.

The total energy (E) versus volume (V) for the $LiGa_2Ir$ structure is plotted in Fig. 2. The equilibrium geometry is established by minimizing the energy E(V) as a function of volume using the GGA-PBE approximations, where the optimized volume is the volume corresponding to the minimum of the E(V) curve. On the other hand, the ground-state energy of the unit cell, corresponding to the optimized lattice parameter, is the energy obtained as the minimum energy. Table 1 shows the estimated ground-state parameters, with a lattice constant value of a = 6.0927Å, which is in good agreement with previous theoretical and experimental data [34]. In addition, the table shows the results of another Li-based full-Heusler compound, $LiGa_2Rh$, indicating that the lattice constant of $LiGa_2Rh$ is a little lower than that of $LiGa_2Ir$, which may be due to the larger size of Ir atoms compared to Rh.

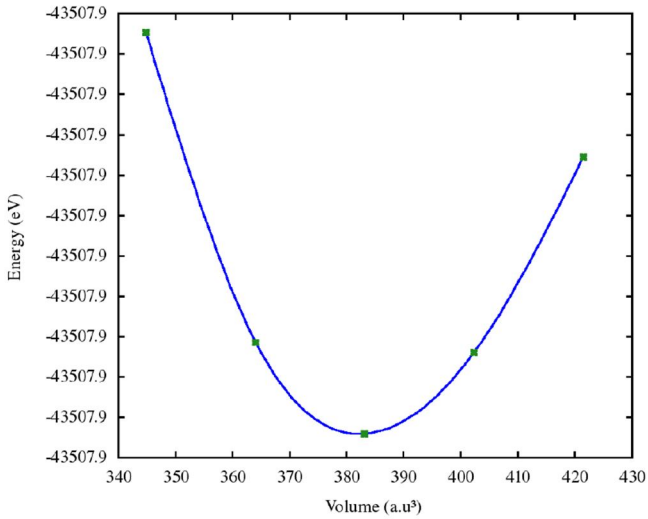

FIG. 2. Optimized energy-volume curves of $LiGa_2Ir$ Heusler alloy compounds under the PBE-GGA exchange-correlation function.

TABLE 1. The calculated values of lattice constant (a), unit cell volume at P = 0 GP_a (V_0), bulk modulus (B_0), pressure derivative of bulk modulus (B_0'), minimum total energy (E_0), and band gap (E_g) for $LiGa_2Ir$ Heusler alloy compound.

	V_{xc}	a (Å)	V_0 (Å^3)	B_0 (GPa)	B_0' (GPa)	E_0 (Ry)	E_g (eV)
$LiGa_2Ir$ (This work)	PBE	6.0927	381.57	123.191	5.2317	-43507.937	0
	PBE+ SOC						0
	PBE+U						0
	PBE+U +SOC						0
	TB-mBJ						0
	TB-mBJ+ SOC						0
	Other	6.0322 [1]	-	-	-	-	0 [2]
		6.0161 [2]	-	-	-	-	0 [3]
		6.0164 [3]	-	-	-	-	
$LiGa_2Rh$		5.9997 [4]	215.97 [4]				0 [4]

To investigate the stability and the possibility of synthesis of the $LiGa_2Ir$ compound, we calculated the formation energy using Eq. (2) [36, 37]:

$$E_f = \frac{E_{tot}(LiGa_2Ir) - \mu_{Li} - 2\mu_{Ga} - \mu_{Ir}}{4} \quad (2)$$

where $E_{tot}(LiGa_2Ir)$ is the total energy of the $LiGa_2Ir$ compound, while μ_{Li}, μ_{Ga}, and μ_{Ir} are the chemical potentials for Li, Ga, and Ir atoms, respectively. These chemical potentials are calculated as the total energy per atom of the most stable structure of the elements. The bulk forms of these atoms are considered the most stable structures. A negative calculated formation energy (E_f = -0.65 eV) indicates that the $LiGa_2Ir$ compound is structurally stable and experimentally synthesizable [38, 39, 11].

3.2. Electronic properties

3.2.1 Exchange-correlation Effects on the Electronic Band Structure

The generalized gradient approximation PBE and PBE+U are used to treat the potential exchange-correlation function, where U is the Hubbard site [40]. A Coulomb interaction correction of U = 0.50 eV was employed in this work for transition metal Ir. Due to the confined 3d or 4f orbitals of transition metal atom Ir in Heuslers, the GGA+U method on Coulomb repulsion may provide important benefits.

Additionally, we used the TB-mBJ approximation, where the combination coefficient is set in the mBJ potential according to the electron density distribution of each system under study (mBJ) [41]. The mBJ, which is a part of the Kohn-Sham (KS) DFT, is a semilocal technique with a low computational cost that can create KS band gaps that are more consistent with experimental bands than conventional GGA functionals [41, 42].

This section contains the calculation of the band structure of the $LiGa_2Ir$ compound along the highly symmetrical directions of the first Brillouin zone, specifically the *W-L-Γ-X-W-K* path, as shown in Fig. 3. In addition, we detail how the band structure and band gap are affected by the XC functionals and the SOC effect.

Using PBE, PBE+U, and TB-mBJ, we notice that all three approaches exhibit similar behavior. For the most part, a few valence bands touching the Fermi level can be seen clearly lying to a metallic.

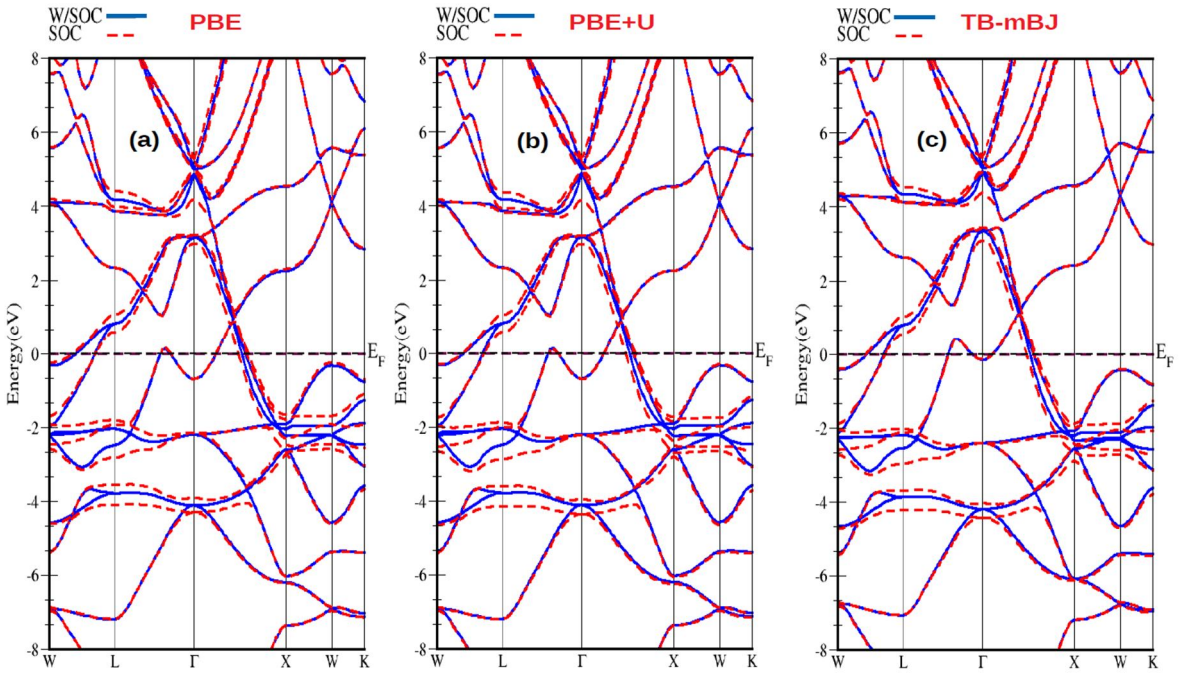

FIG. 3. Calculated band structures without (blue lines) and with (red lines) SOC for *$LiGa_2Ir$* using PBE, PBE + U, and TB-mBJ XC approximations.

In Fig. 3(a), we present the calculated band structure with GGA-PBE approximation, which denotes metallic character in the region where the Fermi level crosses the energy valence bands. Although U is used, the electronic band structure of PBE+U is still quite similar to those of PBE, as seen in Fig. 3(b). However, the band structures under TB-mBJ, depicted in Fig.3(c),

are slightly different. We may observe that the bands separate along the X direction, especially at energies below 7 eV, while the bands move toward one another along the G direction in the conduction band. The mBJ causes the valence bands to shift upward, placing the Ef within the valence band. Under all three XC estimates, *$LiGa_2Ir$* exhibited metallic behavior.

3.2.2 SOC Effects on the Band Structure

The spin-orbit coupling (SOC) effect plays a crucial role in compounds containing heavy elements like Iridium (Ir), as it significantly impacts the electronic properties. SOC increases the kinetic energy of electrons and the relativistic effects become very important. Furthermore, SOC interactions were taken into account in this study to enhance the XC approximation calculations of our material [43].

To better understand the application of first-principles approaches, we need to clarify the physical basis for the observed behavior of $LiGa_2Ir$. The band structures of $LiGa_2Ir$ obtained by PBE, PBE+U, and TB-mBJ with and without SOC are plotted with blue and red lines, respectively, and are shown in Fig. 3. The lower and upper part of the valence band consists of the Ir-5d, Ga-4s, and Ga-4p states (about 10 eV), while the lower part of the conduction band consists of Ga-4s and I-p states. The contribution from Li is negligible, as detailed in the DOS section. From the band structure obtained by the TB-mBJ method, it can be seen that the Ir-5d states move to higher energy levels, and a blurring along VB leads to passing the Fermi level. The Fermi level was set as 0 eV. The constituent atoms of the compound are not particularly heavy, so spin-orbit coupling has no visible effect on the electronic states near the Fermi level [42]. However, for electronic states with energies below Ef, we observe much stronger SOC effects, such as band anticrossing in the W-Γ direction. Therefore, upon further analysis, three bands cross the Fermi level. So, it is clear that most of the bands in the XC approximation used in this study are metallic.

All atomic sites in the cubic structure of $LiGa_2Ir$ have T_d symmetry, which causes the crystal field to split the d-orbitals of Ir atoms into degenerate double and triple orbitals, E(dx2-y2, dz2) and T2 (dxy, dyz, dzx), respectively [44-46]. The p-orbitals reside in the T2 state, resulting in a triplet which the SOC then produces. This is the nearest neighbor for our structures, and the d-states with the same T2 or E symmetry hybridize with each other.

The SOC in the X-W-K direction has no significant impact on the degeneracy of the CBM bands. The point-occupied state is VBM, which is a degenerate triplet (T2) in the absence of SOC, as shown in Fig.3. XC and SOC have a similar effect for each of the three estimates. The states with the highest and lowest occupancy rates are adjusted up and down to maintain balance. However, the most and least occupied states are moved up and down for W-L-Γ-X, respectively. In the following subsection, we will delve into the details of our findings by combining the total and partial density of states (DOS and PDOS) computations.

3.2.3 Density of States (DOS) Profile

In order to understand the contributions of Ir, Ga, and Li atoms to the formation of the valence band (VB) and conduction band (CB) energies for the $LiGa_2Ir$ compound, as well as the possible hybridization and interactions between these atoms, we performed total and partial density of states (TDOS and PDOS, respectively) calculation. Figures 4 and 5 summarize the calculated TDOS and PDOS, respectively, of LiGa2 Ir structure with the presence and absence of SOC effect in the energy range between -11 eV and 7 eV with different XC approximations: PBE, PBE+U, and TB-mBJ. The Fermi level separates the VB from CB and is set at 0.0eV. The results show that the choice of XC approximation does not significantly affect the TDOS and PDOS profiles. However, significant SOC effects are seen in the TDOS profile at the energy range -4.5 eV to -2 eV, which may be due to relativistic effects, which play an important role in the accurate description of the electronic properties of compounds. The SOC effect corrects the total energy, thereby enhancing our understanding of the various characteristics of the compound. This effect becomes particularly pronounced when the inner shell electrons of heavy atoms, such as Ir, are close to the nucleus. Thus, the relativistic effects become crucial in this case because the SOC effect may enhance the kinetic energy of electrons [47, 48].

As can be seen from the TDOS graphs in Figs. 4(a)-4(c), in all XC approximations with and without SOC effects the $LiGa_2Ir$ compound has a metallic behavior confirming the results found in the band structure profile. We can

understand the TDOS and PDOS profiles between the region -11 eV to 7 eV by dividing this interval into three different regions: the first region from -11 eV to -5 eV, the second region from -5 eV to 1 eV, and the third region from 1 eV to 7.0 eV.

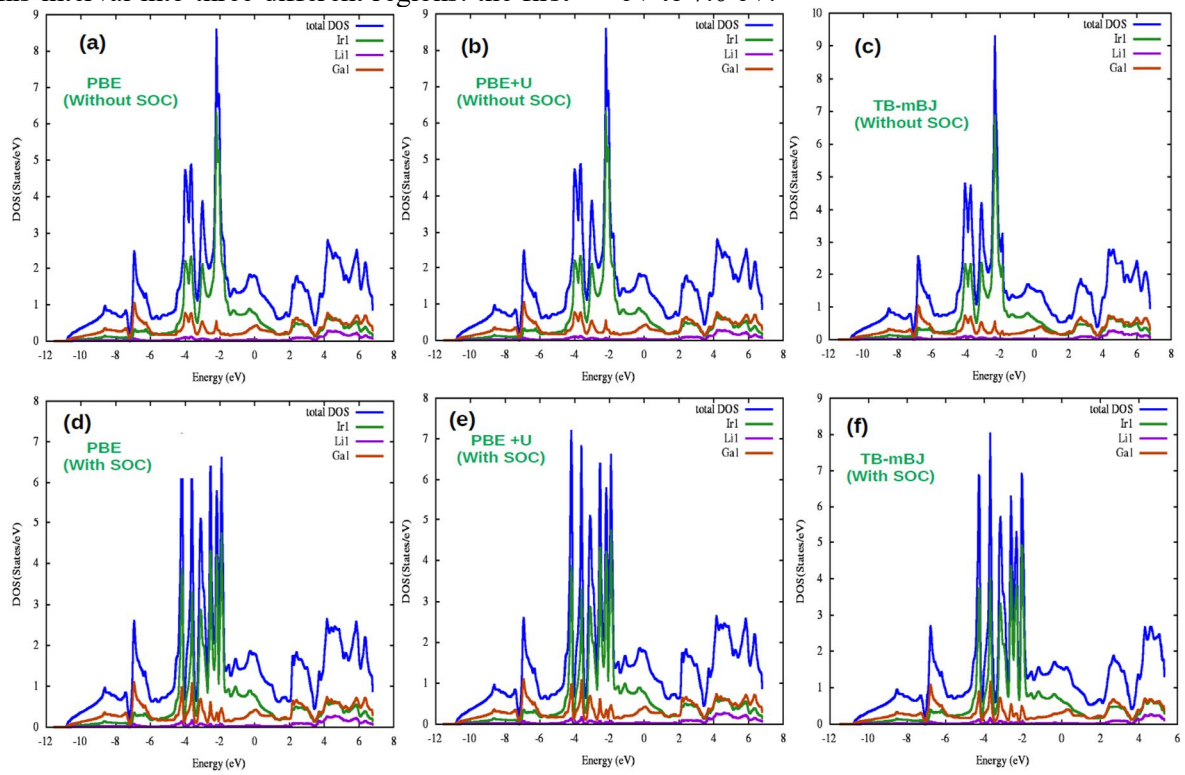

FIG. 4. Total DOS without SOC and with SOC for *$LiGa_2Ir$* using PBE, PBE+U, and TB-mBJ XC approximations.

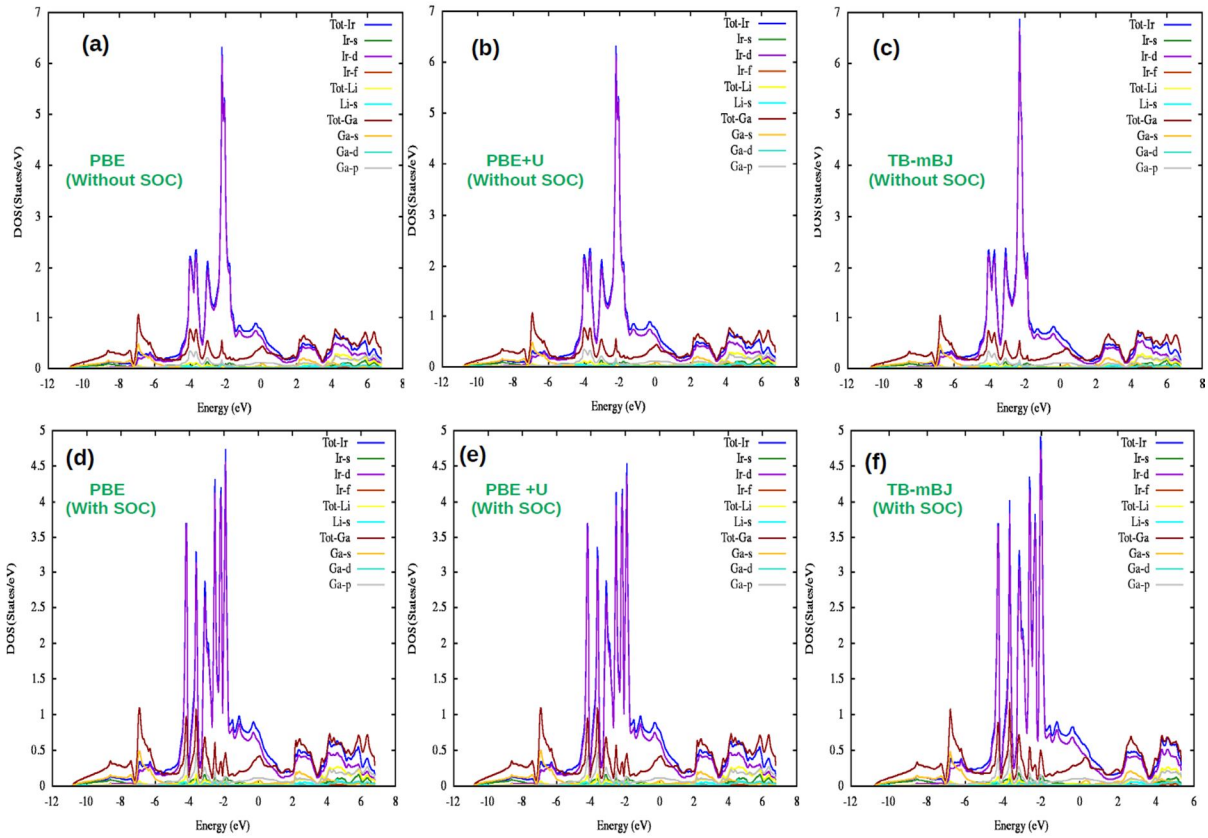

FIG. 5. Partial DOS without SOC and with SOC for *$LiGa_2Ir$* using PBE, PBE+U, and TB-mBJ XC approximations.

In the first region, deep inside the VB, across all XC approximations with and without SOC, it can be observed that the Ga atom (more precisely the Ga-s orbitals) predominantly contributes to the TDOS of the $LiGa_2Ir$ compound, with minimal contributions due to the Ir and Li atoms in this region.

In the second region (from -5 to 1 eV), strong peaks appeared clearly in the case of all XC approximations with and without SOC effect. The SOC effect is particularly noticeable here, especially with the TBmBJ approximation, as shown in Figs. 4(c), 4(f), 5(c), and 5(f), where there is an increase in the maximum values of the observed peaks. This region's maximum and high contribution comes from Ir-d orbitals for all XC approximations. There is also a smaller contribution from the Ga-p orbitals, suggesting that the hybridization between Ir-d and Ga-p orbitals is responsible for the observed TDOS profile, indicating strong interactions between these atoms. In contrast, the PDOS of the Li atom shows a weak contribution of Li orbitals.

In the CB's third region (from 1 eV to 7 eV), the TDOS and PDOS profiles change significantly, with a noticeable decrease in the intensity of the peaks compared to the second region in all cases of XC approximations with and without SOC. It can be observed that the major contribution is due to Ir and Ga atoms. The electronic states of Ir-d and Ga-p orbitals hybridize and contribute significantly to the TDOS profile in this region, indicating strong interactions between these atoms within the CB. The contribution from the Li atoms in the CB remains minimal.

4. Conclusion

In this work, the Li-based Heusler alloy $LiGa_2Ir$ was investigated using different XC in DFT calculations, both with and without the SOC effects. The stability, structural, and electronic properties were studied. The structure was found to be energetically stable, with a lattice parameter of a = 6.0927Å, which aligns well with experimental results. The electronic band structure and the DOS profile indicated a metallic behavior of $LiGa_2Ir$.

The results showed no significant differences between all XC approximations. However, it was observed that the SOC effects are much stronger for electronic states within the valence band (VB) at energies lower than the Fermi level (E_F), especially in the energy range of -4.5 eV to -2 eV. Understanding the $LiGa_2Ir$ and Heusler compounds' bonding structure was made possible by the PDOS profile. The findings revealed that Ir and Ga atoms make a significant impact, while Li atoms make a weaker contribution. This indicates a strong interaction between Ir and Ga atoms and their responsibility for the electronic behavior of the LiGa2 Ir compound.

Our findings suggest that the Li-based Heusler compound $LiGa_2Ir$ holds promise for further theoretical and experimental studies, particularly for applications in electronic devices such as metallic interconnectors.

References

[1] Graf, T., Felser, C., and Parkin, S.S., Prog. Solid State Chem., 39 (1) (2011) 1.

[2] Heusler, F., Starck, W., and Haupt, E., Verh. Dtsch. Phys. Ges, 5 (1903) 219.

[3] Belasri, A., Rached, D., Rached, H., Bourachid, I., Guermit, Y., and Caid, M., Eur. Phys. J. B, 94 (5) (2021) 1.

[4] Bainsla, L., Suresh, K., Nigam, A., Manivel Raja, M., Varaprasad, B.C.S., Takahashi, Y., and Hono, K., J. Appl. Phys., 116 (20) (2014) 203902.

[5] Wang, X., Cheng, Z., Wang, J., Wang, X.-L., and Liu, G., J. Mater. Chem. C, 4 (30) (2016) 7176.

[6] Klimczuk, T. et al., Phys. Rev. B, 85 (17) (2012) 174505.

[7] Guezmir, A., Rached, H., Bentouaf, A., Caid, M., Benkhettou, N., Rached, D., and Sidoumou, M., Comput. Condens. Matter, 28 (2021) e00573.

[8] Guermit, Y., Caid, M., Rached, D., Drief, M., Rekab-Djabri, H., Lantri, T., Rached, H., and Benkhettou, N., Int. J. Thermophys., 42 (6) (2021) 1.

[9] Huang, L., Zhang, Q., Yuan, B., Lai, X., Yan, X., and Ren, Z., Mater. Res. Bull., 76 (2016) 107.

[10] Elphick, K., Frost, W., Samiepour, M., Kubota, T., Takanashi, K., Sukegawa, H., Mitani, S., and Hirohata, A., Sci. Technol. Adv. Mater., 22 (1) (2021) 235.

[11] Cherif, H.S., Bentouaf, A., Bouyakoub, Z., Rached, H., and AÃ´rssa, B., J. Alloys Compd., 894 (2022) 162503.

[12] Berrahal, M., Bentouaf, A., Rached, H., Mebsout, R., and Aissa, B., Mater. Sci. Semicond. Process., 134 (2021) 106047.

[13] Bourachid, I., Rached, D., Rached, H., Bentouaf, A., Rached, Y., Caid, M., and Abidri, B., Appl. Phys. A, 128 (6) (2022) 1.

[14] Amudhavalli, A., Rajeswarapalanichamy, R., Iyakutti, K., and Kushwaha, A., Comput. Condens. Matter, 14 (2018) 55.

[15] Wang, C., Meyer, J., Teichert, N., Auge, A., Rausch, E., Balke, B., Hütten, A., Fecher, G.H., and Felser, C., J. Vac. Sci. Technol. B, 32 (2) (2014) 020802.

[16] Gottschall, T., Skokov, K.P., Benke, D., Gruner, M.E., and Gutfleisch, O., Phys. Rev. B, 93 (18) (2016) 184431.

[17] Yan, B. and de Visser, A., MRS Bull., 39 (10) (2014) 859.

[18] Bachaga, T., Zhang, J., Khitouni, M., and Sunol, J., Int. J. Adv. Manuf. Technol., 103 (5) (2019) 2761.

[19] Kojima, T., Kameoka, S., and Tsai, A.-P., Sci. Technol. Adv. Mater., 20 (1) (2019) 445.

[20] Benaisti, I., Guechi, N., Dehbaoui, M., and Boukaoud, A., preprint, Res. Sq., https://doi.org/10.21203/rs.3.rs-215061/v1.

[21] Damewood, L., Busemeyer, B., Shaughnessy, M., Fong, C., Yang, L., and Felser, C., Phys. Rev. B, 91 (6) (2015) 064409.

[22] Kandpal, H.C., Felser, C., and Seshadri, R., J. Phys. D: Appl. Phys., 39 (5) (2006) 776.

[23] Yadav, M.K. and Sanyal, B., J. Alloys Compd., 622 (2015) 388.

[24] Yao, W., Zhou, J., Zeng, D., Wan, H., Ruan, W., Liu, L., and Wen, Y., J. Magn. Magn. Mater., 503 (2020) 166642.

[25] Hadji, T., Khalfoun, H., Rached, H., and Azzouz-Rached, A., Comput. Condens. Matter, 27 (2021) e00557.

[26] Carnicom, E.M., Xie, W., Yang, Z., Górnicka, K., Kong, T., Klimczuk, T., and Cava, R.J., Chem. Mater., 31 (6) (2019) 2164.

[27] Hadji, T., Khalfoun, H., Rached, H., and Azzouz-Rached, A., Mater. Res. Bull., 143 (2021) 111461.

[28] Schwarz, K., Blaha, P., and Madsen, G.K., Comput. Phys. Commun., 147 (1-2) (2002) 71.

[29] Kandpal, H.C., Fecher, G.H., and Felser, C., J. Phys. D: Appl. Phys., 40 (6) (2007) 1507.

[30] Nakamura, K., Arita, R., Yoshimoto, Y., and Tsuneyuki, S., Phys. Rev. B, 74 (23) (2006) 235113.

[31] Liu, P., Khmelevskyi, S., Kim, B., Marsman, M., Li, D., Chen, X.-Q., Sarma, D., Kresse, G., and Franchini, C., arXiv preprint arXiv:1503.06753.

[32] Antonov, V., Bekenov, L., and Kukusta, D., Phys. Rev. B, 102 (19) (2020) 195134.

[33] Mazin, I., Jeschke, H.O., Foyevtsova, K., Valentí, R., and Khomskii, D., Phys. Rev. Lett., 109 (19) (2012) 197201.

[34] Górnicka, K., Kuderowicz, G., Winiarski, M.J., Wiendlocha, B., and Klimczuk, T., Sci. Rep., 11 (1) (2021) 1.

[35] Murnaghan, F.D., Proc. Natl. Acad. Sci. U.S.A., 30 (9) (1944) 244.

[36] Rached, H., Int. J. Quantum Chem., 121 (12) (2021) e26647.

[37] Elahmar, M.H., Rached, H., and Rached, D., Materials Chemistry and Physics 267 (2021) 124712.; Anisimov, V.I., Zaanen, J. and Andersen, O.K., Phys. Rev. B, 44 (1991) 943.

[38] Abada, A. and Marbouh, N., J. Supercond. Nov. Magn., 33 (3) (2020) 889.

[39] Dehghan, A. and Davatolhagh, S., J. Alloys Compd., 772 (2019) 132.

[40] Lone, I.U.N., Sirajuddeen, M., Khalid, S., and Raza, H.H., J. Supercond. Nov. Magn., 34 (5) (2021) 1523.

[41] Hadji, T., Khalfoun, H., Rached, H., Guermit, Y., Azzouz-Rached, A., and Rached, D., Eur. Phys. J. B, 93 (11) (2020) 1.

[42] Haid, S., Benstaali, W., Abbad, A., Bouadjemi, B., Bentata, S., and Aziz, Z., Mater. Sci. Eng. B, 245 (2019) 68.

[43] Kumar, A. et al., Optik, 249 (2022) 168250.

[44] Ahmadian, F., J. Alloys Compd., 576 (2013) 279.

[45] Rasool, M.N., Hussain, A., Javed, A., Khan, M.A., and Iqbal, F., Mater. Chem. Phys., 183 (2016) 524.

[46] Khandy, S.A. and Chai, J.-D., J. Magn. Magn. Mater., 487 (2019) 165289.

[47] Mellah, D.E. and Demmouche, K., Comput. Condens. Matter, 32 (2022) e00690.

[48] Verstraete, M.J., Torrent, M., Jollet, F.M.C., Zérah, G., and Gonze, X., Phys. Rev. B, 78 (2008) 045119.

Volume 17, Number 3, 2024. pp. 341-348

Jordan Journal of Physics

ARTICLE

Indicators of Radioactive Contamination by Radionuclides for Samples of Plant Fertilizers and Pesticides

Entesser F. Salman[a], **Azhar S. Alaboodi**[b], **Ali A. Abojassim**[b] and **Hussien A. A. B. Mraity**[b]

[a] *Department of physics, Faculty of Basic Education, University of Babylon, Iraq.*
[b] *Department of physics, Faculty of Science, University of Kufa, Najaf, Iraq.*

Doi: **https://doi.org/10.47011/17.3.9**
Received on: 01/11/2022; *Accepted on: 05/02/2023*

Abstract: This study aims to evaluate the radiation levels resulting from plant fertilizers and pesticides in Babylon City, Iraq. The specific activity of the studied radionuclides (e.g. ^{238}U, ^{232}Th, and ^{40}K) was identified using the spectroscopy approach of the sodium-activated iodide thallium (NaI (Tl)) with dimensions of 3" × 3". The resulting data revealed that the specific activities for the aforementioned nuclides were 6.254 Bq/kg, 4.3694 Bq/kg, and 112.751 Bq/kg, respectively. The results indicated that the average radiation hazard metrics for fertilizers (i.e., gamma index, alpha index, absorbed dose rate, ambient dose equivalent rate, annual gonadal dose equivalent, and excess lifetime cancer risk) were lower than the reference levels.

Keywords: Radiation hazard, Fertilizer, Pesticides, Risk parameters, Gamma activity.

1. Introduction

Soil is considered to be one of the key elements of the environment. This is because it is a medium that provides humans with food resources. However, when soil becomes contaminated, it can lead to long-term environmental pollution, affecting food, water, and air. Using phosphate-based fertilizers, which are expected to involve high levels of radiation in the surrounding environment, is the most important human activity that causes radiological exposure [1]. Natural radiological elements are known to be widely spread out in the environment and constitute the main source of human radiation exposure. In this regard, the agricultural activity of human affects the radioactivity in soil [2].

The Earth has harbored radioactive elements since its formation, many of which have decayed over time. Considering what remains to this day of the aforementioned radionuclides of terrestrial origin, they have a lifespan that is greater than the age of the Earth. These are known by the series of ^{238}U, ^{235}U, and ^{232}Th, as well as potassium ^{40}K [3]. Humans and other living organisms are expected to be subjected to radiation on a regular basis from both natural and anthropogenic sources [4].

Soil pollution depends on the movement of radioactive materials and their accumulation or transmission, which are governed by the interaction of the materials and compounds with the hard part of the soil. The soil's physical, chemical, and biological characteristics affect how well it can bury radioactive contaminants. Moreover, the amount and type of radionuclides movement are determined by soil management practices, the types of cultivated plants, rainfall rates, and the amount of irrigation water used [5, 6]. In this context, fertilizers are very important since they enrich the agricultural soil with

Corresponding Author: Ali Abid Abojassim **Email**: ali.alhameedawi@uokufa.edu.iq

essential elements such as potassium, nitrogen, and phosphorous, which are often depleted due to repeated cultivation. Phosphate fertilizers are valuable because of their phosphorous content, a key element for plant growth.

However, phosphate fertilizers are also a source of concern because they often contain uranium, a naturally occurring radioactive element that is geochemically associated with phosphate wherever it is found. The excessive use of fertilizers has been shown, through many investigations, to increase the levels of nuclides in the soil and even in groundwater. These nuclides can then enter the human body via the intake of contaminated drinking water and food [6].

In order to establish a database on the radioactivity level to be later used as a reference point for radiological accidents, a large number of studies have been undertaken to measure radioactivity. One such study was conducted in the northern regions of Sudan [7]. In this work, the dose ranged from 44 to 53 nGy, while the annually effective dose ranged from 53 to 65 μSv y^{-1}. The average absorbed dose in eastern Sudan ranged from 24 to 48, with an average of 38 nGy h^{-1}. Central Sudan showed air-absorbed dose measurements at a height of 1 m ranging from 31 to 47 nGy h^{-1}, and the effective annual dose was between 6 and 47.8 Sv y^{-1}. In western Sudan, the absorbed dose ranged from 500 to 7000 nGy h^{-1} [8]. Through the latter studies, it was found that agricultural awareness among the farmers in these regions is generally low. However, there is a potential for improvement in agricultural practices by using natural animal fertilizers instead of chemical fertilizers and adopting modern irrigation systems that are more compatible with the requirements of crops [9]. These measures could help preserve agricultural products and reduce the environmental risks posed by radioactive contamination.

The aim of this study is to evaluate the natural radioactivity levels of ^{238}U, ^{232}Th, and ^{40}K in samples of plant fertilizers available in Babylon City, Iraq, using gamma-ray spectroscopy with NaI (Tl). Additionally, the radiological hazard risks are calculated in all samples of the present study.

2. Materials and Methods

2.1 Preparation of the Study Samples

Various types of fertilizers and pesticides utilized in the soils of agricultural land were gathered from local markets in Iraq. Table 1 provides an overview of the different fertilizers considered in this study, including the country of origin and the fundamental elements of each type.

The fertilizer and pesticide samples were crushed in a grain mill to convert them into a fine powder and then sieved using a single-hole sieve with a diameter of 2 mm. These samples were then left to dry for one day at ambient temperature to obtain a steady weight. After drying, each sample weighed 700 grams.

The dried samples were put in cylindrical plastic containers, chosen to fit the detector container. The containers were sealed tightly and stored for 30 days to allow the radium and its decay products to reach equilibrium. After this period, the samples were ready for gamma radiation spectroscopic analysis.

2.2 Measuring System

The technique of gamma-ray spectroscopy based on the activated sodium iodide detector NaI(Tl) whose dimensions are 3"x3" was employed to identify the concentration levels of ^{238}U, ^{232}Th, and ^{40}K in all fertilizer and pesticide samples. The scintillation detector operates at a voltage of 778 V, with an efficiency limit of around 95%, and the detector's energy resolution ranges between 6.5% and 8.5%. The detector base is supported by a lead shield to minimize background radiation. The analysis of the resulting gamma-ray spectra was done using the laboratory's newly developed Maestro-32 software.

2.3 Theoretical equations

The specific activity (in Bq/kg) of the radionuclides investigated in this work was computed as follows [14-16]:

$$A\left(\frac{Bq}{kg}\right) = \frac{N}{t*\varepsilon*I_\gamma*m} \pm \frac{\sqrt{N}}{t*\varepsilon*I_\gamma*m} \quad (1)$$

where N refers to the count under the photopeak, t is the counting time (in seconds), Iγ refers to the probability of absolute transition gamma emission, m refers to the net sample mass (kg), and ε represents the detectors' efficiency for a specific gamma energy.

The absorbed dose rate (AD_γ) for external gamma dose irradiation in the air at a distance of 1 m above the ground surface, due to ^{238}U, ^{232}Th, and ^{40}K, was calculated using the equation [17]:

$$AD_{out}\left(\frac{nGy}{h}\right) = DCF_U\ A_U + DCF_{Th}\ A_{Th} + DCF_K\ A_K \quad (2)$$

where DCF_U, DCF_{Th}, and DCF_K refer to the absorbed dose rate conversion factors for ^{232}Th, ^{238}U, and ^{40}K, respectively, (in nGy/h), while A_{Th}, A_K, and A_U are the activity concentrations of ^{232}Th, ^{40}K, and ^{238}U, respectively. The $DCF_k = 0.0417$ nGy/h/Bq/kg, $DCF_U = 0.462$ nGy/h/Bq/kg, and $DCF_{Th} = 0.604$ nGy/h/Bq/kg. The γ-ray dose (Din) from ^{238}U, ^{232}Th, and ^{40}K indoors was calculated using the equation [18]:

$$AD_{in}\left(\frac{nGy}{h}\right) = 0.92\ A_U + 1.1\ A_{Th} + 0.081\ A_K \quad (3)$$

The annual effective dose comes in two different forms, namely the annual indoor effective dose rate and the annual outdoor effective dose rate (AEDEout) (AEDEin). The following equations were used to determine the AEDEout and AEDEin. [19, 20]:

$$AEDE = \text{Absorbed Dose Rates}\ (AD\gamma) * 0.7 * 8760 * 0.2 \quad (4)$$

$$AEDE_{outdor} = \left[AD_{out}\left(\frac{nGy}{h}\right) * 8760\left(\frac{h}{y}\right) * 0.2 * 0.7\left(\frac{10^3 mSv}{10^9 nGy}\right)\right] \quad (5)$$

$$AEDE_{outdor} = AD_{out} * 1.2264 * 10^{-3}\left(\frac{mSv}{y}\right) \quad (6)$$

$$AEDE_{indoor} = \left[AD_{in}\left(\frac{nGy}{h}\right) * 8760\left(\frac{h}{y}\right) * 0.8 * 0.7\left(\frac{10^3 mSv}{10^9 nGy}\right)\right] \quad (7)$$

$$AEDE_{indoor} = AD_{in} * 4.9056 * 10^{-3}\left(\frac{mSv}{y}\right) \quad (8)$$

The total dose from internal and external effects was calculated by summing the $AEDE_{indoor}$ and $AEDE_{outdoor}$.

It is used to compute the sum of the activities of each of ^{232}Th, ^{238}U, and ^{40}K in (Bq/kg) and then to assess the associated hazards with sample materials that contain ^{232}Th,^{238}U, and ^{40}K in Bq/kg as follows [21]:

$$Ra_{eq.}\left(\frac{Bq}{kg}\right) = A_U + 1.43\ A_{Th} + 0.077\ A_K \quad (9)$$

To calculate the dose rates in air due to the existence of radionuclides in soil via adopting the appropriate conversion factors, the activity utilization index (AUI) can be assessed using the following formula[22,23]:

$$AUI = \frac{A_U}{50\frac{Bq}{Kg}} * f_U + \frac{A_{Th}}{50\frac{Bq}{Kg}} * f_{Th} + \frac{A_k}{500\frac{Bq}{Kg}} * f_K < 2 \quad (10)$$

where f_U = (0.462), f_{Th} = (0.604), and f_K = (0.041) are the partial contributions to the overall dose rate in air resulting from the gamma irradiation by the decay of the radionuclides. The reported standard activities for ^{232}Th, ^{238}U, and ^{40}K in soil (A_{Th}, A_U, and A_K) are 50, 50, and 500 Bq kg^{-1}, respectively.

The annual gonadal dose equivalent (AGDE) refers to the quantity of radiation that is received by the gonads, bone marrow, and bone cells. The following formula can be used to compute AGDE resulting from activity concentrations of 232Th, 238U, and 40K in the tailing enriched soil samples [24]:

$$AGDE\left(\frac{mSv}{y}\right) = 3.09\ A_{(U)} + 4.14\ A_{(Th)} + 0.314\ A_{(K)} \quad (11)$$

where 3.09, 4.14, and 0.314 are the corresponding conversion factors that convert the specific activities of ^{238}U, ^{232}Th, and ^{40}K into the overall organs dose.

Considering the assumption that the highest value of the external hazard index (Hex.) corresponds to the upper limit of Raeq (i.e. 370 Bq kg-1), it can be obtained using the expression for Raeq. It indicates the risk associated with exposure to radiation from ^{238}U, ^{232}Th, and ^{40}K in the analyzed soil samples. The following formula was used to calculate it [25]:

$$H_{ex.} = \frac{A_U}{370} + \frac{A_{Th}}{259} + \frac{A_K}{4810} \quad (12)$$

The internal radiation hazard (Hin.) plays an important role in assessing the internal exposure to ^{222}Rn and gamma rays. This index can be estimated as follows [26]:

$$H_{in.} = \frac{A_U}{185} + \frac{A_{Th}}{259} + \frac{A_K}{4810} \quad (13)$$

The quantity I-alpha, suggested by Kriege and Stoulos, is given by [27]:

$$I_\alpha = \frac{A_{238_U}}{200} \quad (14)$$

The representative level index (Iγ) is a monitoring index that confirms the analogy of environmental samples to established dose standards for soil. Iγ can be estimated via the equation below [28]:

$$I_\gamma = \frac{A_U}{150} + \frac{A_{Th}}{100} + \frac{A_K}{1500} \quad (15)$$

Iγ should be ≤ 1, which refers to the annual effective dose of ≤ 1 mSv, in order to coincide with the given dose criteria [16].

To assess the probability of cancer risk in a population exposed to radiation from soil, the excess lifetime cancer risk (ELCR) can be calculated. This calculation is based on the estimated AEDE using the following equations [29]:

$$ELCR_{outdoor} = AEDE_{outdoor} * LF * RF \quad (16)$$

$$ELCR_{indoor} = AEDE_{indoor} * LF * RF \quad (17)$$

where LE refers to the life expectancy (60 years), and RF (Sv^{-1}) refers to the risk factor per Sievert, which is 0.05. The overall excess lifetime cancer risk can be determined as below [30]:

$$ELCR_{total} = ELCR_{outdoor} + ELCR_{indoor} \quad (18)$$

3. Results and discussion

The average reported activity of ^{238}U, ^{232}Th, and ^{40}K have mean values of 35 Bq/kg, 30 Bq/kg, and 400 Bq/kg, respectively, according to the UNSCEAR report 2008 [31]. The results of the specific activity levels of these natural radioactive elements in the analyzed plant fertilizers and insecticides are presented in Table 1. Among the fertilizer samples, NPK Granules had the lowest specific activity of ^{238}U at 2.12±1.09 Bq/kg, while the Combe Star sample had the greatest specific activity of ^{238}U at 26.91±5.69 Bq/kg, with a mean of 6.254 Bq/kg. According to recent studies, the globally permitted limit for ^{238}U specific activity in fertilizer samples is below 35 Bq/kg (UNSCEAR). The elevated specific activity of ^{238}U in certain samples could be attributed to the higher phosphate content, which often occurs due to the blending of phosphate ores with nitrogen and potassium during fertilizer production. The average specific activity of ^{232}Th was found to be 4.3694 Bq/kg, with values ranging from 0 Bq/kg in NPK Powder to 21.01±2.93 Bq/kg in Norwegian Chemical / Root Fertilizer. The findings demonstrate that the amount of ^{232}Th in the fertilizer samples exceeded the recommended levels. The specific activity levels of ^{40}K varied significantly among the samples, with the lowest value of 40.99±6.11Bq/kg observed in NPK 10 20 10+6S Chemical Magnesium, and the highest value of 495.04±19.31 Bq/kg found in agricultural sulfur, with a mean of 112.751 Bq/kg (see Fig.1). The specific activity levels of ^{40}K were lower than the universally reported limit of 400 Bq/kg, which is considered acceptable according to UNSCEAR 2008.

TABLE 1. The specific activity of ^{40}K, ^{238}U, and ^{232}Th in fertilizer and pesticide samples (Bq/kg)

No.	fertilizer and pesticides	^{40}K Series	^{238}U Series	^{232}Th Series
		^{40}K	^{214}Bi (Bq/kg)	^{208}Tl (Bq/kg)
1	Shoot	218.95±19.28	18.19±5.34	14.28±2.86
2	Man colax	412.15±16.61	10.82±2.59	4.02±0.95
3	Master power	288.50±15.86	4.27±1.85	3.00±0.94
4	Carbaryl Chemical Compound	226.24±13.64	11.40±2.94	1.72±0.69
5	Norwegian Chemical / Root Fertilizer	309.16±19.36	6.39±2.67	21.01±2.93
6	NPK 10-20-10. Granular Compound Fertilizer	336.74±17.32	16.46±3.68	4.18±1.12
7	NPK Powder	416.70±19.43	10.21±2.92	0.00
8	agricultural sulfur	495.04±19.31	4.18±1.71	4.56±1.08
9	NPK 10 20 10+6S (Chemical Magnesium)	165.23±10.47	3.62±1.49	3.41±0.87
10	DAP $(NH_4)_2HPO_4$)	40.99±6.11	4.88±2.03	7.91±1.56
11	NPK Granules	353.29±14.61	2.12±1.09	4.28±0.93
12	Sulphur –dusting fungicide	471.57±26.78	21.93±5.55	10.17±2.29
13	Master flour	274.94±16.86	9.07±2.94	0.00
14	Vector(chania)	162.69±15.30	14.23±4.35	7.98±1.97
15	Di ammonium phosphate	52.44±8.29	5.21±2.51	8.28±1.91
16	ORTs 509 mg	434.04±21.89	4.08±2.04	6.90±1.60
17	ATLAS	396.83±20.38	22.45±4.66	5.48±1.39
18	Qanas super	408.49±25.05	12.06±4.14	15.04±2.79
19	EDTA iron sodium salt(Hunan, China)	374.27±23.53	7.11±3.12	7.90±1.99
20	Master Power Phosphoric Acid	349.60±22.34	7.38±3.12	8.72±2.05
21	NPK 20-20-20(Combe star) China	275.68±18.93	26.91±5.69	8.43±1.92
	Mix	495.04±19.31	26.91±5.69	21.01±2.93
	Min	40.99±6.11	2.12±1.09	
	Average	112.751	6.254	4.3694

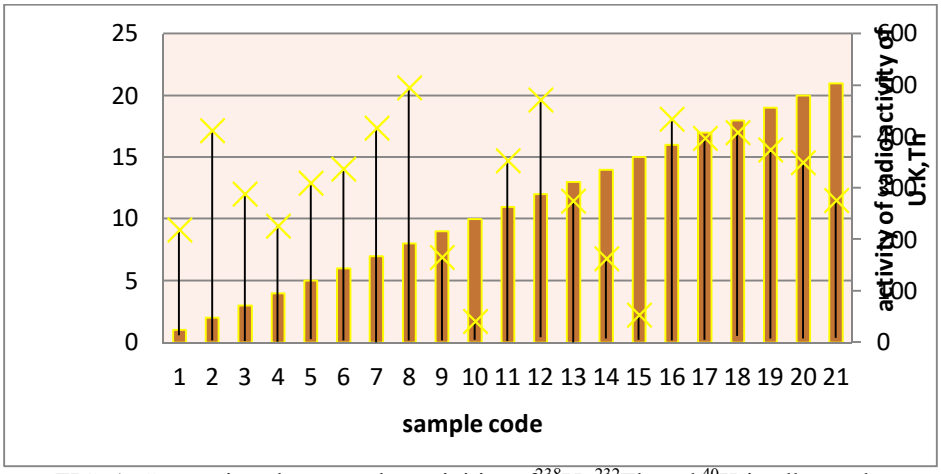

FIG. 1. Comparison between the activities of ^{238}U, ^{232}Th and ^{40}K in all sample.

The radium equivalent activity (Ra_{eq}) was found to be less than the safe levels set by the Organization for Economic Co-operation and Development, ranging from 19.34753 to 72.78399 Bq/kg equivalent in all regions (ECD). For the conversion of the absorbed dose rate into the effective dose equivalent, a conversion factor of 0.7 mSv/y was used. Additionally, an outdoor occupancy factor of 0.2 was employed to estimate the annual effective dose rate equivalent. According to Table 2, the average absorbed dose rates for indoor (D_{in}) and outdoor (D_{out}) exposure were 6 nGy/h and 12.90 nGy/h, respectively. Outdoor exposure values ranged from 16.51 to 69.56 nGy/h. These figures are slightly below the global average absorbed dose rate of 55 nGy/h.

TABLE 2. Absorbed dose rate (AD) indoor and outdoor (nGy/h), annual effective dose (AEDE) indoor, outdoor, and total dose ($mSvy^{-1}$) in the studied types of plant fertilizer and pesticides samples.

No.	Ra_{eq} (Bq/kg)	Absorbed dose rate(AD) (nGy/h)		Annual effective dose equivalent (AEDE) ($mSvy^{-1}$)		$AEDE_{total}$ (mSv/y)
		$AD_{outdoor}$	AD_{indoor}	OUTDOOR	INDOOR	
1	55.46955	25.61478	50.17775	0.031414	0.246152	50.20916
2	48.30415	24.31216	47.76055	0.029816	0.234294	47.79037
3	30.7745	15.68917	30.5969	0.019241	0.150096	30.61614
4	31.28008	15.43489	30.70544	0.018929	0.150629	30.72437
5	60.23962	28.263	54.03176	0.034662	0.265058	54.06642
6	48.36638	23.72244	47.01714	0.029093	0.230647	47.04623
7	42.2959	21.82795	43.1459	0.02677	0.211657	43.17267
8	48.81888	25.19709	48.95984	0.030902	0.240177	48.99074
9	21.21901	10.511	20.46503	0.012891	0.100393	20.47792
10	19.34753	8.575053	16.51079	0.010516	0.080995	16.52131
11	35.44373	18.22023	35.27489	0.022345	0.173045	35.29724
12	72.78399	35.31778	69.55977	0.043314	0.341232	69.60308
13	30.24038	15.41952	30.61454	0.01891	0.150183	30.63345
14	38.16853	17.76847	35.04749	0.021791	0.171929	35.06928
15	21.08828	9.418028	18.14884	0.01155	0.089031	18.16039
16	47.36808	24.01145	46.50084	0.029448	0.228115	46.53029
17	60.84231	29.61853	58.82523	0.036324	0.288573	58.86155
18	65.02093	31.30115	60.72689	0.038388	0.297902	60.76528
19	47.22579	23.43912	45.54707	0.028746	0.223436	45.57582
20	46.7688	23.01928	44.6992	0.028231	0.219276	44.72743
21	60.19226	28.27819	56.36028	0.03468	0.276481	56.39496
Mix	72.78399	35.31778	69.55977	0.043314	0.341232	69.60308
Min	19.34753	8.575053	16.51079	0.010516	0.080995	16.52131
Average	13.5432	6.573181	12.89831	0.008061	0.063274	12.90637
Worldwide [32]	370	55	84	0.07	0.34	≤1

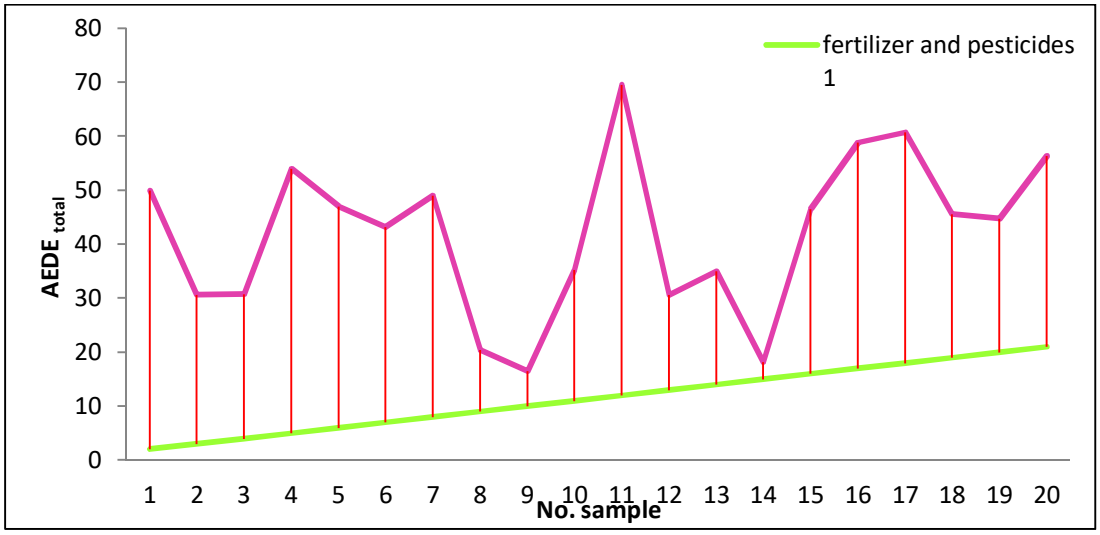

FIG. 2. Relationship between $AEDE_{total}$ and fertilizer samples

The health risks associated with naturally occurring radionuclides in the test samples were investigated and reported in Table 3. For a sample to be considered safe, both H_{ex} and H_{in} must be numerically less than 1. The representative level index was estimated using Eq. (16). It was noticed that all the obtained values exceeded the safety limits advised by UNSCEAR. Table 3 demonstrates the excess lifetime cancer risk (ELCR), which was computed according to Eqs. (17)-(19). The ELCR for the samples was determined to be 1.480503 times greater than the UNSCEAR safety level. Prolonged exposure to these radionuclides, such as in the case of factory workers or phosphate ore miners, may significantly increase the risk of developing cancer.

TABLE 3. Annual gonadal dose equivalent (AGDE), activity utilization index (AUI) in excessive lifetime cancer risk in soil samples, gonadal dose equivalent (AGDE), and activity utilization index (AUI) in excessive lifetime cancer risk in soil samples.

No.	H_{ex}	H_{in}	I_Y	$ELCR_{out}$	$ELCR_{in}$	$ELCR_{total}$ X10^{-3}	AGDE	AUI
1	0.149817	0.198979	0.221922	0.120944	0.947685	1.068629	183.772	0.358094
2	0.130451	0.159694	0.173341	0.114793	0.902032	1.016826	178.0039	0.18151
3	0.083103	0.094643	0.100029	0.074079	0.57787	0.651949	115.1693	0.098775
4	0.084487	0.115298	0.129676	0.072878	0.57992	0.652798	112.55	0.144213
5	0.162664	0.179935	0.187994	0.133448	1.020474	1.153922	203.4065	0.337577
6	0.130634	0.17512	0.195881	0.112009	0.887992	1.000001	172.7232	0.229524
7	0.114227	0.141821	0.154699	0.103064	0.814878	0.917941	160.7259	0.127676
8	0.131822	0.14312	0.148392	0.118972	0.924683	1.043655	185.4394	0.133311
9	0.057301	0.067085	0.071651	0.049629	0.386514	0.436143	76.6609	0.08786
10	0.052252	0.065441	0.071596	0.040488	0.311832	0.35232	60.8499	0.143923
11	0.095704	0.101434	0.104107	0.086029	0.666221	0.752251	133.9611	0.099554
12	0.196576	0.255846	0.283506	0.166758	1.313745	1.480503	256.461	0.363212
13	0.081674	0.106187	0.117627	0.072805	0.578203	0.651009	113.2577	0.105802
14	0.103094	0.141553	0.159501	0.083896	0.661927	0.745823	127.761	0.240899
15	0.056952	0.071034	0.077605	0.044469	0.342769	0.387238	66.9657	0.152358
16	0.127905	0.138932	0.144078	0.113373	0.878241	0.991614	176.0016	0.155774
17	0.164335	0.225011	0.253326	0.139848	1.111006	1.250854	215.2942	0.305383
18	0.175589	0.208184	0.223395	0.147793	1.146922	1.294715	226.7645	0.325797
19	0.127529	0.146745	0.155713	0.110671	0.860227	0.970899	171.0156	0.19107
20	0.126296	0.146242	0.15555	0.108689	0.844214	0.952903	167.6298	0.201497
21	0.162592	0.235322	0.269262	0.133519	1.064452	1.197971	203.8501	0.372537
Mix.	0.196576	0.255846	0.283506	0.166758	1.313745	1.480503	256.461	0.372537
Min.	0.052252	0.065441	0.071596	0.040488	0.311832	0.35232	60.8499	0.08786
Average	0.036576	0.047676	0.054191	0.031036	0.243605	0.274641	47.885	0.088761
Ref. [33]	0353	0.451	0.60	-	-	0.994	-	-

Fig. 3 shows the change in the lifetime cancer risk in fertilizer samples depending on the ^{238}U concentration. It can be noted that the lifetime cancer risk exceeded the internationally permissible limit in sample 12. Fig. 4 illustrates the excess lifetime cancer risk value levels in fertilizer samples.

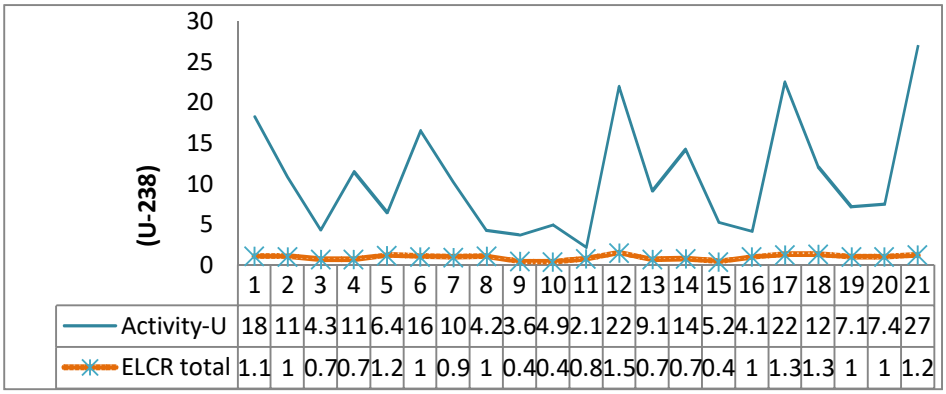

FIG. 3. Relationship between U-238 and $ELCR_{total}$ in all samples of fertilizers and pesticides.

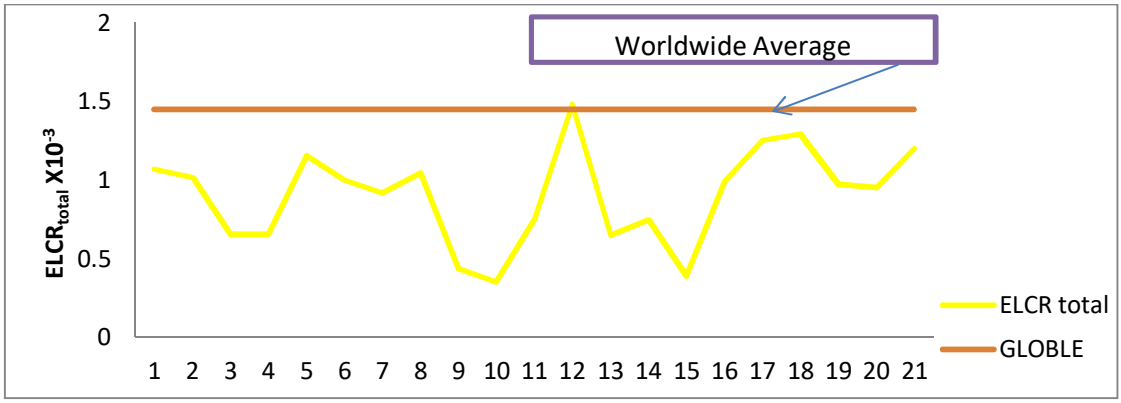

FIG. 4. Excess lifetime cancer risk value levels in fertilizer samples.

Conclusion

The external and internal risks associated with fertilizers are generally less than one. However, caution is advised when using phosphate fertilizers, especially those with high concentrations of phosphates, as they can contain significant amounts of uranium and its decay products. When comparing the results of the current study with those from UNSCEAR, it is clear that all findings are within the internationally permissible limits, although the risk increases with cumulative doses. Based on the results obtained, the following recommendations are made for the use of phosphate fertilizers when planting:

1. The use of chemical or phosphate fertilizers, as well as pesticides, to treat plants should be reduced, because this increases the possibility of contamination with radioactive elements.
2. It is preferable to use environmentally friendly fertilizers that do not cause radioactive or chemical pollution, affecting human and animal health and increasing soil, air, and water pollution.

References

[1] Ahmed, F.H., MJPS, 8 (2) (2021) 76.

[2] Alharbi, W.R., Journal Mod. Phys., 4 (3) (2013) 344.

[3] Mazzilli, B., Palmiro, V., Saueia, C., and Nisti, M.B., J. Environ. Radioact., 49 (1) (2000) 113.

[4] Al-Ubaidi, A.M., Ph.D. Thesis, University of Baghdad, Faculty of Science for Women, (2015).

[5] Beretka, J. and Mathew, P.J., Health Phys., 48 (1985) 87.

[6] Hassan, N.M., Chang, B.U., and Tokonami, S., J. Chem., 2017 (2017) 1.

[7] Basheir, E., Salih, I., and Sam, A.K., J. Radiat. Prot. Dosim., 3 (151) (2012) 1.

[8] Hassan, W.B., Habbani, F., and Shaddad, I., Sudan J. Sci., 2 (5) (2013) 83.

[9] Fadol, N., Salih, I., Idriss, H., Elfaki, A., and Sam, A., Res. J. Phys. Sci., 3 (7) (2015) 1.

[10] Smith, L. , Inman, A., Lai, X., Zhang, H., Fanqiao, M., Jianbin, Z., Burke, S., Rahn, C., Siciliano, G., Haygarth, Ph.M., Bellarby, J., and Surridge, B., J. Land Use Policy, 61 (2017) 208.

[11] Nain, M., Chauhan, R.P., and Chakarvarti, S.K., Iran J. Radiat. Res., 3 (4) (2006) 171.

[12] Rehman, S.U., Ph.D. Thesis, (PIEAS) Pakistan, 2005.

[13] Ritcey, G.M., Environ. Behav. Rad., 310 (1990) 27.

[14] Abojassim, A.A., Muhamad, Q.B., Jafer, N.A., and Mohammed, H.A., Jordan J. Phys., 15 (4) (2022) 353.

[15] Franzluebbers, A.J., Soil Tillage Res., 66 (2) (2002) 95.

[16] Abojassim, A.A. and Rasheed, L.H., Environ. Earth Sci., 80 (1) (2021) 1.

[17] Doran, J.W. and Zeiss, M.R., Appl. Soil Ecol., 15 (1) (2000) 3.

[18] Pavlidis, G. and Tsihrintzis, V.A., Water Resour. Manag., 32 (2018) 1.

[19] Paz-Ferreiro, J. and Fu, S., Land Degrad. Dev., 27 (1) (2016) 14.

[20] Celik, I.C., Ph.D. Thesis, University of Surrey, (2014).

[21] Krieger, R., Betonwerk und Fertigteil-Technik/Concrete Precasting Plant and Technol., 47 (1981) 468.

[22] Nyanda, P.B. and Nkuba, L.L., Phys. Sci. Int. J., 16 (2) (2017) 1.

[23] NEA Group of Experts, "Nuclear Energy Agency, Exposure to radiation from the natural radioactivity in building materials", report by a group of experts OECD Organization for Economic Co-operation and Development, (1979), p.1.

[24] Qureshi, A.A., Tariq, S., Din, K.U., Manzoor, S., Calligaris, C., and Waheed, A., J. Radiat. Res. Appl. Sci., 7 (4) (2014) 438.

[25] UNSCEAR United Nations Scientific Committee on the Effect of Atomic Radiation, "Ionizing Radiation: Sources and Biological Effects", Report to General Assembly, with Annexes, United Nations, New York, (1982), p.1.

[26] UNSCEAR, "Sources, Effects and Risks of Ionizing Radiation", Report to General Assembly, with Annexes. United Nations, New York, (1988), p.1.

[27] UNSCEAR, "Sources, Effects and Risks of Ionizing Radiation", Report to the General Assembly with Scientific Annexes, United Nations, New York, (2017), p. 183.

[28] UNSCEAR, "Radiation sources and Effects of ionizing radiation", Report to General Assembly, with Scientific Annexes, United Nations, New York, (2000).

[29] UNSCEAR, "Annex B: Exposure from Natural Radiation Sources", Report to General Assembly, New York, (2000).

[30] Yıldız, N., Oto, B., Turhan, Ş., Uğur, F.A., and Gören, E., J. Geochem. Explor., 146 (2014) 34.

[31] UNSCEAR, "Sources, Effects and Risks of Ionizing Radiation", Report to the General Assembly SCIENTIFIC ANNEXES A, B, C and D, United Nations, New York, (2016), P:1-512.

[32] UNSCEAR, "Sources and Effects of Ionizing Radiation", Report to the General Assembly with Scientific Annexes, Vol. I, United Nations, New York, (2008), P:1-683.

[33] Najam, L.A., Mahmmod, R.H. and Albanna, O.M., Iran J. Sci. Technol. Trans. Sci., 46 (2022) 979.

Volume 17, Number 3, 2024. pp. 349-360

Jordan Journal of Physics

ARTICLE

An Investigation into Properties for $^{156}_{66}Dy$ Isotope Using IBM-1 and IVBM Model

Dalenda M. Nasef

Physics department, Faculty of Sciences, University of Tripoli, Libya.

Doi: **https://doi.org/10.47011/17.3.10**

Received on: 24/11/022; *Accepted on: 17/01/2023*

Abstract: The $^{156}_{66}Dy$ isotopes in the O (6) region were investigated. The positive ground-state band of $^{156}_{66}Dy$ nuclei was calculated using the interacting boson model (IBM-1) and the interacting vector boson model (IVBM). The negative parity band energies of the above isotope were calculated using (IVBM) only. We plotted the ratios ($\frac{\mathrm{E(I+2)}}{E(2_1^+)}$, $\frac{\mathrm{E(I+2)}}{\mathrm{E(I)}}$, $r(\frac{(I+2)}{I})$) and the E-GOS curve as a function of the spin (I) to investigate the properties of the yrast band. Accordingly, the best-fit values of the parameters were used to construct the Hamiltonian, and the electromagnetic transition probability B(E2) of this nucleus was determined. Theoretical energy levels of dysprosium-156 isotope with a neutron number N = 90 and spin parity up to 30_1^+ were obtained using the MATLAB-20 simulation program. A comparison of these calculated energy levels with the corresponding experimentally measured ones shows a good agreement. The results also draw our attention to the fact that the nucleus of interest deforms and exhibits gamma-instability properties.

Keywords: Dysprosium Isotopes, Even-even nuclei, Interacting Boson Model-1, Interacting Vector Boson Model, Negative parity, Yrast band.

Abbreviations and Acronyms, IBM: Interacting Boson Model, IVBM: Interacting Vector Boson Model, U(5): Spherical limit, SU(3): Axially deformed shape limit O(6): γ-unstable limit, SP(12; R): the non-compact symplectic group.

Introduction

Nuclear physics has generated a large amount of theoretical and experimental data related to the atomic nucleus. This wealth of information arises from numerous studies that attempt to penetrate the atomic nucleus, breaking it down into its various components. A critical task for nuclear physics researchers is to adopt one or more nuclear models, which serves as the first step in understanding observed and measured data, making connections, and drawing conclusions.

Despite the great success of many proposed nuclear models in combining data and "explaining nuclear properties", scientists have not yet reached a consensus on a definitive model, a unified comprehensive theory that can explain everything about nuclear composition and interactions [1].

The interacting boson model (IBM) is one of the outstanding approaches for describing the nuclear structure of medium-heavy nuclei with collective properties. Additionally, IBM was found to provide a phenomenological description of spectral data for a wide range of atomic nuclei exhibiting collective features, including those typically interpreted as anharmonic oscillators or deformed rotors [2]. IBM introduced a simple connection between IBM's parametric and geometric descriptions [3]. The states in IBM consist of s and d bosons with intrinsic momentums of 0 and 2, respectively [4]. The

Corresponding Author: Dalenda M. Nasef **Email**: d.nasef@uot.edu.ly

first and simplest version "of the interacting boson model" (IBM-1), described in Refs. [2, 5, 6], is based on some of the "concepts and fundamentals" used in earlier nuclear models. It characterizes nuclear properties using a fixed number of boson systems, with no distinction between proton bosons and neutron bosons [7, 8].

The interacting vector boson model (IVBM) [9-11] has proven to be suitable for an accurate description of the low-lying ground band of well-deformed even-even nuclei. It has been used to describe the negative parity band of the atomic nucleus as well, by considering the proton and the neutron bosons separately. The IVBM is fundamentally based on the algebra of the non-compact symplectic group SP(12; R), which serves as the dynamical symmetry group of the model. This algebra is based on the creation and annihilation operators for two types of vector bosons, called p and n bosons. These bosons differ in their pseudospin by ±1/2, within the three-dimensional oscillator potential. In the rotational limit of the IVBM, the reduction from the SP (12; R) to the So (3) angular momentum group is carried out by the compact unitary subgroup U(6) [12, 13]. The symplectic extension of the IVBM allows us to treat bands with positive and negative parity to be considered as yrast bands, meaning that the states with a given L minimize the energy value with respect to the number of bosons N to form the base state of the model [14]. For most deformed nuclei, the description of axisymmetric and reflection symmetric spheres is sufficient to reproduce the spectrum of the band [15].

The energy ratio $R_{4/2}$ of the first $4_1^+$and 2_1^+ excited states in an even-even nucleus, $R_{4/2} = \frac{E(4_1^+)}{E(2_1^+)}$, is often used as a good indicator that takes into account different collective motions of the nuclei and critical point symmetries, especially in the deep structure close to the core. It is known that, based on some ideal assumptions, the energy ratio is expected to be 10/3 for a well-deformed axisymmetric rotor, 2.5 for the gamma instability limit, and 2.0 for a spherical vibrator, corresponding to the dynamical symmetries SU(3), O(6), and U(5), respectively. These symmetries degenerate from the group U(6), which governs the most general two-body Hamiltonian within the boson space among bosons [16-20].

Furthermore, the E-GOS curve (E-gama over spin) is a good tool for classifying nuclei. The E-GOS curve can actually follow the expected trend [17, 21].

Various nuclear observations have indicated multiple types of deformations after measuring certain multipole moments. Numerous signs of nuclear shape phase transitions were also observed [22]. For some isotopes, there is a shape transition from vibration to axial rotation or gamma-labile rotation associated with neutron number changes [23]. A type of collective movement can involve different characteristics. For example, along the yrast line transitions between rotations can occur, with a different relationship between angular momentum and rotational frequency, which is called a band crossing (with back-bending) [24, 25]. To correctly describe phenomena like the moment of inertia and back-bending frequency, it is important to consider not just pairs of monopoles but also pairs of double-stretched quadrupoles, despite their minimal impact on energy [20, 26].

In this research, the dysprosium-(156) isotope with atomic number Z = 66 was studied theoretically using the IBM-1 and the IVBM modules. While the IBM-1 model and IVBM modules were used to calculate the energy of the positive ground state band of the $^{156}_{66}Dy$ nucleus, the negative parity band energies of $^{156}_{66}Dy$ were calculated using the IVBM model only [17].

Theoretical Description

1) **IBM-1 Model:**

In the interacting boson model-1, the low-energy collective property of even nuclei can be generated as the state of N bosons. Namely, there is no difference in the degrees of freedom of the proton and neutron bosons. The N bosons are integrated by introducing six boson degrees of freedom and occupy two levels: one with angular momentum L = 0, called the s bosons, and the other a quadrupole boson with angular momentum L = 2, called the d boson [27, 28]. Furthermore, the model assumes that the structure of the low-lying band is determined by the excitations between valence particles outside the closed main shell [29].

The underlying structure of the model's six-dimensional unitary group U(6) leads to a simple Hamiltonian capable of describing the

three dynamical symmetries U(5), SU(3), and O(6) [30, 31]. The most general IBM Hamiltonian can be expressed as [32, 33]:

$$H = \sum_{i=1}^{N} \varepsilon_i + \sum_{i<j}^{N} V_{ij} \quad (1)$$

where ε_i is the fundamental boson energy and V_{ij} is the potential interaction between bosons i and j [34].

The Hamiltonian, in its multipole form, is written as [35]:

$$\hat{H} = \varepsilon\hat{n}_d + \alpha_o\hat{P}\hat{P} + \alpha_1\hat{L}\hat{L} + \alpha_2\hat{Q}\hat{Q} + \alpha_3\hat{T}_3\hat{T}_3 + \alpha_4\hat{T}_4\hat{T}_4 \quad (2)$$

where $n_d = (d^{\dagger}.d)$ is the total number of d boson operators, P = 1/2[(d.d) – (s.s)] is the pairing operator, $L = \sqrt{10}[d^{\dagger} \times d]^{l}$ is the angular momentum operator, and Q is the quadrupole operator, defined as:

$$Q = [d^{\dagger} \times s \times s^{\dagger} \times d]^{(2)} + \chi[d^{\dagger} \times d]^{(2)}.$$

Here, (χ) is the quadrupole structure parameter, with values of 0 and $\pm\sqrt{7}/2$.

In Eq. (2), Tr represents the octupole (r = 3) and hexadecapole (r = 4) operators, while $\varepsilon = \varepsilon_d - \varepsilon_s$ is the intrinsic boson energy [33, 35]. The parameters $\alpha_o, \alpha_1, \alpha_2, \alpha_3, and\ \alpha_4$ represent the pairing strength, angular momentum, quadrupole, octupole, and hexadecapole interactions between bosons, respectively. The Hamiltonian can be rewritten in terms of the Casimir operator of the U(6) group, in which case the Hamiltonian H can be said to have dynamical symmetries; these symmetries are called the SU(5) vibrational symmetry, SU(3) rotational symmetry, and O(6) γ-unstable symmetry [36].

The eigenvalues of O(6) dynamic symmetry can be written as [2]:

$$E = K_3(N - \sigma)(N + \sigma + 4) + K_4\tau(\tau + 3) + K_5L(L + 1) \quad (3)$$

where K_3 =$\alpha_o/4$, K_4= $\alpha_3/2$, K_5=$\alpha_1 - \alpha_3/10$. $N = N_{\pi} + N_{\nu}$ with N representing the absolute number of bosons, N_{π} the number of valence protons relative to the nearest closed shell, and N_{ν} the corresponding number of valence neutrons. The variable σ = N, N−2, ..., 0 or 1, but for the low energy-momentum band we can set σ = N.

O(6) is marked with quantum numbers τ = σ, σ−1, ..., 0; L = 2λ, 2λ −2, ..., λ +1, where λ is a non-positive integer defined as λ = τ−3υ_, υ_= 0, 1, and υ_ is the number of triplet bosons. σ is O(6) non-reducible representations, while τ is the O(5) [37, 38]. The preceding equation starts out as follows;

$$E = K_4\tau(\tau + 3) + K_5L(L + 1) \quad (4)$$

2) **E-GOS:**

E-GOS (E-gama over spin) is one of the most important methods for determining the properties of the nuclei at different energy states, and it can be done by plotting the relationship between the gamma energy (E_{γ}) divided by the spin (I) as a function of the spin (I). This relationship for the three limits (vibrational, rotational and γ-unstable) is given as follows [39]:

$$U(5): R = \frac{\hbar\omega}{I} \xrightarrow{I\to\infty} 0 \quad (5)$$

$$SU(3): R = \left(\frac{\hbar^2}{2J}\right)\left(4 - \frac{2}{I}\right) \xrightarrow{I\to\infty} 4\left(\frac{\hbar^2}{2J}\right) \quad (6)$$

$$O(6): R = \frac{\mathrm{E}(2_1^+)}{4}\left(1 + \frac{2}{I}\right) \xrightarrow{I\to\infty} \frac{\mathrm{E}(2_1^+)}{4} \quad (7)$$

3) **Back-bending:**

To determine if the isotope has got back-bending property and to identify the location of the back-bending if it was found, we should examine the relationship between the moment of inertia ($2J/\hbar^2$) and gamma energy (E_{γ}). This relationship can be written as [8, 39]:

$$2J/\hbar^2 = \frac{4I-2}{E_{\gamma}} \quad (8)$$

While the relation between the ħω and E_{γ} is given by [40]:

$$\hbar\omega = \frac{E_{\gamma}}{\sqrt{I(I+1)} - \sqrt{(I-2)(I-1)}} \quad (9)$$

4) **B(E2) Values:**

A successful nuclear model must be able to accurately describe the energy spectrum of the nucleus and its electromagnetic properties. This property provides a good test of the nuclear structure and the wave function of the nuclear model [37, 41]. The reduction probability of the electric quadrupole transition B(E2) depends on the available experimental data on the half-lives of quantum transitions between energy levels. This probability is given by the relationship:

$$B(E2) = \frac{0.05657}{T_{\frac{1}{2}}^{\gamma}(ps)E_{\gamma}^{5}(MeV)}(e^2b^2) \quad (10)$$

In the case of just one transition out of the level, the relationship is:

$$T_{\frac{1}{2}}^{\gamma} = T_{\frac{1}{2}}(\exp)(1 + \propto_{tot}) \quad (11)$$

where $\propto_{tot}$ is the internal transformation coefficient [42].

5) **IVBM Model:**

The scientists extended the IVBM by incorporating its symplectic dynamical symmetry Sp(12, R), which makes it possible to vary the number of bosons representing blockages in the Hamiltonian model. This symplectic extension of the interacting vector boson model enables a more comprehensive classification of states than the single version and provides more opportunities to consider other collective bands [43].

Nuclear states are considered as a system of an even number of p-bosons with isospin T = 1/2 in the interacting vector boson model. This model is somewhat similar to the interacting boson model. For example, both models have solvable dynamic symmetries SU(3). By assigning angular momentum L and isospin T (LT = 01, 21, 10) for each boson pair in the ideal space of S, D bosons (T = 1) and P bosons (T = 0), we can find the relationship between the two models. We use the results that we can get by applying the dynamical symmetry algebra of IVBM, which is the non-compact symplectic algebra Sp(12, R), for the boson mapping[43-45].

The permissible values of energy states of the two bands, GSB and NPB, are given in the IVBM model by [43, 46]:

$$E(I)_{GSB} = \beta I(I+1) + \gamma I \quad (12)$$

and

$$E(I)_{NPB} = \beta I(I+1) + (\gamma + \eta)I + \zeta \quad (13)$$

Here, the parameter β represents the intensity of the effect of the rotational properties, while γ represents the intensity of the effect of the vibrational properties on the nucleus. The parameters η and ζ are crucial for determining the values of the energy states in the NPB beam. The values of these parameters can be determined by matching the experimental values of the energy states with Eqs. (1) and (2).

The GSB and NPB bands, with their distinct states $I^{\pi} = 0^+, 2^+, 4^+, \ldots \; and \; I^{\pi} = 1^+, 3^+, 5^+, \ldots$, respectively, overlap to form a single band called the octupole band $I^{\pi} = 0^+, 1^-, 2^+, 3^-, 4^+, 5^-, \ldots$. This overlap is a good example of the staggering of energies between these two bands, caused by the fact that an energy level of I exchanges its location with an energy level of I+1 [47]. The relationship of the staggering of patterns between the two bands is given as:

$$\Delta E_{1,\gamma}(I) = \frac{1}{16}\Big(6E_{1,\gamma}(I) - 4E_{1,\gamma}(I-1) - 4E_{1,\gamma}(I+1) + E_{1,\gamma}(I-2) + E_{1,\gamma}(I+2)\Big) \quad (14)$$

and

$$E_{1,\gamma}(I) = E(I+1) - E(I) \quad (15)$$

The ratio between any two consecutive states in the beam is important for determining state properties for the even-even nucleus and is given by:

$$r\left(\frac{(I+2)}{I}\right) = \left(R\left(\frac{I+2}{I}\right)_{exp} - \frac{(I+2)}{I}\right) \times \frac{I(I+1)}{2(I+2)} \quad (16)$$

Here, $R\left(\frac{I+2}{I}\right)_{exp}$ represents the ratio between experimental states I+2 and I. If the ratio $r\left(\frac{(I+2)}{I}\right)$ falls between 0.1 and 0.35, the nuclei have vibrational properties; if it is between 0.4 and 0.6, the nuclei have $\gamma - unstable$ properties; and if it is between 0.6 and 1.0, the nuclei have rotational properties.

Results and Discussion

The investigation of the nuclear structure and its deformation of the dysprosium isotope (156) was conducted using the IBM-1 and IVBM models. Dysprosium isotope (156) has an atomic number Z = 66, so it has eight proton bosons (middle shell) and four neutron bosons, so the total number of bosons for this isotope is 12. Eq. (4) is used to calculate the values of the parameters K_4 and K_5 twice, once for the baseband and once for the s-band, and Table 1 shows these values along with the number of isotopic bosons.

TABLE 1. Number of bosons and IBM-1 parameters of g and s bands in KeV.

isotope	N_π	N_ν	Total # of Bosons	g-band		s-band	
				K_4	K_5	K_4	K_5
$^{156}_{66}Dy$	8	4	12	24.023	6.9464	91.787	-17.12

By simulating the IBM-1 eigenvalue Eq. (4) using the MATLAB-20 program, we obtained the energy levels of the positive Yrast band. Furthermore, we also calculated the energy levels of the negative parity bands using Eqs. (12) and (13) obtained from the IVBM. Table 3 shows that the results are very close to the experimental data, and the IBM-1 model gives more accurate results than the positive parity band of the IVBM model, as shown in Fig. 1.

TABLE 2. IVBM parameters of GSB and NPB in KeV.

Isotop	β	γ	η	ζ
$^{156}_{66}Dy$	9.7	39.9	-38.8	1272.7

TABLE 3. Positive and negative energy levels for $^{156}_{66}Dy$.

Spin (I^π)	*E_{exp} (KeV)*	*E_{clc} (KeV)*	*Error (%)*
0^+	*0*	*0*	*0*
1^-	*1293.2*	*1293.2*	*0*
2^+	*137.77*	*137.8*	*0*
3^-	*1368.4*	*1392.3*	*-1.75*
4^+	*404.19*	*379.2*	*6.19*
5^-	*1526.3*	*1569.0*	*-2.80*
6^+	*770.44*	*724.2*	*6.01*
7^-	*1810*	*1823.3*	*-0.74*
8^+	*1215.61*	*1172.8*	*3.52*
9^-	*2186.6*	*2155.2*	*1.43*
10^+	*1725.02*	*1725*	*0.0*
11^-	*2636.6*	*2564.8*	*2.72*
12^+	*2285.88*	*2285.9*	*0.0*
13^-	*3154.2*	*3051.9*	*3.24*
14^+	*2887.82*	*2830*	*2.00*
15^-	*3719.6*	*3616.6*	*2.77*
16^+	*3523.3*	*3420.8*	*2.90*
17^-	*4331.1*	*4258.9*	*1.67*
18^+	*4178.1*	*4058.2*	*2.87*
19^-	*4978.8*	*4978.8*	*0.0*
20^+	*4859*	*4742.2*	*2.40*
21^-	-	-	-
22^+	*5573*	*5472.8*	*1.80*
23^-	-	-	-
24^+	*6328.7*	*6250*	*1.24*
25^-	-	-	-
26^+	*7130.3*	*7073.9*	*0.79*
27^-	-	-	-
28^+	*7978.5*	*7944.4*	*0.43*
29^-	-	-	-
30^+	*8875.9*	*8861.5*	*0.16*
31^-	-	-	-
32^+	*9825.2*	*9825.2*	*0.0*

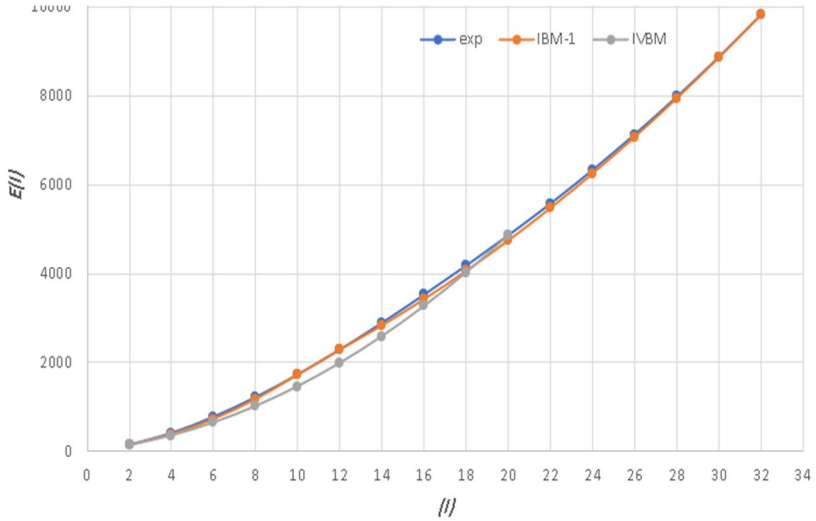

FIG. 1. Theoretical and practical energy levels as a function of angular momentum.

By examining the 2_1^+ energy level value for the $^{156}_{66}Dy$ isotope, we found that it to be approximately 137.8 KeV. This led us to expect rotational symmetry of the isotope, but when we performed other tests, we found dissimilarity! To determine the symmetry of the Dy(156) isotope, we calculated the energy ratios ($\frac{E(I+2)}{E(2_1^+)}$. The result aligned with the γ-unstable symmetry, as the typical ratios for γ-unstable O(6) were closest to the calculated values [1, 5]. Table 4 compares the calculated ratios using the IBM-1 with experimental ratios. Table 5 provides the typical values of the ratios to compare them with the calculated values and determine the type of symmetry that appeared to be O(6), see Fig. 2.

TABLE 4. Comparison of practical and theoretical energy ratios.

Isotope	$E(4_1^+)/E(2_1^+)$		$E(6_1^+)/E(2_1^+)$		$E(8_1^+)/E(2_1^+)$		$E(10_1^+)/E(2_1^+)$	
	EXP	IBM-1	EXP	IBM-1	EXP	IBM-1	EXP	IBM-1
$^{156}_{66}Dy$	2.93	2.75	5.59	5.26	8.82	8.51	13.5	12.52

TABLE 5. Typical values for energy ratios.

Symmetry	$E(2_1^+)$	$E(4_1^+)/E(2_1^+)$	$\frac{R_6}{2}$	$\frac{R_8}{2}$	$\frac{R_{10}}{2}$
U(5)	500	$2 \leq \frac{R_4}{2} \leq 2.4$	3	4	5
O(6)	300	$2.4 \leq \frac{R_4}{2} \leq 2.7$	4.5	7	10
SU(3)	100	$3 \leq \frac{R_4}{2} \leq 3.3$	7	12	18.33

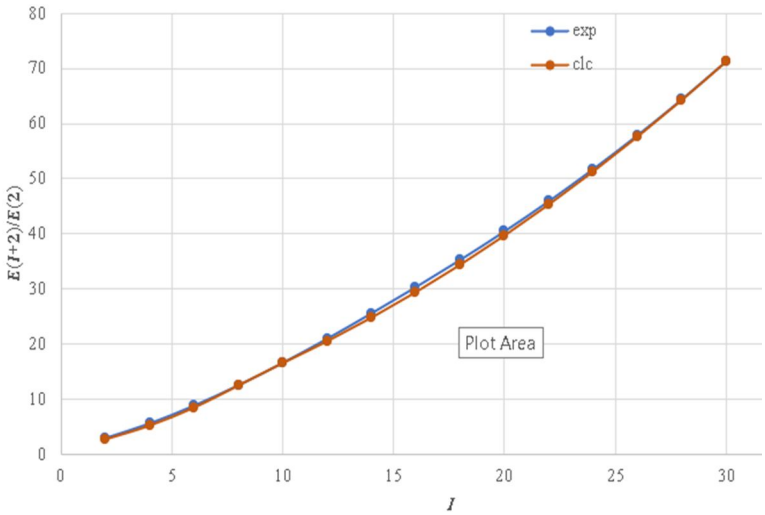

FIG. 2. Ratios with respect to the first energy level (2_1^+)

In addition, the ratios $\frac{E(I+2)}{E(I)}$ were calculated and compared with the typical values (Table 6 and Fig. 3), where the results showed that the Dy-156 isotope is closer to following the O(6) limit. Moreover, we have determined the symmetry using the E-GOS method and we have made sure that the isotope has γ-unstable symmetry (Fig. 4).

TABLE 6. Comparison between typical and calculated values for energy ratios.

symmetry	$R_{4/2}=E(4_1^+)/E(2_1^+)$	$R_{\frac{6}{4}}$	$R_{\frac{8}{6}}$	$R_{\frac{10}{8}}$	$R_{\frac{12}{10}}$
U(5)	2	1.5	1.33	1.25	1.2
O(6)	2.5	1.8	1.56	1.43	1.35
SU(3)	3.33	2.1	1.71	1.53	1.42
$^{156}_{66}Dy$ EXP	2.93	1.90	1.58	1.42	1.33
$^{156}_{66}Dy$ CLC	2.75	1.91	1.62	1.47	1.33

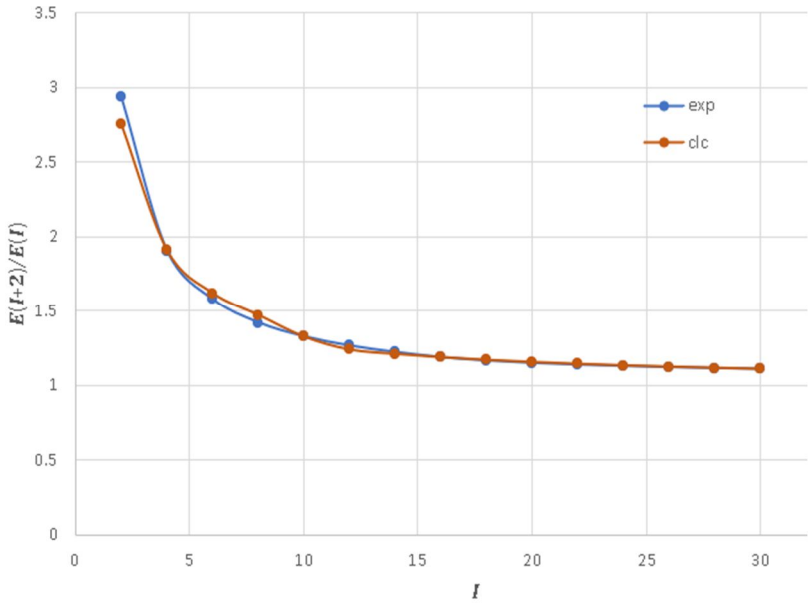

FIG. 3. Ratios with respect to variable states.

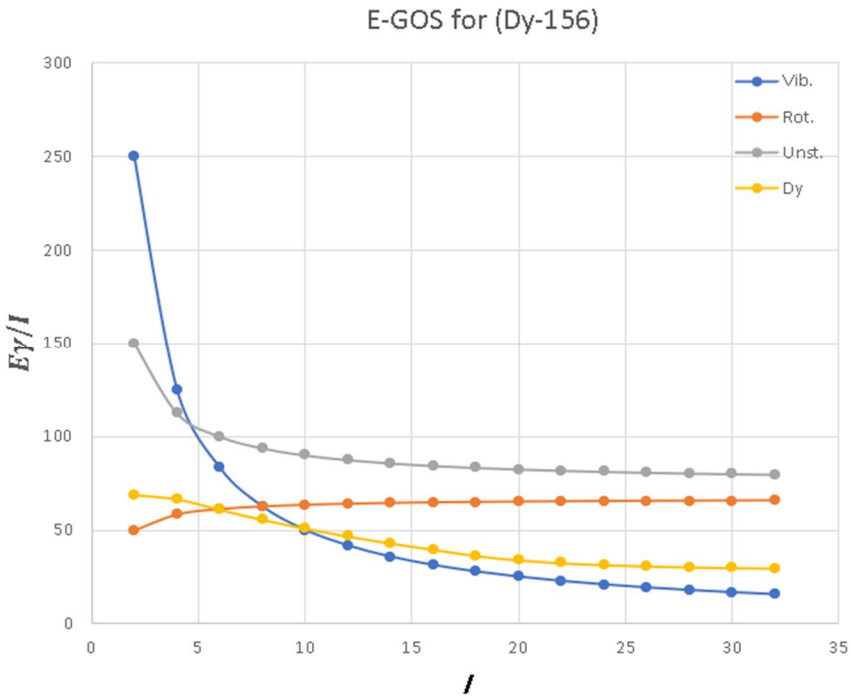

FIG. 4. E-GOS for $^{156}_{66}Dy$.

To determine the presence and location of back-bending in this isotope, the moment of inertia was calculated using Eq. (8), along with the transition energy E_γ between consecutive energy levels. The rotational frequency $\hbar\omega$ for each even spin was also calculated using Eq. (9). Fig. 5 shows the relationship between the moment of inertia and the rotational frequency for the isotope under study. Unbending rather than back-bending was observed due to the strong interaction between the ground-state band and the spin-aligned S-band [48, 49]. However, there was a difference in the isotope behavior at angular momentum in the range of 10-20 compared to the ranges of 0-10 and 20-30.

The energy of each level was plotted as a function of the angular momentum J(J+1) in Fig. 6, to check what we had found in the previous figure. In order to know more about the nature of the back-bending, we plotted E_γ as a function of J in Fig. 7. This plot shows that there is a continuous increase without a decrease in the transmission energy with an increase in momentum, and this confirms the observations from the last two figures.

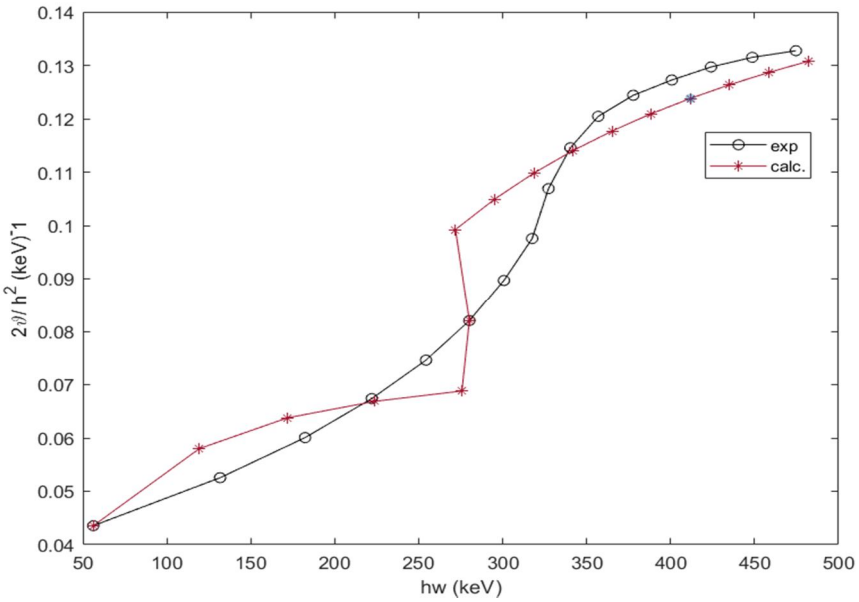

FIG. 5. Back-bending phenomena.

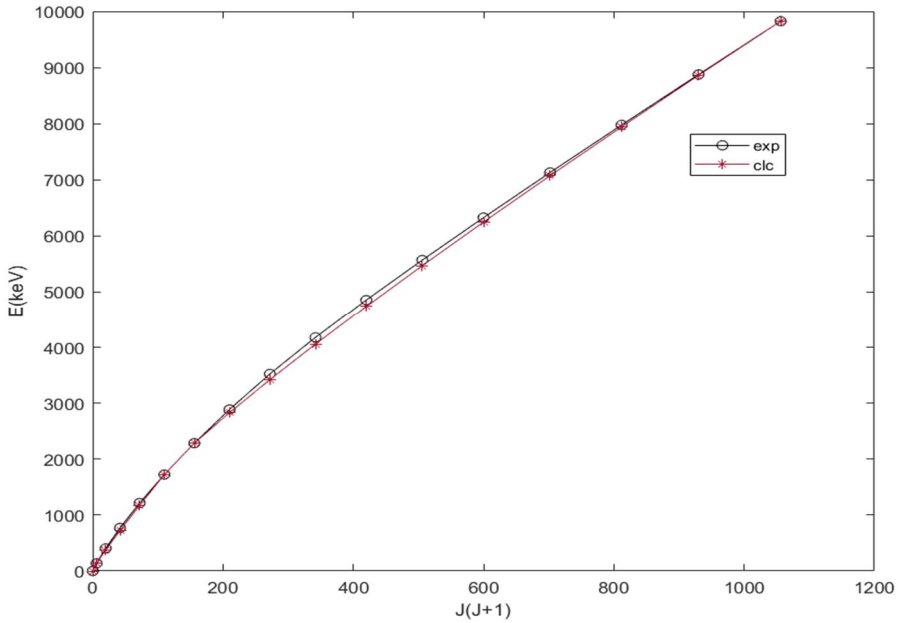

FIG. 6. Experimental and IBM-1 calculated energy levels as a function of spin.

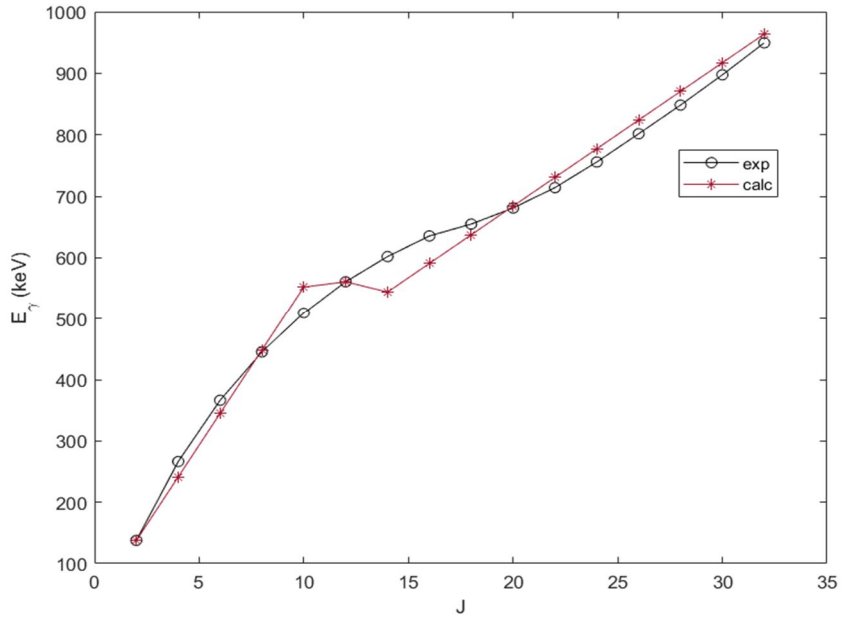

FIG. 7. Transition energy (E_γ) changes with momentum (J).

Gama transitions and their probabilities between different energy levels are important parameters in the study of the nuclear properties of any isotope. We calculated this function, B(E2), for different transitions between multiple levels of the isotope under study and compared it with the experimental results. This calculation was based on available laboratory values for the gamma energies of different transitions, the half-life of the gamma transition, and the available values for the isotope internal transformation coefficient. Using Eq. (10), we determined the electric transition probabilities of the quadrupole, B(E2). Table 7 shows that the results are in good agreement with the experimental values.

TABLE 7. Electromagnetic transitions using the half-life of the $^{156}_{66}Dy$ isotope.

I^π	$T_{\frac{1}{2}(exp)}(ps)$	$E_\gamma(KeV)$	$\propto^+_{tot}$	B(E2) W.u		error
				exp	clc	
$2^+ \rightarrow 0^+$	823	137.77	0.849	150	150.07	0.049
$4^+ \rightarrow 2^+$	31.6	266.42	0.0933	244.8	244.43	0.151
$6^+ \rightarrow 4^+$	6.3	366.25	0.0356	264	263.63	0.140
$8^+ \rightarrow 6^+$	2.26	445.17	0.0206	281	281.07	0.026
$10^+ \rightarrow 8^+$	1.06	509.41	0.01444	310	307.29	0.875
$12^+ \rightarrow 10^+$	0.62	560.86	0.01131	330	325.74	1.292
$14^+ \rightarrow 12^+$	0.56	601.94	0.0095	250	253.72	1.488
$16^+ \rightarrow 14^+$	0.32	635.48	0.00833	340	338.96	0.305
$18^+ \rightarrow 16^+$	0.24	654.8	0.00776	390	389.32	0.175
$20^+ \rightarrow 18^+$	0.24	680.9	0.0708	320	320.42	0.132
$22^+ \rightarrow 20^+$	0.21	714	0.00634	290	289.04	0.331
$24^+ \rightarrow 22^+$	0.155	755.7	0.00557	300	295.07	1.644

Fig. 8 shows the relationship between the ratio $r\left(\frac{(I+2)}{I}\right)$ and the spin I. This figure provides numerical values for this ratio. It is clear that the ratio was between 0.4≤ r ≤0.6 for the spin higher than 6, so we can say that the Dy (156) isotope has γ-unstable properties with the O(6) limit. However, for the lower spins of 2, 4, and 6 these ratios reached up to 0.7, so the nuclei could have rotating properties. Despite this, most of the given spin ranges were found within the O(6) limit. Table 8 shows the typical ratio value (r) for each limit.

TABLE 8. Typical values for ratios.

Symmetry	$r\left(\frac{(I+2)}{I}\right)$
U (5)	$0.1 \leq r \leq 0.35$
O (6)	$0.4 \leq r \leq 0.6$
SU (3)	$0.6 \leq r \leq 1$

Fig. 9 shows the staggering between the energy states of the GSB and NPB bands in the Dy (156) isotope. This staggering is evidence of the interference of the energy states between the two bands.

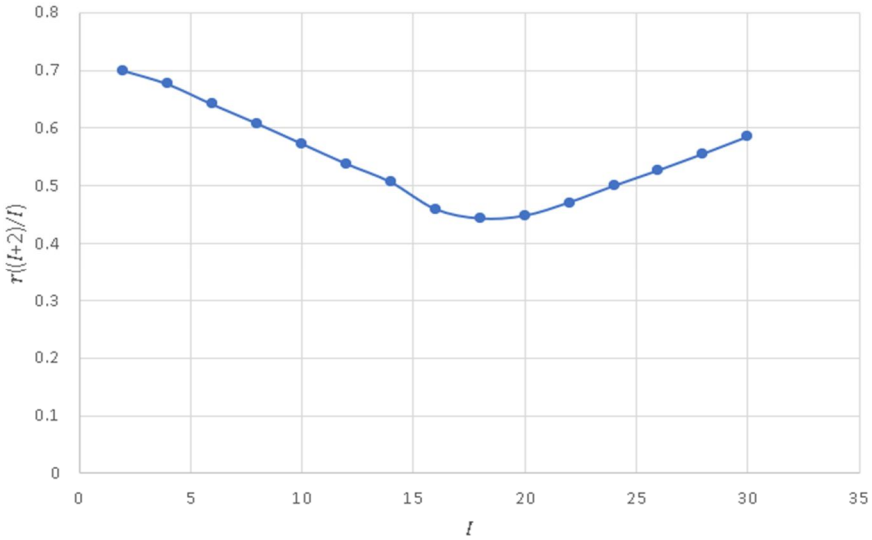

FIG. 8. The ratio between any two consecutive states in the beam.

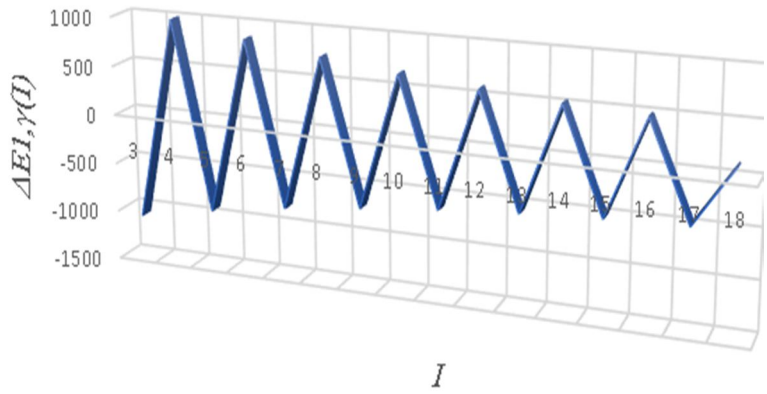

FIG. 9. Staggering patterns between GSB and NPB.

Conclusion

In this work, we carried out a systematic investigation of the even-even $^{156}_{66}Dy$ isotope within the IBM-1 and IVBM frameworks. We calculated the yrast and negative band energy levels. The ratio values ($E(I+2)/E_2^+$), ($E(I+2)/E(I)$), and $r\left(\frac{(I+2)}{I}\right)$ indicate that this isotope is due to the γ - unstable symmetry. Additionally, the calculated moment of inertia and ħω values show good agreement with experimental data. In this isotope, the back-bending phenomenon does not appear clearly at J =10, but there is a slight change in the track of the curve of the relationship between photon energy and moment of inertia in the interval $10 \geq J \geq 20$.

References

[1] Safauldeen, O.A. and Shatti, W.A., Diyala J. Pure Sci., 14 (2018) 1.

[2] Arima, A. and Iachello, F., Phys. Lett. B, 53 (1974) 309.

[3] Hasan, M., Tabussum, M., Roy, P. et al., Res. Trends Challenges Phys. Sci., 7 (2022) 1.

[4] Abood, S.N. and Najim, L.A., Int. J. of Phys., 4 (2016) 1.

[5] Alnejm, M.A.A., Kirkuk Univ. J. Sci. Stud. (KUJSS), 16 (2021) 1.

[6] Arias, J.M., Dukelsky, J., et al., Phys. Rev., C, 75 (2007) 014301.

[7] Al-Khudair, F.H., Long, G.L., and Sun, Y., Phys. Rev., 77 (2008) 034303.

[8] Nasef, D. et al., The Fourth Int. Conf. Sci. Tech., 20 (2021) 4.

[9] Georgieva, A., Raychev, P., and Raussev, R., J. Phys. G, Nucl. Phys., 8 (1982) 1377.

[10] Ganev, H., Garistov, V.P., and Georgieva, A.I., Phys. Rev. C, 69 (2004) 014305.

[11] Ganev, H. et al., Phys. Rev. C, 70 (2004) 054317.

[12] Georgieva, A., Raychev, P., and Roussev, R., Bulg. J. Phys., 12 (1983) 147/ J. Phys. G, 9 (1985) 521.

[13] Georgieva, A. and Garistov, V.P., J. Phys.: Conf. Ser., 590 (2015) 012033.

[14] Khalaf, A.M., Ahmed, G.S.M. et al., Nuclear Physics A, 988 (2019) 1-8.

[15] Ganev, H., Garistov, V.P., and Georgieva, A.I., Institute of Nuclear Research and Nuclear Energy, 1 (2003) 25.

[16] Giannatiempo, A., Phys. Rev. C, 84 (2011) 024308.

[17] Nasef, D. et al., Sebha University J. Pure Appl. Sci., 20 (2021) 2.

[18] Abood, S., Najim, L., and Jundy, Y., Int. J. Recent Res. Rev., VII (2014) 2.

[19] Bohr, A. and Mottelson, B.R., "Nuclear Structure", (Word Sci., Singapore, 1998), Vol. 2.

[20] Hossain, I., Sharrad, F. et al., Chiang Mai J. Sci., 42 (2015) 1.

[21] Meng, H., Hao, Y., et al., Prog. Theor. Exp. Phys., 103 (2018) D02.

[22] Liu, Y.X., Mu, L.-Z., and Wei, H.Q., Phys. Lett. B, 633 (2006) 49.

[23] Iachello, F. and Isacker, V.P., "The Interacting Boson-Fermion Model", (Cambridge University Press, 1991).

[24] Stephens, F.S. and Simon, R.S., Nucl. Phys. A, 183 (1972) 257.

[25] Yang, J., Hua-Lei, W., and Chai, Q., Prog. Theor. Exp. Phys., 063 (2016) D03.

[26] Satuła., W. and Wyss, R., Phys. Scripta T, 56 (1995) 159.

[27] Dieperink, A.E.L. and Wenes, G., Ann. Rev. Nucl. Part. Sci., 35 (1985) 1.

[28] Hossain, I. et al., J. Theo. App. Phys., 7 (2013) 46.

[29] Al-Jubboria, M. et al., Nucl. Phys. A, 971 (2018) 1.

[30] Casten, R.F. and Warner, D.D., Rev. Mod. Phys., 60 (1988) 389.

[31] Arima, A. and Iachello, F., Phys. Rev. lett., 35 (1975) 1069.

[32] Muaffaq, O.A. et al., Int. J. App. Eng. Res., 13 (2018) 11.

[33] Iachello, F., "Nuclear Structure", Eds. K. Abrahams, K. Allaart, and A.E.L. Dieperink (New York, Plenum Press, 1981).

[34] Islam, J. and Hossain, I., Prob. Atom. Sci. Tech., N5 (2016) 105.

[35] Iachello, F. and Arima, A., "The Interacting Boson Model. Cambridge Monographs on Mathematical Physics", (Cambridge University Press, 1987).

[36] Küçükbursa, A. et al., Math. Comput. Appl., 10 (2005) 1.

[37] Mutshera, S.M., Sharradb, F.I., and Salmand, E.A., Nucl. Phys. A, 1017 (2022) 1.

[38] Kassim, H.H. et al., 2nd Int. Sc. Conf. of Al-Ayen Univ., 928 (2020) 7.

[39] Regan, P.H., Beausang, C.W., Zamfir, N.V., et al., Phys. Rev. Lett., 90 (2003) 152502.

[40] Eshaftri, N.S. et al., Libyan J. Sci., 24 (2021) 1.

[41] Mutsher, S.M., Salman, E.A. and Sharrad, F.I., 2nd Int. Sc. Conf. of Al-Ayen Univ., 928 (2020) 7

[42] Ahmed, I.M. and Al-Jabbori, M.A., J. Rafidain Sci., 20 (2009) 4.

[43] Georgieva, A. et al., Phys. Part. Nucl., 40 (2009) 4.

[44] Ganev, H.G., Bulgarian J. Phys., 48 (2021) 421.

[45] Arima, A. et al., Phys. Lett. B, 66 (3) (1977) 205.

[46] A-Jubbori, M.A., Kassim, H.H. et al., Phys. Atom. Nuclei., 82 (2019) 201.

[47] Ahmed, M.A. and Ahmed, I.M., J. Rafidain Sci., 28 (2019) 4.

[48] Johnson, A., Ryde, H., and Sztarkier, J., Phys. Lett. B, 34 (1971) 605

[49] Chapman, R. et al., Phys. Rev. Lett., 51 (1983) 2265.

Volume 17, Number 3, 2024. pp. 361-369

Jordan Journal of Physics

ARTICLE

Dose Measurement and Cancer Risk from Natural Radioactivity in Cleaning Powders at Kurdistan Markets, Iraq

Adeeb O. Jafir, Hallo M. K. Abdullah and **Ali H. Ahmed**

Department of physics, College of Science, Salahaddin University-Erbil, Erbil, Kurdistan Region, Iraq.

Doi: **https://doi.org/10.47011/17.3.11**

Received on: 29/11/2022; *Accepted on: 14/03/2023*

Abstract: The Kurdistan region of Iraq has seen a rise in the use of cleaning powders due to their favorable effects on health. However, various levels of radioactive isotopes, including ^{238}U, ^{232}Th, and ^{40}K, can be found in the ore used to make some cleaning powders. Therefore, washing powder is regarded as one of the environmental sources of radionuclides and radioactivity. In this study, 25 samples of ordinary cleaning powder were analyzed to estimate the specific activities of ^{238}U, ^{232}Th, and ^{40}K using a gamma-ray sodium iodide NaI(Tl) detector. The mean activity concentrations of ^{238}U, ^{232}Th, and ^{40}K were found to be 0.27±0.027, 1.881±0.149, and 19.213±0.899 $Bq.kg^{-1}$, respectively, which are well below the recommended values set by UNSCEAR 2000: 32, 45, and 400 Bq/kg for ^{238}U, ^{232}Th, and ^{40}K, respectively. The radiological hazard parameters determined for each sample of detergent were also found to be lower than the maximum allowable values recommended by international organizations. Therefore, cleaning powders sold in the Kurdistan region markets pose no radioactive risk to users.

Keywords: Cancer risk, NaI(Tl) detector, Detergent, Radioactivity, Primordial radionuclide.

1. Introduction

Radionuclides are present in all raw materials and minerals. However, some human activities can increase exposure to naturally occurring radioactive materials (NORM). This enhanced exposure necessitates strict regulatory supervision. Since the earth's origin, the planet has accumulated primordial radionuclides that continue to persist in various environments [1]. Environments contain natural radionuclides at all times. Natural radionuclides are found ubiquitously in water, air, soil, food, and raw material products.

Due to the ionization that is formed when radiation interacts with living things, it can have a negative impact on an organism's shape and functionality, which can disrupt the normal operation of cells, organs, and tissues and cause cancer and a rise in mortality [2].

Cleaning is an essential part of daily life, helping to maintain hygiene in our clothes, homes, and other belongings. For example, purification materials are collected from multiple resources containing varying amounts of these energy powders such as sodium sulfate, phosphate, sodium silicate, soda ash, sodium chloride, clay, and moisture [3].

Cleaning products, like all man-made products, are made from raw materials from which radioactive substances cannot escape, so it is important to adhere to tolerance limits for these substances [3]. Detergents are a major group of products containing chemical raw

Corresponding Author: Adeeb Omer Jafir **Email**: adeeb.jafir@su.edu.krd

materials such as phosphates, which contain radioactive elements that can migrate into consumer products, raising health concerns in some instances [4].

Earlier studies of natural radioactivity were carried out on detergent powder samples from surrounding and neighboring regions [4-8]. However, there is a lack of comprehensive studies on the levels of natural radiation in detergents available in the local Erbil market, which is open to a wide range of manufactured goods.

In general, radiation special effects can be evaluated by estimating radiation threat factors using gamma spectroscopy. This study focused on the assessment of natural primordial radionuclide levels in detergent powder samples used for washing clothes that were present in a local market in Erbil and the determination of dose and cancer risk due to ^{40}K, ^{232}Th, and ^{238}U radionuclide activity concentrations.

2. Method and Analytical Techniques

2.1 Sampling

As shown in Table 1, 25 detergent samples, imported from 10 neighboring countries, were collected from markets in Erbil, the capital of the Kurdistan region of Iraq. A constant weight of 1 kg and a 1 L Marinelli beaker filled with detergents were used to convert the activity to a specific activity. The samples, in powder form, were brought to the laboratory and oven-dried at a temperature of 70 °C until they reached a constant weight. Collected samples were stored and sealed in Marinelli beakers for approximately one month before being counted for secular equilibrium between parents and progeny. The gamma-ray spectrum of each sample was acquired by placing it in contact with the detector for 21 600 seconds. This duration is sufficient to obtain the spectrum and reduce uncertainty due to the high efficiency of the NaI(Tl) detector [9].

TABLE 1. The collected samples' type and country of origin.

Sample code	Cleaning powder type	Country of production
ST1	Bright	UAE
ST2	Altunsa	Turkey
ST3	Polex	Iraq - Kurdistan
ST4	Maria	Iran
ST5	Liby	China
ST6	Carrefour	France
ST7	Ariel	Saudi Arabia
ST8	Noura	Syria
ST9	Active	Iran
ST10	Falcon	UAE
ST11	Tide	Saudi Arabia
ST12	ABC (red)	Turkey
ST13	Super royal	Iraq
ST14	Teobeby	Bulgaria
ST15	Ave	Iran
ST16	Alwazir	Jordan
ST17	Alwazir	Iraq
ST18	Persil	Turkey
ST19	Savex	Bulgaria
ST20	Barf	Iran
ST21	Mega	Thailand
ST22	ABC (black)	Turkey
ST23	Finish	Turkey
ST24	Peros	Turkey
ST25	Galgom	Turkey

2.2 Gamma Spectrometry

The specific activity of the primordial radionuclides in washing powder samples is determined using a high-efficiency gamma spectroscopy system with a low-background design. The system consists of a NaI(Tl) detector with lead castle shielding, a high-voltage power supply connected to a preamplifier, an amplifier, a multichannel analyzer (MCA), and a desktop computer.

The NaI(Tl) scintillation detector (SILENA model 3S3) used in this work, as shown in Fig. 1, has an active region of 3" × 3" and an energy resolution of 7.4% at the 662 KeV gamma-line of ^{137}Cs. Energy calibration for the NaI(Tl) gamma-ray spectrometry was performed using a point source of ^{226}Ra and its progeny ^{214}Pb (242, 295, and 352 KeV) and ^{214}Bi (609 and 1120 KeV), as shown in Fig. 1. In this study, efficiency calibration of the NaI(Tl) gamma-ray spectrometry was performed in a 1 L Marinelli beaker using a multi-nuclide standard source of ^{210}Pb, ^{241}Am, ^{109}Cd, ^{57}Co, ^{123m}Te, ^{51}Cr, ^{113}Sn, ^{85}Sr, ^{137}Cs, ^{88}Y, and ^{60}Co prepared by the International Atomic Energy Agency (IAEA-315), covering the energy range of 25 KeV to 1500 KeV. The standard source was placed above the detector, maintaining an equal distance between the sample and the detector. Figure 2 shows a graph of efficiency versus gamma-ray energy.

Both ^{238}U and ^{232}Th are long-lived, so their concentrations were determined from the spectra using an indirect method. The concentration of ^{238}U was determined from the average concentrations of ^{214}Pb at 352 KeV and ^{214}Bi at 609 KeV in the detergent samples. The ^{232}Th concentration was determined from the average concentrations of the decay products of ^{208}Tl at 583 KeV and ^{228}Ac at 911 KeV. Finally, the ^{40}K concentration was determined directly from the 1460 KeV photopeak.

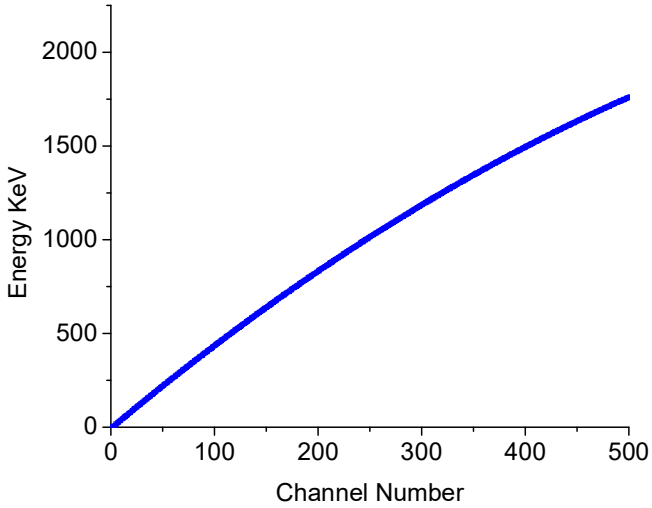

FIG. 1. Energy calibration for the NaI (Tl) scintillation detector.

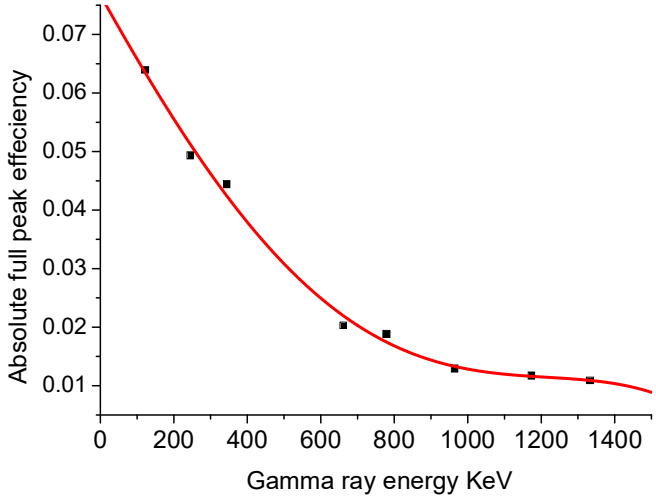

FIG. 2. Photopeak efficiency for gamma-ray energy of the NaI (Tl) detector.

2.3 Specific Activity Measurements

The radioactivity concentration (Bq.kg^{-1}) is defined as the activity per unit mass of the detergent samples. The specific activity of a radionuclide in detergent powder samples is given by the formula [10]:

$$A_s(Bq.kg^{-1}) = \frac{A_{net}}{\varepsilon \times I_\gamma \times m \times t} \quad (1)$$

where A_{net}, Iγ,m,t, and ε are the net count of the full range of photopeaks, the decay probability emission, the mass of the detergent sample, the time for running the samples, and the absolute efficiency of the photopeak at a certain energy, respectively.

2.4 Radium Equivalent (Ra_{eq})

To combine the specific activities of the elements and to assess the associated risks from materials containing different concentrations of natural radionuclides, such as ^{238}U, ^{232}Th, and ^{40}K, a single equivalent parameter is calculated based on the following equation [11]:

$$Ra_{eq} = A_U + 1.43A_{Th} + 0.077A_K \quad (2)$$

where A_U, A_{Th}, and A_K are the specific activities of ^{238}U, ^{232}Th, and ^{40}K (in Bq/kg), respectively. This equation defines Ra_{eq} as a single parameter, where 1Bq/kg of ^{238}U, 0.7 Bq/kg of ^{232}Th, and 13 Bq/kg of ^{40}K create a similar gamma-ray dose rate [12].

2.5 Outdoor and Indoor External Doses Rate

The D_{out} is calculated using gamma radiation from ^{238}U, ^{232}Th, and ^{40}K at a height of 1 meter above the Earth's surface. The radiation transfer factors for ^{238}U, ^{232}Th, and ^{40}K are 0.436 nGy.h^{-1} per Bq.kg^{-1}, 0.599 nGy.h^{-1} per Bq.kg^{-1}, and 0.0417 nGy.h^{-1} per Bq.kg^{-1}, respectively.

D_{out} is calculated using the following equation [13, 14]:

$$D_{0ut}(\text{nGy}.h^{-1}) = 0.436A_U + 0.599A_{Th} + 0.0417A_K \quad (3)$$

The absorbed dose rate can be converted to the indoor effective dose rate using the following conversion factors: 0.92 nGy.h^{-1} per Bq.kg^{-1} for ^{238}U, 1.1 nGy.h^{-1} per Bq.kg-1 for ^{232}Th, and 0.081 nGy.h^{-1} per Bq.kg^{-1} for ^{40}K. To calculate D_{in}, the following equation is utilized in conjunction with the previously stated conversion factors [15]:

$$D_{in}(\text{nGy}.h^{-1}) = 0.92A_U + 1.1A_{Th} + 0.081A_K \quad (4)$$

2.6 Annual Outdoor and Indoor External Effective Dose

The annual effective dose is divided into two categories: indoor annual effective dose (E_{in}) and outdoor annual effective dose (E_{out}). To calculate E_{out}, the occupancy dwelling factor (OF = 20% of 8760 h in a year) and the conversion factor (CF = 0.7 Sv Gy^{-1}) are applied. The following equations are used to determine E_{out}, which is used to convert the absorbed dose present in the atmosphere into an effective dose [1]:

$$E_{out} = D_{out}(nGyh^{-1}) \times 20\%\ of\ 8760h \times 0.7(Sv.Gy^{-1}) \quad (5)$$

$$= D_{out} \times 1.226\ \mu Sv.y^{-1} \quad (6)$$

The dose that a person receives indoors is known as E_{in}. The following equation can be used to derive the E_{in} from the indoor dose (D_{in}), which is the γ-ray dose within the building, the dose conversion factor (CF = 0.7 Sv Gy^{-1}), and the indoor occupancy factor (80% of a year) [16].

$$\mathrm{E_{in}} = \mathrm{D_{in}}(\mathrm{nGyh^{-1}}) \times 80\%\ \mathrm{of}\ 8760\mathrm{h} \times 0.7(\mathrm{Sv.Gy^{-1}}) \quad (7)$$

$$= \mathrm{D_{in}} \times 4.905\ \mu\mathrm{Sv.y^{-1}} \quad (8)$$

2.7 External Hazard Index (H_{ex})

The external hazard index is used to assess and quantify the risks associated with naturally occurring gamma radiation. It is calculated using the following equation [17]:

$$\mathrm{H_{ex}} = \frac{\mathrm{A_U}}{370} + \frac{\mathrm{A_{Th}}}{259} + \frac{\mathrm{A_K}}{4810} \quad (9)$$

The H_{ex} values must be less than 1, which corresponds to the highest R_{eq} value (370 Bq/kg).

2.8 Internal Hazard Index (H_{in})

Radon is harmful to the respiratory system and is responsible for more than 50% of the total annual effective dose from natural radionuclides, making it a major factor in internal exposure [1]. The internal hazard index (H_{in}) is calculated thus:

$$\mathrm{H_{in}} = \frac{\mathrm{A_U}}{185} + \frac{\mathrm{A_{Th}}}{259} + \frac{\mathrm{A_K}}{4810} \quad (10)$$

2.9 Excess Lifetime Cancer Risk (ELCR)

Using the annual effective gamma dose as a reference point, the following equations determine the indoor and outdoor ELCR [18]:

$$(\mathrm{ELCR})(\mathrm{Outdoor}) = (\mathrm{E_{out}}) \times \mathrm{LE} \times \mathrm{RF} \quad (11)$$

$$(\mathrm{ELCR})(\mathrm{Indoor}) = (\mathrm{E_{in}}) \times \mathrm{LE} \times \mathrm{RF} \quad (12)$$

where LE is the life expectancy (67 years) and RF (Sv^{-1}) is the fatal risk factor per Sievert, which is 0.05 [19].

3. Results and Discussion

Table 2 presents the calculated specific activity of ^{40}K, ^{232}Th, and ^{238}U found in the cleaning powder samples, while Fig. 3 depicts these results as a graph.

TABLE 2. The specific activity in $Bq.kg^{-1}$ of ^{238}U, ^{232}Th, and ^{40}K radionuclides in cleaning samples.

Sample code	Specific Activity in ($Bq.kg^{-1}$)		
	^{238}U	^{232}Th	^{40}K
ST1	1.148± 0.056	7.713± 0.303	70.279± 1.720
ST2	0.262± 0.027	0.142± 0.041	40.484± 1.305
ST3	0.011± 0.005	1.115± 0.115	46.754± 1.403
ST4	2.762± 0.086	9.256± 0.331	61.189± 1.605
ST5	0.143± 0.02	0.119± 0.038	28.027± 1.086
ST6	0.216± 0.024	1.59± 0.137	32.173± 1.164
ST7	ND	0.498± 0.077	29.269± 1.11
ST8	0.216± 0.024	0.985± 0.108	12.667± 0.73
ST9	ND	4.284± 0.225	11.068± 0.682
ST10	ND	1.24± 0.121	11.194± 0.686
ST11	0.227± 0.025	1.104± 0.114	21.862± 0.959
ST12	0.367± 0.031	0.403± 0.069	21.484± 0.951
ST13	0.189± 0.023	0.125± 0.038	15.234± 0.801
ST14	0.003± 0.003	1.75± 0.144	15.318± 0.803
ST15	0.317± 0.029	4.153± 0.222	5.892± 0.498
ST16	ND	0.819± 0.099	3.872± 0.404
ST17	0.005± 0.004	0.926± 0.105	8.438± 0.596
ST18	0.03± 0.009	3.643± 0.208	6.796± 0.535
ST19	0.111± 0.017	0.498± 0.077	22.599± 0.975
ST20	0.285± 0.028	0.237± 0.053	1.262± 0.230
ST21	ND	0.771± 0.096	1.515± 0.252
ST22	0.046± 0.011	1.258± 0.122	1.010± 0.206
ST23	0.123± 0.018	1.982± 0.153	2.399± 0.318
ST24	0.276± 0.027	1.394± 0.129	5.576± 0.484
ST25	0.011± 0.005	1.009± 0.109	3.956± 0.408

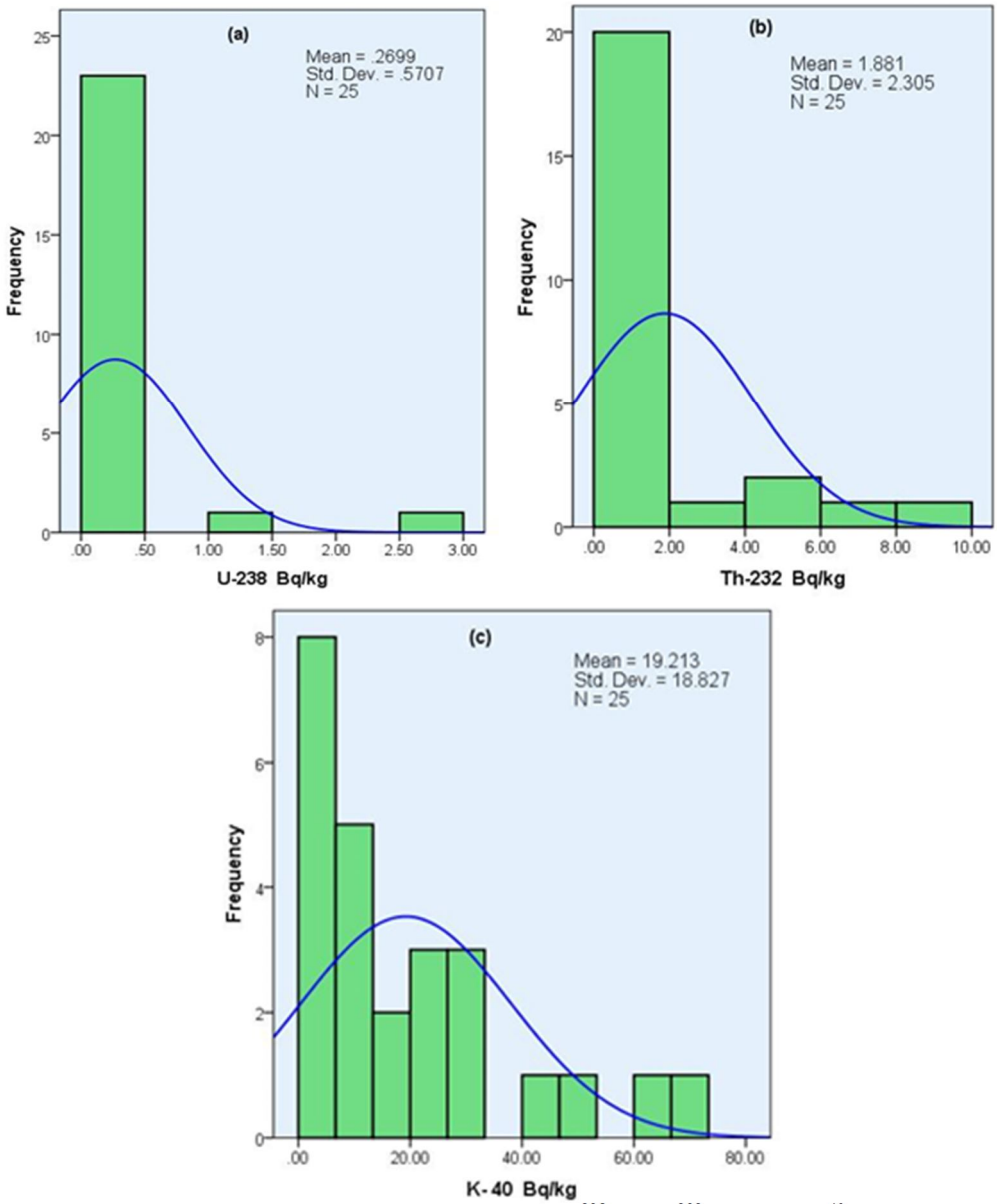

FIG. 3. The frequency distributions of (a) ^{238}U, (b) ^{232}Th, and (c) ^{40}K.

The specific activity of ^{238}U was detected in almost 80% of all samples, ranging from ND to 2.762±0.086 Bq/kg, with a mean value of 0.27±0.027 Bq/kg. For ^{232}Th, the specific activity varied from 1.115±0.115 Bq/kg to 9.256±0.331 Bq/kg with a mean value of 1.881±0.149 Bq/kg. Finally, the specific activity for ^{40}K ranged from 1.010± 0.206 Bq/kg to 70.279±1.720 Bq/kg with a mean value of 19.213±0.899 Bq/kg.

The highest specific activity for ^{238}U was detected in ST4 (Maria), which is lower than the value of 32 Bq/kg for raw materials declared by UNSCEAR [20]. ST4 (Maria) and ST1 (Bright) have the highest specific activity for ^{232}Th and ^{40}K, which are less than the limits of 45 and 412 Bq/kg, respectively, set by UNSCEAR [20].

Table 3 compares the results of the current investigation with values from previous studies obtained locally and in a neighboring country. The comparison reveals that, except for the activity concentration of ^{232}Th, the present analysis shows lower estimated activity concentrations of ^{238}U and ^{40}K radionuclides compared to those observed in previous studies [4-8].

TABLE 3. The measured activity concentrations compared to those of previous studies.

Country	Specific activities Bq/kg			References
	^{238}U	^{232}Th	^{40}K	
Iraq	22.342±6.984	4.664±2.438	45.642±30.637	[4]
Iraq	3.50 ± 0.60	1.77 ± 0.22	119.60 ± 7.27	[5]
Iraq	10.621±2.346	------	----------	[6]
Iraq	4.80±0.87	1.34±0.43	108.76±15.11	[7]
Saudi Arabia	MDA-85.4±5.9	MDA-7.19±0.8	26.0±1.8-133±10	[8]
Iraq-Kurdistan	0.27± 0.570	1.881± 2.305	19.213± 18.827	Present study

Figure 4 shows the determined Ra_{eq}. activity values for the cleaning powder samples, derived from Eq. (2). The Ra_{eq} values across all samples ranged from 1.963 Bq/kg to 82.533 Bq/kg, with an average of 22.248 Bq/kg. Fortunately, the Ra_{eq} values for all detergent samples examined are below the accepted limit of 370 Bq/kg [1]. Thus, these cleaning agents available on the market do not present a radioactive risk when used as cleaning powders.

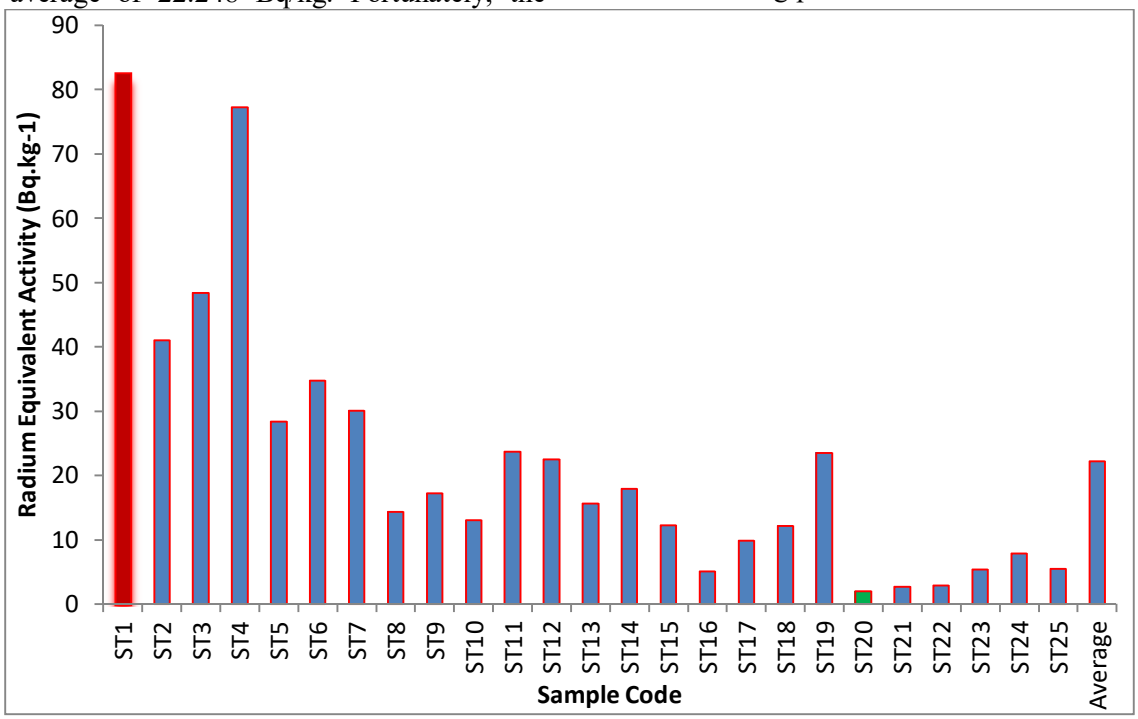

FIG. 4. Radium equivalent activity in cleaning powder samples.

The mean outdoor annual effective dose was 2.507 μSv y^{-1}, and the average indoor annual effective dose was 18.997μSv y^{-1}, both of which are lower than the global mean value of 410 μSv.y^{-1} [1]. As shown in column 6 of Table 4, the external hazard index (H_{ex}) values ranged from 0.002 (ST20) to 0.056 (ST4), with an average of 0.012. All H_{ex} values for the detergent samples were less than unity, indicating that using these detergent products for cleaning is safe in terms of radioactivity. The average H_{in} for the detergent samples was 0.013, with individual values ranging from 0.003 to 0.063, all of which were < 1 [21].

The (ELCR) for outdoor exposure, presented in column 8 of Table 4, ranged from 0.13×10^{-5} to 3.26×10^{-4}, with a mean value of 0.83×10^{-5}. For indoor exposure (last column of Table 4), the ELCR values ranged from 0.101×10^{-4} to 2.466×10^{-4}, with a mean of 0.627×10^{-4}. Consequently, the average ELCR value is less than the world's average value of 1.45×10^{-3} [16].

TABLE 4. The calculated radiological hazard indices for the studied detergent samples.

Sample code	D_{out} nGy.h-1	D_{in} nGy.h-1	E_{out} (μSv.y-1)	E_{in} (μSv.y-1)	H ex	Hin	ELCR (Outdoor)* 10^{-3}	ELCR (Indoor)* 10^{-3}
ST1	8.051	15.233	9.871	74.717	0.047	0.051	0.03257	0.24657
ST2	1.888	3.677	2.314	18.033	0.010	0.010	0.00764	0.05951
ST3	2.623	5.024	3.215	24.643	0.014	0.014	0.01061	0.08132
ST4	9.3	17.679	11.402	86.713	0.056	0.063	0.03763	0.28615
ST5	1.302	2.532	1.596	12.421	0.007	0.007	0.00527	0.04099
ST6	2.388	4.554	2.928	22.335	0.013	0.014	0.00966	0.07371
ST7	1.519	2.919	1.862	14.318	0.008	0.008	0.00615	0.04725
ST8	1.212	2.308	1.486	11.32	0.007	0.008	0.0049	0.03736
ST9	3.027	5.609	3.712	27.51	0.019	0.019	0.01225	0.09078
ST10	1.21	2.271	1.483	11.138	0.007	0.007	0.00489	0.03676
ST11	1.671	3.193	2.049	15.663	0.009	0.010	0.00676	0.05169
ST12	1.297	2.521	1.591	12.368	0.007	0.008	0.00525	0.04081
ST13	0.792	1.545	0.971	7.577	0.004	0.005	0.00321	0.025
ST14	1.688	3.169	2.07	15.542	0.010	0.010	0.00683	0.05129
ST15	2.872	5.337	3.521	26.179	0.018	0.019	0.01162	0.08639
ST16	0.652	1.214	0.799	5.956	0.004	0.004	0.00264	0.01965
ST17	0.909	1.707	1.114	8.371	0.005	0.005	0.00368	0.02762
ST18	2.478	4.585	3.039	22.49	0.016	0.016	0.01003	0.07422
ST19	1.289	2.48	1.58	12.167	0.007	0.007	0.00522	0.04015
ST20	0.319	0.625	0.391	3.066	0.002	0.003	0.00129	0.01012
ST21	0.525	0.971	0.644	4.764	0.003	0.003	0.00212	0.01572
ST22	0.816	1.508	1	7.395	0.005	0.005	0.0033	0.0244
ST23	1.341	2.487	1.644	12.199	0.008	0.009	0.00542	0.04026
ST24	1.188	2.24	1.457	10.986	0.007	0.008	0.00481	0.03625
ST25	0.774	1.44	0.949	7.062	0.005	0.005	0.00313	0.02331
Average	2.045	3.873	2.507	18.997	0.012	0.013	0.00827	0.06269

4. Conclusion

The study has provided data on the specific activity of primordial radionuclides in some of the common cleaning powders in the north-eastern Kurdistan region of Iraqi markets. The uptake of the natural radionuclides of ^{238}U, ^{232}Th, and ^{40}K is low in samples compared to the maximum values (32, 45, and 412 Bq/kg) declared by (UNSCEAR, 2008). All the samples contain a significant concentration of ^{40}K. However, the level of ^{40}K is relatively higher than that of ^{238}U and ^{232}Th.

The average annual external effective dose indoors and outdoors is less than the global average value of 70 μSv/y, and the obtained value of (ELCR) is less than the level 1.45 * 10^{-3} indicated by (National Cancer Institute, 2009). Therefore, there is no significant radiological risk to the general public from using the examined detergent formulations as cleaning agents

It has been determined that the amounts of natural radioactivity in the detergent powders available in Erbil-Iraq are well below the permissible ranges and do not present any radioactive risk to users.

References

[1] UNSCEAR, "Effects of Ionizing Radiation". (United Nations, New York, 2000), p. 453

[2] UNSCEAR, "Effects of Atomic Radiation", (United Nations, New York, 2000).

[3] Tai, L.H.T. and Nardello-Rataj, V., "Application of Personal Care Detergent Formulations", Handbook of detergents, Part E: Applications, (CRC Press Taylor & Francis Group, New York, 2009), p. 123

[4] Abojassim, A.A., Abd, H.H., Hamed, D.N., and Abdullah, A.A., J. Radiat. Res. Appl. Sci., 7 (4) (2014) 532.

[5] Abojassim, A.A., Al-Gazaly, H.H., and Obide, E.S., Asian J. Chem., 28 (10) (2016) 2173.

[6] Abojassim, A.A., Al-kufI, F.A., and Mohsen, A.A., "Determination of Effective Radium Content and Uranium Concentrations for the Soap and the Detergent Powder Samples in Iraq". (Current Pediatric Research, 2017).

[7] Alabood, A.S., Kadhim, S.H., Harjan, A.H., Ahmed, A.Q., and Hadi, M.Y., J. Phys.: Conf. Ser., 1294 (2019) 22024.

[8] Alshahri, F., J. Radiat. Res. Appl. Sci., 13 (1) (2020) 426.

[9] Tufail, M. et al., Environ. Sci. Pollut. Res., 19 (8) (2012) 3327.

[10] Mohammad, K.K. and AL-Ramahy, S.A., J. Kufa-Phys., 3 (1) (2011) 1.

[11] Ibraheim, N.M., Shawky, S., and Amer, H.A., Appl. Radiat. Isot., 46 (5) (1995) 297.

[12] Chowdhury, M., Alam, M., and Ahmed, A., J. Radioanal. Nucl. Chem., 231 (1–2) (1998) 117.

[13] Jacob, P., Paretzke, H.G., Rosenbaum, H., and Zankl, M., Radiat. Prot. Dosim., 14 (4) (1986) 299.

[14] Kocher, D.C. and Sjoreen, A.L., Health Phys., 48 (2) (1985) 193.

[15] Commission, E.-E. et al., Radiat. Prot., 112 (1999) 1.

[16] Qureshi, A.A., Tariq, S., Din, K.U., Manzoor, S., Calligaris, C., and Waheed, A., J. Radiat. Res. Appl. Sci., 7 (4) (2014) 438.

[17] Beretka, J. and Matthew, P.J., Health Phys., 48 (1) (1985) 87.

[18] Ravisankar, R., Chandrasekaran, A., Vijayagopal, P., Venkatraman, B., Senthilkumar, G., Eswaran, P., and Rajalakshmi, A., Radiat. Phys. Chem., 81 (12) (2012) 1789.

[19] Ahmed, A.H., Jafir, A.O. and Abdullah, H.M., Jordan J. Phys., 13 (1) (2020) 73.

[20] UNSCEAR, "Effects of Ionizing Radiation", United Nations Scientific Committee on the Effects of Atomic Radiation (UNSCEAR) 2006 Report, Volume I: Report to the General Assembly, Scientific Annexes A and B. United Nations, (2008).

[21] ICRP, "Protection of the Public in Situations of Prolonged Radiation Exposure". (2000).

Volume 17, Number 3, 2024. pp. 371-382

Jordan Journal of Physics

ARTICLE

Radon Gas Detection of Soil Samples in Primary Schools at Najaf City, Iraq

Rukia J. Dosh[a], **Ali K. Hasan**[b] and **Ali A. Abojassim**[a]

[a] *Department of Physics, Faculty of Science, University of Kufa, Al-Najaf, Iraq.*
[b] *Department of Physics, Faculty of Education for Girls, University of Kufa, Al-Najaf, Iraq.*

Doi: **https://doi.org/10.47011/17.3.12**
Received on: 05/12/2022; *Accepted on: 24/01/2023*

Abstract: The radon concentration, specific activity of ^{226}Ra (C_{Ra}), and ^{238}U concentrations (C_U) in soil samples from 100 primary schools of Al-Najaf province, Iraq, were measured to determine the safety of students and staff using the CR-39 nuclear track detector based on the sealed can technique. The mean values of ^{222}Rn concentration in the air space of the container (C) and the soil sample (C_{Rn}) were 23.53±1.149Bq/m3 and 960.38±47 Bq/m3, respectively. The mean values of C_{Ra} and C_U were 0.035±0.002 Bq/kg and 0.043±0.002 ppm, respectively. The ^{222}Rn,^{226}Ra, and ^{238}U concentrations were lower than the worldwide level. Radiological parameters such as annual effective dose (AED) and radon exhalation rate per unit mass (E_M) and per unit surface (E_S) also were determined. The results indicate normal levels for these parameters, except for higher values of AED in some primary schools, according to UNSCEAR data.

Keywords: Radon, CR-39 detector, Soil of primary schools, Al-Najaf province.

1. Introduction

Radon is a radioactive, colorless, odorless, and tasteless noble gas that naturally occurs as an indirect decay product of uranium or thorium in the soil. It was first discovered by F.E. Dorn in 1900. Its most widespread and stable isotope, ^{222}Rn, has a half-life of approximately 3.8 days and contains 99 percent of radon. Unlike radon, a noble gas, uranium and all of its daughters (up to lead) are solid elements. The short-lived radionuclides ^{218}Po, ^{214}Pb, ^{214}Bi, and ^{214}Po, produced as ^{222}Rn decays, are called radon daughters or progeny. Eventually, ^{206}Pb (stable lead) is produced. On average, 33 Bq/kg^3 of natural uranium (mainly ^{238}U) may be detected throughout the Earth's crust, and consequently, in major earthen building materials. The gas dissipates fast in open areas; however, it can accumulate inside buildings, particularly in regions where the underlying ground is permeable and has a higher-than-average uranium concentration. Radon is present in all rocks and soils, both outdoors and indoors. Since outdoor air is constantly mixed and diluted, radon and its daughters rarely accumulate to dangerous levels. On the other hand, indoors, where ventilation may be limited, radon and its daughters can accumulate, reaching levels many orders of magnitude higher than those seen outdoors. Because radon's decay products can stick to ambient aerosols, inhaling them can cause the particles to be trapped in the lungs, delivering a dose to the lung's lining via alpha particle emission. As a result, instead of the radon progenitor, it is the radon progeny that poses the greatest health risk. The majority of radon exposure occurs indoors due to the high

Corresponding Author: Ali Abid Abojassim **Email**: ali.alhameedawi@uokufa.edu.iq

percentage of time people spend indoors and the elevated indoor radon concentrations compared to outdoor concentrations. Radon and its daughters are the primary sources of natural radiation exposure for the population, and many lung cancer cases have been documented as a result [2, 3]. The primary radiological exposure that humans experience internally comes from ^{222}Rn. Geological and geophysical characteristics, as well as atmospheric factors like barometric pressure and rain, significantly impact the radon concentration range in the air. Radon can leak into the environment through rock fissures and soil pores close to the earth [4, 5].

Radon enters buildings through various channels, including soil gas, which infiltrates through tiny pores in the floor, cavities in interior walls, structural connections, gaps in walls, communication lines, building materials, and drinking water [1]. According to studies of radon's behavior in the geological environment, there is a clear relationship between indoor radon rates and soil gas concentration [2]. Therefore, testing for radon levels in as many schools and homes as feasible is one of the most efficient and effective strategies to lessen the risks to students in schools and other facilities [4]. Radon exposure in schools could have a significant public health effect. The chance of developing lung cancer in children exposed to radon could be as much as three times higher than in adults exposed to similar levels of radon. This is because children's lungs are not the same shape as those of adults, and children breathe more quickly than adults. Children generally spend more time indoors and are more vulnerable to environmental hazards. On average, Iraqi children spend 5 hours in school buildings daily, five days a week. Schools are also workplaces for teachers, administrators, and service staff, who may spend even more time in school buildings than students [6].

In order to determine long-term mean radon concentrations that can be used as the baseline data, passive measuring techniques are required. These techniques have been demonstrated to be effective and suitable for identifying radon and its daughters in soil samples [7-9]. This research aimed to establish a baseline for the Al-Najaf province by measuring the alpha emitters ^{222}Rn, ^{226}Ra, and ^{238}U in soil samples taken from elementary schools. Values of radiological hazard indices like AED, E_M, and E_S were also investigated.

2. The Study Area

The studied area of Al Najaf (Fig. 1) is located in southwestern Iraq, about 160 km southwest of Baghdad. It is situated at the intersection of longitude 44019E and latitude 31059N with an elevation of 70 meters above sea level [3].

One hundred primary public schools within Najaf city were chosen to study the concentrations of ^{222}Rn, ^{226}Ra, and ^{238}U in the soil of these schools. The locations of these schools were identified using a GPS, as detailed in Table 1, and plotted using a GIS approach (ArcGIS 10.7.1.), as depicted in Fig. 1. Table 1 displays the chosen schools' names, locations, codes, types, dates of establishment, and coordinates.

TABLE 1. Information on schools included in the study.

No.	Name	Location	Code	Type	Date	longitude	latitude
1	Alghaffari	Aljodaydat-2	p1	boys	1919	436150.9	3539909
2	Altahdhib	Aljodaydat-4	p2	boys	1952	435944.2	3539177
3	Malik Aliashtir	Aljodaydat-4	p3	boys	1954	436064.3	3539492
4	Halif Alquran	Al.Mothana	p4	boys	1958	438415.8	3540403
5	Aishab Alkasa	Aljodaydat-3	p5	boys	1959	436456.2	3539630
6	Alhaidariya	Aljodaydat-1	p6	boys	1933	436900.3	3540156
7	Altaysir	Al.Karama	p7	boys	1964	438040.7	3542154
8	Aleasifa	Al.Askan	p8	boys	1964	438584.1	3541338
9	Dabel Al Khuzaie	Al.Moalmen	p9	boys	1968	437753.4	3539855
10	Damascus Al'asasia	Alhussein	p10	boys	1973	436954.3	3541674
11	Alsaadiq	Aljodaydat-3	p11	boys	1953	437108.5	3539453
12	Baghdad Al'asasia	Imam Mahdi	p12	boys	1964	437675.5	3539487
13	Alghari	Al.Ansar	p13	boys	1964	438410	3538993
14	Alamam Alhadi Al'asasia	Al.Ameer	p14	boys	1968	437237.6	3541669
15	Eidun	Al.Shorta	p15	boys	1973	438586.6	3539133
16	Mustafa Jawad	Al.Karama	p16	boys	1980	438162.7	3542366

No.	Name	Location	Code	Type	Date	longitude	latitude
17	Alwathbi	Al.Ansar	p17	boys	1980	437318.7	3539070
18	Sharif Al-Razi	Al.Zahraa	p18	boys	1980	438536.5	3540399
19	Alshaeb	Aloroba	p19	boys	1982	437260.1	3545330
20	Al-Safi Najafi	Alhawraa	p20	boys	1984	437418.1	3540301
21	Badr Al-Kubra	AL gari	p21	boys	1984	436555.7	3542982
22	Umm Qasr	Aloroba	p22	girls	1985	437645	3545648
23	Alzainabiya	Aljodaydat-4	p23	girls	1937	436100.7	3539435
24	Sikina	Old City (AlBuraq)	p24	girls	1958	435403.2	3540360
25	Ramallah	Old City (AlHoiesh)	p25	girls	1958	435289.5	3539809
26	Alfadila	Alsaad	p26	girls	1955	437282.4	3540847
27	Alsanabil	Al.Karama	p27	girls	1963	437555.3	3542139
28	Fath	Alhussein	p28	girls	1968	437122.1	3541664
29	Aleafa	Aljodaydat-4	p29	girls	1963	436205.9	3539477
30	Bilqis Al'asasia	Alhanana	p30	girls	1980	437418.1	3540301
31	Al-Faraged	Al.Askan	p31	girls	1964	438584.1	3541338
32	Almaqasid	Al.Moalmen	p32	girls	1964	437533.9	3539752
33	Dijula	Aljodaydat-4	p33	girls	1964	436003.5	3539253
34	Mustafa Gamal El Din	Algahdeer	p34	girls	1968	438195.4	3542141
35	Alanisaf	Al.Mothana	p35	girls	1973	438062.6	3540571
36	Birdaa	Aljodaydat-2	p36	girls	1953	435724.3	3539683
37	Al-Bariq	Al.Moalmen	p37	girls	1979	437773.1	3539563
38	Alamiani	Al.Ansar	p38	girls	1975	438284.5	3539077
39	Nahj Al-Balaghah	Al.Ameer	p39	girls	1976	439542.8	3541498
40	Alshiyma	Alshueara	p40	girls	1982	436966.2	3542333
41	Alrisala	Al.Zahraa	p41	girls	1980	440067.1	3540535
42	Alturath Alearabiu	Aljodaydat-3	p42	girls	1981	437178.2	3539517
43	Tabuk	AL gari	p43	girls	1981	436376.5	3542842
44	Almakasib	Alhawraa	p44	girls	1980	439420.7	3539935
45	Safin	Aladala	p45	boys	1984	439918	3542398
46	Altadhia	Alwafaa (Alhindiya homes)	p46	girls	1986	438173.5	3546738
47	Habib Bin Mazahir Al Asadi	Al.Askary	p47	boys	1986	437051.9	3548134
48	Fataa Alaslam	Alwafaa (Alhindiya homes)	p48	boys	1986	437569	3546526
49	Almasoudi	Alnasor	p49	boys	1988	434719.8	3544694
50	Haifa	Aljameea	p50	boys	1988	436583.3	3546154
51	Alhuru Alriyahiu	Almakrama	p51	boys	1988	436527.9	3547370
52	Alyaequbi	Almilad	p52	girls	2001	435123.5	3546295
53	Alainsar	Al.Ansar	p53	boys	1989	439450	3539128
54	Almujd	Alishtiraki	p54	girls	1989	438880.2	3540828
55	Alsahl Aliakhdaru	Alnasor	p55	boys	1989	434740.7	3545084
56	Altabirsiu	Alqadisiya	p56	girls	1998	440709.1	3540836
57	Alabirar	Alresalah	p57	boys	1989	436215.2	3545075
58	Almuhajirin	Al.Ameer	p58	girls	1989	440263.9	3541439
59	Alrahma	Aloroba	p59	boys	1989	436926.1	3546038
60	6 Kanun	Al.Askary	p60	girls	1990	437684.3	3547671
61	Albayeat Alkubraa	Almakrama	p61	girls	1990	436707.1	3547077
62	Sawr	Technical Institute	p62	mixed	1992	439985	3538170
63	Albaraq	Al.Askary	p63	girls	1989	437014.8	3548494
64	Alraazi	Alresalah	p64	girls	1994	436215.2	3545078
65	Aliraq Alhuru	Al.Askary	p65	boys	1988	437727.2	3547168
66	Saeed Bin Jubair	Alqadisiya	p66	boys	1988	440751	3540817
67	Aldhaariat	New Almilad	p67	girls	2012	434860.7	3545810
68	Alrabab	Alhussein	p68	girls	1998	436951.7	3541683
69	Altawhid	Aljamea	p69	boys	1999	438828.5	3544025
70	Ibrahim Al-Khalil	Aljamea	p70	boys	2000	439024.4	3544753
71	Aalhaqu Almubin	Aloroba	p71	girls	2000	437260.1	3545330
72	Alamam Alrida	Aljamea	p72	girls	2001	439249	3544157
73	Alrafah	Aljamea	p73	girls	2001	439075.4	3544962
74	Ali Al-Akbar	Aladala	p74	girls	2002	439427.9	3542919
75	Aliaskandaria	Aljodaydat-4	p75	girls	2004	436211	3538606

No.	Name	Location	Code	Type	Date	longitude	latitude
76	Aljamie	Campus	p76	mixed	2004	437436.7	3548248
77	Alshahid Mahdi Alhakim	Alsalam	p77	girls	2005	437404.1	3544440
78	Albalad Al'amin	Alforat	p78	girls	2006	438923.4	3542786
79	Khayr Albariya	Alsalam	p79	boys	2007	437920.6	3543540
80	Alduea' Almustajab	Alsalam	p80	girls	2007	437920.6	3543539
81	Eabuwd Ghafla	Abotalib	p81	boys	2007	435028.7	3543777
82	Eadnan Zuin	Alkudos	p82	boys	2007	436911.5	3538568
83	Aliaetimad	Abotalib	p83	girls	2007	435028.7	3543777
84	Altaqwaa	AL gari	p84	boys	2009	436376.5	3542842
85	Albayinat	AL gari	p85	girls	2009	436376.5	3542842
86	Almawlaa Almuqadas	Alrahma	p86	boys	2010	435429.1	3542789
87	Alsaafaat	Alrahma	p87	girls	2010	435429.1	3542789
88	Abi Talib	Alforat	p88	boys	2010	439004.8	3542798
89	Mohammed Jawad Mughniyeh	Alwafaa	p89	boys	2011	437972.2	3545979
90	Sayf Alhaqi	Alrahma	p90	boys	2011	435429.1	3542789
91	Alrusul	Alrahma	p91	girls	2011	435429.1	3542789
92	Altasnim	Alnidaa	p92	boys	2013	434270.2	3548592
93	Alsalam	majmae Alsalam	p93	boys	2013	436949.2	3544255
94	Almathir	Alnidaa	p94	girls	2014	435106.2	3549344
95	Jarf Alnasr	Alsalam	p95	girls	2014	436969.2	3544094
96	Alamam Zayn Aleabidin	Alwafaa	p96	girls	2002	435412.3	3550484
97	Alnasamat	New Almilad	p97	girls	2015	435005.5	3547121
98	Alshahid Karim Alkhaqani	Alwafaa	p98	boys	2018	438734.5	3546279
99	Aleawali	Algahdeer village	p99	boys	2018	437154.1	3549829
100	Eata' Alnajaf	Algahdeer village	p100	boys	2018	436722.2	3550365

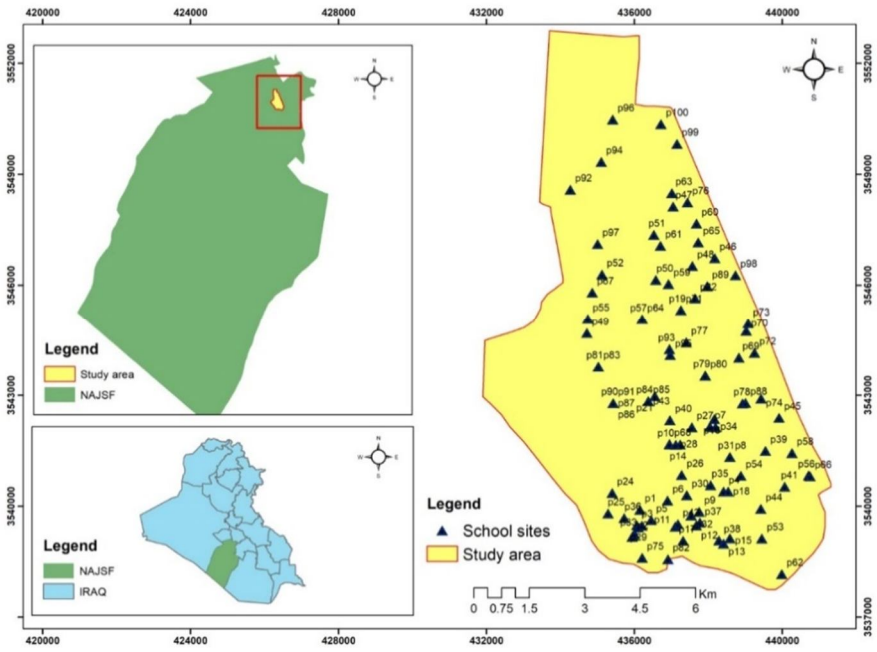

FIG. 1. A map of the field of study.

3. Materials and Methods

A total of 100 soil samples were collected at a depth of 15 cm from primary schools in Al Najaf city. Each sample was assigned a special code (refer to Table 1) and then sent to the laboratory at the Faculty of Science, University of Kufa. Each soil sample was dried inside an electrical furnace set to 105ºC for about 2-3 hours until all moisture was removed. Then the samples were crushed using a mill and passed through a 2 mm sieve. After this process, the samples were placed in cylindrical plastic containers with screw caps to provide a tight seal and prevent the release of radon gases.

To attain secular equilibrium, all samples were stored for at least one month. [4]. Following the sealed cup procedure, 70 g of the dried materials was placed at the bottom of a

cylinder measuring 7 cm in height and 5 cm in diameter, as shown in Fig. 2. A CR-39 detector with a thickness of 1 mm, a density of 0.32 gm/m^3, and dimensions of 2.5 cm × 2.5 cm was fixed at the top of a plastic container. The containers were tightly sealed with covers for an exposure period to radon for 90 days.

After the exposure period, the detectors were removed from the containers and placed in a solution of 6.25N NaOH in a water bath at 98° C for one hour [5]. The detectors were then removed from the bath, properly rinsed, and cleaned using distilled water to remove digging leftovers from the surface. Following the chemical process, these detectors were dried and scanned with an optical microscope at a magnification of 400X to calculate the number of tracks per cm^2 for each detector according to the following equation [6].

$$\text{The density of tracks } (\rho) = \frac{number\ of\ tracks\ in\ sample}{Area\ of\ field\ view} \quad (1)$$

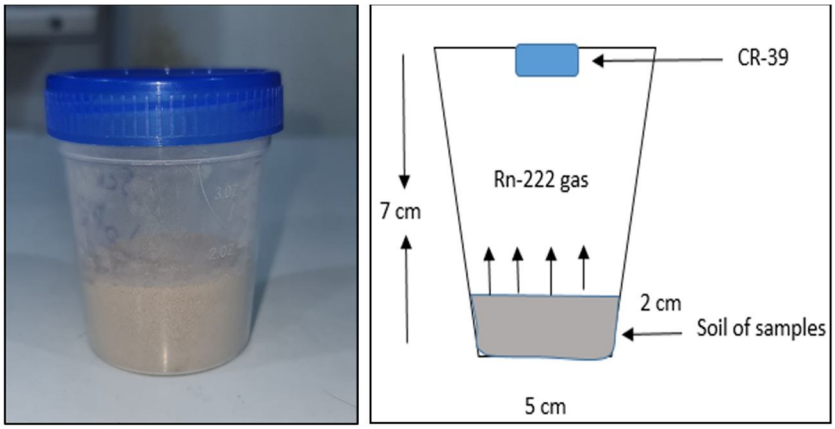

FIG. 2. The radon dosimeter used in this study.

3.1 Theoretical Considerations

The closed container's radon concentration (C) can be calculated as [7]:

$$C\left(\frac{Bq}{m^3}\right) = \frac{\rho}{K\,T} \quad (2)$$

where K represents the calibration factor for the CR-39 detector (K= 0.28±0.043 Track.cm^{-2} /Bq.m^{-3}.day). The calibration of the CR-39 detector was determined using a standard source of ^{226}Ra (radon source) with exposure times of 0.5, 1, 1.5, 2, 2.5, and 3 days. T is the exposure time (90 days).

The radon concentration (C_{Rn}) in the soil samples can be calculated as [8]:

$$C_{Rn}\left(\frac{Bq}{m^3}\right) = \frac{C\,\lambda_{Rn}\,h\,T}{l} \quad (3)$$

where λ_{Rn} represents the radon decay constant, h is the distance between the soil sample and the CR-39 detector, and l is the soil sample thickness in the container.

The specific activity of ^{226}Ra, $^{226}C_{Ra}$, in the soil samples can be determined using the following equation [9]:

$$C_{Ra}\left(\frac{Bq}{kg}\right) = \frac{C\,h\,A}{M} \quad (4)$$

where the distance between the soil surface of the sample inside the container and the CR39 detector is given by h, A is the sample's surface area, and M is the sample's mass.

Using the secular equilibrium property of uranium-238 and radon-222, we can find the uranium-238 concentrations (C_U) in units ppm, which depend on the mass of uranium-238 (M_U) and mass of the soil sample (M), as follows [8, 10]:

$$C_U(ppm) = \frac{M_U(mg)}{M\ (kgm)} \quad (5)$$

The annual effective dose (AED) was determined using the following relation [8]:

$$AED\ \left(\frac{mSv}{y}\right) = 0.4 \times 0.8 \times 8760 \times 9.0 \times 10^{-6}\ C \quad (6)$$

where 0.4 is the equilibrium factor, 0.8 is the occupancy factor for residents, 8760 is the number of hours in a year, 9×10^{-6} mSv/ Bq.h.m^{-3} is the dose effective factor, and C is the indoor Rn concentration factor.

Also, radon surface exhalation rate (E_S) and mass exhalation rate (E_M) were evaluated using the following formulas [8, 10]:

$$E_S = \frac{C\,V\,\lambda}{A\,T_e} \quad (7)$$

$$E_M = \frac{C\,V\,\lambda}{M\,T_e} \quad (8)$$

where V is the air volume in the cup in m^3 and T_e is the effective exposure time, determined by employing the formula [11]:

$$T_e = T - \frac{1}{\lambda}\left(1 - e^{-\lambda T}\right) \quad (9)$$

4. Results and Discussion

The radon concentration (C) results in the closed container, radon concentration (C_{Rn}) in the soil samples, the specific activity of ^{226}Ra (C_{Ra}), and uranium-238 concentrations (C_U) are presented in Table 2. The radon concentration in the air space of the container varied from 7.47Bq/m^3 in school P5 to 66.51 Bq/m^3 in school P74, with an average value of 23.53±1.149Bq/m^3. The C_{Rn} values ranged from 305.02 to 2714.66 Bq/m^3, with an average of 960.38±47 Bq/m^3. The maximum values of both C and C_{Rn} are lower than the world average for radon gas in air, which is 100 Bq/m^3 according to WHO [12] and 7400 Bq/m^3 [8, 13].

The specific activity of ^{226}Ra showed a minimum value of 0.011 Bq/kg in school P5 and a maximum value of 0.099 Bq/kg in school P74, with an average of 0.035±0.002 Bq/kg. The uranium-238 concentrations (C_U) varied from 0.014 to 0.123 ppm, with an average value of 0.043±0.002 ppm. The maximum values of C_{Ra} and C_U were below the global average values of 35 Bq/kg for C_{Ra} [14] and 11 mg/kg (ppm) for uranium-238 concentrations [15].

Fig. 3 illustrates the concentration of radon in the air space of the container, showing that all results were below the worldwide level. Figure 4 shows the histograms of the distribution of radon concentration in both air space and soil samples within the container, specific activity of ^{226}Ra, and concentration of ^{238}U. These distributions exhibit a normal (bell-shaped) distribution pattern.

TABLE 2. The radon concentration (C) in the closed container, the radon concentration in the soil samples (C_{Rn}), specific activity of ^{226}Ra,($^{226}C_{Ra}$), and the uranium-238 concentrations (C_U) for studied schools.

Sample code	C (Bq/m^3)	C_{Rn}(Bq/m^3)	C_{Ra}(Bq/kg)	C_U(ppm)
P 1	19.43	793.05	0.029	0.036
P 2	14.87	606.98	0.022	0.027
P 3	31.39	1281.07	0.047	0.058
P 4	16.44	671.04	0.025	0.030
P 5	7.47	305.02	0.011	0.014
P 6	25.41	1037.06	0.038	0.047
P 7	23.91	976.06	0.036	0.044
P 8	35.87	1464.08	0.054	0.066
P 9	25.41	1037.06	0.038	0.047
P 10	28.40	1159.07	0.042	0.052
P 11	8.22	335.52	0.012	0.015
P 12	52.31	2135.12	0.078	0.097
P 13	16.44	671.04	0.025	0.030
P 14	17.94	732.04	0.027	0.033
P 15	23.91	976.06	0.036	0.044
P 16	16.44	671.04	0.025	0.030
P 17	58.29	2379.14	0.087	0.108
P 18	17.94	732.04	0.027	0.033
P 19	16.44	671.04	0.025	0.030
P 20	26.90	1098.06	0.040	0.050
P 21	13.45	549.03	0.020	0.025
P 22	23.91	976.06	0.036	0.044
P 23	15.77	643.59	0.024	0.029
P 24	15.69	640.54	0.023	0.029
P 25	16.59	677.14	0.025	0.031
P 26	28.40	1159.07	0.042	0.052
P 27	26.53	1082.81	0.040	0.049
P 28	21.52	878.45	0.032	0.040
P 29	20.92	854.05	0.031	0.039
P 30	19.95	814.40	0.030	0.037

Sample code	C (Bq/m^3)	C_{Rn}(Bq/m^3)	C_{Ra}(Bq/kg)	C_U(ppm)
P 31	20.92	854.05	0.031	0.039
P 32	35.72	1457.98	0.053	0.066
P 33	11.96	488.03	0.018	0.022
P 34	14.95	610.03	0.022	0.028
P 35	22.42	915.05	0.033	0.041
P 36	17.94	732.04	0.027	0.033
P 37	35.12	1433.58	0.052	0.065
P 38	37.37	1525.09	0.056	0.069
P 39	17.94	732.04	0.027	0.033
P 40	23.91	976.06	0.036	0.044
P 41	16.44	671.04	0.025	0.030
P 42	17.41	710.69	0.026	0.032
P 43	44.84	1830.10	0.067	0.083
P 44	41.10	1677.60	0.061	0.076
P 45	26.90	1098.06	0.040	0.050
P 46	26.90	1098.06	0.040	0.050
P 47	48.58	1982.61	0.073	0.090
P 48	14.95	610.03	0.022	0.028
P 49	11.96	488.03	0.018	0.022
P 50	13.45	549.03	0.020	0.025
P 51	11.96	488.03	0.018	0.022
P 52	10.46	427.02	0.016	0.019
P 53	26.16	1067.56	0.039	0.048
P 54	16.44	671.04	0.025	0.030
P 55	12.70	518.53	0.019	0.023
P 56	23.91	976.06	0.036	0.044
P 57	20.92	854.05	0.031	0.039
P 58	46.33	1891.11	0.069	0.086
P 59	19.43	793.05	0.029	0.036
P 60	20.92	854.05	0.031	0.039
P 61	25.41	1037.06	0.038	0.047
P 62	23.17	945.55	0.035	0.043
P 63	31.39	1281.07	0.047	0.058
P 64	21.67	884.55	0.032	0.040
P 65	16.44	671.04	0.025	0.030
P 66	11.96	488.03	0.018	0.022
P 67	20.92	854.05	0.031	0.039
P 68	23.91	976.06	0.036	0.044
P 69	25.41	1037.06	0.038	0.047
P 70	23.91	976.06	0.036	0.044
P 71	20.92	854.05	0.031	0.039
P 72	20.92	854.05	0.031	0.039
P 73	52.31	2135.12	0.078	0.097
P 74	66.51	2714.66	0.099	0.123
P 75	20.92	854.05	0.031	0.039
P 76	56.05	2287.63	0.084	0.103
P 77	25.41	1037.06	0.038	0.047
P 78	35.87	1464.08	0.054	0.066
P 79	28.40	1159.07	0.042	0.052
P 80	20.92	854.05	0.031	0.039
P 81	31.39	1281.07	0.047	0.058
P 82	16.44	671.04	0.025	0.030
P 83	10.84	442.28	0.016	0.020
P 84	13.45	549.03	0.020	0.025
P 85	11.96	488.03	0.018	0.022
P 86	14.20	579.53	0.021	0.026
P 87	32.88	1342.08	0.049	0.061
P 88	43.34	1769.10	0.065	0.080
P 89	20.92	854.05	0.031	0.039

Sample code	C (Bq/m^3)	C_{Rn}(Bq/m^3)	C_{Ra}(Bq/kg)	C_U(ppm)
P 90	20.92	854.05	0.031	0.039
P 91	9.72	396.52	0.015	0.018
P 92	13.45	549.03	0.020	0.025
P 93	25.41	1037.06	0.038	0.047
P 94	22.42	915.05	0.033	0.041
P 95	13.45	549.03	0.020	0.025
P 96	8.22	335.52	0.012	0.015
P 97	25.41	1037.06	0.038	0.047
P 98	23.24	948.60	0.035	0.043
P 99	13.23	539.88	0.020	0.024
P 100	13.45	549.03	0.020	0.025
Minimum	7.47	305.02	0.011	0.014
Maximum	66.51	2714.66	0.099	0.123
Average±S.E	23.53 ±1.149	960.38±47	0.035±0.002	0.043±0.002

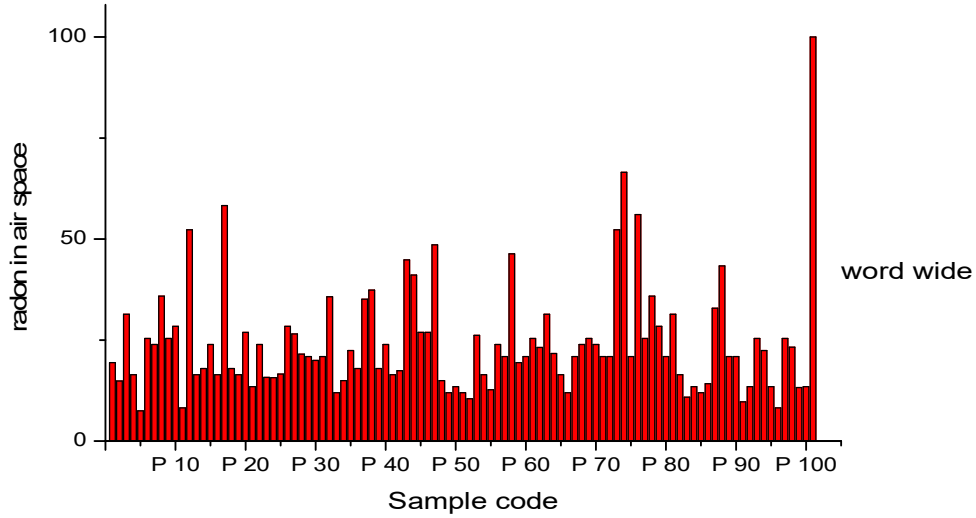

FIG. 3. Radon concentration in the air space of the container for the studied schools and worldwide.

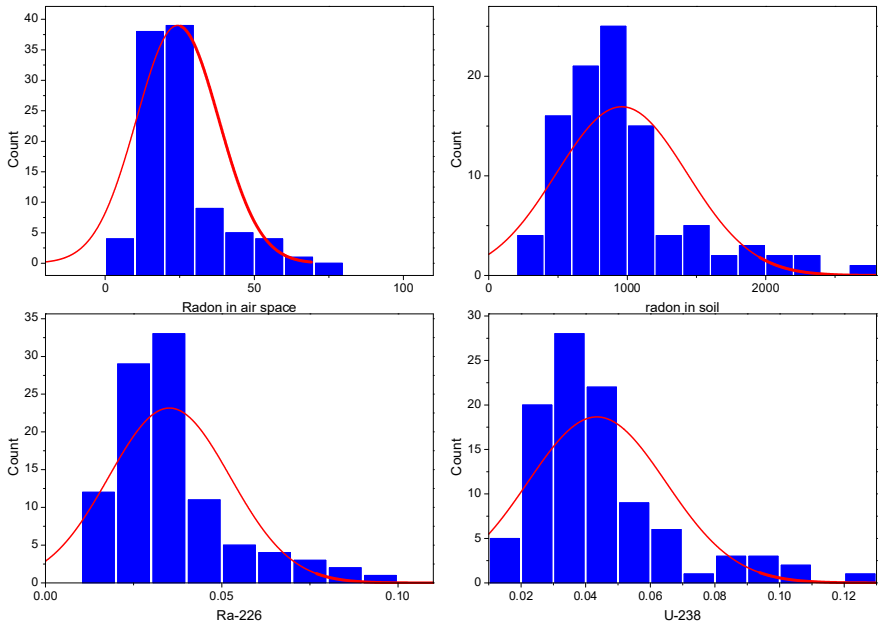

FIG. 4. The histogram of the C, C_{Rn}, C_{Ra}, and C_U concentrations distribution in the selected schools.

The dose obtained by the students and staff in the studied schools was calculated using the annual effective dose related to radon concentrations, as described by Eq. (6). Table 3 displays the results of the AED and radon exhalation rate per unit mass (E_M) and per unit

surface (E_S) for studied schools. The AED values ranged from 0.189 to 1.678 mSv/y, with a mean of 0.59±0.029 mSv/y.

The AED values for all studied schools were within the action levels set by the ICRP (3–10 mSv/y) [16] and by the UNSCEAR (1.2 mSv/y) [17]. However, exceptions were noted in samples P12, P17, P47, P73, P74, and P76, as shown in Fig. 5.

The radon exhalation rate per unit mass (E_M) values varied from 0.059 to 0.528 mBq/kg.h with an average of 0.19±0.009 mBq/kg.h.

The radon exhalation rate per unit surface (E_s) values ranged from 2.076 to 18.475 mBq/m^2.h, with an average of 6.54±0.319 mBq/m^2.h. The study showed that the radon exhalation rates varied according to radon concentrations inside the container. Also, it was found that all values of E_S in the present study were below the action level of 57.6 Bqm^2.h [17].

TABLE 3. The annual effective dose (AED), mass exhalation rate (E_M), and surface exhalation rate for monitored schools.

Sample code	AED (mSv/y)	E_M (mBq/kg.h)	E_S (mBq/m^2.h)
P 1	0.490	0.154	5.397
P 2	0.375	0.118	4.131
P 3	0.792	0.249	8.719
P 4	0.415	0.130	4.567
P 5	0.189	0.059	2.076
P 6	0.641	0.202	7.058
P 7	0.603	0.190	6.643
P 8	0.905	0.285	9.964
P 9	0.641	0.202	7.058
P 10	0.716	0.225	7.888
P 11	0.207	0.065	2.283
P 12	1.320	0.415	14.531
P 13	0.415	0.130	4.567
P 14	0.452	0.142	4.982
P 15	0.603	0.190	6.643
P 16	0.415	0.130	4.567
P 17	1.471	0.463	16.192
P 18	0.452	0.142	4.982
P 19	0.415	0.130	4.567
P 20	0.679	0.214	7.473
P 21	0.339	0.107	3.737
P 22	0.603	0.190	6.643
P 23	0.398	0.125	4.380
P 24	0.396	0.125	4.359
P 25	0.419	0.132	4.608
P 26	0.716	0.225	7.888
P 27	0.669	0.211	7.369
P 28	0.543	0.171	5.979
P 29	0.528	0.166	5.812
P 30	0.503	0.158	5.543
P 31	0.528	0.166	5.812
P 32	0.901	0.284	9.923
P 33	0.302	0.095	3.321
P 34	0.377	0.119	4.152
P 35	0.566	0.178	6.228
P 36	0.452	0.142	4.982
P 37	0.886	0.279	9.757
P 38	0.943	0.297	10.379
P 39	0.452	0.142	4.982
P 40	0.603	0.190	6.643
P 41	0.415	0.130	4.567
P 42	0.439	0.138	4.837
P 43	1.131	0.356	12.455
P 44	1.037	0.326	11.417

Sample code	AED (mSv/y)	E_M (mBq/kg.h)	E_S (mBq/m^2.h)
P 45	0.679	0.214	7.473
P 46	0.679	0.214	7.473
P 47	1.226	0.386	13.493
P 48	0.377	0.119	4.152
P 49	0.302	0.095	3.321
P 50	0.339	0.107	3.737
P 51	0.302	0.095	3.321
P 52	0.264	0.083	2.906
P 53	0.660	0.208	7.266
P 54	0.415	0.130	4.567
P 55	0.321	0.101	3.529
P 56	0.603	0.190	6.643
P 57	0.528	0.166	5.812
P 58	1.169	0.368	12.870
P 59	0.490	0.154	5.397
P 60	0.528	0.166	5.812
P 61	0.641	0.202	7.058
P 62	0.584	0.184	6.435
P 63	0.792	0.249	8.719
P 64	0.547	0.172	6.020
P 65	0.415	0.130	4.567
P 66	0.302	0.095	3.321
P 67	0.528	0.166	5.812
P 68	0.603	0.190	6.643
P 69	0.641	0.202	7.058
P 70	0.603	0.190	6.643
P 71	0.528	0.166	5.812
P 72	0.528	0.166	5.812
P 73	1.320	0.415	14.531
P 74	1.678	0.528	18.475
P 75	0.528	0.166	5.812
P 76	1.414	0.445	15.569
P 77	0.641	0.202	7.058
P 78	0.905	0.285	9.964
P 79	0.716	0.225	7.888
P 80	0.528	0.166	5.812
P 81	0.792	0.249	8.719
P 82	0.415	0.130	4.567
P 83	0.273	0.086	3.010
P 84	0.339	0.107	3.737
P 85	0.302	0.095	3.321
P 86	0.358	0.113	3.944
P 87	0.830	0.261	9.134
P 88	1.094	0.344	12.040
P 89	0.528	0.166	5.812
P 90	0.528	0.166	5.812
P 91	0.245	0.077	2.699
P 92	0.339	0.107	3.737
P 93	0.641	0.202	7.058
P 94	0.566	0.178	6.228
P 95	0.339	0.107	3.737
P 96	0.207	0.065	2.283
P 97	0.641	0.202	7.058
P 98	0.586	0.184	6.456
P 99	0.334	0.105	3.674
P 100	0.339	0.107	3.737
Minimum	0.189	0.059	2.076
Maximum	1.678	0.528	18.475
Average±S.E	0.59 ±0.029	0.19 ±0.009	6.54 ±0.319

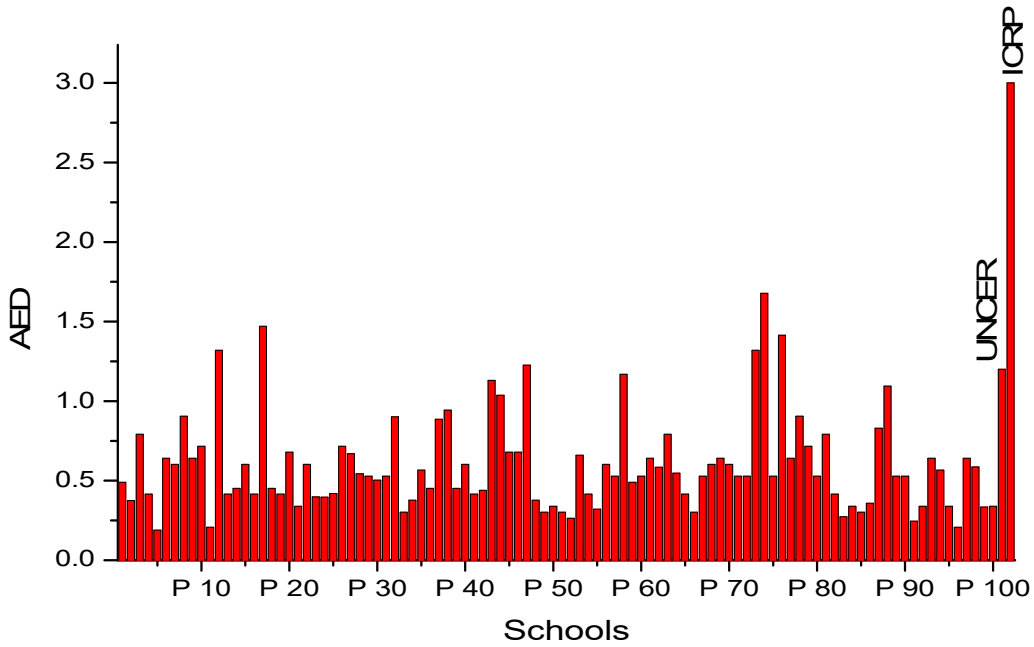

FIG. 5. The annual effective dose (AED) for measured schools, UNSCEAR, and ICRP.

The differences in the measurement of radon concentration among the soil samples from the studied schools under study are attributed to the varying concentrations of ^{238}U and ^{226}Ra within these soils. Schools with higher ^{238}U and ^{226}Ra content in the soil exhibit increased exhalation rates, as illustrated in Fig. 5. Also, these differences depend on the density, porosity, permeability, grain size of the soil samples, and other factors.

Fig. 6 shows the correlation between the ^{226}Ra concentration in the soil samples and the radon exhalation rates (E_M and E_s) for the investigated schools. The figure demonstrates a linear relationship between the ^{226}Ra content and exhalation rates, with a correlation coefficient of 0.999 for both.

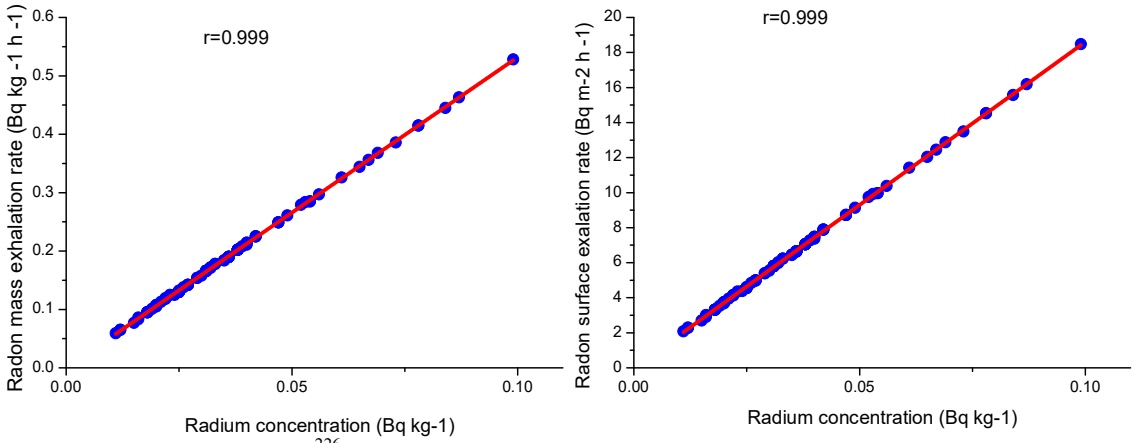

FIG. 6. The correlation between ^{226}Ra concentration and radon exhalation rates (EM and Es) for the investigated schools.

Conclusions

The study of radon concentration in the air and soil of containers with soil samples in primary schools in Najaf indicates normal levels. The average C, C_{Rn}, $226C_{Ra}$, and C_U values are significantly lower than the worldwide limit. The results of the surface exhalation rate (E_s) are lower than the global limit. The measurements of the AED for the studied schools are lower than those recommended by the ICRP and the results of UNSCEAR, except for samples P12, P17, P47, P73, P74, and P76. Consequently, the occupants of these schools (children and staff) are not at risk of radiological exposure from their immediate surroundings.

References

[1] Daniel, V., Kremena, I., Zdenka, S., Bistra, K., and Viktor, B., Rom. J. Phys., 58 (2013) S328.

[2] Abojassim, A.A., Muhamad, Q.B., Jafer, N.A., and Mohammed, H.A., Jordan J. Phys., 15 (4) (2022) 353.

[3] Abojassim, A.A., Groundwater Sustain. Dev., 11 (2020) 100476.

[4] Abojassim, A.A. and Rasheed, L.H., Int. J. Energy Environ., 10 (2019) 143.

[5] Tate, B. and Long, S., "Acceptance testing of the tasl radon dosimetry system: ARPANSA Technical Report No. 175", Commonwealth of Australia, (2016).

[6] Al-Gharabi, M. and Al-Hamzawi, A., Iran. J. Med. Phys., 17 (2020) 220.

[7] Abojassima, A.A., Shltake, A.R., Najam, L.A. and Merzaa, I.R., Pak. J. Sci. Ind. Res. Ser. A: Phys. Sci., 60 (2017) 72.

[8] Ibrahim, A.A., Hashim, A.K., and Abojassim, A., Ann. Agri Bio Res., 26 (2021) 125.

[9] Azam, A., Naqvi, A., and Srivastava, D., Nucl. Geophys., 9 (1995) 653.

[10] Al-Omari, S., International Journal of Low Radiation, 10 (2015) 61.

[11] Khan, M.S., Naqvi, A.H., Azam, A., and Srivastava, D.S., Iran. J. Radiat. Res., 8 (4) (2011) 207.

[12] WHO, "WHO handbook on indoor radon: a public health perspective", (World Health Organization, 2009).

[13] Gupta, P. and Kaur, G., Int. J. Comput. Appl., 119 (2015) 1.

[14] UNSCEAR, "Sources, Effects and Risks of Ionizing Radiation", Report to the General Assembly, with Scientific Annexes, 9210600029, (2016).

[15] UNSCEAR, "Sources and effects of ionizing radiation". Report to the General Assembly, with scientific annex, (1996).

[16] Brenner, D., "Protection against radon-222 at home and at work. ICRP publication 65", (Taylor & Francis, 1994).

[17] UNSCEAR, "Sources, effects and risks of ionizing radiation", (1988).

الجداول: تعطى الجداول أرقاما متسلسلة يشار إليها في النص. ويجب طباعة كل جدول على صفحة منفصلة مع عنوان فوق الجدول. أما الحواشي التفسيرية، التي يشار إليها بحرف فوقي، فتكتب أسفل الجدول.

الرسوم التوضيحية: يتم ترقيم الأشكال والرسومات والرسومات البيانية (المخططات) والصور، بصورة متسلسلة كما وردت في النص.

تقبل الرسوم التوضيحية المستخرجة من الحاسوب والصور الرقمية ذات النوعية الجيدة بالأبيض والأسود، على ان تكون أصيلة وليست نسخة عنها، وكل منها على ورقة منفصلة ومعرفة برقمها بالمقابل. ويجب تزويد المجلة بالرسومات بحجمها الأصلي بحيث لا تحتاج إلى معالجة لاحقة، وألا تقل الحروف عن الحجم 8 من نوع Times New Roman، وألا تقل سماكة الخطوط عن 0.5 وبكثافة متجانسة. ويجب إزالة جميع الألوان من الرسومات ما عدا تلك التي ستنشر ملونة. وفي حالة إرسال الرسومات بصورة رقمية، يجب أن تتوافق مع متطلبات الحد الأدنى من التمايز (1200 dpi Resolution) لرسومات الأبيض والأسود الخطية، و 600 dpi للرسومات باللون الرمادي، و300 dpi للرسومات الملونة. ويجب تخزين جميع ملفات الرسومات على شكل (jpg)، وأن ترسل الرسوم التوضيحية بالحجم الفعلي الذي سيظهر في المجلة. وسواء أرسل المخطوط بالبريد أو عن طريق الشبكة (Online)، يجب أرسال نسخة ورقية أصلية ذات نوعية جيدة للرسومات التوضيحية.

مواد إضافية: تشجع المجلة الباحثين على إرفاق جميع المواد الإضافية التي يمكن أن تسهل عملية التحكيم. وتشمل المواد الإضافية أي اشتقاقات رياضية مفصلة لا تظهر في المخطوط.

المخطوط المنقح (المعدّل) والأقراص المدمجة: بعد قبول البحث للنشر وإجراء جميع التعديلات المطلوبة، فعلى الباحثين تقديم نسخة أصلية ونسخة أخرى مطابقة للأصلية مطبوعة بأسطر مزدوجة، وكذلك تقديم نسخة إلكترونية تحتوي على المخطوط كاملا مكتوبا على Microsoft Word for Windows 2000 أو ما هو استجد منه. ويجب إرفاق الأشكال الأصلية مع المخطوط النهائي المعدل حتى لو تم تقديم الأشكال إلكترونيا. وتخزن جميع ملفات الرسومات على شكل (jpg)، وتقدم جميع الرسومات التوضيحية بالحجم الحقيقي الذي ستظهر به في المجلة. ويجب إرفاق قائمة ببرامج الحاسوب التي استعملت في كتابة النص، وأسماء الملفات على قرص مدمج، حيث يعلَم القرص بالاسم الأخير للباحث، وبالرقم المرجعي للمخطوط للمراسلة، وعنوان المقالة، والتاريخ. ويحفظ في مغلف واقٍ.

حقوق الطبع

يُشكِّل تقديم مخطوط البحث للمجلة اعترافاً صريحاً من الباحثين بأنّ مخطوط البحث لم يُنْشَر ولم يُقَدَّم للنشر لدى أي جِهَة أخرى كانت وبأي صيغة ورقية أو إلكترونية أو غيرها. ويُشترط على الباحثين ملء أنموذج يَنُصُّ على نقْل حقوق الطبع لتُصبح ملكاً لجامعة اليرموك قبل الموافقة على نشر المخطوط. ويقوم رئيس التحرير بتزويد الباحثين بإنموذج نقل حقوق الطبع مع النسخة المُرْسَلَة للتنقيح. كما ويُمنع إعادة إنتاج أيِّ جزء من الأعمال المنشورة في المجلّة من دون إذن خَطِّيٍّ مُسْبَق من رئيس التحرير.

إخلاء المسؤولية

إن ما ورد في هذه المجلة يعبر عن آراء المؤلفين، ولا يعكس بالضرورة آراء هيئة التحرير أو الجامعة أو سياسة اللجنة العليا للبحث العلمي أو وزارة التعليم العالي والبحث العلمي. ولا يتحمل ناشر المجلة أي تبعات مادية أو معنوية أو مسؤوليات عن استعمال المعلومات المنشورة في المجلة أو سوء استعمالها.

الفهرسة: المجلة مفهرسة في:

Scopus	**Emerging Sources Citation Index (ESCI)** Journal Impact Factor 2022 0.7
ULRICHSWEB GLOBAL SERIALS DIRECTORY	

معلومات عامة

المجلة الأردنية للفيزياء هي مجلة بحوث علميّة عالمية متخصصة مُحكمة تصدر بدعم من صندوق دعم البحث العلمي والابتكار، وزارة التعليم العالي والبحث العلمي، عمان، الأردن. وتقوم بنشر المجلة عمادة البحث العلمي والدراسات العليا في جامعة اليرموك، إربد، الأردن. وتنشر البحوث العلمية الأصيلة، إضافة إلى المراسلات القصيرة Short Communications، والملاحظات الفنية Technical Notes، والمقالات الخاصّة Feature Articles، ومقالات المراجعة Review Articles، في مجالات الفيزياء النظرية والتجريبية، باللغتين العربية والإنجليزية.

تقديم مخطوط البحث

تقدم المخطوطات إلكترونيًا عن طريق موقع المجلة: https://jjp.yu.edu.jo/index.php/jjp

ويجري تحكيمُ البحوثِ الأصيلة والمراسلات القصيرة والملاحظات الفنية من جانب مُحكِّمين اثنين في الأقل من ذوي الاختصاص والخبرة. وتُشَجِّع المجلة الباحثين على اقتراح أسماء المحكمين. أما نشر المقالات الخاصّة في المجالات الفيزيائية النَشِطَة، فيتم بدعوة من هيئة التحرير، ويُشار إليها كذلك عند النشر. ويُطْلَب من كاتب المقال الخاص تقديم تقرير واضح يتّسم بالدقة والإيجاز عن مجال البحث تمهيداً للمقال. وتنشر المجلةُ أيضاً مقالات المراجعة في الحقول الفيزيائية النشطة سريعة التغيُّر، وتُشَجّع كاتبي مقالات المراجعة أو مُستَكتبيها على إرسال مقترحٍ من صفحتين إلى رئيس التحرير. ويُرْفَق مع البحث المكتوب باللغة العربية ملخص (Abstract) وكلمات دالة (Keywords) باللغة الإنجليزية.

ترتيب مخطوط البحث

يجب أن تتم طباعة مخطوط البحث ببنط 12 نوعه Times New Roman، وبسطر مزدوج، على وجه واحد من ورق A4 (21.6 × 27.9 سم) مع حواشي 3.71 سم ، باستخدام معالج كلمات ميكروسوفت وورد 2000 أو ما استُجِدَ منه. ويجري تنظيم أجزاء المخطوط وفق الترتيب التالي: صفحة العنوان، الملخص، رموز التصنيف (PACS)، المقدّمة، طرق البحث، النتائج، المناقشة، الخلاصة، الشكر والعرفان، المراجع، الجداول، قائمة بدليل الأشكال والصور والإيضاحات، ثَمَّ الأشكال والصور والإيضاحات. وتُكْتَب العناوين الرئيسة بخطٍ **غامق**، بينما تُكْتَب العناوين الفرعية بخطٍ *مائل*.

صفحة العنوان: وتشمل عنوان المقالة، أسماء الباحثين الكاملة وعناوين العمل كاملة. ويكتب الباحث المسؤول عن المراسلات اسمه مشارا إليه بنجمة، والبريد الإلكتروني الخاص به. ويجب أن يكون عنوان المقالة موجزا وواضحا ومعبرا عن فحوى (محتوى) المخطوط، وذلك لأهمية هذا العنوان لأغراض استرجاع المعلومات.

الملخص: المطلوب كتابة فقرة واحدة لا تزيد على مائتي كلمة، موضحة هدف البحث، والمنهج المتبع فيه والنتائج وأهم ما توصل إليه الباحثون.

الكلمات الدالة: يجب أن يلي الملخص قائمة من 4-6 كلمات دالة تعبر عن المحتوى الدقيق للمخطوط لأغراض الفهرسة.

PACS: يجب إرفاق الرموز التصنيفية، وهي متوافرة في الموقع http://www.aip.org/pacs/pacs06/pacs06-toc.html.

المقدمة: يجب أن توضّح الهدف من الدراسة وعلاقتها بالأعمال السابقة في المجال، لا أن تكون مراجعة مكثفة لما نشر (لا تزيد المقدمة عن صفحة ونصف الصفحة مطبوعة).

طرائق البحث (التجريبية / النظرية): يجب أن تكون هذه الطرائق موضحة بتفصيل كاف لإتاحة إعادة إجرائها بكفاءة، ولكن باختصار مناسب، حتى لا تكون تكرارا للطرائق المنشورة سابقا.

النتائج: يستحسن عرض النتائج على صورة جداول وأشكال حيثما أمكن، مع شرح قليل في النص ومن دون مناقشة تفصيلية.

المناقشة: يجب أن تكون موجزة وتركز على تفسير النتائج.

الاستنتاج: يجب أن يكون وصفا موجزا لأهم ما توصلت إليه الدراسة ولا يزيد عن صفحة مطبوعة واحدة.

الشكر والعرفان: الشكر والإشارة إلى مصدر المنح والدعم المالي يكتبان في فقرة واحدة تسبق المراجع مباشرة.

المراجع: يجب طباعة المراجع بأسطر مزدوجة ومرقمة حسب تسلسلها في النص. وتكتب المراجع في النص بين قوسين مربعين. ويتم اعتماد اختصارات الدوريات حسب نظام Wordlist of Scientific Reviewers.

Subscription Form

Jordan Journal of PHYSICS

An International Peer-Reviewed Research Journal issued by the Support of the Scientific Research and Innovation Support Fund

Published by the Deanship of Research & Graduate Studies, Yarmouk University, Irbid, Jordan

Name: ..... الأسم:

Specialty:..... التخصص:

Address: ..... العنوان:

P.O. Box:..... صندوق البريد:

City & Postal Code: ..... المدينة/الرمز البريدي:

Country: ..... الدولة:

Phone: ..... رقم الهاتف:

Fax No:..... رقم الفاكس:

E-mail:..... البريد الإلكتروني:

No. of Subscription: ..... عدد الإشتراكات:

Method of Payment:..... طريقة الدفع:

Amount Enclosed:..... المبلغ المرفق:

Signature: ..... التوقيع:

Cheques should be paid to Deanship of Research and Graduate Studies - Yarmouk University.

I would like to subscribe to the Journal
For

- One Year
- Two Years
- Three Years

One Year Subscription Rates

	Inside Jordan	Outside Jordan
Individuals	JD 8	€ 40
Students	JD 4	€ 20
Institutions	JD 12	€ 60

Correspondence

Subscriptions and Sales:

Prof. Mahdi Salem Lataifeh
Deanship of Research and Graduate Studies
Yarmouk University
Irbid – Jordan
Telephone: 00 962 2 711111 Ext. 2075
Fax No.: 00 962 2 7211121

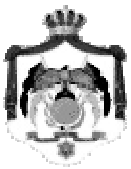

المملكة الأردنية الهاشمية

جامعة اليرموك

المجلة الأردنية
للفيزياء

مجلة بحوث علمية عالمية متخصصة محكّمة

تصدر بدعم من صندوق دعم البحث العلمي والابتكار

المجلد (17)، العدد (3)، آب 2024م / صفر 1446هـ

المجلة الأردنية

للفيزياء

مجلة بحوث علمية عالمية محكّمة

المجلد (17)، العدد (3)، آب 2024م / صفر 1446هـ

المجلة الأردنية للفيزياء: مجلة علمية عالمية متخصصة محكّمة تصدر بدعم من صندوق دعم البحث العلمي والإبتكار، عمان، الأردن، وتصدر عن عمادة البحث العلمي والدراسات العليا، جامعة اليرموك، إربد، الأردن.

ترسل البحوث إلى العنوان التالي:

الأستاذ الدكتور مهدي سالم لطايفة

رئيس تحرير المجلة الأردنية للفيزياء

عمادة البحث العلمي والدراسات العليا، جامعة اليرموك

إربد ، الأردن

هاتف 7211111 2 962 00 **فرعي** 2075

E-mail: *jjp@yu.edu.jo* **Website**: *http://Journals.yu.edu.jo/jjp*